Final Report
U.S. Department of Energy

Material Property Estimation for Direct Detection of DNAPL using Integrated Ground-Penetrating Radar Velocity, Imaging and Attribute Analysis

Technical Report: BSU CGISS 04-03

Principal Investigator: John H. Bradford
Institution: Center for Geophysical Investigation of the Shallow Subsurface
Boise State University
Co P.I.'s: W. Stephen Holbrook, Scott B. Smithson
Institution: University of Wyoming

Project Number:70052
Grant Number: DE-FG07-99ER15008
Grant Project Officers: Nicholas Woodward, Chet Miller
Project Duration: 9/15/1999 - 9/14/2004

TABLE OF CONTENTS

1 EXECUTIVE SUMMARY 1

2 RESEARCH OBJECTIVES 4

3 METHODS AND RESULTS 5
- 3.1 Principles of GPR Investigation 5
- 3.2 Principles of DNAPL Detection with GPR 6
- 3.3 Development and Evaluation of Data Processing Methodologies 8
  - 3.3.1 Velocity Analysis of Multi-Fold GPR Data 8
  - 3.3.2 GPR AVO Analysis: The Thin Bed Problem 10
  - 3.3.3 Attenuation Analysis 11
- 3.4 Summary of Field Results 12
  - 3.4.1 3D Multi-offset, Multi-polarization Acquisition and Processing of GPR Data: a Controlled DNAPL Spill Experiment 13
  - 3.4.2 Savannah River Site 16
  - 3.4.3 Hanford Site (Appendix A) 18
  - 3.4.4 Hill Air Force Base 23
  - 3.4.5 Former Wurtsmith AFB NETTS 26
  - 3.4.6 Cape Fear Wood Preserving Site 29
  - 3.4.7 Cincinnati, Ohio Refinery Site 31
  - 3.4.8 Controlled DNAPL Injection at the Dover National Test Site (NETTS) 33
  - 3.4.9 Discussion of Field Results 33

4 RELEVANCE, IMPACT AND TECHNOLOGY TRANSFER 34

5 PROJECT PRODUCTIVITY 37

6 PERSONNEL SUPPORTED 38

7 PUBLICATIONS 39

8 INTERACTIONS 40

9 TRANSITIONS 41

10 LITERATURE CITED 41

APPENDIX A: APPLYING REFLECTION TOMOGRAPHY IN THE POST MIGRATED DOMAIN TO GROUND PENETRATING RADAR DATA 47

APPENDIX B: GROUND-PENETRATING RADAR THEORY AND APPLICATION OF THINBED OFFSET-DEPENDENT REFLECTIVITY 73

APPENDIX C: ALGORITHM FOR GPR_RAY_MOD 118

APPENDIX D: CALCULATING ATTENUATION ATTRIBUTES 131

APPENDIX E: 3D MULTI-OFFSET, MULTI-POLARIZATION ACQUISITION AND PROCESSING OF GPR DATA: A CONTROLLED DNAPL SPILL EXPERIMENT 135

APPENDIX F: COMPLETE TECHNICAL REPORT OF GPR EXPLORATION ACTIVITIES AT HILL AIR FORCE BASE 150

APPENDIX G: GPR OFFSET DEPENDENT REFLECTIVITY ANALYSIS FOR CHARACTERIZATION OF A HIGH-CONDUCTIVITY LNAPL PLUME 223

APPENDIX H: APPLICATION OF TWO-PASS MIGRATION TO GROUND-PENETRATING RADAR DATA 239

APPENDIX I: CHARACTERIZATION OF AN AQUITARD AND DIRECT DETECTION OF LNAPL AT HILL AIR FORCE BASE USING GPR AVO AND MIGRATION VELOCITY ANALYSES 255

1 EXECUTIVE SUMMARY

The focus of this project is direct detection of DNAPLs, specifically chlorinated solvents, via material property estimation from multi-fold surface ground-penetrating radar (GPR) data. We combine state-of-the-art GPR processing methodology with quantitative attribute analysis and material property estimation to determine the location and extent of residual and/or pooled DNAPL in both the vadose and saturated zones. An important byproduct of our research is state-of-the-art imaging which allows us to pinpoint attribute anomalies, characterize stratigraphy, identify fracture zones, and locate buried objects.

Chlorinated solvents have much lower electric permittivity and conductivity than water. An electrical property contrast is induced when solvents displace water in the sediment column resulting in an anomalous GPR signature. To directly identify zones of DNAPL contamination, we focus on three aspects of reflected wave behavior - propagation velocity, frequency dependent attenuation, and amplitude variation with offset (AVO). Velocity analysis provides a direct estimate of electric permittivity, attenuation analysis provides a measure of effective conductivity, and AVO behavior is used to estimate the permittivity ratio at a reflecting boundary, or to measure subwavelength permittivity anomalies. Areas of anomalously low electric permittivity and conductivity may be identified as potential DNAPL rich zones. LNAPLs have similar electrical properties to DNAPL and therefore detection methodologies are complementary. For this reason, our work has included characterization of both LNAPL and DNAPL contamination. It is important to note that the GPR NAPL signature is non-unique, ie in most cases it is possible that an uncontaminated earth model could produce a similar result. The key to successful application of these methodologies is in identifying significant departures from the background GPR response that are consistent with the expected NAPL anomaly. Further, it is important to incorporate other available information in data interpretation such as the geologic setting and typical distribution geometries for naturally occurring fluids or lithologies.

Our previous modeling and test pit studies suggested that these methodologies had significant potential to detect DNAPL source terms. The next phase in developing the technologies was detailed field testing. To this end, this project was field oriented with three primary objectives:

1) Develop a suite of methodologies for direct detection of DNAPLs from surface GPR data
2) Controlled field verification at well characterized, contaminated sites
3) Exploratory contaminant detection in a field setting to be verified through direct sampling

We have met or exceeded all objectives outlined in our original workplan, including an extensive field effort involving over 12 sites located throughout the continental U.S. (Figure 1). Additionally we have conducted a number of ancillary experiments at little or no additional cost to the project. We have acquired full scale 2D and 3D multi-offset, multi polarization datasets at 10 research sites in 8 field areas. These include:

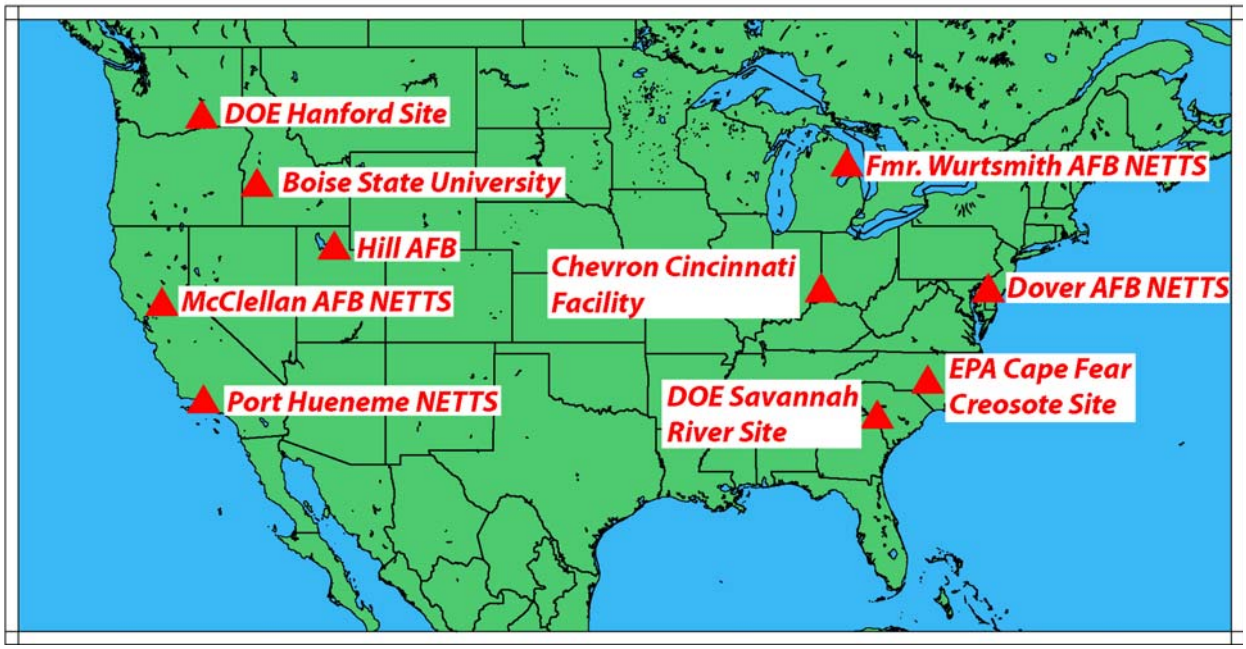

Figure 1. Locations of GPR experiments conducted during this study.

- DOE Savannah River Site (A-14 Outfall)
- DOE Hanford Site (Z-9 Trench, 618-10 Burial Ground/316-4 Crib, 100N-65 Interception Trench)
- Hill Air Force Base (Operable Unit 1)
- Dover Air Force Base - Dover National Test Site NETTS
- Former Wurtsmith Air Force Base NETTS (FT-02)
- EPA Cape Fear Wood Preserving Site, Fayetville, NC.
- Former Chevron Refinery, Cincinnati, OH.
- Boise State University, Boise, ID (Laboratory Scale Experiment).

The data are comprised of 11,354 linear m of 25-30 fold, multi-offset GPR data which includes 8,528 m^2 of multi-fold 3D acquisition. It should be noted that our original work plan called for acquiring datasets at two National Environmental Technology Test Sites (NETTS) in California (Port Hueneme and McClellan AFB). Feasibility tests during September, 2001, demonstrated that soil conditions at these sites were not suitable for GPR investigation, and we began to search for additional contaminated test sites. This led to the identification of the former Chevron refinery outside Cincinnati, OH (LNAPL), and the Cape Fear Wood Preserving Site (DNAPL) as substitute test sites. Additionally, we conducted an extensive controlled injection experiment at the Dover National Test Site NETTS, Dover Air Force Base, DE. Although we are continuing to work with these data, unexpectedly high noise levels prevented us from successfully imaging the DNAPL injection. This led us to conduct a laboratory scale, controlled injection experiment at Boise State University in which the DNAPL injection was successfully imaged.

We have developed a suite of software for detailed modeling and quantitative processing of GPR data. Packages include broadband reflectivity modeling (MOD_{TB}), ray based, full

Table 1. Summary of field experiment results for this project.

RESEARCH SITE	RESULTS SUMMARY NAPL DETECTED/METHOD
DOE Savannah River A-014 Outfall	**Unconfirmed Detection:** DNAPL (PCE/TCE) /PSDM velocity analysis
DOE Hanford 100-N-65 Trench	**Unconfirmed Detection:** LNAPL (Weathered Diesel Fuel)/ Attenuation, Reflection Tomography
DOE Hanford 618-10 Burial Ground/316-4 Crib	**Possible LNAPL/Radionuclide Detection:** Imaged likely contaminant transport route/Reflection Tomography, Attenuation
DOE Hanford 200W Z-9 Trench	Could not reach target depth, measured near surface water content variability/Reflection Tomography
Hill AFB Operable Unit 1	**Confirmed Detection:** Weathered mixed LNAPL (jet fuel, light oil)/PSDM Velocity Analysis, Thinbed AVO
Former Wurtsmith AFB NETTS FT-02 Plume	**Confirmed Detection:** Weathered LNAPL (jet fuel),/Reflection Tomography, Thinbed AVO, Attenuation
EPA Cape Fear Wood Preserving Site	**Confirmed Detection:** DNAPL (creosote)/Reflection Tomography, Attenuation
Former Chevron Refinery	**Confirmed Detection:** LNAPL (gasoline)/Reflection Tomography
Controlled Spill Experiment BSU Tank Facility	**Confirmed Detection:** DNAPL (mixed solvent)/Reflection Tomography
Dover National Test Site, Controlled Spill	Could not reach target, Successful 3D imaging of reactive barrier emplacement
Port Hueneme NETTS	Not suitable for GPR investigation
McClellan AFB NETTS	Not suitable for GPR investigation

waveform 2D modeling (GPR_RAY_MOD), non-linear AVO inversion for reflectivity, and Q* inversion for frequency dependent attenuation analysis.

We have achieved a number of important successes during the project period. These include the first reported field demonstrations of NAPL detection using GPR pre-stack depth migration analysis and reflection tomography, GPR thinbed AVO analysis to detect thin layers of floating hydrocarbon, and attenuation analysis to detect DNAPL. These results are summarized in Table 1. Sites noted as confirmed detection are sites where adequate independent characterization data (boreholes, CPT data etc.) was available to verify the correlation of GPR anomalies with the presence of NAPL. Sites noted as unconfirmed detection are sites where the GPR analysis strongly suggests the presence of NAPL, but independent confirmation was not possible. Attenuation analysis is the most sensitive to noise, and since the spectrum can be impacted significantly by the presence of shortwavelength reflectivity, appears to be the least

robust of the three methods we applied. However, we were able to successfully quantify attenuation anomalies associated with a high conductivity LNAPL plume and a low conductivity accumulation of DNAPL. GPR AVO analysis is less sensitive to noise than attenuation analysis, and can significantly improve the detail in the GPR image by enabling measurement of subwavelength permittivity anomalies using thinbed analysis. Generally, we've found that velocity analysis, particularly through the application of reflection tomography, is the most robust tool for the identification of NAPL contamination. In fact, a significant velocity anomaly associated with known or suspected locations of NAPL was identified at all sites where the GPR signal was able to reach the target zone.

As part of the field verification effort, we hoped to define the detection limits for the various methods. Difficulty in obtaining detailed independent characterization data have prevented us from conducting this work with as rigorously as we had planned. However, at Hill AFB we verified detection of volumetric hydrocarbon concentrations as low as 1-4%. We believe that this likely defines the lower detection limit for velocity or AVO analyses. For high conductivity LNAPL plumes, where significant attenuation results from secondary biodegradation products, it may be possible to detect significantly lower NAPL accumulations.

In addition to NAPL detection we've demonstrated that we can provide accurate 3D estimates of other important physical properties such as lithologic heterogeneity, volumetric water content, and porosity (in the saturated zone). Further, the detailed images produced as a part of our analysis strategy can provide information such as the 3D geometry of stratigraphic units that control contaminant migration.

In the course of completing this project we have had the opportunity to collaborate with both DOE and private industry personnel both in choosing good sites with real problems, and in survey planning and logistics. Collaborating agencies include, PNNL, Westinghouse Savannah River, Bechtel Hanford, Fluor Hanford, Chevron Inc, Black and Veach Inc., Intera Inc., CH2MHill Inc., Sverdrup Technology, Inc., Dover National Test Site, Hill Air Force Base Environmental Management, Wurtsmith Air Force Base Transition Authority, Port Hueneme NETTS, McClellan AFB NETTS.

Training of six undergraduate research assistants and one graduate student have been supported by this project, exceeding the goals outlined in the original proposal. To date, we have presented 7 papers resulting from this project at 6 national meetings. Further, we have submitted 2 papers to peer reviewed journals and plan to submit an additional 6-8 peer reviewed papers within the next 6 months.

2 RESEARCH OBJECTIVES

The focus of this project was field testing and verification of methods for detecting DNAPL induced electrical property anomalies through quantitative analysis of multi-fold ground-penetrating radar (GPR) data. We focused on three analysis tools we believed most likely to provide reliable contaminant indicators: 1) Depth domain velocity analysis, 2) amplitude variation with offset (AVO) analysis (time domain attribute), and 3) attenuation analysis (time-frequency domain attribute). To develop an understanding of the GPR response under varying hydrogeologic conditions and varying contaminant composition and distribution, we have conducted field investigations at 10 research sites located throughout the continental

United States (Figure 1). Independent characterization data for control of the GPR experiments has varied from extensive borehole and cone-penetrometer sampling and detailed background information (e.g. Hill AFB), to one or two boreholes and minimal background information (e.g. Hanford 100-N-65). Even at the sites with the best control, we've found that our work has included a significant exploratory component. This is reflective of the difficulty in characterizing NAPL contamination with direct sampling methods alone.

Our efforts have included study of of residual and/or pooled NAPL in both the vadose and saturated zones. Consistent with our original proposal, we've generalized the study to include LNAPL characterization since many LNAPLs have electric properties similar to chlorinated solvents and therefore have a similar GPR attribute signature. Quantitative material property studies are necessarily incorporated with sophisticated imaging analysis. Therefore, an important byproduct of our research is state-of-the-art image processing, originally developed for seismic exploration and not commonly applied in GPR investigations. Not only do these imaging methods allow us to pinpoint attribute anomalies, but the resulting images are used to characterize lithology, identify fracture zones, and locate buried objects.

A secondary, but integral objective of the project has been continued development of forward modeling and data analysis algorithms. The software we've developed has improved the efficiency and accuracy with which we can measure and model the GPR response to subsurface NAPLs.

3 METHODS AND RESULTS

3.1 Principles of GPR Investigation

In GPR studies, the transmitting antenna generates an oscillating electric field that then propagates through the earth and is reflected at boundaries separating materials with differing electric properties (dielectric permittivity, magnetic permeability, and conductivity). The reflected wavefield is recorded and used to produce a reflector map that is an image of electric impedance contrasts in the subsurface. The reflector map is similar to a cross section of the earth, as impedance contrasts are often present at lithologic or pore fluid boundaries.

For most earth materials in which the GPR signal will propagate efficiently, the magnetic permeability is roughly constant and the conductivity is low, so we primarily image contrasts in dielectric permittivity. Conductivity controls attenuation of electromagnetic waves, with signal attenuation increasing with increasing conductivity. Conductivity is the primary parameter controlling the success of GPR studies, with essentially no signal penetration in highly conductive soils. Clays are typically relatively good conductors whereas sandy, coarse grained materials have relatively low conductivity and generally provide a suitable sedimentary environment for GPR investigation. High conductivity materials in the earth such as a clay aquitard, metal objects, or highly mineralized ground water, produce a strong reflection at the upper boundary, but also act as a barrier to GPR signal penetration.

GPR operates in the frequency band from 10 MHZ - 1 GHZ, with a peak frequency of 50 - 225 MHZ typical for groundwater studies. Lower frequencies correspond to greater depth of penetration and lower resolution whereas high frequencies correlate with shallow penetration at higher resolution. Velocities in dry and water saturated sands are on the order of 0.15 m/ns and

0.05 m/ns respectively. Thus we can expect to resolve features on the order of 10 - 40 cm in the water saturated zone and 30 - 120 cm in the vadose zone. Depth of penetration varies from ~ 0 m under the worst conditions to as much as 50 m under ideal conditions. The best results in GPR studies are obtained in dry sandy environments (low conductivity), but excellent results can be obtained with variable sediment composition and within the water saturated zone (see Section 3.4).

Most ground-penetrating radar (GPR) data are acquired with a constant transmitter-receiver offset and often investigators apply little or no processing in generating a subsurface image. This mode of operation can provide useful information, but does not take full advantage of the information the GPR signal can carry. In continuous multi-offset (CMO) mode, one acquires several traces with varying source-receiver separations at each point along the survey. CMO acquisition is analogous to common-midpoint acquisition in exploration seismology and gives rise to improved subsurface characterization through three key features: 1) Processes such as stacking and velocity filtering significantly attenuate coherent and random noise resulting in subsurface images that are easier to interpret, 2) CMO data enable measurement of vertical and lateral velocity variations which leads to improved understanding of material distribution and more accurate depth estimates, and 3) CMO data enable observation of reflected wave behaviour (ie variations in amplitude and spectrum) at a common reflection point for various travel paths through the subsurface - quantification of these variations can be a valuable tool in material property characterization. Although there are a few examples in the literature, investigators rarely acquire CMO GPR data. This is, in large part, due to the fact that CMO acquisition with a single channel system is labor intensive and time consuming. At present, no multi-channel GPR systems designed for CMO acquisition are commercially available. Over the course of this project, we have designed, conducted, and processed numerous 2D and 3D CMO GPR surveys using a single channel GPR system. We have developed field procedures that enable a three man crew to acquire CMO GPR data at a rate comparable to a similar scale multi-channel seismic reflection survey.

3.2 Principles of DNAPL Detection with GPR

NAPLs typically have low relative permittivity (K~2.5) and high electric resistivity (~10^4- 10^5 ohm-m) relative to water which make them attractive targets for characterization using electric geophysical methods. As the NAPL displaces water in the sediment pore space, a zone of anomalous electric properties may be induced (Figure 2). An attractive first order conceptual model is based on the premise that NAPL contaminated zones will have low permittivity and low conductivity relative to the surrounding formation. A number of controlled spill experiments have been consistent with this model (Brewster and Annan, 1994; Campbell et al., 1995; DeRyck et al., 1993), and this has proved to be an effective working model in the interpretation of geophysical data acquired over a fresh LNAPL spill (Orlando, 2002), and over aged LNAPL and DNAPL spills at one field site (Deeds and Bradford, 2002; Lien and Enfield, 1998; Newmark et al., 1998). However, it is now well established that aged hydrocarbon spills at some sites, have anomalously high electric conductivity in direct contrast to the simple conceptual model stated above (Atekwana et al., 2000; Monier-Williams, 1995; Sauck et al., 1998). This divergence stems from the incorrect assumption that the electric properties of the

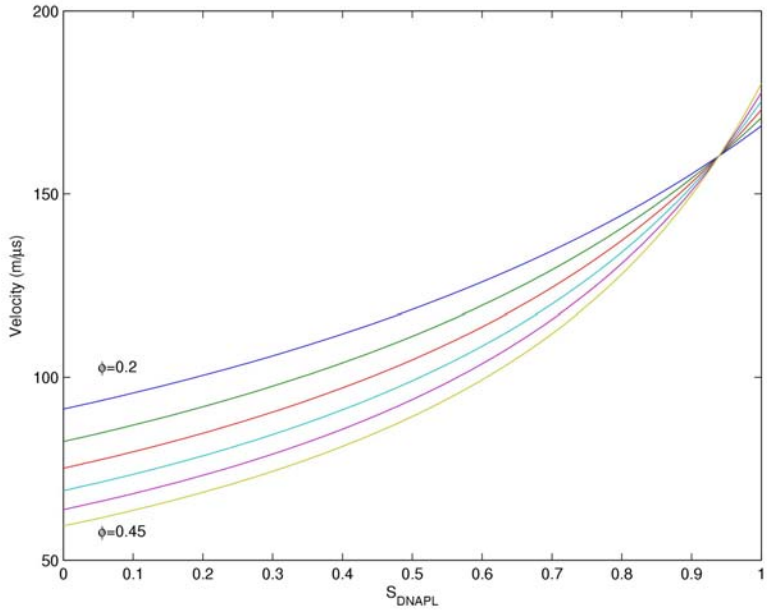

Figure 2. GPR velocity vs DNAPL saturation for porosity (ϕ) varying from 0.2 to 0.45. The curves were computed using the CRIM equation assuming a 3-phase system consisting of a quartz matrix ($\varepsilon/\varepsilon_o$=3.5), water ($\varepsilon/\varepsilon_o$=80), and DNAPL ($\varepsilon/\varepsilon_o$=2).

contaminated zone will be controlled by the electric properties of the unaltered LNAPL. Sauck (1998) proposes a conceptual model that explains the high conductivity LNAPL plume in terms of increased dissolved solid concentrations in the ground water related to biogenic activity. The relatively low number of LNAPL plumes documented as having low electric conductivity and low electric permittivity suggests that the conductive LNAPL plume model may be more widely applicable. It should be noted that conductive LNAPL plume model does not necessarily apply to DNAPL contamination. Examples in the literature (Newmark et al., 1998), and our own work (presented with this report), are consistent with the resistive model for DNAPL source zones.

In either the conductive or resistive NAPL case, the amplitude of the induced property contrast depends on the wetting phase and relative concentrations of water and NAPL. Modeling and laboratory studies have illustrated that when the organic is the wetting phase, the conductivity and dielectric permittivity drop sharply with very low concentrations of DNAPL, whereas the change is more gradual when water is the wetting phase (Endres and Redman, 1996; Santamarina and Fam, 1997).

We expect the GPR signature associated with the presence of NAPL to be manifest in essentially three ways. First, changes in dielectric permittivity result in anomalous EM propagation velocity. Second, changes in permittivity can significantly alter reflectivity. If the NAPL is in a discreet pool or plume, we may observe increased reflectivity or variations in the AVO response associated with the NAPL boundaries. If the NAPL is smeared vertically we may observe decreased reflectivity in the sediment column due to homogenization of the permittivity profile. Finally, alteration of the conductivity structure leads to signal attenuation anomalies.

A number of previous workers have investigated the potential to detect both DNAPL and LNAPL using GPR (Atekwana et al., 2000; Brewster and Annan, 1994; Campbell et al., 1995; Daniels et al., 1995; DeRyck et al., 1993; Powers and Olhoeft, 1996; Sauck et al., 1998; Saunders et al., 1993). Grumman and Daniels (1995) review a number of organic contaminant studies for both vadose and saturated zone applications. In general the published studies have met with moderate or variable success, but so far have relied on relatively simple data processing schemes and qualitative interpretation of GPR signal anomalies. While this may be sufficient under tightly controlled conditions where the location of contaminants is known, these techniques are not adequate for exploratory studies or where the GPR NAPL response is more

subtle. Our approach, in which we combine detailed velocity analysis and imaging with reflected waveform attribute analysis, has proven successful in identifying NAPL rich zones at several field sites.

3.3 Development and Evaluation of Data Processing Methodologies

3.3.1 Velocity Analysis of Multi-Fold GPR Data (Appendix A)

Accurate estimation of electromagnetic (EM) velocity is critical in ground penetrating radar investigations. Not only does the velocity enable accurate time to depth image transforms, but the velocity is a direct measure of subsurface electrical properties that may be used to improve our understanding of the subsurface. When coupled with a suitable mixing equation (Figure 2), the velocity can be used to estimate permittivity which in turn may lead to estimates of pore fluid content (Brewster and Annan, 1994; Greaves et al., 1996; Huisman et al., 2003; Powers and Olhoeft, 1996; Topp et al., 1980). Most GPR surveys are acquired with a constant transmitter-receiver offset. EM velocity estimates can made from common-offset data with one of two methods. The first method utilizes qualitative interpretation to correlate reflectors in the radar section with significant boundaries identified in the borehole data followed by velocity calibration. Of course borehole data are not always available, there is potential for misinterpretation, and this method suffers from a lack of lateral resolution. In the second method we measure the moveout of scattering diffractions which provides an estimate of EM velocity, but the distribution of scattering events limits the precision of the velocity model and in many cases no diffractions are present.

Given these limitations, it is typical to acquire one or more sparsely located CMP gathers within a broader survey area to obtain a 1D or coarse laterally varying velocity structure for interpreting a common-offset survey. From the CMP gather, an RMS velocity distribution is estimated using normal moveout analysis (Bradford et al., 1996; Campbell et al., 1995; Young and Sun, 1996). A common strategy for computing effective interval velocities from the RMS velocity utilizes Dix inversion (Dix, 1955). This approach does not correctly account for lateral velocity heterogeneity, and is sensitive to velocity errors resulting from dipping reflections or diffraction tails (Yilmaz, 2001).

We can overcome these limitations by acquiring data in continuous multi-offset (CMO) mode. With this method we use the well established acquisition geometries of seismic exploration to acquire several traces, with varying source-receiver separations, at each point within a survey. Acquiring CMO data has a number of advantages including suppression of coherent and random noise (Bradford, 2003b; Bradford, 2004b; Liberty and Pelton, 1994; Pipan et al., 1999; Pipan et al., 2003).

CMO data enable detailed measurement of lateral velocity variability (Greaves et al., 1996). However, NMO based processing schemes are subject to the fundamental assumptions of NMO velocity analysis which include small offset-to-depth ratios, small vertical and horizontal velocity gradients, and planar flat lying reflections. These assumptions are often violated in GPR investigations. For example, EM velocity can decrease by a factor of 3 or more across the water table as the sediment grades from dry to full water saturation (Bradford, 2003a; Bradford, 2004a). This can result in severe departure from normal moveout leading to very large

overestimates of interval velocity (Al-Chalabi, 1973; Al-Chalabi, 1974). When NMO velocity analysis fails, we must resort to more rigorous methods of velocity estimation.

Pre-stack depth migration (PSDM) focuses scattered energy, moves dipping events to the correct spatial location, and treats lateral and vertical velocity gradients correctly. As long as precise amplitude reconstruction is not a primary interest (e.g. we are only measuring wavefield kinematics), and with the basic assumption that the subsurface electric properties are independent of frequency, many of the migration algorithms developed for seismic data analysis can be applied directly to GPR data without modification. While not generally true, the assumption of frequency independent material properties is a reasonable first order approximation in most cases and often good migration results (Bradford et al., 1996; Bradford, 2004a; Bradford and Harper, submitted; Bradford and Loughridge, 2003; Deeds and Bradford, 2002) are obtained with any of the standard migration tools (Yilmaz, 2001).

PSDM depends strongly on the depth velocity model so that accurate velocity estimation is critical. Methods for estimating the velocity distribution fall into two categories: 1) Reflection tomography, and 2) PSDM velocity analysis.

Most tomography algorithms are designed to invert for the velocity structure based on travel time picks of specific reflecting horizons in the premigration domain. As pointed out by Stork (1992), tomography has the advantage that computational methods for solving the inverse problem are well understood and solutions can be found quickly and efficiently. A significant disadvantage arises when there is significant subsurface complexity and wavefield distortion makes it difficult to pick the traveltimes of specific reflecting horizons.

PSDM velocity analysis takes advantage of the strong velocity dependence of PSDM. When the data are migrated with the correct velocity model, reflections in common image point (CIP) gathers (the post-migration analog of CMP gathers) will migrate to the same depth and will appear flat. If the velocity model is wrong, there is an apparent offset dependent depth which can be characterized as residual moveout. The residual moveout is positive or negative depending on whether the velocity is too high or too low respectively. After migration with an initial velocity model, the velocity model is updated to remove residual moveout with a top-to-bottom method known as layer stripping. With this method the data are remigrated after each velocity update and checked for RMO, often using coherence panels in the CIP domain (Lafond and Levander, 1993). The process is repeated until all residual moveout is removed. PSDM analysis takes advantage of reflector coherence and continuity in the postmigration domain. This improves the processor's ability to evaluate specific reflecting horizons, particularly in a complex subsurface setting. Further, the output of PSDM velocity analysis is a suburface velocity model and PSDM image.

Both reflection tomography and PSDM velocity analysis have been applied to ground-penetrating radar data. For example, Cai and McMechan (1999) describe a method for estimating the subsurface EM velocity and attenuation models using a reflection tomography algorithm. And Leparoux et al. (2001) discuss the application of PSDM migration velocity analysis to GPR data.

Stork (1992) presents a method of reflection tomography that seeks to minimize RMO in CIP gathers in the post-migration domain. This method combines the computational advantages of tomography with the inherent interpretational advantage of PSDM velocity analysis.

Reflection tomography in the post migration domain is a robust tool and the software

needed to implement this method is commercially available and convenient to use. While more commonly applied in seismic reflection data processing, such tools are rarely used in GPR data analysis. As with most forms of geophysical inversion, it is not a "black box" process and requires careful quality control by the data processer. However, we have begun to use this method as a standard part of our processing stream for multi-fold GPR data, and recommend this method for all but the simplest GPR velocity analysis problems.

We have applied both conventional PSDM velocity analysis (Savannah River Site, Hill AFB) and reflection tomography in the post migration domain (Controlled Spill Experiment, Hanford Site, Wurtsmith AFB, Chevron Refinery, Cape Fear Creosote Site). Both methods have proven to be effective at accurately delineating the subsurface EM velocity structure. Further we have used both methods to identify both LNAPL (Hill AFB, Wurtsmith AFB, Chevron Refinery, all confirmed and Hanford 100N-65 probable but not verified), and DNAPL (Controlled Spill Experiment, Cape Fear Creosote Site both confirmed). These studies are the first reported examples of the use of multi-fold GPR velocity analysis techniques to identify NAPL contaminated zones in uncontrolled field spills. In the work completed as part of this study we have found that detailed velocity analysis is more robust than either AVO or attenuation analysis in identifying NAPL related material property anomalies. In fact, at every site that the GPR signal could reach the contaminated interval, we identified a velocity anomaly associated with the NAPL.

3.3.2 GPR AVO Analysis: The Thin Bed Problem (Appendix B)

Over the past 20-25 years, the study of offset-dependent reflectivity, or amplitude variation with offset (AVO) analysis, of seismic data has been used successfully to associate shear and compressional wave properties with the presence of oil or natural gas (Allen and Peddy, 1993; Bradford et al., 1997; Castagna, 1993; Castagna et al., 1993; Ostrander, 1984). We show here that with careful consideration of the physics and material properties governing electromagnetic (EM) wave propagation, similar analysis methodologies may be applied to ground-penetrating radar (GPR) data to make detailed material property measurements of the shallow subsurface.

Over the past decade, several workers have investigated the potential for various applications of GPR AVO analysis. Lehmann (1996) discussed complex reflection coefficients and the effects of conductivity, Bergmann et al. (1998) briefly discussed AVO response in the context of a broader synthetic case study, Reppert et al. (2000) examined the potential for measuring the electric permittivity contrast at a boundary using Brewster's Angle, and Zeng et al. (2000) presented a detailed modeling study considering the effects of varying the Cole-Cole parameters on the AVO response.

The Fresnel reflection coefficient curves (Griffiths, 1989) serve as a starting point in understanding the GPR AVO response. This response depends strongly on the polarity of the incident electric field and the electric permittivity contrast at the reflecting boundary. The Fresnel equations are derived assuming a monochromatic EM plane-wave incident on a half space boundary separating two isotropic non-conducting media. In field studies, all of these assumptions are violated to some degree. We have found that greatest value in GPR AVO analysis may be in analyzing the response to the presence of a thinbed, with thinbed defined as a

layer having thickness less than a wavelength (λ) at the dominant signal frequency. We have successfully used thinbed AVO analysis to measure the shortwavelength electric permittivity structure, thereby increasing the detail in the subsurface prediction (See Hill AFB, Wurtsmith AFB, and controlled spill experiment). Typical GPR frequencies for groundwater contaminant studies are 50 - 100 MHz with corresponding wavelengths on the order of 1 m - 2.5 m. There are numerous potential GPR targets that may fall into the thinbed category.

We have found that multi-fold GPR profiling coupled with quantitative analysis of GPR offset dependent reflectivity is a potentially valuable tool that can improve the detail and accuracy of GPR subsurface characterization. Thus far the method has seen limited application, probably in large part due to the difficulty of collecting continuous multi-fold data with commercially available single channel GPR systems. With future hardware advances we expect that multi-fold acquisition will become more efficient and more widely employed.

We've developed two forward modeling tools to aid in predicting and interpreting GPR AVO data. The first (MOD_{TB}) is a broad-band formulation of the three-layer reflection coefficients which can be used to evaluate offset dependent reflectivity in a 1-D earth model. Using this model we've found that, in most cases when the thinbed is greater than 0.5λ - 0.75λ, the Fresnel equations are a reasonable approximation, but below this limit investigators should use thinbed modeling. The second model, GPR_RAY_MOD, (Appendix C) is a ray based algorithm that incorporates antenna radiation patterns, conductivity, frequency dependent electric permittivity and magnetic permeability, and 2D subsurface geometries. This algorithm provides a good approximation of the thinbed reflectivity and can be used to simulate complete 2D multi-fold GPR surveys. Both codes simulate both TE and TM polarization modes.

By making simplifying assumptions such as constant antenna coupling, constant radiation pattern, and frequency independent material properties, the GPR AVO response is reduced to a manageable problem. These assumptions, in some cases, appear to provide a reasonable approximation of field subsurface conditions. We've also found that acquiring coincident TE and TM data allows us to take advantage of the polarity dependence of the reflection coefficients to limit the non-uniqueness in data interpretation.

Pre-processing for GPR AVO analysis is not straightforward and requires careful application of amplitude correction schemes to minimize artifacts associated with antenna directivity, signal attenuation, and wave spreading. We have integrated this method as a standard component of our multi-fold data processing scheme and believe that in many cases it has the potential to identify permittivity anomalies that would not otherwise be recognized in GPR data. We have developed a number of tools for GPR AVO analysis including a non-linear inversion for reflectivity.

At Hill AFB, Wurtsmith AFB, and the controlled DNAPL spill experiment, we have demonstrated that it is possible to use thinbed AVO analysis to identify small scale permittivity anomalies associated with NAPL contamination. These are the first reported examples of using GPR AVO analysis for direct detection of NAPL anomalies in a field setting.

3.3.3 Attenuation Analysis (Appendix D)

Propagating electromagnetic waves are subject to frequency dependent attenuation which depends primarily on conductivity (intrinsic attenuation). Typically, over the bandwidth of a

GPR pulse, the attenuation can be approximated as a linear function of frequency with a DC component that is controlled by the DC electric conductivity and frequency dependent component parameterized by an effective quality factor Q*. This quality factor can be shown to be a measure of the complex permittivity. While the DC component of attenuation shares an inherent ambiguity with the reflectivity, Q* is independent of the long wavelength reflectivity.

To extract Q* from field data, it is necessary to analyze spectral variation of the GPR signal through time, which is the basis of time-frequency (t-f) analysis (Chakraborty and Okaya, 1995; Li and Ulrych, 1996; Morlet et al., 1982a; Morlet et al., 1982b; Tobbock et al., 1996). Traditional methods of t-f analysis are the windowed Fourier transform (WFT) and the Wigner Distribution (WD) (Boudreaux-Bartels, 1985). The WFT provides a good spectral representation, but has poor time localization properties. The WD, which is the Fourier transform of the instantaneous autocorrelation, has both time and frequency localization, but suffers from cross-term interference. Wavelet methods have good localization in both time and frequency domains, and do not suffer from cross term interference associated with the WD (Chakraborty and Okaya, 1995; Daubechies, 1991; Li and Ulrych, 1996; Mallat and Zhang, 1992; Morlet et al., 1982a; Morlet et al., 1982b; Tobbock et al., 1996).

The spectral ratio method is commonly used for estimating seismic Q* values in laboratory measurements or sonic logs, but can also be applied to GPR reflection data, given an accurate t-f distribution. It is an attractive method because, ideally, it allows one to separate frequency dependent attenuation from attenuation due to reflection and transmission losses, spherical spreading and source and receiver effects, which are assumed frequency independent . Effects other than intrinsic attenuation, such as the presence of thin beds, can lead to frequency dependent losses, and an *apparent* attenuation. The Q* we measure in reflection data is an effective Q* (Q^*_{eff}) value that includes all frequency dependent losses. In general, intrinsic attenuation is large compared to other frequency dependent losses, and we can extract relative attenuation profiles that are reliable indicators of variations in intrinsic attenuation.

Bradford developed a method of Q* inversion from reflection data using a spectral ratio method which can be implemented with any t-f distribution (Bradford, 1998; Bradford and Wu, 1997). In this method, we first extract Q^*_{eff} at primary reflecting boundaries based a single reference spectrum. Q^*_{eff} extracted in this way is analogous to the RMS velocity obtained from NMO velocity analysis. Interval Q* values can then be calculated using a method similar to Dix inversion for interval velocities from an RMS velocity field (Appendix D).

We have found that the WFT is fast, robust, and provides adequate time resolution to estimate attenuation anomalies on the order of one wavelength at the dominant signal frequency. We've found that the spectral ratio method is unstable in low signal to noise data. However, the frequency shift method, presented by (Quan and Harris, 1997) works well with noisy data, and gives results comparable to the spectral ratio method in high signal to noise data. Our results at the Cape Fear Creosote and Wurtsmith AFB sites demonstrate that Q* can be an effective contaminate indicator for either conductive or resistive contaminated zones.

3.4 Summary of Field Results

We have completed an extensive field program involving 12 research sites located at 10 field locations throughout the continental U.S. (Figure 1). Additionally, we have completed a

number of ancillary experiments at little or no additional cost to the project. We have completed our field program with acquisition of full scale 2D and 3D multi-offset, multi polarization datasets at 10 research sites in 8 field areas. These include:

- DOE Savannah River Site (A-14 Outfall)
- DOE Hanford Site (Z-9 Trench, 618-10 Burial Ground/316-4 Crib, 100-N-65 Interception Trench)
- Hill Air Force Base (Operable Unit 1)
- Dover Air Force Base - Dover National Test Site
- Former Wurtsmith Air Force Base (FT-02)
- EPA Cape Fear Wood Preserving Site, Fayetville, NC.
- Former Chevron Refinery, Cincinnati, OH.
- Boise State University (Lab Scale Experiment)

The data are comprised of 11,354 linear m of 25-fold multi-offset GPR data which includes 8,528 m^2 of 3D surveying. It should be noted that our original work plan called for acquiring datasets at two National Environmental Technology Test Sites (NETTS) in California (Port Hueneme and McClellan AFB). Feasibility tests during September, 2001, demonstrated that soil conditions at these sites were not suitable for GPR investigation, and we began to search for additional contaminated test sites. This led to the identification of the former Chevron refinery outside Cincinnati, OH (LNAPL), and the Cape Fear Wood Preserving Site (DNAPL) as substitute test sites. In the following sections, we summarize the result from each field site.

3.4.1 3D Multi-offset, Multi-polarization Acquisition and Processing of GPR Data: a Controlled DNAPL Spill Experiment (Appendix E)

To test multi-offset methods for identifying DNAPL induced permittivity anomalies, we constructed a physical model for a controlled DNAPL spill experiment. The experiment is similar to a controlled DNAPL spill detailed by Brewster and Annan (1994), Redman and DeRyck (1994), and Kueper et al (1993) at the Canadian Air Force Base Borden. Brewster and Annan (1994) found significant GPR reflectivity anomalies in common-offset data associated with pooled DNAPL. Additionally, they measured a significant increase in radar velocity using normal moveout (NMO) analysis at a single CMP location. Our objective was to further Brewster and Annan's earlier efforts by focusing on detailed processing and analysis of 3D multi-offset data including data acquired in both TE and TM polarizations. Additionally, we investigated DNAPL migration through both the vadose and saturated zones as opposed to the Borden experiment in which only fully water saturated conditions were investigated.

The physical model was contained within a cylindrical polyethylene tank that was 122 cm in diameter and 107 cm deep. A bowl shaped bentonite layer lined the base of the tank. We used this configuration to route migrating DNAPL to the valved drain at the center of the tank. Above the clay, the tank fill consisted primarily of a medium to coarse grained sand with the exception of an 11 cm thick gravel layer 32 cm above the bottom of the tank.

The DNAPL consisted of a mixture of 4 liters of 1,1,1-carbon trichloroethane (specific gravity =1.4, $\varepsilon/\varepsilon_o$ =7.3), and 16 liters of tetrachloroethylene (specific gravity=1.6, $\varepsilon/\varepsilon_o$ =2.3). We added red

Sudan IV dye to the DNAPL mixture so that we could visually detect DNAPL during post-injection tank excavation. We injected the DNAPL mixture into the tank via gravity feed through a small, perforated funnel inserted 15.25 cm below the surface.

We acquired surface GPR data in a wagon wheel geometry with 5.08 cm source and receiver intervals. This geometry yields high CMP fold in the center of the tank where we wanted the highest signal-to-noise ratio for detailed amplitude analysis. We acquired both TE and TM surface data with both 450 MHz and 900 MHz antennas. Additionally, we acquired 900 MHz GPR transmission data with source and receiver positions every 5.08 cm across the top and down the sides of the tank.

Using detailed surface GPR velocity analysis, including reflection tomography, we constructed a detailed velocity distribution both prior to, and 48 hr after the injection of 20 liters of the solvent solution (Figure 3). We found an average 33% increase in velocity associated with a DNAPL pool that formed near the bottom of the tank. Using the CRIM equation, we estimated that 39% DNAPL saturation was required to cause this velocity increase. The DNAPL saturation measured in the pooled area during post injection chemical sampling was 37%. This demonstrates that PSDM velocity tomography can be used to make accurate, quantitative estimates of subsurface electrical properties, and that relatively simple petrophysical models can, in some cases, be used to estimate fluid concentrations (Figure 4).

Using thin bed AVO analysis, we found that a DNAPL pool model (S_{DNAPL}=0.27) with a 5.5 mm thick zone of 98% DNAPL saturation along the upper boundary produces an ODR response consistent with both the TE and TM data. As with data acquired at the Wurtsmith AFB site, we found that combined analysis of the TE and TM data was necessary to constrain subsurface model. The results demonstrate that AVO analysis has significant potential to reveal subsurface details that are not resolved with conventional imaging methods or velocity analysis alone.

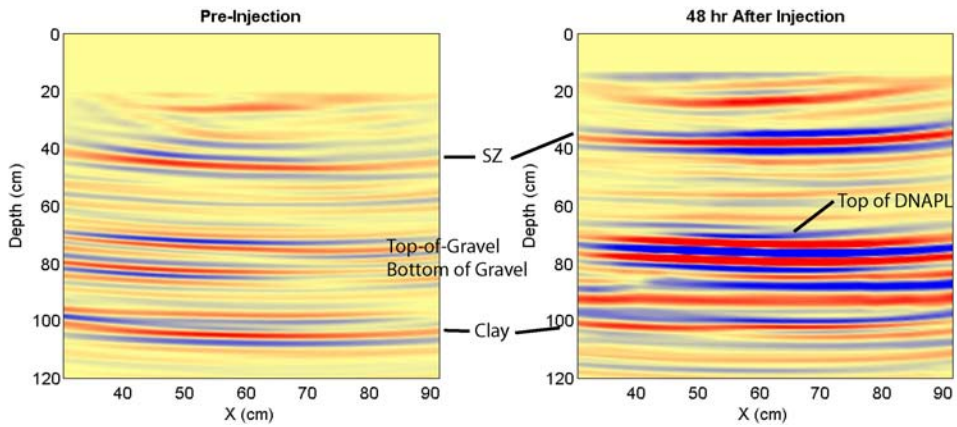

Figure 3. PSDM images before and after the DNAPL injection. Amplitude scaling of the two plots is the same for comparison. The clay reflection has been migrated to the approximate spatial position using the reflection tomography models in Figure 8, although the distortion in the post injection data has not been completely eliminated. The gravel layer is not well resolved after formation of the DNAPL pool due to the velocity increase (leading to a longer wavelength) and masking by the high amplitude DNAPL reflection.

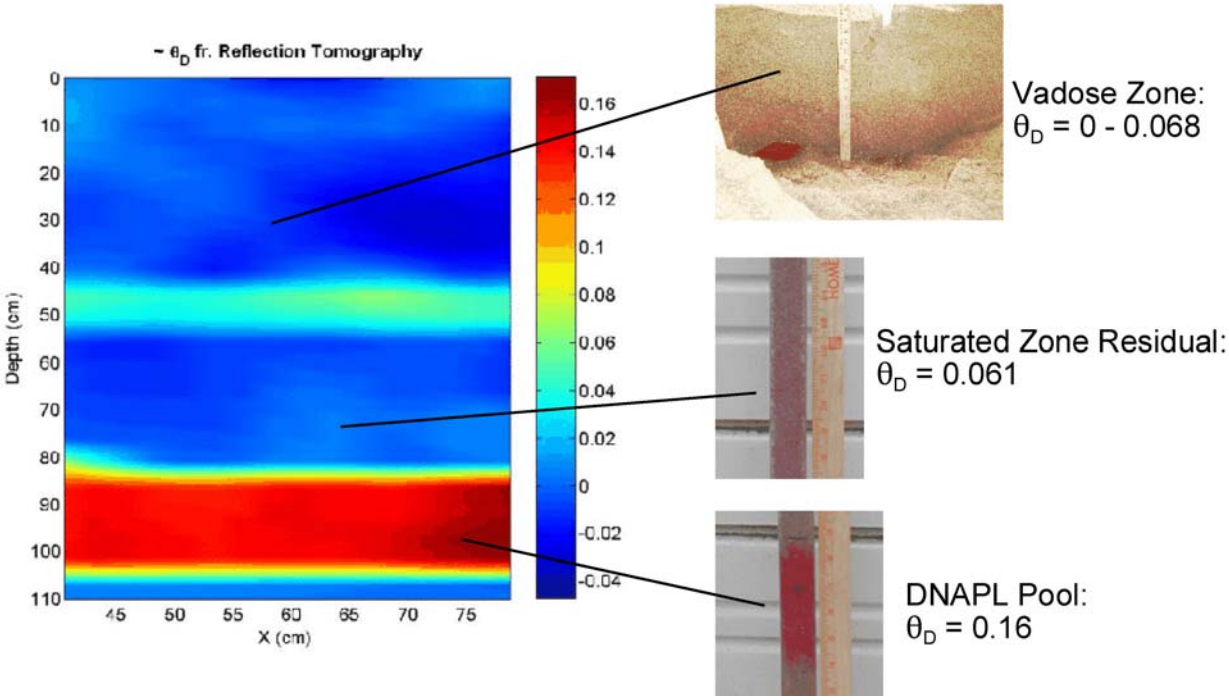

Figure 4. Volumetric DNAPL concentration distribution estimated as the change in apparent water content from pre- and post- injection data . Water content estimates were computed using the Topp Equation and GPR velocity models derived from reflection tomography. Photos show the red stained DNAPL along with measured DNAPL concentrations in the vadose and saturated zones. Generally the GPR estimates correlate reasonably well with the lab measured values.

3.4.2 Savannah River Site

Between 1952 and 1979, approximately 1,395,000 lbs of chlorinated solvents were released at the A-014 outfall of A/M area (U) at the Savannah River site (Jackson et al., 1999). About 72% was tetrachloroethylene (PCE). Until recently, it was thought that significant concentrations of DNAPL were confined to the deeper section of the vadose zone. In 1999, significant accumulations of solvent were discovered at depths less than 30 ft in the vicinity of the A-014 outfall. Sediments at the site consist of relatively coarse grained sands at the surface, a primarily kaolinitic clay layer at a depth ranging from 5 - 10 ft, and a thick, coarse grained sand unit at with top-of-sand at a depth of about 22 ft.

In January, 2000, we conducted a 2366 sq. ft., 3-D, multi-offset, GPR survey at the A-014 outfall. The survey was designed to encompass the shallow DNAPL zone, with little or no contamination near the edges and a strongly contaminated zone near the center. Kaolinite typically has relatively low conductivity, so we felt there was a good chance we could penetrate the clay.

Using pre-stack depth migration velocity analysis and imaging, we have identified a high velocity anomaly associated with a channel-like feature that had not been previously identified (Figure 5). The channel appears to cut about 3- 4 ft into the top of the clay, is adjacent to previously identified areas of DNAPL concentration and lies below the current position of the A-14 outfall. Since the channel is directly below the outfall, which maintains a stream of running water, we would expect higher water saturation, and therefore lower velocities within the channel. However, the velocity within the channel (350 ft/ns) is near the highest velocity in the survey (390 ft/ns) which is measured from the direct wave traveling at the surface near the east side of the survey. Our initial interpretation was that the high velocity within the trough could be related to high levels of DNAPL concentration or lithologic variation. In either case, the channel likely formed a DNAPL migration route, and that once trapped at the base of the channel, DNAPL migrated laterally into the adjacent clay formation.

Independent soil sampling was performed adjacent to our survey area in 2003 by Westinghouse Savannah River personnel (Rossabi et al., 2004) as part of a study designed to test a variety of downhole electrical geophysical methods for detecting DNAPL (Briggs et al., 2004; Grimm and Olhoeft, 2004; Minsley et al., 2004). They found significant DNAPL contamination in the upper 10 ft of the sediment column that produced a significant electrical property anomaly. The DNAPL distribution is aligned with the velocity anomaly we measured in the GPR experiment and lies along the DNAPL release path. Although we do not have direct confirmation of the presence of DNAPL within our survey area, we believe it is likely that the anomaly is caused by elevated levels of DNAPL.

This experiment demonstrates three valuable attributes of our methodology; 1) we identified an electric property anomaly that is aligned with adjacent DNAPL contamination and was independently verified using a different geophysical methods, 2) we identified a likely contaminant migration route which improves understanding of the hydrogeologic system, and 3) we extracted an accurate estimate of near surface water content which may also be valuable in understanding the vadose zone hydrology.

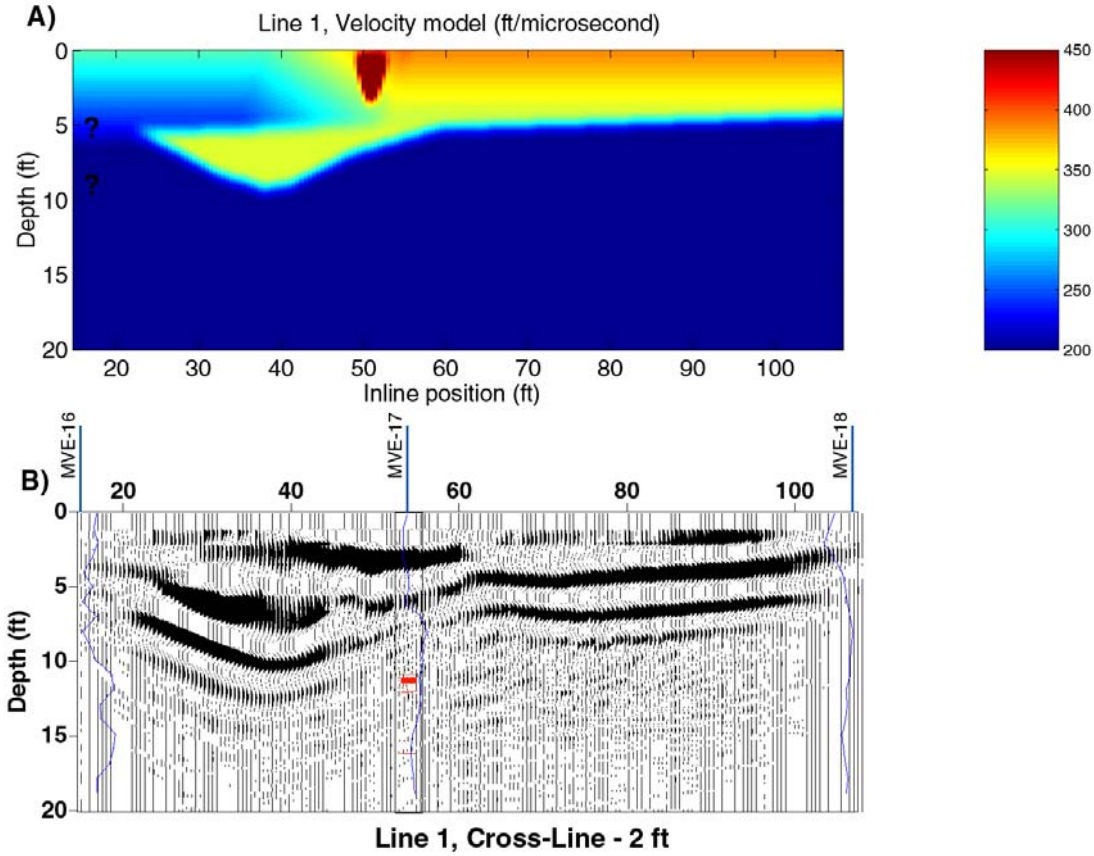

Figure 5. A) Migration velocity model for Line 1 from the Savannah River Site study. B) Pre-stack depth migrated image. Neutron logs converted to water saturation from MVE-16, MVE-17, and MVE-18 are overlain. Also a log showing the position of observed DNAPL in MVE-17 is shown with the presence of DNAPL indicated in red. The continuous reflection from in-line positions 25 to 106 ft appears to correlate with an increase in moisture content that is slightly shallower than the top-of-clay surface. This is expected and the reflector likely tracks the top-of-clay topography. A flat event below MVE-17 appears to correlate with the top-of-DNAPL, and is consistent across several lines. However, the quality of data in this zone does not warrant a confident interpretation at this time. Further processing and analysis is necessary. The topographic low between in-line positions 25 and 55 ft is interpreted as a channel and is consistent across the entire survey. This feature had not been previously identified.

3.4.3 Hanford Site (Appendix A)

In April, 2002, we acquired two 3D surveys near the Z-9 trench, in the 200W Area. The Z-9 trench received the majority of the CCl_4 at the Hanford site, and is thought to be the primary source area for the extensive CCl_4 groundwater plume that now exists below 200W. Our target was a caliche layer at a depth of approximately 30m, where it is believed that some CCl_4 is trapped and is a likely location for DNAPL pooling. Unfortunately, we were unable to penetrate to the target depth, with the maximum penetration ranging from 10 - 15 m. On a positive note, the detailed surveys are proving valuable in demonstrating the utility of the multi-offset approach in characterizing water content variation and other properties in the shallow sediments (Figure 6).

In September, 2002, we returned to the Hanford Site to conduct reconnaissance surveys at the 100-N-65 Interceptor Trench, and the 618-10 Burial Ground/316-N Crib, both of which are LNAPL contaminated sites. We were able to reach the target depths at both of these sites and made some interesting findings.

The 100-N-65 Interceptor Trench was excavated along the Columbia River just northeast of the 166N Tank Farm. The purpose of the trench was to intercept diesel fuel that had reached the water table through several unplanned releases totaling more than 80,000 gallons. Fuel that accumulated in the trench was ignited and burned. In 1994, the trench was backfilled, but gross contamination was found in characterization wells (Jacques, 1985). It is likely that a significant component of the fuel was not burned and remains in the subsurface. To evaluate the potential for using GPR to characterize the site, and to look for anomalies related to remaining NAPL contamination, we acquired a set of 183 m long, multi-offset surveys, along the axis of the in-filled trench, in both TE and TM modes. We supplemented these data with a short (27 m) cross-axis multi-offset profile.

The target depth was at the water table about 6 m below the surface and we were able to image to a depth of about 9 m. We found a strong radar signature associated with the trench and identified additional radar anomalies that are likely associated with remaining LNAPL contamination (Figure 7). Within the trench area, we reach water table depths, but the signal is strongly attenuated below this depth. This high attenuation may be associated with LNAPL contamination as was observed at the Wurtsmith AFB site. There is additional strong evidence of a NAPL signature at the 100-N-65 site. Using reflection tomography we identified a significant high velocity anomaly that appears to emanate from the base of the trench. Because of the geometry of this feature, and its position relative to the trench, we believe that this is an LNAPL induce anomaly as we have observed at other sites. This may be weathered fuel present in a smear zone, or less volatile (and likely more viscous) hydrocarbon components that remained after burning. No wells are in place within the anomaly for independent confirmation, although NAPL is present in water samples taken from other wells around the site.

The 618-10 Burial Ground is located approximately 4 miles northeast of Hanford's 300 Area. This site contains several pits that received solid mixed waste from the mid 1950's until 1960. The pits were later backfilled. During a surface stabilization project in 1983, a black oily substance was observed bubbling to the surface above one of the pits. No samples were taken, but this is thought to be a potential contributor to groundwater contamination. The 316-4 Crib is located about 30 m southeast of 618-10 and consists of two buried, open bottomed tanks. Approximately 200,000 l of liquid organic and uranium wastes were pumped into the disposal

tanks during the 1950s and 1960s. Radiological and volatile organic contamination has been found in a well near the site (Bechtel Hanford Inc., 1995). Groundwater lies approximately 18 m below the surface. What is thought to be a low permeability cemented gravelly layer, at a depth of about 11 m, is suspected of having a significant role in contaminant migration (Department of Energy, 1997), and was our primary target at this site. Sediments at the site are comprised of surficial eolian deposits overlying the sands and gravels of the Hanford Formation (Bergstrom et al., 1995).

We acquired 610 linear m of multi-offset, 2D profiles at the site consisting of three roughly East/West profiles, and two North/South profiles (Appendix A). Along two of the East/West profiles we acquired data in both TE and TM modes. We obtained excellent results at the site with 9-12 m of penetration with 100 MHz antennas, and 14-18 m of penetration with 50 MHz antennas. Reflection tomography in the post-migration domain made it possible to accurately resolve significant lateral and vertical velocity heterogeneity (Figure 8). The resulting detailed velocity models could be interpreted directly to locate significant features such a the waste disposal pits within the 618-10 Burial Ground. Further, the velocity models helped guide the interpretation of significant lithologic units and constrain the likely relative grain size distribution. Both the 618-10 Burial Ground and 316-4 Crib are underlain by a paleochannel network that appears to have a low permeability cemented unit at its base. The channel fill, U4, consists of coarse grained and likely high permeability sands and gravels. It is likely that this paleochannel network forms a prime migration route for contaminates emanating from either the 618-10 Burial Ground or the 316-4 Crib. Furthermore, the tanks in the 316-4 Crib are clearly imaged, and a large paleochannel lies below the tanks. Spreading laterally beneath the tanks is a zone of high attenuation. The high attenuation may be due to increased metal concentrations along the contaminant migration route, or potentially due to degradation of the organics as we have observed at other sites.

Our early results suggest that radar imaging can provide a significant contribution to the characterization and potentially future remediation of Hanford's 618-10, 316-4, and 100-N-65 sites.

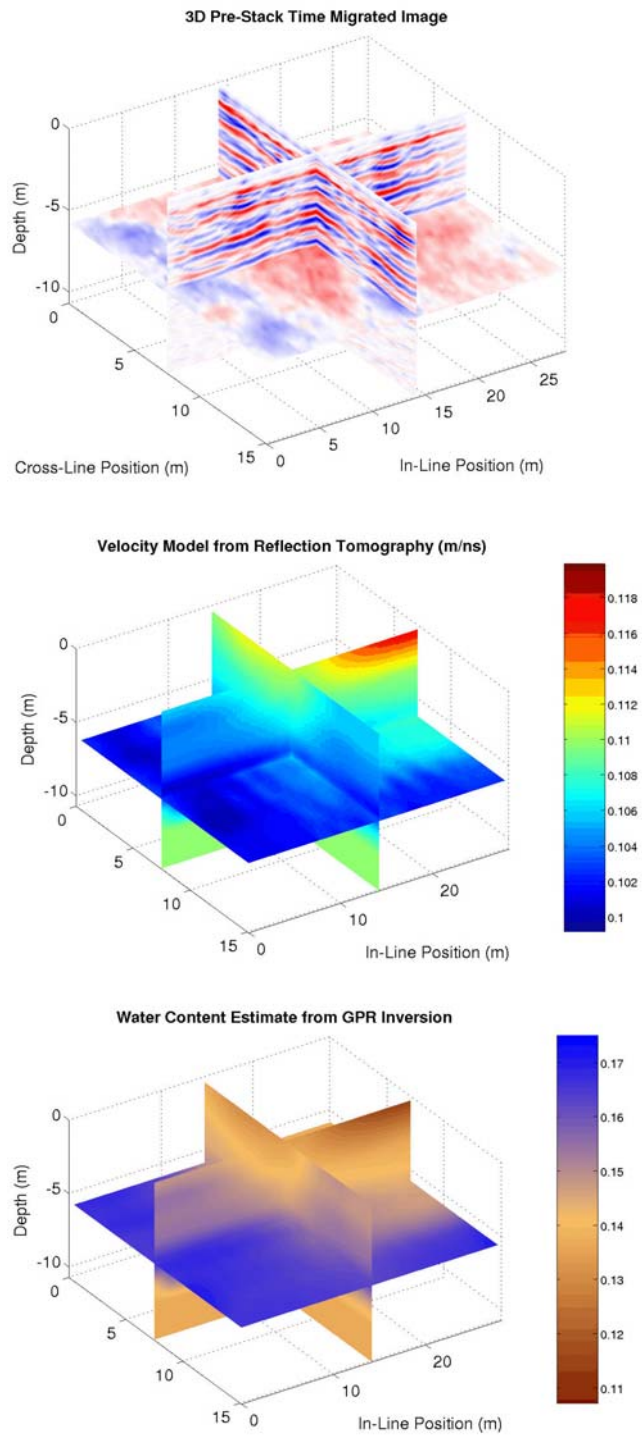

Figure 6. Two, subhorizontal reflections at ~4 m and 6 m dominate radar stratigraphy at the site. The 6 m reflection deepens at low in-line positions. This deepening correlates with an increase in water content. Velocities generally increase with in-line position and decrease with crossline position. A low velocity/high water content layer is present between 4 m and 7 m.

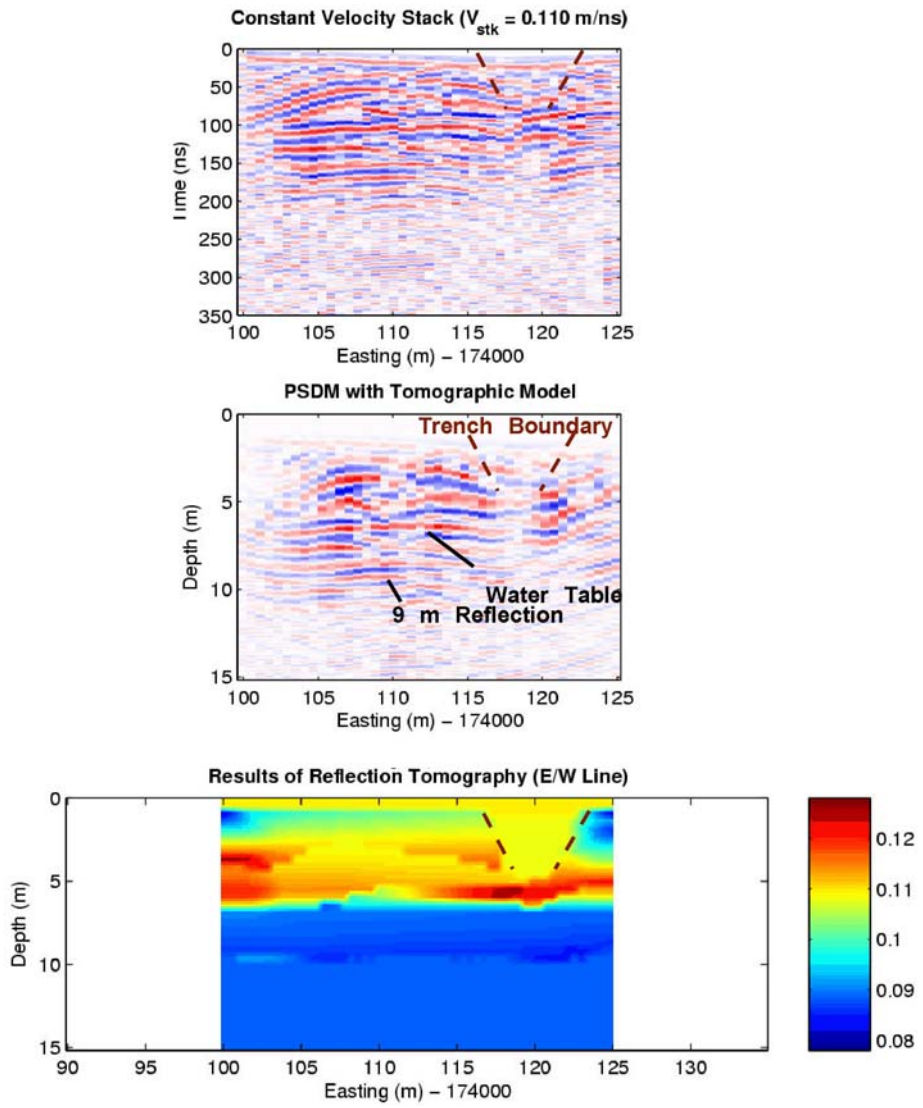

Figure 7. Results from the 100-N -65 Diesel Oil Interceptor Trench. A zone of anomalously high radar velocity emanates from the base of the trench. We interpret this as a likely zone of elevated LNAPL contamination as we have observed at other sites. Although no soil or groundwater data are available from this zone, free NAPL is present in nearby wells.

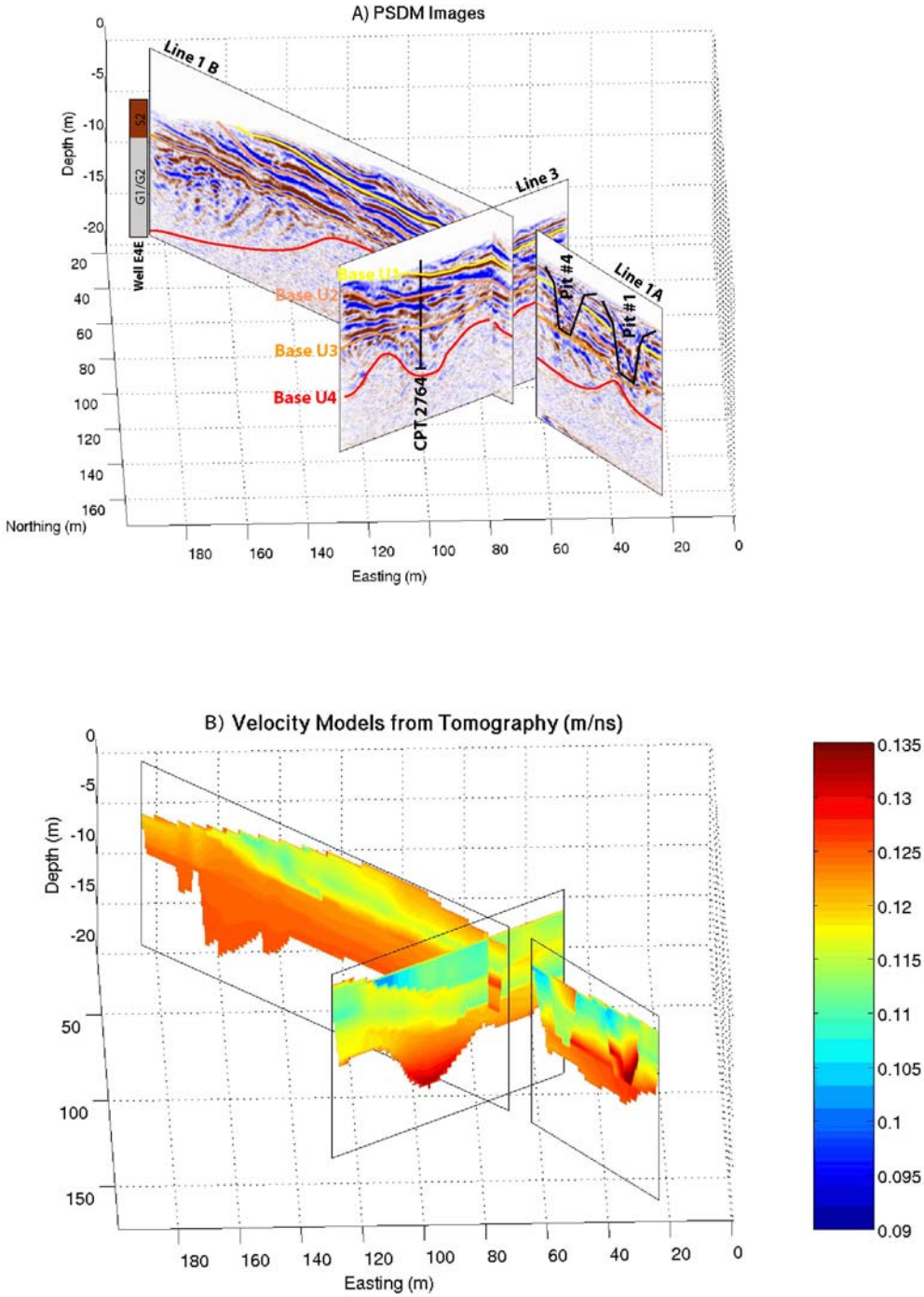

Figure 8. Results from the 618-10/316-4 field study: A) PSDM reflection images of Line 1 and Line 3, and B) tomographic velocity models. Based on high radar velocity and borehole observations, we interpret U4 to be comprised of relatively coarse grained and likely high permeability sandy gravels. The cemented gravel unit identified in CPT 2764 and Well E4E appears to lie at the base of U4 which defines a NW/SE trending paleochannel network that likely forms primary contaminant transport routes.

3.4.4 Hill Air Force Base (Appendix F and I)

At Operable Unit 1 (OU-1), Hill AFB, UT, a variety of both LNAPL and DNAPL contaminants were dumped in two chemical disposal pits (CDPs 1 & 2) and burned from 1952-1973. A significant quantity of non-combusted liquids leaked from the CDPs to the underlying aquifer and now comprise a free product plume that covers approximately 7 acres with measured thickness as much as 0.3 m. The plume is a highly heterogenous mixture composed primarily of jet fuel and light lubricating oil with a significant dissolved solvent phase. In addition to the floating pool, the contaminant accumulates in a smear zone that is controlled by water table fluctuation, with the relative amounts of pooled and smeared NAPL dependent on water table elevation. Previous work by Enfield et al. (1998) indicated that contaminated soil at the site has relatively low electric conductivity. We also expect low electric permittivity to be associated with zones of soil contamination. This, coupled with favorable results of previous GPR imaging work (Young and Sun, 1996; Young and Sun, 1998) led us to select Hill Air Force Base as a research site. At the site, 6 - 10 m of gravel to silty sand comprising the Provo Alluvium overly the clays of the Alpine Formation. The Alpine clay acts as an aquitard as the water table fluctuates about the sand/clay boundary on an annual cycle. This site was particularly challenging for three primary reasons:

- Significant heterogeneity in the surface material related to variations in fill material associated with capping and landfill activities.
- Significant heterogeneity at the target depth. The NAPL is present near the sand/clay boundary. Variable topograpy along this surface had a significant impact on contaminant migration. This was further complicated by seasonal water table fluctuations about the sand/clay interface.
- A highly heterogeneous NAPL resulting in variable electric properties and heterogeneous contaminant migration and distribution.

In October of 2000, we acquired a 2,973 m^2, 3-D multi-offset GPR survey designed to bound CDP 1 on the east, west and north sides and to extend beyond the known boundary of the free LNAPL plume. Survey objectives included imaging the sand/clay interface and direct detection of the LNAPL plume. Using pre-stack depth migration velocity analysis and imaging we were able to extract a detailed map of the sand/clay boundary. Depth to clay interpreted from the processed radar image is accurate to within about 0.3 m based on extensive borehole information located within the 3-D patch. The radar image indicates that the clay surface topography is significantly more complicated than previously mapped using borehole information alone.

We identified an anomalous reflection arching roughly 1.5 m over a topographic low in the clay surface. We found a high velocity anomaly in the interval between the anomalous reflector and clay reflector (Figure 9). Additionally, we found that the AVO response of the anomalous reflection departs significantly from that of the clay reflection (Figure 9). Forward modeling of the top-of-anomaly reflection using the velocity model derived through PSDM velocity analysis shows that while simple Fresnal Equation analysis predicts the general trend of the data, thinbed modeling produces a significantly better fit to the field data.

Suspecting that the high velocity anomaly was associated with a NAPL rich zone, we initiated a verification coring program. In September, 2001, four continuous cores (UW-1 – UW-4) were pulled from within the anomalous zone. Additionally, a fifth core was pulled just outside of anomalous zone for background control (UW-5) where only a thin trace of hydrocarbon was detected. The cores indicate a relatively homogeneous stratigraphy from the surface to the clay layer, and no lithologic boundary is evident that explains the anomalous reflection. Elevated hydrocarbon levels (varying from 1% - 4% total volume) were discovered in sediments pulled from within the high velocity zone. The hydrocarbon rich zone forms the only significant boundary in the cores and is the most likely explanation for the origin of the reflection. The large velocity increase below the reflection indicates low electric permittivity. This is in contrast with the background effect where increasing water saturation with depth, particularly near the water table, leads to decreased velocity. Given all the available information, we interpret the high velocity zone as correlating with a zone of elevated NAPL saturation. The correlation of low permittivity with NAPL contaminated soil at this site is consistent with the results of a previous resistivity study (Lien and Enfield, 1998) located several hundred feet south of our survey area.

While we are confident that the measured GPR response is caused by the NAPL rich zone, it is difficult to explain how the large observed velocity increase can originate from the relatively low NAPL concentration recorded in the verification boreholes. Using simple mixing laws or an empirical formulation such as the Topp equation (Topp et al., 1980), the velocity we measured would require nearly total displacement of the pore water with NAPL or air. This is not likely the case. We believe that either 1) the contaminant has replaced water as the wetting agent in which case relatively low concentrations of NAPL may lead to large increases in velocity, or 2) the viscous NAPL has clogged the pore throats leading to a low permeability zone that is largely free of water. Previous work has indicated that the OU1 plume is a mixed wet system (Meinardus, 2000) so this is a reasonable interpretation. Endres and Redman (1996) present the results of a modeling study of a NAPL/water pore fluid that illustrate the significance of fluid distribution within the pore system. Their results are not directly applicable to this study since we are dealing with a three-phase pore fluid – NAPL/water/air. Further analysis is needed to develop a petrophysical model that describes the measured radar response.

In May and July 2002, we conducted a large scale exploration survey at OU-1. We first acquired a 92,903 m^2 common-offset survey to identify anomalies or stratigraphic features potentially containing elevated NAPL concentrations. Through these data we identified an anomaly similar to that investigated in the 2000 study, and located within 60 m of that anomaly. This feature was also a stratigraphic low with an unusual arching reflector approximately 1.5 m, above the clay surface. Subsequent multi-offset profiling verified that this reflection was associated with a high-velocity zone. Laser induced fluorescence profiling conducted by Intera, Inc. in September, 2002, indicated that a low level of NAPL was present within the anomalous zone. In addition to identification of this anomaly, we identified a previously unmapped paleo-channel that has been identified as a major contaminant transport route and contains a significant, previously unidentified NAPL accumulation.

Our results at OU-1 are significant for several reasons. First, we believe that this was the first reported case of GPR AVO and migration velocity analysis being used for direct detection of NAPL in an uncontrolled field setting. And second, the NAPL was found in a location previously thought to lie outside the NAPL plume. The key to this success was quantitative analysis of

multi-offset radar data to identify electric property anomalies that may otherwise have gone unnoticed in qualitative interpretation of conventional radar profiles.

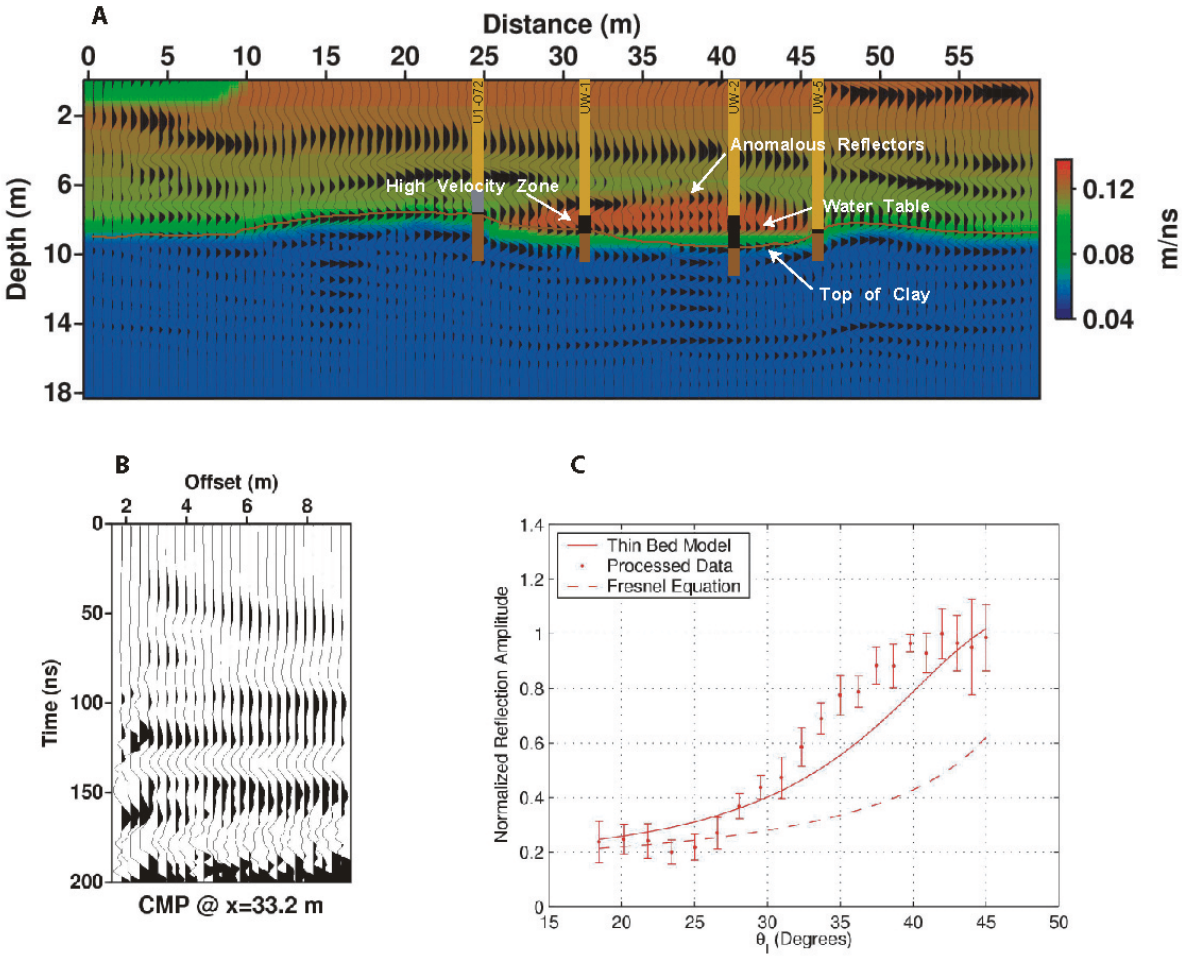

Figure 9. A) PSDM velocity model with migrated trace overlay. We identified a high velocity zone within a topographic low on the clay surface. In a subsequent coring effort, hydrocarbon contamination was found within this zone (the contaminated interval is indicated with black). B) The amplitude of the reflection from the top of the high velocity zone (~ 100 ns) in the CMP coincident with core UW-1 shows a clear increase in amplitude with increasing offset. This is qualitatively consistent with the Fresnel reflection coefficients. C) Reflection amplitudes taken from 20 CMPs centered on the core UW-1. Although the Fresnel equation predicts the general trend of the data, the thinbed computation is in much closer agreement with the field observations. Note that we only used offsets of less than 8 m in the quantitative analysis to minimize artifacts related to weak interference of the ground coupled wave at far offsets.

3.4.5 Former Wurtsmith AFB NETTS (Appendix G)

This site is a former fire training facility, designated FT-02, located on the now decommissioned Wurtsmith AFB, in Oscoda, MI. Over a period of about 24 years, large quantities of fuel were burned on open ground during weekly training exercises. A significant volume of hydrocarbons did not burn and seeped into the underlying aquifer. In 1982 a concrete catch basin was constructed to minimize the amount of contaminant reaching the subsurface. By the early 1990s, the free product plume was up to 0.3 m thick, and extended more than 180 m downgradient from FT-02 (Bermejo et al., 1997; Sauck et al., 1998).

The stratigraphy below the site consists of fine to medium grained sand and gravel deposits extending to a depth of approximately 20 m. Below this is a 6 - 30 m thick silty clay layer which is thought to be the lower boundary for contaminant migration. The surficial aquifer is unconfined, with the water table present 3 - 5 m below the surface. The site was formerly a National Environmental Technology Test Site (NETTS), and was the site of a long term natural bioremediation investigation. Although no longer an active NETTS site, the wealth of characterization data available make this an excellent location for a semi-controlled GPR field experiment. Central to the selection of this site for the current study are a series of geophysical investigations carried out by Sauck et al. (1998) and Bermejo et al. (1997). They found that the site provided excellent conditions for GPR with strong reflections well below the water table. Additionally, they found that there was a well defined, high attenuation anomaly coincident with the LNAPL plume. Through resistivity and self potential measurements, and by inference from the GPR data, they concluded that high electric conductivity was associated with both the LNAPL and the dissolved phase plume. This site provided an excellent opportunity to study a conductive type plume.

During July, 2002, we acquired 1676 linear m of multi-offset data, including a 930 m^2 3D survey and data acquired in both TE and TM modes. The 3D survey was oriented such that one edge of the plume would cross diagonally through the 3D patch. Additionally,data were acquired along two 122 m east/west profiles that bounded the 3D patch to the north and south. These profiles extend well beyond the east and west boundaries of the plume. Our first objective was to reproduce the results of Sauck et al. (1998) and we found a similar attenuation anomaly. This is most evident as an area of low reflection amplitudes, or “shadow zone”, beginning just below the water table and extending to depth (Figure 10). Although the character of the attenuation anomaly is the same, the geometry of the LNAPL plume appears to have changed significantly in the 8 years since Sauck et al.’s initial investigation. Most notably, the width of the plume has decreased significantly, being only about half as wide as that measured by Sauck et al. Additionally, the plume axis appears to have shifted.

Plots of the AVO gradient show a clear, well defined anomaly, in both TE and TM modes, that roughly coincides with the attenuation anomaly (Figure 10). We also find that the water table reflection amplitude decreases by as much as 40% over the attenuation anomaly. This decrease in amplitude correlates with the AVO gradient anomaly. Through quantitative analysis, we have shown that the observed response cannot be due to an attenuation or radiation pattern anomaly, or to topographic effects. Furthermore, through thin-bed modeling using an analytical solution to Maxwell’s equations for a multi-layered medium (King and Owens, 1992), we have shown that the trend of the AVO response correlates very well with a model having a 0.3 m thick

intermediate permittivity anomaly just above the water table in the on-plume area, and a simple boundary in the off-plume area (Figures 10). Critical to this analysis were the additional constraints provided by including both the TE and TM data.

In addition to quantifying the offset dependent reflectivity, we have recently measured a significant high velocity anomaly associated with the plume using reflection tomography. We believe this to be the first reported example of a high velocity anomaly associated with a conductive LNAPL plume. Further, we've computed the frequency dependent, plume induced attenuation using Q* inversion (Figure 11), where previous studies relied on qualitative interpretation of muted reflectivity. This has the potential to lead to quantitative estimates of contaminant concentration, but such analysis requires additional research.

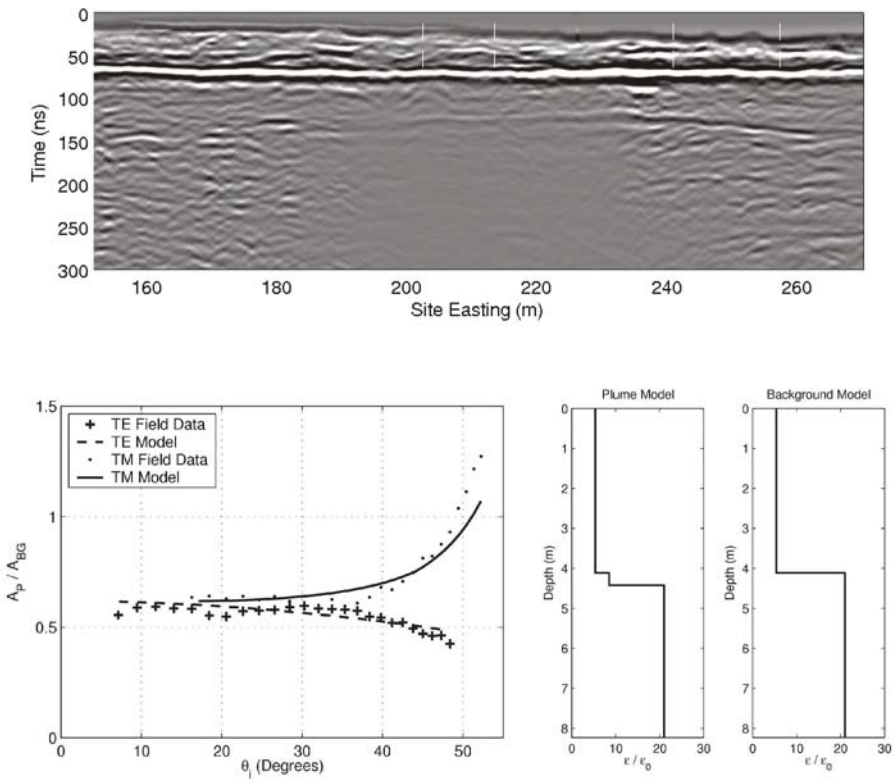

Figure 10. The location of the FT-02 plume is clearly evident as a zone of muted reflection strength in the stacked radar image. The low reflection amplitude is caused by increased signal attenuation related to anomalously high electric conductivity in the plume. Taking the ratio of the water table reflection amplitude in the plume to the background water table reflection amplitude illustrates an offset dependent reflectivity anomaly. A thinbed model that includes a 30 cm thick intermediate permittivity anomaly at the water table agrees well with the field data. This thickness agrees with the smear zone thickness measured in core data. Data sections used to compute the amplitude curves are indicated with dashed lines in the stack.

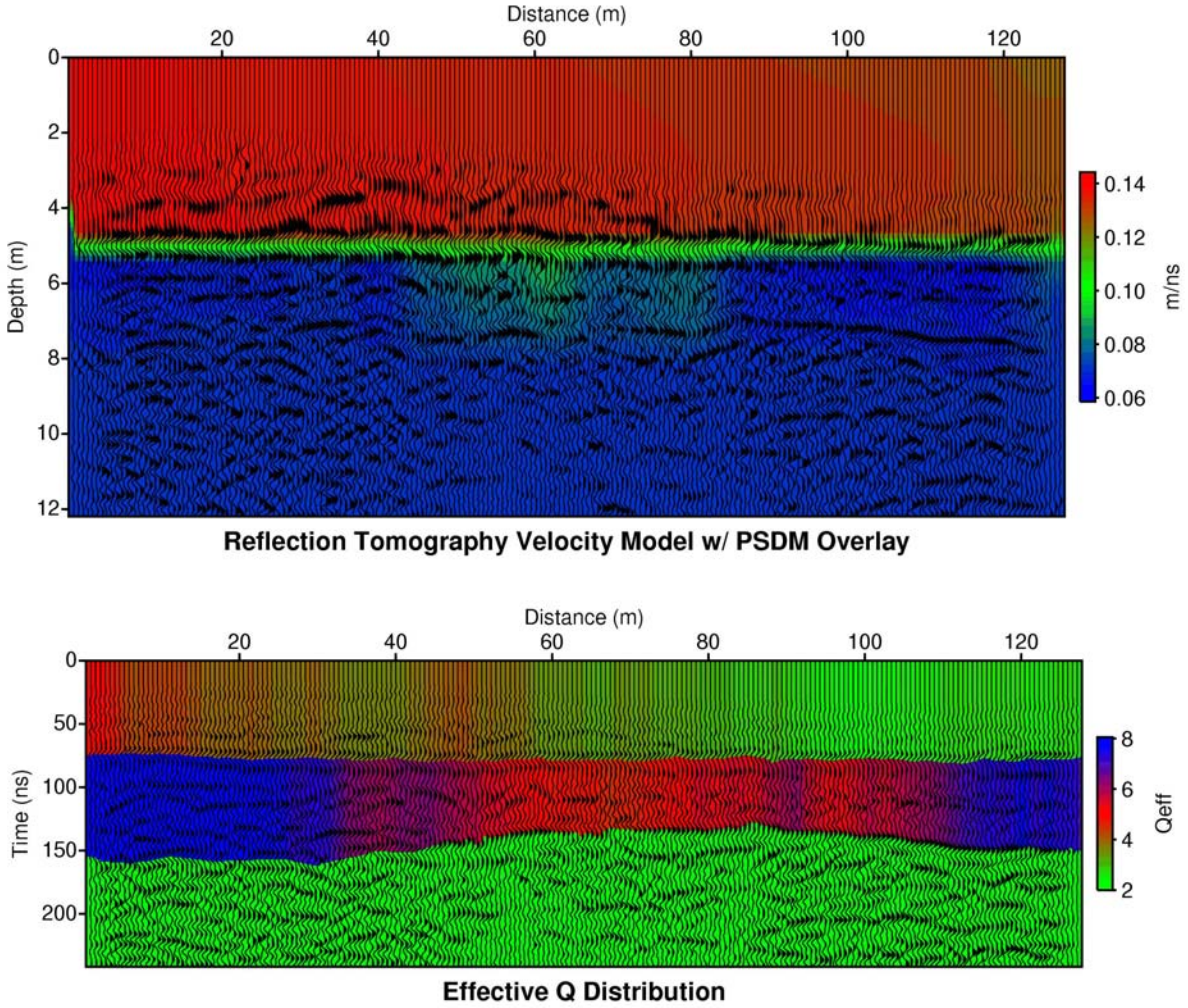

Figure 11. Both the reflection tomography model and the Q^*_{eff} distribution illustrate significant property anomalies associated with the LNAPL plume at Wurtsmith AFB. Anomalously high radar velocities below the water table in the plume core (45 m - 85 m) are likely within a mixing zone. In this case the colormap for Q^*_{eff} is set to highlight zones of high frequency dependent attenuation. The high attenuation zone is significantly wider than the high velocity zone. At this site, the attenuation is caused by secondary biodegradation products and is sensitive to much lower NAPL concentrations than the velocity analysis.

3.4.6 Cape Fear Wood Preserving Site

The Cape Fear Wood Preserving Site is located in Fayeteville, North Carolina. The facility produced creosote-treated wood between 1953 and 1978. In 1977 the site was found to be contaminated with coal tar and coal tar creosote of which the primary constituents are PAHs (DNAPL). In the mid 1980s some remediation activities were initiated including excavation and removal of some contaminated soils. In 2001 and 2002 additional characterization revealed that a significant quantity of DNAPL remained. Current activities include a new round of characterization and remediation design. Shallow sediments at the site consist of fine grained sands and silty sands to a depth of about 30 ft where a thick silty clay unit is present. A shallow (3 ft) water table is present in the unconfined surficial aquifer.

The primary objectives of the radar study at the Cape Fear Creosote Site were 1) to map the shallow stratigrapy, and 2) testing methods for direct detection of DNAPL. Initial tests indicated that the site was conducive to radar investigation with good data quality to depths of 20 - 30 ft.

The 50 MHz reflection profile along Line 2 is typical of data acquired elsewhere at the site (Figure 12). The profile was placed to span an area of low contamination to a zone of high contamination and additionally we acquired coincident 100 MHz data. There are strong, laterally coherent reflections recorded to depths up to 30 ft. For the following analysis, we focus on two depth intervals; 10-23ft and 23-30ft. These two intervals are bounded by strong reflections and thus represent significant stratigraphic units. It should be noted that from 0 to approximately 75 ft along Line 2, the interval from the surface to a depth of 18 ft was previously excavated and backfilled, and therefore is not representative of the natural stratigraphy. More importantly for the radar analysis, this section produces significant lateral heterogeneity that has a strong impact on the radar analysis. This is evident qualitatively in the reflection profile.

We have analyzed the data using reflection tomography and two independent methods of attenuation analysis. For the first attenuation computation, we estimated attenuation coefficients from the log of amplitude ratios of reflections bounding a specific interval. Conductivity was then computed from the attenuation coefficients (Figure 12) using the equation for low loss media given by Davis and Annan (Davis and Annan, 1989). This analysis provides a measure of relative conductivity variation within each layer assuming constant reflectivity at the boundaries. For the second attenuation measurement we applied Q* inversion (Figure 13) which is independent of reflection amplitude. Throughout the formation, we find relatively high-conductivity/high attenuation to the east that gradually decreases toward the west. This is consistent with increasing DNAPL toward the west. For the 10 - 23 ft interval, there is a minima in conductivity (potentially maximum DNAPL) just to the east of the excavated section. Conductivity in the 23 - 30 ft interval decreases gradually reaching a minimum at the beginning of the profile. This is consistent with velocity analysis which shows increasing velocity toward the west. Using a form of the CRIM equation (Greaves et al., 1996), we estimate both DNAPL and water concentration from the velocity profile in the 23 - 30 ft interval. This yields a maximum volumetric DNAPL concentration of around 4.5% near the west end of the line. The general trend of the conductivity and DNAPL concentration estimates, in both intervals, are consistent with the DNAPL distribution mapped using CPT LIF, and ROST logs (Black and Veach Special Projects Corp.,

2002). It must be noted that the analysis is non-unique and that significant lithologic changes could potentially give similar results. However, two independent modes of analysis (attenuation and velocity) produce consistent results, and these results are consistent with direct observations. This is the first reported use of GPR attenuation analysis and PSDM velocity analysis for detection of a DNAPL induced anomaly.

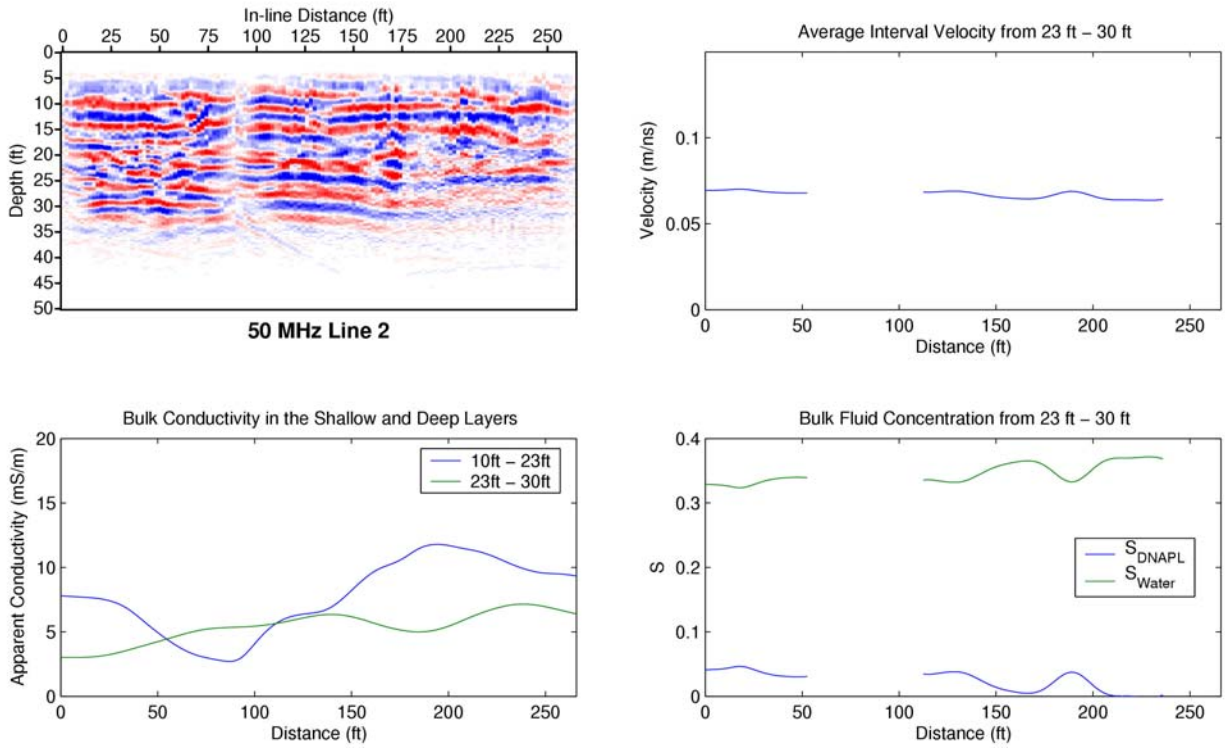

Figure 12. Data from the Cape Fear Wood Preserving Site showing: PSDM, 50 MHz TE stack, velocity estimates from PSDM velocity analysis, and conductivity and DNAPL concentration estimates. See text for computational details. The general trend and relative variability of all computated values indicates increasing DNAPL concentration toward the west. This is consistent with DNAPL accumulations mapped using CPT LIF, and ROST logs. The water table is at a depth of 3 ft. Computed conductivities and velocities are consistent with tabulated values for water saturated silty sands. Note that the low amplitude zone between 75 and 100 ft is a migration artifact related to a no-data zone. We completed amplitude analyses with the unmigrated data so artifacts did not effect the conductivity estimates.

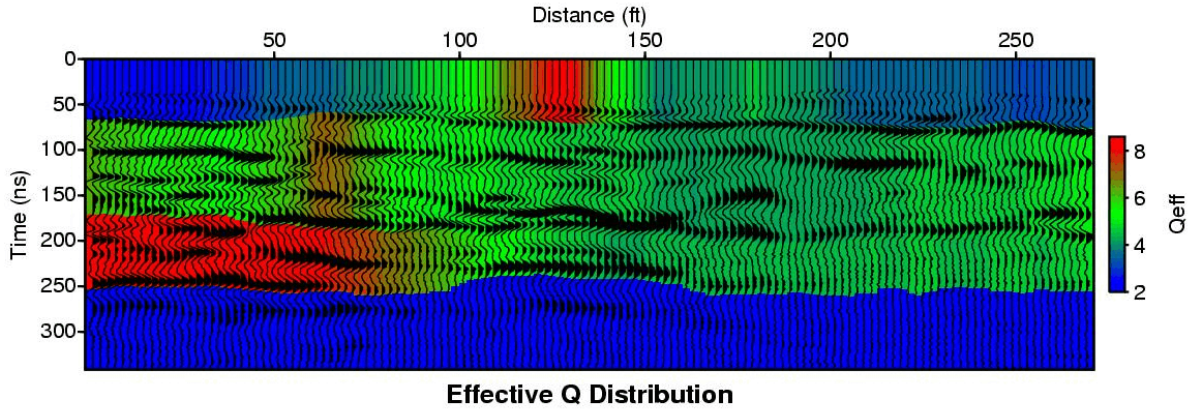

Figure 13. The Q^*_{eff} distribution from the Cape Fear site is plotted to highlight zones of low attenuation. This plot clearly indicates a zone of low attenuation within a sandy layer near the bottom of the section from 0 - 120 ft. This is consistent with significant DNAPL accumulations mapped with CPT LIF and ROST logs.

3.4.7 Cincinnati, Ohio Refinery Site

At this site, an estimated minimum of 4,000,000 gallons of leaded gasoline and diesel fuel were released to the environment from the early 1930s to the early 1980s. This contaminant now forms a thick zone of hydrocarbon contamination that interacts dynamically with the fluctuating water table. Approximately 2,500,000 gallons of contaminant have been removed through extraction wells over the last 10 - 15 years, but a significant source term remains. The water table fluctuates by 3 - 5 m annually. At low water table conditions, the hydrocarbon forms a pool at the top of the water saturated zone, and at high water table conditions, the contaminant remains trapped in the pore space below the water table forming a thick smear zone. The sediment column consists of course sands and gravels to a depth of 24 m to 30 m where a clay aquitard is present. The water table is roughly 9 m - 18 m below the ground surface depending on topographic relief and temporal ground water variations.

In January, 2002 we acquired approximately 1710 linear m of 2D multi-fold GPR data (50 MHz) consisting of both TE and TM configurations along three transects ranging in length from 152 m to 274 m. We chose a large scale 2D acquisition geometry to evaluate "regional" variations in plume geometry due to the sparse distribution of borehole characterization points. We acquired data at high water table conditions with the contaminant forming a 3 - 5 m thick smear zone and essentially no floating product. We intended to revisit the site during low water table conditions, but this possibility was eliminated due to ongoing development activities.

Data quality at the site is excellent with good penetration to depths of 12 - 25 m. In initial processing, we identified reflections from the top and bottom of an interval consistent with the contaminated zone identified in boreholes (Figure 14). Reflection tomography revealed a highly heterogeneous velocity structure in the vadose zone with a large lateral gradient where the fill transitions from gravel to clay rich and the velocity decrease sharply by approximately 30 %. A sharp increase in signal attenuation is also observed at the gravel/clay fill transition and south of this lithologic change the water table reflection is still evident, but energy does not reach the base

of the contaminated interval. To the north, where the overburden is dominated by gravel, we find elevated velocity below the water table within the contaminated zone. The velocity decreases further to north where well data indicate a significant decrease in LNAPL concentrations. Interpretation at this site is complicated by stratigraphic changes that are coincident with the lateral increase in velocity below the water table. The velocity increase is within the range of saturated sediments so we cannot rule out the interpretation of velocity increase as purely due to a lithologic change, however, the high concentrations of LNAPL at this site, coupled with a nearly universal observation of increased velocity associated with NAPL contamination at better controlled and stratigraphically simpler sites leads us to believe that the more likely interpretation is that the stratigrapy is controlling the NAPL distribution, but that the increased radar velocity is due to the presence of LNAPL. It should be noted that the contaminated interval is ~ one wavelength thick and so is near the limit of PSDM velocity analysis resolution. We attempted to apply AVO analysis to the water table reflection at this site, but found that the interference from the steeply dipping reflectors in the vadose zone produced an erratic AVO response and the analysis did not produce useful results.

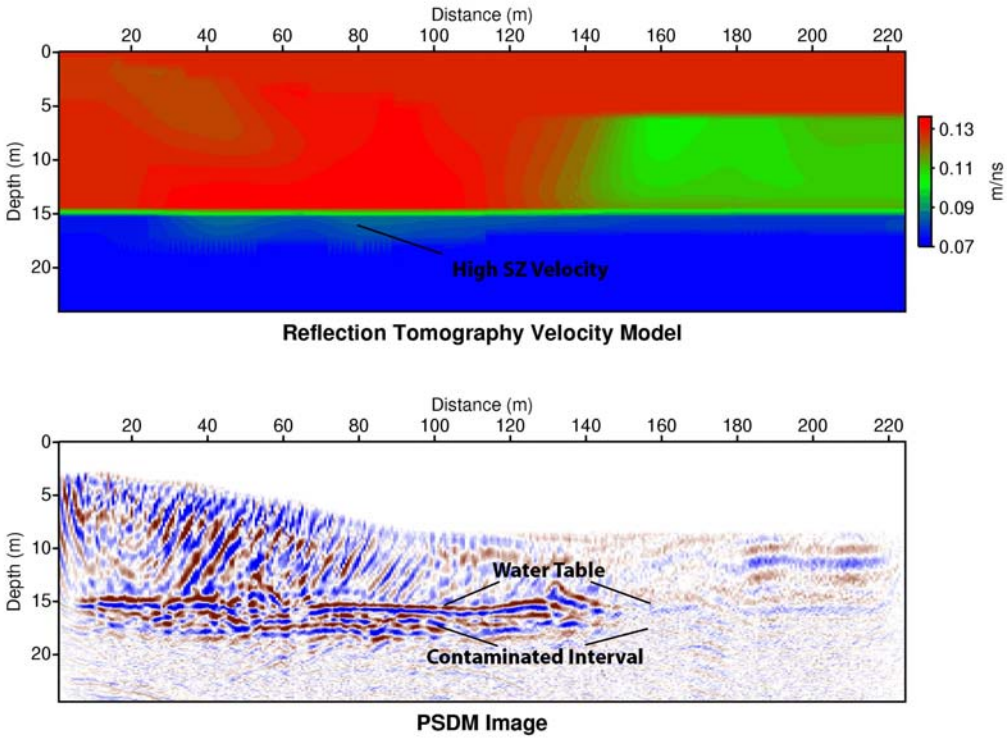

Figure 14. The reflection tomography model at the Chevron Refinery site shows significant lateral heterogeneity in the vadose zone related to variability in the fill composition. The fill on the right side of the image is clay rich, while to the left the fill is gravel dominated. Note that there is significantly higher signal attenuation associated with the large decrease in velocity. A high velocity zone just below the water table begins at 25 m and continues to the right across the section. This is consistent with the distribution of increased levels of LNAPL observed in monitoring wells at the site. The data were acquired at high water table conditions and the high velocity zone is likely indicative of the LNAPL smear zone.

3.4.8 Controlled DNAPL Injection at the Dover National Test Site (NETTS)

In July 2001, we completed data acquisition for a controlled DNAPL (tetrachloroethylene) injection and GPR monitoring project at the Dover National Test Site, Dover AFB, DE. Data from this site contain significantly higher noise levels than initially expected. Processing of these data are ongoing and we are testing a variety of noise suppression techniques. The data may prove valuable in demonstrating effective methodologies in high noise areas. In conjunction with planning the controlled injection experiment, we have implemented a methodology for integrating multi-phase flow and GPR modeling. This allows us to investigate temporal changes in GPR response to a dynamic contaminant distribution.

In August, 2002, we revisited the Dover National Test Site in an attempt to better understand the GPR response to site conditions. This field effort included conductivity profiling using a Geoprobe mounted instrument. Conductivity data were acquired adjacent to the test cell, and at several other locations around the site. In conjunction with this effort, we acquired a set of 2D and 3D multi-offset surveys. Analyses are ongoing, but we believe these data will lead to a fuller understanding of the GPR response observed during the DNAPL injection. In addition to the DNAPL detection experiments at the DNTS we conducted a series of 3D common and multi-offset experiments designed to image subsurface reactive barriers. We are using these data to investigate the migration response of a variety of migration algorithms to various acquisition geometries (Appendix H).

3.4.9 Discussion of Field Results

During the current project period, we have demonstrated that direct detection of NAPL contaminated sediments is possible using quantitative analysis of surface GPR data attributes. We submit that anywhere that GPR operates effectively, the same quantitative approach may be used to identify contaminate related electrical anomalies, regardless of whether they are high or low conductivity or permittivity deviations. The key is that the contaminant causes a departure from the background electrical properties. It is extremely important to note that there is an inherent non-uniqueness to these methodologies and that positive NAPL identification requires direct sampling of the soils. However, with some site specific calibration coupled with an understanding of the hydrogeology, we believe these analysis tools can help guide and optimize a coring program, both by identifying likely NAPL zones, and by mapping stratigraphic variations that may control contaminant transport. Additionally, the tools likely have even greater strength in imaging changes through time, monitoring a remediation project for example.

We've found that all three analysis methods tested in this study - PSDM velocity analysis and reflection tomography, AVO analysis, and attenuation analysis - have the potential to detect NAPL contamination, but are not equally beneficial at all sites. Attenuation analysis is the most sensitive to noise, but has proven effective at some sites. This tool may have the potential to identify zones of high conductivity associated with secondary biodegradation products in the presence of low levels of NAPL. We've demonstrated that GPR AVO analysis can be effective in identifying short wavelength permittivity anomalies. In particular, combined analysis of both TE and TM can constrain the reflectivity response and provide added detail to the subsurface image. Velocity analysis has proven the most robust tool, and at all sites where the GPR signal reached

the target depth, a significant velocity high was found to correlate with a known or suspected location of NAPL.

4 RELEVANCE, IMPACT AND TECHNOLOGY TRANSFER

The results of this research address several key problems that have been identified as critical technology needs, both at specific DOE sites, and on a complex wide basis (National Research Council, 2000a; National Research Council, 2000b):

- Improving capabilities for in-situ characterization of the physical and chemical properties of the subsurface
- Improving capabilities for characterizing physical and chemical heterogeneity
- Improving capabilities for measuring contaminant migration and system properties that control contaminant migration
- Methods to integrate data collected at different spatial and temporal scales to better estimate contaminant and subsurface properties and processes

More specifically, the complex wide need assessment, noted in "Research Needs Collected for the EM Science Program", Section 8.1 - "Remedial Action Need: Characterization and Location of Contamination in the Soil and Groundwater", lists the following research needs

CS-88: Characterization techniques for determining quantity and extent of DNAPLs
CS-96: High resolution imaging of the shallow subsurface (<30 m) to guide and monitor remediation processes
CS-101: Non-intrusive detection and delineation of DNAPL source terms, e.g. pools and residual saturation zones, in the subsurface
CS-103: Inexpensive methods for monitoring contaminant migration through the vadose zone
CS-106: Burial ground characterization

Our research represents a new approach to the analysis of surface GPR data, that directly addresses several of DOE's technology needs. The approach is innovative and we have shown that our methods are effective in the characterization of hydrogeologic features and NAPLs. It should also be noted that, although the focus of this project was NAPL detection, the same methodologies are applicable to detection of any contaminant that creates an electrical property anomaly, such as high electric conductivity associated with zones of concentrated radionuclides.

a. How does this new scientific knowledge focus on critical DOE environmental management problems?

Through consideration of the full range of measurements we can make with GPR, coupled with careful processing and interpretation we can dramatically increase the amount and quality of subsurface information derived from the method. The results of this study demonstrate that quantitative evaluation of velocity, attenuation and reflectivity attributes of multi-fold GPR data can be used to identify subsurface electrical anomalies caused by the presence of NAPL. Further,

the same analysis methodologies can be used more generally to improve the quality of GPR images in the presence of random and coherent noise, map lateral and vertical variations in soil moisture content, improve the spatial accuracy of GPR images and maximize the detail in the subsurface models we derive. These capabilities meet the needs of DOE environmental management problems by providing reliable methods to characterize NAPL contaminated sites by:

1) locating NAPL rich zones such as at Hanford's 100N-65 site and Savannah Rivers A-14 outfall,
2) identifying potential contaminant transport pathways such as at Hanfords 618-10 Burial Ground
3) measuring other parameters that effect contaminant fate in the subsurface such as the variations in soil moisture as demonstrated at Hanford's 200 W area.

b. How will the new scientific knowledge that is generated by this project improve technologies and cleanup approaches to significantly reduce future costs, schedules, and risks and meet DOE compliance requirements?

While the benefits of this technology are self evident, they must be weighed against the costs of other available characterization technologies. There are two primary cost limitations of multi-fold GPR, 1) data acquisition is labor intensive and time consuming relative to single-fold GPR, and 2) data processing and interpretation is considerably more complex requiring added expertise, software, and processing time. Through the course of this project we have devised field procedures that enable us to acquire multi-fold GPR data, using currently available single channel GPR systems, at a rate comparable to multi-channel seismic data acquisition. For example, at a sampling density of 0.15 m, we can acquire approximately 300 - 400 m of data per/day at a cost of roughly $3000 including data processing and analysis. Compared to a single shallow borehole cost of a minimum of $5,000 this expense is relatively small. Of course, the non-uniqueness inherent in all geophysical data means that multi-fold GPR cannot completely replace direct sampling methods. But by first carefully characterizing a site using GPR (and/or other geophysical tools where applicable), the number of boreholes needed can be minimized and the placement optimized by drilling directly on suspect anomalies or in likely contaminant transport routes. This is the proven approach used for several decades in the vast industry of hydrocarbon exploration. The problem of NAPL site characterization is conceptually analogous to the hydrocarbon exploration problem and similar cost benefits will be seen in contaminant remediation projects through similarly extensive use of geophysical methodologies.

c. To what extent does the new scientific knowledge bridge the gap between broad fundamental research that has wide-ranging applications and the timeliness to meet needs driven applied technology development?

Much of the technology needed to conduct large, detailed multi-fold GPR characterization projects is currently available. For example, three commercial GPR vendors, Sensors and Software, Mala Geosciences, and GSSI, manufacture single channel GPR systems that could be used to conduct this work. The software needed to manage the data is identical to that used to

manage multi-channel seismic data and is readily available through a number of sources. Some of the advanced data processing algorithms, such as the reflection tomography software, are commercially available. Other software developed as part of this project such as the GPR AVO and attenuation analysis packages could be made available for distribution with a relatively small programming effort. In summary, the capability exists to use the methodologies investigated as part of this project to conduct large scale characterization project at DOE sites. Continued research will better define the limitations and improve the capabilities of the analysis methodologies. And significant field cost benefits could be seen with the development of multi-channel GPR systems designed for common-midpoint data acquisition.

d. What is the project's impact on individuals, laboratories, departments, and institutions? Will results be used? If so, how will they be used, by whom, and when?

During the course of this project we have achieved a number of important milestones in the field of contaminant characterization and more generally in the development of data acquisition and analysis tools using GPR, for example our work is the first reported use of velocity, AVO or attenuation analysis to directly detect NAPL rich zones in a field setting. To the best of our knowledge, the data we have acquired as part of this project is the largest compilation of multi-fold GPR data in the world and therefore forms a valuable resource for the geophysics community. We are in the process of disseminating the results to the larger geophysical community through the peer reviewed literature, but believe that the work will have a significant impact on the field in general.

We believe the of our work at Hanford's 618-10 Burial Ground and 100N-65 site can provide important input for ongoing remediation efforts, and are currently consulting with Fluor-Hanford. Further we are investigating the potential for a larger scale project at one or both of these sites. The results of our work at Hill Air Force Base and the Cape Fear Creosote site were used directly by Intera, Inc. in the design and implementation of a characterization and remediation plan.

e. Are larger scale trials warranted? What difference has the project made? Now that the project is complete, what new capacity, equipment, or expertise has been developed?

We believe that our results in this project warrant additional research and development. Potential projects could include hardware development to improve the efficiency of acquiring multi-fold GPR data. Additional benefit would be derived from continued development of data analysis methodologies and software that may include full-wavefield inversion coupled with joint inversion of coincident GPR and complex resistivity measurements to better constrain the electrical properties of the subsurface. A large scale field experiment, at a site such as Hanford's 100N-65 site, that includes simultaneous acquisition of multi-fold GPR and complex resisitivity data, coupled with a significant algorithm and software development effort is warranted and has the potential to significantly improve our ability to predict subsurface fluid distributions.

The extensive (~9,290 m^2) characterization effort we completed at Hill AFB serves as a template for conducting large scale projects, where rapid common-offset is used for

reconnaissance and more expensive, multi-fold GPR data acquisition is reserved more targeted investigation (Appendix F).

g. How has this research advanced our understanding in the area? Although it has long been recognized that NAPLs induce electric property anomalies that can potentially be detected using GPR, rarely have quantitative studies been done. Rather, field studies generally depended on qualitative interpretation of GPR images. We have demonstrated that multi-fold GPR analysis can produced quantitative estimates of subsurface properties, and that NAPL induced anomalies can be consistently detected in the field under a variety of hydrogeologic conditions. To accomplish this task we have applied or developed data processing tools that have not previously been applied to radar. This is a significant advance in the field of NAPL detection and in GPR characterization in general.

h. What additional scientific or other hurdles must be overcome before the results of this project can be successfully applied to DOE Environmental Management problems? Although a number of improvements in both hardware and software can still be developed, as outlined above, the technology is presently available to apply the methods to DOE problems.

5 PROJECT PRODUCTIVITY

As stated in our original project proposal, the primary objective of the work was field verification of GPR velocity, AVO, and attenuation measurements as indicators of NAPL contaminants with a particular emphasis on locating DNAPLs. Within this large objective we planned to develop an understanding of the detection limits, both in terms of spatial scale of the contaminant distribution, and in NAPL concentrations required to produce a measurable GPR response. Generally, we believe that the project has been greatly successful both in terms of general contributions to radar geophysics and in demonstrating that quantitative analysis of multi-fold GPR data provides the ability to detect contaminated zones that would not be detected with conventional radar acquisition and processing methodologies. Additionally, by coordinating with independent remediation projects being conducted by private consulting firms at Hill AFB and the Cape Fear Creosote site, we were able to realize significant cost savings to the project that enabled us to conduct additional experiments such as the controlled DNAPL injection experiment at Boise State University. However, several difficulties were encountered that forced us to deviate from our original workplan.

Most importantly, we found that it was significantly more difficult than anticipated to locate well characterized sites for the controlled component of the project. Essentially every site we worked at had a significant exploration component and we uncovered unexpected NAPL anomalies at most sites. This serves to illuminate the difficulty in characterizing NAPLs using only direct sampling methods. The fact that our research program was largely successful under these conditions strongly supports the continued development and use of these site characterization tools by DOE. However, the lack of control makes it difficult to clearly define detection limits of the methods. In our best controlled experiments, Hill AFB and the tank spill, we were able to measure anomalies associated with NAPL at volumetric concentrations as low as 1-4% and we believe this is likely the lower detection limit using GPR. Where the GPR response

is measuring a secondary property, such as high-electrical conductivity at Wurtsmith AFB associated with LNAPL biodegradation biproducts, it may be possible to detect lower concentrations. At most sites, however, we were only able to conclude that NAPL was present. We could not determine whether there was a null response, ie a significant NAPL anomaly was not measured.

A second problem that forced significant deviation from the workplan was our failed DNAPL detection experiment at the Dover National Test Site. This failure was caused by greater than anticipated interference from coherent noise caused by surface objects. This is an important result in itself and highlights one of the limitations of GPR. However, we were able to conduct several successful ancillary experiments in our field time at the DNTS. Recognizing the need for a tightly controlled experiment, we conducted a controlled DNAPL spill experiment at Boise State University that was very successful. Additional significant deviations from the workplan were due to our finding that the Port Hueneme and McClellan AFB NETTS sites were not suitable for surface GPR investigation due to electrically conductive near surface sediments. As stated earlier, project cost savings allowed us to add two replacement sites, the Chevron refinery near Cincinnati, OH, and the Cape Fear Creosote site near Fayetteville, NC. In all we conducted field experiments at 10 research sites which exceeds the proposed objective of 7 sites.

Secondary objectives of the project, including development of a new forward modeling code and continued development of GPR AVO and attenuation software, were completed successfully.

The project was not completed on the proposed schedule, but with two, one year, no cost extensions. There are three primary reasons for this. First, P.I. Bradford suffered a broken leg and missed the entire summer field season during the first year of the project resulting in a significant delay in completion of field data acquisition. Second, P.I. Bradford moved from the University of Wyoming to Boise State University during the second year of the project. Finally, the problems at the originally proposed field sites, as stated above, coupled with identification, experiment planning, and data acquisition at replacement sites further delayed the project. We believe that the projects successes far outweigh problems associated with deviation from the original workplan.

6 PERSONNEL SUPPORTED

The following personnel were supported under this project:

Lead P.I.:	John H. Bradford, Research Professor, Boise State University
Co. P.I.:	W. Stephen Holbrook, Professor, University of Wyoming
Co. P.I.:	Scott B. Smithson, Professor, University of Wyoming
Senior Technical Personnel:	Allen Tanner, Geophysics Technician, University of Wyoming
Graduate Student:	Jacob C. Deeds, M.S. 2002, University of Wyoming
Undergraduate Students:	Aaron Bennett, University of Idaho
	Alex McKinley, Pacific University
	Mark Nell, Boise State University
	Chris Paul, Boise State University
	Jason Broome, Boise State University

7 PUBLICATIONS

Publications submitted to peer reviewed journals:

Bradford, J.H., in review, Applying reflection tomography in the post-migration domain to multi-fold GPR data: Geophysics. Appendix xx

Bradford, J.H., and Deeds, J.C. in review, Ground-penetrating radar theory and application of thinbed offset dependent reflectivity: Geophysics. Appendix xx

Publications nearing completion and planned for submission within the next two months:

Bradford, J.H., Quantitative analysis of the GPR response to a weathered LNAPL plume at the former Wurtsmith AFB, *Geophysics*

Bradford, J.H., A method for complex permittivity inversion from surface GPR data and application in DNAPL detection, *Geophysics*

Bradford, J.H., Resolving lateral changes in lithology using reflection tomography of multi-fold surface GPR data, *Groundwater*

Bradford, J.H., Full-waveform, frequency dependent modeling for AVO analysis of GPR data using a ray based algorithm, *Environmental and Engineering Geoscience*

Bradford, J.H., Using GPR reflection tomography to measure the water content distribution at contaminated sites within the DOE Hanford complex, *Environmental and Engineering Geoscience*

Publications in preparation and planned for submission within the next six months:

Bradford, J.H., Direct detection of LNAPL contamination at Hill Air Force Base using quantitative GPR analysis, *Environmental and Engineering Geoscience*

Bradford,J.H., Detecting DNAPL using reflection and transmission GPR tomography: A laboratory scale experiment, *Geophysics*

Posters and Oral presentations (Extended abstracts are included in the Appendices):

Bradford, J.H., 2003a, GPR offset-dependent reflectivity analysis for characterization of a high-conductivity LNAPL plume, SAGEEP 2003 Symposium on the Application of Geophysics to Environmental and Engineering Problems: San Antonio, TX, Env. Eng. Geophys. Soc., p. 238-252.

—, 2004a, 3D Multi-Offset, Multi-Polarization Acquisition and Processing of GPR Data: A Controlled DNAPL Spill Experiment, SAGEEP 2004 Symposium on the Application of Geophysics to Environmental and Engineering Problems: Colorado Springs, CO, Env. Eng. Geophys. Soc., p. 514-527.

—, 2004b, Acquisition and Processing of Multi-Fold GPR Data for Characterization of Shallow

Groundwater Systems, Eos Trans. AGU, Volume 85: Jt. Assem. Suppl.: Montreal, Quebec, Canada, p. Abstract NS41A-06.
—, 2004c, Multi-offset acquisition and processing of GPR data, Geological Society of America Abstracts with Programs, Volume Vol. 36, p. 76.
Bradford, J.H., and Clement, W.P., 2003, Using GPR to estimate water content at the Hanford Site: Acquisition and Processing Methodologies, 2003 GSA Ann. Mtg., Volume 35: GSA Abstracts with Programs: Seattle, Geol. Soc. Amer.
Bradford, J.H., and Loughridge, J., 2003, Application of two-pass migration to 3D GPR data, SAGEEP 2003: San Antonio, Env. Eng. Geophys. Soc.
Deeds, J.C., and Bradford, J.H., 2002, Characterization of an aquitard and direct detection of LNAPL at Hill Air Force Base using GPR AVO and migration velocity analysis, in Koppenjan, S., and Lee, H., eds., GPR 2002, Ninth International Conference on Ground Penetrating Radar, Volume 4758: Proceedings: Santa Barbara, CA, Intl. Soc. for Optl. Eng., p. 323-329.

8 INTERACTIONS

In addition to the conferences noted above, the work has led to two invited lectures:

"LNAPL detection using GPR attribute analysis", 2002, School of Civil Engineering, Purdue University
"LNAPL detection using GPR attribute analysis", 2002, Department of Civil and Environmental Engineering, Utah State University

In an effort to ensure that the data acquired as part of this research was relevant to current DOE, DOD, and EPA problems, we collaborated with the following institutions and personnel for site selection, site background information, survey planning, and site access:

PNNL:	Mark Freshley
Fluor Hanford:	Virginia Rohay, Scott Peterson
Westinghouse Savannah River:	Brian Looney, Dennis Jackson
Hill Air Force Base EM:	Jon Ginn
Wurtsmith Air Force Base TA:	Paul Rekowski
Dover National Test Site (NETTS):	Tim McHale
Port Hueneme NETTS:	Ernie Lorey
Ft. McClellan NETTS:	Timothy Chapman
Intera, Inc. (Hill AFB, Cape Fear):	Hans Meinardus, Kimberly Gordon
Sverdrup (Hill AFB):	Wayd Weber
Black and Veach, Inc. (Cape Fear):	Ed Hicks
Chevron Production, Inc.:	Mark Altic

Additionally, we collaborated with Intera, Inc. for soil sampling and chemical analysis at Hill AFB and the Cape Fear site. Columbia Technologies and DNTS personnel conducted CPT, geoprobe, and soil sampling at Dover National Test Site.

9 TRANSITIONS

We collaborated with Intera Inc. to incorporate the results of our work at Hill Air Force Base into a characterization drilling program and recommended remediation strategy. Our GPR data were used to contruct a map of the clay aquitard underlying the site that controls the distribution of DNAPL. During the drilling program it was found that the aquitard map was accurate to ± 1ft over the 7 acre site. Additionally, we identified drilling locations as possible contaminated zones. LIF probing conducted at these locations identified NAPL contamination at more than 75% of the sites. Collaborating engineers at Intera Inc. were Hans Meinardus and Kimberly Gordon.

We collaborated with Intera Inc. to incorporate the results of our work at the Cape Fear Creosote site into a characterization drilling program and recommended remediation strategy. Our field program at this site was relatively limited, but we identified drilling sites for DNAPL characterization. Collaborating engineers at Inter Inc. were Hans Meinardus and .

10 LITERATURE CITED

Al-Chalabi, M., 1973, Series approximation in velocity and traveltime computations: Geophys. Prosp., **21**, 783-795.

Al-Chalabi, M., 1974, An analysis of stacking, RMS, average, and interval velocities over a horizontally layered ground: Geophys. Prosp., **22**, 458-475.

Allen, J.L., and Peddy, C.P., 1993, Amplitude variation with offset: Gulf Coast case studies, Geophys. Dev. Ser., **4**, Soc. Expl. Geophys.

Atekwana, E.A., Sauck, W.A., and Werkema Jr., D.D., 2000, Investigations of geoelectrical signatures at a hydrocarbon contaminated site: J. Appl. Geophys., **44**, 167-180.

Bechtel Hanford Inc., 1995, Unexpected radiological contamination and organics at well #699-S6-E4A, RL--BHI-REMACT-1995-003.

Bergmann, T., Robertsson, J.O.A., and Holliger, K., 1998, Finite-difference modeling of electromagnetic wave propagation in dispersive and attenuating media: Geophysics, **63**, 856-867.

Bergstrom, K.A., Mitchell, T.H., and Bolin, B.J., 1995, Geophysical investigations of the 316-4 (300 North Crib), the 618-8 Burial Ground, the 618-13 (Mound), the Undocumented Solid Waste Burial Ground, the Solid Waste Burial Ground (Early Burial Ground), and the burial trench west of the process trenches, 300-FF-2 Operable Unit, BHI-00212, Rev 00, Bechtel Hanford, Inc.

Bermejo, J.L., Sauck, W.A., and Atekwana, E.A., 1997, Geophysical discovery of a new LNAPL plume at the former Wurtsmith AFB, Oscoda, Michigan: Groundwater Monitoring and Remediation, **17**, 131-137.

Black and Veach Special Projects Corp., 2002, Final NAPL Investigation Report: Cape Fear Wood Preserving Site Fayeteville, Cumberland County, North Carolina, U.S. Environmental Protection Agency.

Boudreaux-Bartels, G.F., 1985, Time-varying signal processing using the Wigner-Distribution time-frequency signal representation, Advances in geophysical data processing: JAI Press Inc. **2**, 33-79.

Bradford, J., Ramaswami, M., and Peddy, C., 1996, Imaging PVC gas pipes using 3-D GPR: SAGEEP '95, Soc. Appl. Geophys. Env. Eng., Expanded Abstracts, 519-524.

Bradford, J.H., 1998, Characterizing shallow aquifers with wave-propagation based geophysical techniques: Imaging and attribute analysis: Ph. D. thesis, Rice University.

Bradford, J.H., 2003a, GPR offset-dependent reflectivity analysis for characterization of a high-conductivity LNAPL plume: SAGEEP 2003 Symposium on the Application of Geophysics to Environmental and Engineering Problems, Env. Eng. Geophys. Soc., 238-252.

Bradford, J.H., 2003b, Using GPR to estimate water content at the Hanford Site: Acquisition and Processing Methodologies: 2003 GSA Ann. Mtg., Geol. Soc. Amer., GSA Abstracts with Programs.

Bradford, J.H., 2004a, 3D Multi-offset, multi-polarization acquisition and processing of gpr data: a controlled DNAPL spill experiment: SAGEEP 2004 Symposium on the Application of Geophysics to Environmental and Engineering Problems, Env. Eng. Geophys. Soc., 514-527.

Bradford, J.H., 2004b, Acquisition and Processing of Multi-Fold GPR Data for Characterization of Shallow Groundwater Systems: Eos. Trans., Jt. Assem. Suppl., **85,** No., 17.

Bradford, J.H., and Harper, J.T., submitted, Evidence for hydrostratification in a temperate glacier based on migration velocity analysis of ground-penetrating radar data: Geophys. Res. Let.

Bradford, J.H., and Loughridge, J., 2003, Application of two-pass migration to 3D GPR data: SAGEEP 2003 Symposium on the Application of Geophysics to Environmental and Engineering Problems, Env. Eng. Geophys. Soc., 598-612.

Bradford, J.H., Sawyer, D.S., and Zelt, C.A., 1997, AVO analysis of low-velocity, shallow sands (<50m): 67th Ann. Internat. Mtg., Soc. Expl. Geophys., Expanded abstracts, 158-162.

Bradford, J.H., and Wu, Y., 1997, Time-frequency representation of seismic signals via matching pursuit decomposition with complex Ricker wavelets: AGU Fall meeting, Amer. Geophys. Union, EOS Supplement, 33.

Brewster, M.L., and Annan, A.P., 1994, Ground-penetrating radar monitoring of a controlled DNAPL release: 200 MHz radar: Geophysics, **59**, 1211-1221.

Briggs, V., Sogade, J., Minsley, B., Lambert, M., Reppert, P.M., and Coles, D., 2004, Mapping of TCE and PCE contaminant plumes using a 3-D induced polarization data: SAGEEP 2004 Symposium on the Application of Geophysics to Environmental and Engineering Problems, Env. Eng. Geophys. Soc., 472-483.

Cai, J., and McMechan, G.A., 1999, 2-D ray-based tomography for velocity, layer shape, and attenuation from GPR data: Geophysics, **64**, 1579-1593.

Campbell, D.L., Lucious, J.E., Ellefson, K.J., and Deszcz-Pan, M., 1995, Monitoring of a controlled LNAPL spill using ground-penetrating radar: SAGEEP '95: Symposium on the Application of Geophysics to Environmental and Engineering Problems, Env. Eng. Geophys. Soc., Proceedings, 511-517.

Castagna, J.P., 1993, AVO Analysis - Tutorial and review, *in* Castagna, J.P., and Backus, M.M., Eds., Offset-dependent reflectivity - Theory and practice of AVO analysis: Soc. Expl. Geophys., Invest. Geophys. **8**, 3-36.

Castagna, J.P., Batzle, M.L., and Kan, T.K., 1993, Rock physics - the link between rock properties and AVO response, *in* Castagna, J.P., and Backus, M.M., Eds., Offset -

dependent reflectivity - Theory and practice of AVO analysis: Soc. Expl. Geophys., Invest. Geophys. **8**, 135-171.
Chakraborty, A., and Okaya, D., 1995, Frequency-time decomposition of seismic data using wavelet-based methods: Geophysics, **60**, 1906-1916.
Daniels, J.J., Robert, R., and Vendl, M., 1995, Ground penetrating radar for the detection of liquid contaminants: J. Appl. Geophys., **33**, 195-207.
Daubechies, I., 1991, Ten lectures on wavelets, SIAM.
Davis, J.L., and Annan, A.P., 1989, Ground-penetrating radar for high-resolution mapping of soil and rock stratigraphy: Geophysical Prospecting, **37**, 531-551.
Deeds, J.C., and Bradford, J.H., 2002, Characterization of an aquitard and direct detection of LNAPL at Hill Air Force Base using GPR AVO and migration velocity analysis: GPR 2002, Ninth International Conference on Ground Penetrating Radar, Intl. Soc. for Optl. Eng., Proceedings, 323-329.
Department of Energy, 1997, Limited field investigation report for the 300-FF-2 Operable Unit, DOE/RL-96-42, Rev 0.
DeRyck, S.M., Redman, J.D., and Annan, A.P., 1993, Geophysical monitoring of a controlled kerosene spill: SAGEEP '93 Symposium on the Application of Geophysics to Environmental and Engineering Problems, Env. Eng. Geophys. Soc., Proceedings, 5-19.
Dix, C.H., 1955, Seismic velocities from surface measurements: Geophysics, **34**, 180-195.
Endres, A.L., and Redman, J.D., 1996, Modeling the electrical properties of porous rocks and soils containing immiscible contaminants: J. Env. Eng. Geophys., **0**, 105-112.
Greaves, R.J., Lesmes, D.P., Lee, J.M., and Toksoz, M.N., 1996, Velocity variation and water content estimated from multi-offset, ground-penetrating radar: Geophysics, **61**, 683-695.
Griffiths, D.J., 1989, Introduction to electrodynamics, Prentice-Hall.
Grimm, R., and Olhoeft, G., 2004, Cross-hole complex resisitivity survey for PCE at the SRS A-014 Outfall: SAGEEP 2004 Symposium on the Application of Geophysics to Environmental and Engineering Problems, Env. Eng. Geophys. Soc., 455-464.
Grumman, J., David L., and Daniels, J.J., 1995, Experiments on the detection of organic contaminants in the vadose zone: J. Env. Eng. Geophys., **0**, 31-38.
Huisman, J.A., Hubbard, S.S., Redman, J.D., and Annan, A.P., 2003, Measuring soil water content with ground-penetrating radar: A review: Vadose Zone Journal, **2**, 476-491.
Jackson, D.G., Hyde, W.K., Rossabi, J., and Riha, B.D., 1999, Characterization activities to determine the extent of DNAPL in the vadose zone at the A-014 outfall of A/M Area (U), Westinghouse Savannah River Company.
Jacques, I.D., 1985, Oil spill, prevention, control and countermeasures plan, UNI-228, Rev 4, UNC Nuclear Industries.
King, R.W.P., and Owens, M., 1992, Lateral electromagetic waves: Theory and Applications to communications, geophysical exploration, and remote sensing, Springer-Verlag New York Inc.
Kueper, B.H., Redman, D., Starr, R.C., Reitsma, S., and Mah, M., 1993, A field experiment to study the behavior of tetrachloroethylene below the water table: Spatial distribution of residual and pooled DNAPL: Ground Water, **31**, 756-766.
Lafond, C.F., and Levander, A.R., 1993, Migration moveout analysis and depth focusing: Geophysics, **58**, 91-100.

Lehmann, F., 1996, Fresnel equations for reflection and transmission at boundaries between conductive media, with applications to georadar problems: GPR '96 6th International Conference on Ground-Penetrating Radar, Intl. Soc. Opt. Eng., Proceedings, 555-560.
Leparoux, D., Gibert, D., and Cote, P., 2001, Adaptation of prestack migration to multi-offset ground-penetrating radar (GPR) data: Geophys. Prosp., **49**, 374-386.
Li, X., and Ulrych, T.J., 1996, Multi-scale attribute analysis and trace decomposition: 66th Ann. Internat. Mtg., Soc. Expl. Geophys., Expanded abstracts, 1634-1637.
Liberty, L.M., and Pelton, J.R., 1994, A comparison of ground-penetrating radar methods: multi-fold data vs. single fold data: 30th Symposium on Engineering Geology and Geotechnical Engineering: Hydrogeology, Waste Disposal, Science and Politics, 321-324.
Lien, B.K., and Enfield, C.G., 1998, Delineation of subsurface hydrocarbon contaminant distribution using a direct push resistivity method: J. Env. Eng. Geophys., **2**, 173-179.
Mallat, S., and Zhang, Z., 1992, Matching pursuit with time-frequency dictionaries: Technical Report 619, IEEE transactions in signal processing.
Meinardus, H.,2000, Personal Communication
Minsley, B., Sogade, J., Briggs, V., Lambert, M., Reppert, P.M., and Coles, D., 2004, Three dimensional self-potential inversion for subsurface contaminant detection and mapping at the DOE Savannah River Site, South Carolina: SAGEEP 2004 Symposium on the Application of Geophysics to Environmental and Engineering Problems, Env. Eng. Geophys. Soc., 465-471.
Monier-Williams, M., 1995, Properties of light non-aqueous phase liquids and detection using commonly applied shallow sensing geophysical techniques: SAGEEP '95 Symposium on the Application of Geophysics to Environmental and Engineering Problems, Env. Eng. Geophys. Soc., Proceedings, 1-15.
Morlet, J., Arens, G., Fourgeau, E., and Giardi, D., 1982a, Wave propagation and sampling theory - Part I: Complex signal scattering in multilayered media: Geophysics, **47**, 203-221.
Morlet, J., Arens, G., Fourgeau, E., and Giardi, D., 1982b, Wave propagation and sampling theory - Part II: Sampling theory and complex waves: Geophysics, **47**, 222-236.
National Research Council, 2000a, Research Needs in Subsurface Science: U.S. Department of Energy's Environmental Management Science Program, National Academy Press.
National Research Council, 2000b, Seeing into the Earth: Non-invasive characterization of the shallow subsurface for environmental and engineering applications, National Academy Press.
Newmark, R.L., Daily, W.D., Kyle, K.R., and Ramirez, A.L., 1998, Monitoring DNAPL pumping using integrated geophysical techniques: J. Env. Eng. Geophys., **3**, 7-13.
Olhoeft, G.R., 1986, Direct detection of hydrocarbon and organic chemicals with ground-penetrating radar and complex resistivity: NWWA/API Conference on petroleum and hydrocarbons and organic chemicals in groundwater -- Prevention, detection, and restoration, NWWA, 284-305.
Orlando, L., 2002, Detection and analysis of LNAPL using the instantaneous amplitude and frequency of ground-penetrating radar data: Geophys. Prosp., **50**, 27-41.
Ostrander, W.J., 1984, Plane-wave reflection coefficients for gas sands at nonnormal angles of incidence: Geophysics, **49**, 1637-1648.
Pipan, M., Baradello, L., Forte, E., Prizzon, A., and Finetti, I., 1999, 2-D and 3-D processing and

interpretation of multi-fold ground penetrating data: a case history from an archaeological site: J. Appl. Geophys., **41**, 271-292.
Pipan, M., Forte, E., Dal Moro, M., Sugan, M., and Finetti, I., 2003, Multifold ground-penetrating radar and resistivity to study the stratigraphy of shallow unconsolidated sediments: The Leading Edge, 876-881.
Powers, M.H., and Olhoeft, G.R., 1996, Modeling the response of leaking, buried pipes: SAGEEP '95 Symposium on the Application of Geophysics to Environmental and Engineering Problems, Soc. Appl. Geophys. Env. Eng., Proceedings, 525-534.
Quan, Y., and Harris, J.M., 1997, Seismic attenuation tomography using the frequency shift method: Geophysics, **62**, 895-905.
Redman, J.D., and DeRyck, S.M., 1994, Monitoring non-aqueous phase liquids in the subsurface with multilevel time domain reflectometry probes: Proceedings of the symposium and workshop on time domain reflectometry in environmental, infrastructure and mining applications, United States Bureau of Mines, Special Publication, 207 - 214.
Reppert, P.M., Morgan, F.D., and Toksoz, M.N., 2000, Dielectric constant determination using ground-penetrating radar reflection coefficients: J. Appl. Geophys., **43**, 189-197.
Rossabi, J., Riha, B., and Jackson, D., 2004, Sediment sampling at the A-014 Outfall for comparison with complex resistivity measurements: SAGEEP 2004 Symposium on the Application of Geophysics to Environmental and Engineering Problems, Env. Eng. Geophys. Soc., 484-495.
Santamarina, J.C., and Fam, M., 1997, Dielectric permittivity of soils mixed with organic and inorganic fluids (0.02 GHz to 1.30 GHz): J. Env. Eng. Geophys., **2**, 37-51.
Sauck, W.A., 1998, A conceptual model for the geoelectrical response of LNAPL plumes in granular sediments: SAGEEP '98 Symposium on the Application of Geophysics to Environmental and Engineering Problems, Env. Eng. Geophys. Soc., Proceedings, 805-817.
Sauck, W.A., Atekwana, E.A., and Nash, M.S., 1998, High conductivities associated with an LNAPL plume imaged by integrated geophysical techniques: J. Env. Eng. Geophys., **2**, 203-212.
Saunders, W.R., Wightman, M., and Windschauer, R., 1993, Detection of subsurface hydrocarbons in the vadose zone with ground penetrating radar - A case study: SAGEEP '93, Env. Eng. Geophys. Soc., Proceedings, 1.
Stork, C., 1992, Reflection tomography in the postmigrated domain: Geophysics, **57**, 680-692.
Tobbock, T., Steeghs, P., Drijkoningen, G.G., and Fokkema, J.T., 1996, Decomposition of seismic signals via time-frequency representations: 66th Ann. Internat. Mtg., Soc. Expl. Geophys., Expanded abstracts, 1638-1641.
Topp, G.C., Davis, J.L., and Annan, A.P., 1980, Electromagnetic determination of soil water content; measurements in coaxial transmission lines: Water Resour. Res., **16**, 574-582.
Yilmaz, O., 2001, Seismic data analysis, Soc. Expl. Geophys.
Young, R.A., and Sun, J., 1996, 3D ground penetrating radar imaging of a shallow aquifer at Hill Air Force Base, Utah: J. Env. Eng. Geophys., **1**, 97-108.
Young, R.A., and Sun, J., 1998, Extracting a radar reflection from a cluttered environment using 3-D interpretation: J. Env. Eng. Geophys., **3**, 121-131.
Zeng, X., McMechan, G.A., and Xu, T., 2000, Synthesis of amplitude versus offset variations in

ground-penetrating radar data: Geophysics, **65**, 113-125.

APPENDIX A: APPLYING REFLECTION TOMOGRAPHY IN THE POST MIGRATED DOMAIN TO GROUND PENETRATING RADAR DATA

(Submitted to Geophysics)

Applying reflection tomography in the post-migrated domain to multi-fold ground-penetrating radar data

John H. Bradford

Boise State University, Center for Geophysical Investigation of the Shallow Subsurface, 1910 University Dr., Boise, ID. 83703

INTRODUCTION

Accurate estimation of electromagnetic (EM) velocity is critical in ground penetrating radar investigations. Not only does the velocity enable accurate time to depth image transforms, but the velocity is a direct measure of subsurface electrical properties that may be used to improve our understanding of the subsurface. When coupled with a suitable mixing equation, the velocity can be used to estimate permittivity which in turn may lead to estimates of pore fluid content (Brewster and Annan, 1994; Greaves et al., 1996; Huisman et al., 2003; Powers and Olhoeft, 1996; Topp et al., 1980). Most GPR surveys are acquired with a constant transmitter-receiver offset. EM velocity estimates can made from common-offset data with one of two methods. The moveout of scattering diffractions provides a measure of EM velocity, but the distribution of scattering events limits the precision of the velocity model and in many cases, no diffractions are present. The second method utilizes qualitative interpretation to correlate reflectors in the radar section with significant boundaries identified in the borehole data followed by velocity calibration. Of course borehole data are not always available, there is potential for misinterpretation, and this method suffers from a lack of lateral resolution.

Given these limitations, it is typical to acquire one or more sparsely located CMP gathers within a broader survey area to obtain a 1D or coarse laterally varying velocity structure for interpreting a common-offset survey. From the CMP gather, an RMS velocity distribution is

estimated using normal moveout analysis (Bradford et al., 1996; Campbell et al., 1995; Young and Sun, 1996). A common strategy for computing effective interval velocities from the RMS velocity utilizes Dix inversion (Dix, 1955). This approach does not account for lateral velocity heterogeneity, and is sensitive to velocity errors resulting from dipping reflections or diffraction tails (Yilmaz, 2001).

We can overcome these limitations by acquiring data in continuous multi-offset (CMO) mode. With this method we use the well established acquisition geometries of seismic exploration to acquire several traces, with varying source-receiver separations, at each point within a survey. Acquiring CMO data has a number of advantages including suppression of coherent and random noise (Bradford, 2003b; Bradford, 2004b; Liberty and Pelton, 1994; Pipan et al., 1999; Pipan et al., 2003).

CMO data enable detailed measurement of lateral velocity variability (Greaves et al., 1996). However, NMO based processing schemes are subject to the fundamental assumptions of NMO velocity analysis which include small offset-to-depth ratios, small vertical and horizontal velocity gradients, and planar flat lying reflections. These assumptions are often violated in GPR investigations. For example, EM velocity can decrease by a factor of 3 or more across the water table as the sediment grades from dry to full water saturation (Bradford, 2003a; Bradford, 2004a). This can result in severe departure from normal moveout leading to very large overestimates of interval velocity (Al-Chalabi, 1973; Al-Chalabi, 1974). When NMO velocity analysis fails, we must resort to more rigorous methods of velocity estimation.

REVIEW OF PSDM VELOCITY ESTIMATION

Pre-stack depth migration (PSDM) focuses scattered energy, moves dipping events to the

correct spatial location, and treats lateral and vertical velocity gradients correctly. As long as precise amplitude reconstruction is not a primary interest (e.g. we are only measuring wavefield kinematics), and with the basic assumption that the subsurface electric properties are independent of frequency, many of the migration algorithms developed for seismic data analysis can be applied directly to GPR data without modification. While not generally true, the assumption of frequency independent material properties is a reasonable first order approximation in most cases and often good migration results (Bradford et al., 1996; Bradford, 2004a; Bradford and Harper, submitted; Bradford and Loughridge, 2003; Deeds and Bradford, 2002) are obtained with any of the standard migration tools (Yilmaz, 2001).

PSDM depends strongly on the depth velocity model so that accurate velocity estimation is critical. Methods for estimating the velocity distribution fall into two categories: 1) Reflection tomography, and 2) PSDM velocity analysis.

Most tomography algorithms are designed to invert for the velocity structure based on travel time picks of specific reflecting horizons in the premigration domain. As pointed out by Stork (1992), tomography has the advantage that computational methods for solving the inverse problem are well understood and solutions can be found quickly and efficiently. A significant disadvantage arises when there is significant subsurface complexity and wavefield distortion makes it difficult to pick the traveltimes of specific reflecting horizons.

PSDM velocity analysis takes advantage of the strong velocity dependence of PSDM. When the data are migrated with the correct velocity model, reflections in common image point (CIP) gathers (the post-migration analog of CMP gathers) will migrate to the same depth and will appear flat (Fig. 1). If the velocity model is wrong, there is an apparent offset dependent depth

which can be characterized as residual moveout. The residual moveout is positive or negative depending on whether the velocity is too high or too low respectively (Fig. 1). After migration with an initial velocity model, the velocity model is updated to remove residual moveout with a top-to-bottom method known as layer stripping. With this method the data are remigrated after each velocity update and checked for RMO, often using coherence panels in the CIP domain (Lafond and Levander, 1993). The process is repeated until all residual moveout is removed. PSDM analysis takes advantage of reflector coherence and continuity in the postmigration domain. This improves the processor's ability to evaluate specific reflecting horizons, particularly in a complex subsurface setting. Further, the output of PSDM velocity analysis is a suburface velocity model and PSDM image.

Both reflection tomography and PSDM velocity analysis have been applied to ground-penetrating radar data. For example, Cai and McMechan (1999) describe a method for estimating the subsurface EM velocity and attenuation models using a reflection tomography algorithm. And Leparoux et al. (2001) discuss the application of PSDM migration velocity analysis to GPR data.

Stork (1992) presents a method of reflection tomography that seeks to minimize RMO in CIP gathers in the post-migration domain. This method combines the computational advantages of tomography with the inherent interpretational advantage of PSDM velocity analysis. A code that utilizes Stork's method is available with Promax™ processing software which I used to process all data presented in this study. A typical work flow for the application of this method is given in Table 1.

FIELD APPLICATION: AN EXAMPLE FROM THE DOE HANFORD SITE

Field Setting

The U.S. Department of Energy's (DOE) Hanford Site, located in southeast Washington (Fig. 2), was the site of the first operational nuclear reactor, and produced much of the plutonium for the U.S. nuclear arsenal. These activities resulted in the release of large amounts of radiological and chemical waste to the environment at a number of locations throughout the Hanford complex. The 618-10 Burial Ground is located approximately 4 miles northeast of Hanford's 300 Area. This site contains several pits that received solid mixed waste from the mid 1950's until 1960 (Fig. 2). The pits were later backfilled. During a surface stabilization project in 1983, a black oily substance was observed bubbling to the surface above Pit #4. No samples were taken, but this substance is thought to be a potential contributor to groundwater contamination. The 316-4 Crib is located about 35 m southeast of 618-10 and consists of two buried, open bottomed tanks (Fig. 2). Approximately 200,000 l of liquid organic and uranium wastes were pumped into the disposal tanks and allowed to drain into the underlying formation during the 1950s and 1960s. Radiological and volatile organic contamination has been found in several borings near the 618-10 and 316-4 sites (Bechtel Hanford Inc., 1995){Department of Energy, 1997 #110}. Groundwater lies approximately 18 m below the surface, and there is concern that the observed radiological and chemical contamination will reach the groundwater and migrate to the Columbia River, located approximately 5 km to the east. Near surface sediments at the site are comprised of surficial eolian sands (~ 0-5 m depth) overlying the interbedded sands and gravels of the Hanford formation (~ 5-80 m depth).

This field campaign was undertaken as part of DOE's effort to identify and improve methods of quantitative geophysical characterization of contaminated sites, with a particular

emphasis on developing detailed subsurface models at the Hanford Site. One of the primary objectives in this study was imaging potential contaminant migration routes within the vadose zone beneath the 618-10 Burial Ground. In a 1997 cone-penetrometer investigation, a low permeability cemented gravelly layer was identified at a depth of about 12 m and is suspected of playing a significant role in contaminant migration (Department of Energy, 1997). This cemented gravel was the primary target of this GPR investigation.

Data Acquisition and Processing

In September, 2002, my field team acquired 293 m of 2D multi-offset data, in common-source point mode, along 3 profiles at the site (Fig. 2). We followed an acquisition procedure similar to that described by Fisher et al. {, 1992 #24} using the parameters listed in Table 2. Generally, data quality varies from excellent to fair with 9-12 m of penetration (Fig. 3). Departure from NMO is clearly evident in the shot gathers (Fig. 3A) indicating significant suburface complexity

Pre-migration processing steps included a bandpass filter (12-25-200-400 MHz), automatic gain control (20 ns time gate), and construction of a starting depth velocity model using sparse (~ every 200 CMPs) NMO velocity analysis. A constant stacking velocity of 0.125 m/ns produced a good stack (Fig. 3). The stacked image shows significant improvement in signal-to-noise over the conventional common-offset image. This improvement in data quality is particularly evident along the southeastern end of Line 1 where steeply dipping clinoforms, infilling a buried palechannel, are clearly evident in the stacked image but are difficult to identify with confidence in the common-offset image. Additionally, coherent noise resulting from an off-end reflection from the chain link fence is present in the common-offset section, but is strongly

attenuated in the stacked section.

Reflection Tomography and PSDM

For the starting depth velocity model, I used a constant velocity of 0.125 m/ns. I migrated the data in the common-offset domain using a Kirchoff PSDM algorithm that includes topography. Note that the datum used for migration is the ground surface at well 699-S6-E4A (Fig. 2). I picked 8 or more horizons for RMO along each profile (Figs. 5 and 6). RMO was computed using semblance analysis in the CIP domain. The first round of RMO analysis showed that there was a significant velocity high associated with Pit #1 and a velocity low associated with Pit #4 (Fig. 4). More subtle velocity anomalies were present throughout the dataset. I constrained the inversion to allow linear vertical velocity gradients between major RMO horizons, arbitrary lateral velocity variations, and discontinuities across RMO horizons. A single iteration of reflection tomography with these constraints produced excellent migration results (Figs. 5, 6 and 7).

Interpretation

I have identified four major stratigraphic units within the survey area. Unit divisions are based on the strength and continuity of radar reflections bounding each unit. As an additional constraint on the interpretation, I used significant divisions in the velocity profile, although it should be noted that there is significant lateral velocity heterogeneity within each unit. Interpretation of the lithology is based on borehole logs from wells 699-S6-E4A and 699-S6-E4E and CPT boring B2764 (Fig. 2) that were acquired as part of an earlier site investigation (Department of Energy, 1997). While the borehole logs lack significant detail in the lithologic description, three sand units are identified in the upper 7 m below datum (b.d.), a brown sand

(S1), black sand (S2) and basalt sand (S3) (Fig. 6). Below this, is a thick sandy gravel unit (G1/G2). In the radar sections, numerous reflectors are evident within each of these coarsely defined units that are likely caused by small grain size changes resulting in water content variability. In Well E4E, the target cemented gravel layer was encountered at 23 m b.d. The cemented gravel is not noted in the E4A log. Further constraint on the depth to gravel unit is taken from CPT boring B2764 where the cemented gravel was encountered at 14 m b.d.

The full stratigraphic profile is most clearly observed along Line 1B (Fig. 5) and Line 3 (Fig. 7) because the surface sediments along Line 1A (Fig. 5) and Line 2 (Fig. 6) were disturbed during waste disposal activities. The upper most unit (U1) extends from 0 m - ~ 4m b.d.. U1 is comprised of the eolian sands that form the dune evident as a topographic high along Lines 1B and Line 2. Unit 2 (U2) extends from ~4 m - ~ 6 m b.d.. This unit is characterized by generally lower velocities. The velocity inversion associated with U2 becomes more pronounced toward the southeastern boundary of the 618-10 Burial Ground where there is an areal topographic low. Unit 3 (U3) extends to a depth of ~ 8 m and the lower bounding horizon is an erosional discontinuity that marks the transition from the shallow sand dominated system, to the deeper gravel dominated system. This surface appears to be approximately flat lying and planar througout the survey area. U3 has generally higher velocities than U1 or U2. The U1-U3 package dips toward the southwest with U2 reaching the surface at the northern portion of the survey area where U1 is not present (Fig. 7). U4 is a sandy gravel unit that forms the fill of a paleochannel network that underlays the entire site. U4 varies in thickness from 0 m to > 10 m. U4 generally has the highest velocities observed at the site. Additionally, the base of U4 marks the maximum extent of radar signal penetration.

In unsaturated sediments, velocity is primarily controlled by soil moisture content (Olhoeft, 1986; Topp et al., 1980) with higher water content resulting in lower radar velocity. Finer grained materials tend to have higher residual water saturation to due capillary forces (Bedient et al., 1994) and it is reasonable to infer that in the vadose zone, low velocities correlate with finer grained materials while higher velocities correlate with coarser grained materials. Under this assumption I interpret U2 as composed of relatively fine grained sand, and U4 of relatively coarse material. While the available lithologic logs do not provide detailed grain size estimates to confirm this interpretion, U4 is primarily a gravel unit which is consistent with the interpretation.

Burial Pits #1 and #4 are evident in the stacked image where stratigraphic reflectors are truncated (Fig. 3). Numerous scattering events from the base of the pits suggests buried debris covered with relatively homogeneous backfill. Burial Pits #1 and #4 are clearly delineated in the PSDM image and inverted velocity model (Fig. 5). Note that I found no evidence for Pits #2 or #3 in either the velocity model or reflection images suggesting that the positions of these pits were not correctly mapped in the historical literature. Pit #1 has a large high velocity anomaly associated with the buried debris located near the base of the pit. Pit #4 has a stratiphied velocity structure with a velocity high located within a fill layer at the top of the pit and a significant velocity low associated with the material filling the deeper portion of the pit. This is opposite the trend observed in the adjacent stratigraphic section where the surface velocity is slow then increases in the deeper strata. The trend in the velocity model is consistent with the observed reflectivity where the 5 m deep reflection within Pit #4 has polarity opposite that of the adjacent 5 m deep stratigraphic reflection (Figs. 3 and 5).

The disposal tank and disturbed surficial sediments associated with the 316-4 Crib are clearly imaged in the PSDM section (Fig. 6). Historical DOE records indicated that these were stainless steel tanks (Bergstrom et al., 1995), but this is necessarily incorrect as there is a clear radar image from both the top and bottom of the tank which would not be possible were it constructed from electrically conductive material. Surprisingly, there is no clear velocity anomaly associated with the tank itself (Fig. 6), since I expect the empty tank to produce a high velocity zone. It is important to note that the velocity of this feature is poorly constrained since there is no continuous horizon imaged below the tank and the dimensions of the tank are only about 1 wavelength (in air) at the dominant signal frequency. Of further interest is the zone of high attenuation that appears to emanate from the base of the disposal tank. This is likely caused by increased conductivity of the sediment column due to residual ion deposition from the dumped radiological contaminants.

As stated in the introduction, the primary objective of this study was to characterize the cemented gravel layer noted in an earlier DOE investigation (Department of Energy, 1997). The cemented gravel was encountered at ~14 m below b.d. in CPT boring B2764 which correlates very well with the erosional surface that forms the base of U4 along Lines 2 and 3 (Figs. 6 and 7). Additionally, the lithologic log from Well 699-S6-E4E, located just beyond the southeast end of Line 1, indicates that cemented gravel was encountered at ~23 m b.d.. This is roughly consistent with the base of U4 which reaches ~ 18 m b.d. at the southeastern end of Line 1 and appears to continue deepening off the end of the profile . Note that precise interpretation of the base of U4 is difficult at this location due to very low reflection strength, and that internal inconsistencies in the E4E lithologic log make its reliability questionable. Generally, however, I interpret the cemented

gravel as lying at or just below the erosional surface that forms the paleochannel network at the base of U4. This is likely caliche which typically forms just below exposure surfaces (American Geologic Institute, 1972; Blatt et al., 1972).

There are two significant problems with the dataset that must be addressed. First, the velocity models at the intersection of Line 1 and Line 3 are not in good agreement, although the general features are similar - i.e. U1 and U3 and U4 are faster, and U2 is slower. First its important to note that the intersection is very near the end of Line 1B in the region where the tomographic solution is damped. Second, there is a clear depositional trend toward the southeast which may result in azimuthal anistropy. And finally, Line 1 intersects Line 3 at a location where there is a significant lateral velocity increase along Line 3. The Line 1 velocities will be preferentially biased toward the higher velocity zone. This leads directly to the second significant problem. The 3D complexity of both the stratigraphy and velocity structure means that the results of my 2D analysis are necessarily contaminated with out-of-plane noise. This may only be resolved in detail through full 3D data acquisition and processing, however generally good agreement between the PSDM images and available lithologic control provides a level of confidence in the general conclusions of the data interpretation.

Both the 618-10 Burial Ground and 316-4 Crib are underlain by a paleochannel network that appears to have a low permeability cemented unit at its base. The channel fill, U4, consists of coarse grained and likely high permeability sands and gravels. It is likely that this paleochannel network forms a prime migration route for contaminates emanating from either the 618-10 Burial Ground or the 316-4 Crib.

CONCLUSIONS

Reflection tomography in the post-migration domain is an attractive tool for velocity analysis of multi-fold GPR data. It combines the computational efficiency of tomographic inversion with the practical advantages of data interpretation in the post-migration domain, specifically semblance within CIP gathers and reflector coherence in horizon picking. As a further benefit, the output of the method is both a depth velocity model and PSDM radar section.

The field example presented here demonstrates the added benefit of CMO data acquisition and processing methodologies. CMP/CIP stacking significantly improved the signal to noise ratio in the GPR sections leading to more confident, detailed interpretation. Reflection tomography in the post-migration domain made it possible to accurately resolve significant lateral and vertical velocity heterogeneity. The resulting detailed velocity models could be interpreted in directly to locate significant features such a the waste disposal pits within the 618-10 Burial Ground. Further, the velocity models helped guide the interpretation of significant lithologic units and constrain the likely relative grain size distribution. Finally, I used the PSDM images, coupled with the detailed velocity models to identify a paleochannel network, underlying the site, as forming likely contaminant migration pathways.

ACKNOWLEGEMENTS

The U.S. Department of Energy funded this work under the Environmental Management Science Program, Grant # DE-FG07-99ER15008.

REFERENCES

Al-Chalabi, M., 1973, Series approximation in velocity and traveltime computations: Geophys. Prosp., **21**, 783-795.

Al-Chalabi, M., 1974, An analysis of stacking, RMS, average, and interval velocities over a horizontally layered ground: Geophys. Prosp., **22**, 458-475.

American Geologic Institute, 1972, Glossary of Geology, Amer. Geol. Inst.

Bedient, P.B., Rifai, H.S., and Newell, C.J., 1994, Ground water contamination: Transport and remediation, Prentice-Hall, Inc.

Bergstrom, K.A., Mitchell, T.H., and Bolin, B.J., 1995, Geophysical investigations of the 316-4 (300 North Crib), the 618-8 Burial Ground, the 618-13 (Mound), the Undocumented Solid Waste Burial Ground, the Solid Waste Burial Ground (Early Burial Ground), and the burial trench west of the process trenches, 300-FF-2 Operable Unit, BHI-00212, Rev 00, Bechtel Hanford, Inc.

Blatt, H., Middleton, G., and Murray, R., 1972, Origin of Sedimentary Rocks, Prentice-Hall, Inc.

Bradford, J., Ramaswami, M., and Peddy, C., 1996, Imaging PVC gas pipes using 3-D GPR: SAGEEP '95, Soc. Appl. Geophys. Env. Eng., Expanded Abstracts, 519-524.

Bradford, J.H., 2002, Depth characterization of shallow aquifers with seismic reflection - Part I: The failure of NMO velocity analysis and quantitative error prediction: Geophysics, **67**, 89-97.

Bradford, J.H., 2003a, GPR offset-dependent reflectivity analysis for characterization of a high-conductivity LNAPL plume: SAGEEP 2003 Symposium on the Application of Geophysics to Environmental and Engineering Problems, Env. Eng. Geophys. Soc., 238-252.

Bradford, J.H., 2003b, Using GPR to estimate water content at the Hanford Site: Acquisition and Processing Methodologies: 2003 GSA Ann. Mtg., Geol. Soc. Amer., GSA Abstracts with

Programs.

Bradford, J.H., 2004a, 3D Multi-offset, multi-polarization acquisition and processing of gpr data: a controlled DNAPL spill experiment: SAGEEP 2004 Symposium on the Application of Geophysics to Environmental and Engineering Problems, Env. Eng. Geophys. Soc.

Bradford, J.H., 2004b, Acquisition and Processing of Multi-Fold GPR Data for Characterization of Shallow Groundwater Systems: Eos. Trans., Jt. Assem. Suppl., **85,** No., 17.

Bradford, J.H., and Harper, J.T., submitted, Evidence for hydrostratification in a temperate glacier based on migration velocity analysis of ground-penetrating radar data: Geophys. Res. Let.

Bradford, J.H., and Loughridge, J., 2003, Application of two-pass migration to 3D GPR data: SAGEEP 2003, Env. Eng. Geophys. Soc.

Bradford, J.H., and Sawyer, D.S., 2002, Depth characterization of shallow aquifers with seismic reflection - Part II: Pre-stack depth migration and field examples: Geophysics, **67**, 98-109.

Brewster, M.L., and Annan, A.P., 1994, Ground-penetrating radar monitoring of a controlled DNAPL release: 200 MHz radar: Geophysics, **59**, 1211-1221.

Cai, J., and McMechan, G.A., 1999, 2-D ray-based tomography for velocity, layer shape, and attenuation from GPR data: Geophysics, **64**, 1579-1593.

Campbell, D.L., Lucious, J.E., Ellefson, K.J., and Deszcz-Pan, M., 1995, Monitoring of a controlled LNAPL spill using ground-penetrating radar: SAGEEP '95: Symposium on the Application of Geophysics to Environmental and Engineering Problems, Env. Eng. Geophys. Soc., Proceedings, 511-517.

Deeds, J.C., and Bradford, J.H., 2002, Characterization of an aquitard and direct detection of

LNAPL at Hill Air Force Base using GPR AVO and migration velocity analysis: GPR 2002, Ninth International Conference on Ground Penetrating Radar, Intl. Soc. for Optl. Eng., Proceedings, 323-329.

Department of Energy, 1997, Limited field investigation report for the 300-FF-2 Operable Unit, DOE/RL-96-42, Rev 0.

Dix, C.H., 1955, Seismic velocities from surface measurements: Geophysics, **34**, 180-195.

Fisher, E., McMechan, G.A., and Annan, A.P., 1992, Acquisition and processing of wide-aperture ground-penetrating radar data: Geophysics, **57**, 495-504.

Greaves, R.J., Lesmes, D.P., Lee, J.M., and Toksoz, M.N., 1996, Velocity variation and water content estimated from multi-offset, ground-penetrating radar: Geophysics, **61**, 683-695.

Huisman, J.A., Hubbard, S.S., Redman, J.D., and Annan, A.P., 2003, Measuring soil water content with ground-penetrating radar: A review: Vadose Zone Journal, **2**, 476-491.

Lafond, C.F., and Levander, A.R., 1993, Migration moveout analysis and depth focusing: Geophysics, **58**, 91-100.

Leparoux, D., Gibert, D., and Cote, P., 2001, Adaptation of prestack migration to multi-offset ground-penetrating radar (GPR) data: Geophys. Prosp., **49**, 374-386.

Liberty, L.M., and Pelton, J.R., 1994, A comparison of ground-penetrating radar methods: multi-fold data vs. single fold data: 30th Symposium on Engineering Geology and Geotechnical Engineering: Hydrogeology, Waste Disposal, Science and Politics, 321-324.

Olhoeft, G.R., 1986, Direct detection of hydrocarbon and organic chemicals with ground-penetrating radar and complex resistivity: NWWA/API Conference on petroleum and hydrocarbons and organic chemicals in groundwater -- Prevention, detection, and

restoration, NWWA, 284-305.

Pipan, M., Baradello, L., Forte, E., Prizzon, A., and Finetti, I., 1999, 2-D and 3-D processing and interpretation of multi-fold ground penetrating data: a case history from an archaeological site: J. Appl. Geophys., **41**, 271-292.

Pipan, M., Forte, E., Dal Moro, M., Sugan, M., and Finetti, I., 2003, Multifold ground-penetrating radar and resistivity to study the stratigraphy of shallow unconsolidated sediments: The Leading Edge, 876-881.

Powers, M.H., and Olhoeft, G.R., 1996, Modeling the response of leaking, buried pipes: SAGEEP '95 Symposium on the Application of Geophysics to Environmental and Engineering Problems, Soc. Appl. Geophys. Env. Eng., Proceedings, 525-534.

Stork, C., 1992, Reflection tomography in the postmigrated domain: Geophysics, **57**, 680-692.

Topp, G.C., Davis, J.L., and Annan, A.P., 1980, Electromagnetic determination of soil water content; measurements in coaxial transmission lines: Water Resour. Res., **16**, 574-582.

Yilmaz, O., 2001, Seismic data analysis, Soc. Expl. Geophys.

Young, R.A., and Sun, J., 1996, 3D ground penetrating radar imaging of a shallow aquifer at Hill Air Force Base, Utah: J. Env. Eng. Geophys., **1**, 97-108.

Table 1. Typical work flow for reflection tomography in the postmigration domain

1. Derive starting depth velocity model
2. Apply PSDM
3. Pick horizons
4. Estimate wavefront kinematics using raytracing
5. Estimate RMO distribution using semblance analysis along coherent horizons
6. Update velocity model via tomography
7. QC/edit velocity model and apply PSDM with new velocity model
8. QC RMO distribution and iterate starting at Step 3 if necessary

Table 2. Data acquisition parameters.

Survey Type	TE, Constant Azimuth
GPR System	Sensors and Software PE 100A, 100 MHz Unshielded Antennas
Min/Max Offset	.91 m/8.2 m
#Receivers/Source	25
Source Interval	0.61 m
Receiver Interval	0.30 m
Sampling Interval	0.8 ns
Recording time	400 ns
#Stacks/Source	16

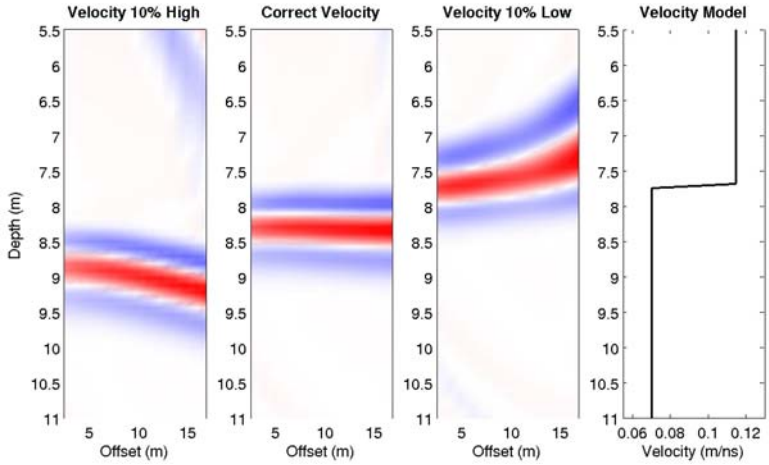

Figure 1. PSDM CIP gathers computed from a simple synthetic dataset. RMO in the CIP gathers is strongly sensitive to even small errors in the velocity model.

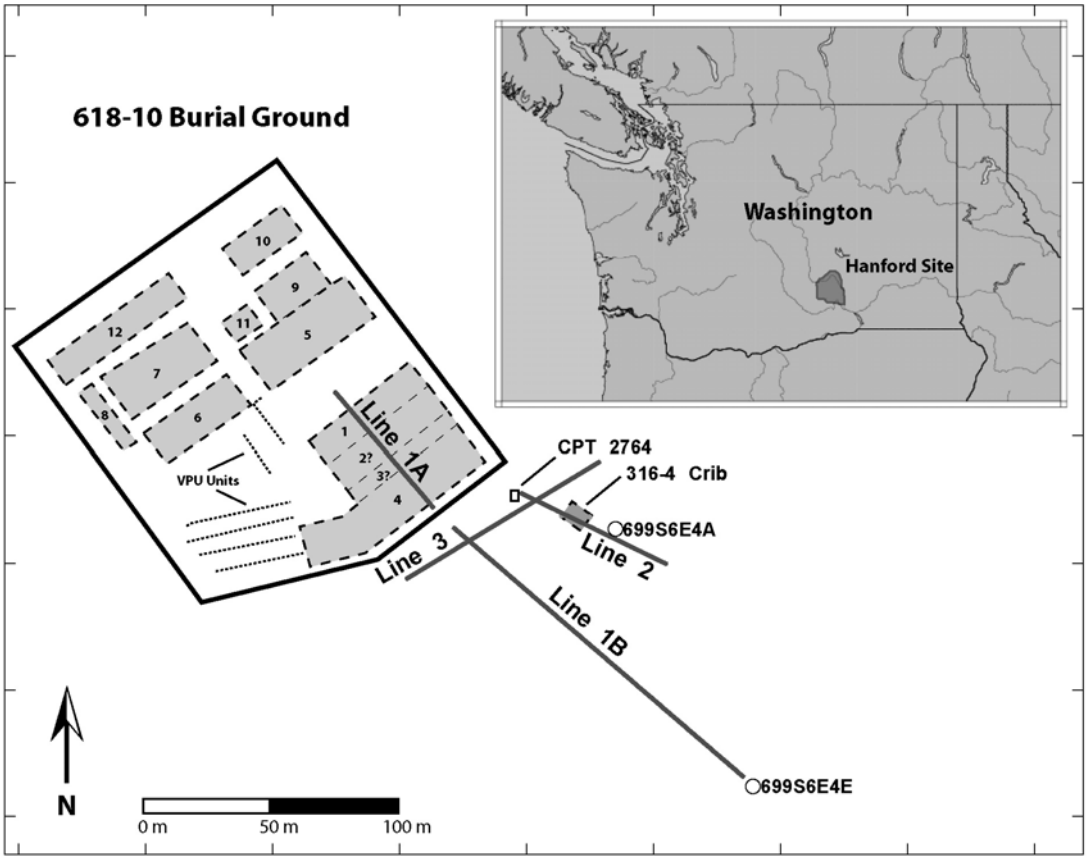

Figure 2. Site location and orientation of profiles discussed in the text.

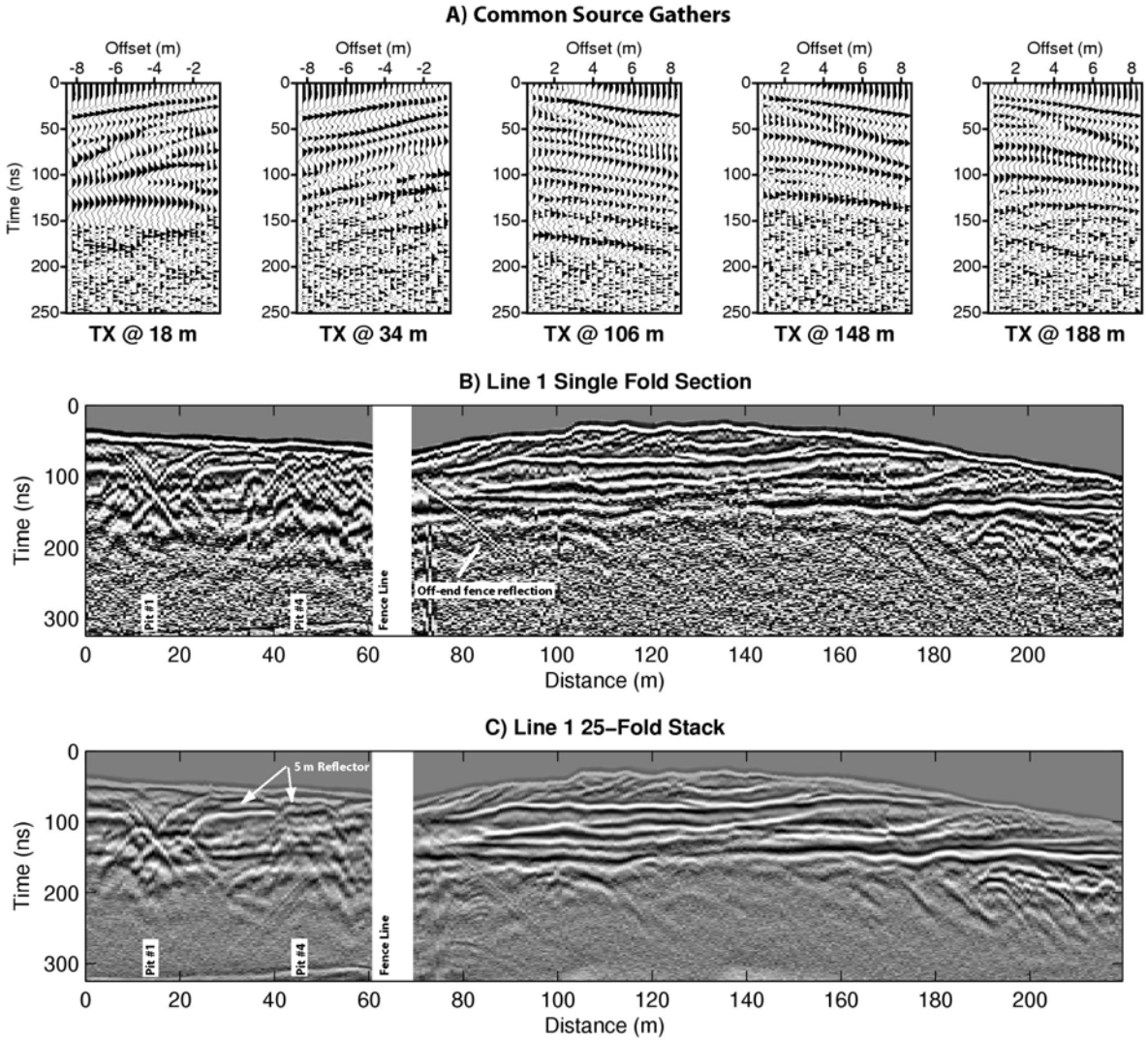

Figure 3. A) Common source gathers along Lines 1A and 1B. B) Conventional common offset GPR section with a 0.61 m trace spacing. C) 25-fold stack computed by combining the data into 0.61 m CMP bins. Significant departure from NMO in the source gathers at TX=18 m and TX=188 m suggest subsurface complexity. Stacking improves the signal to noise ratio, most evident between 150 ns and 300 ns on the right hand side of the profile.

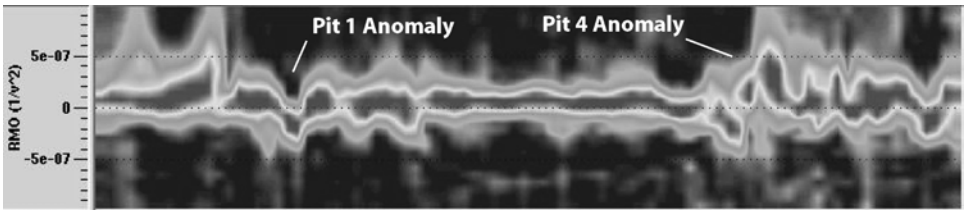

Figure 4. RMO semblance plot showing a high velocity (negative RMO) anomaly associated with Pit 1 and a low velocity (positive RMO) associated with Pit 4.

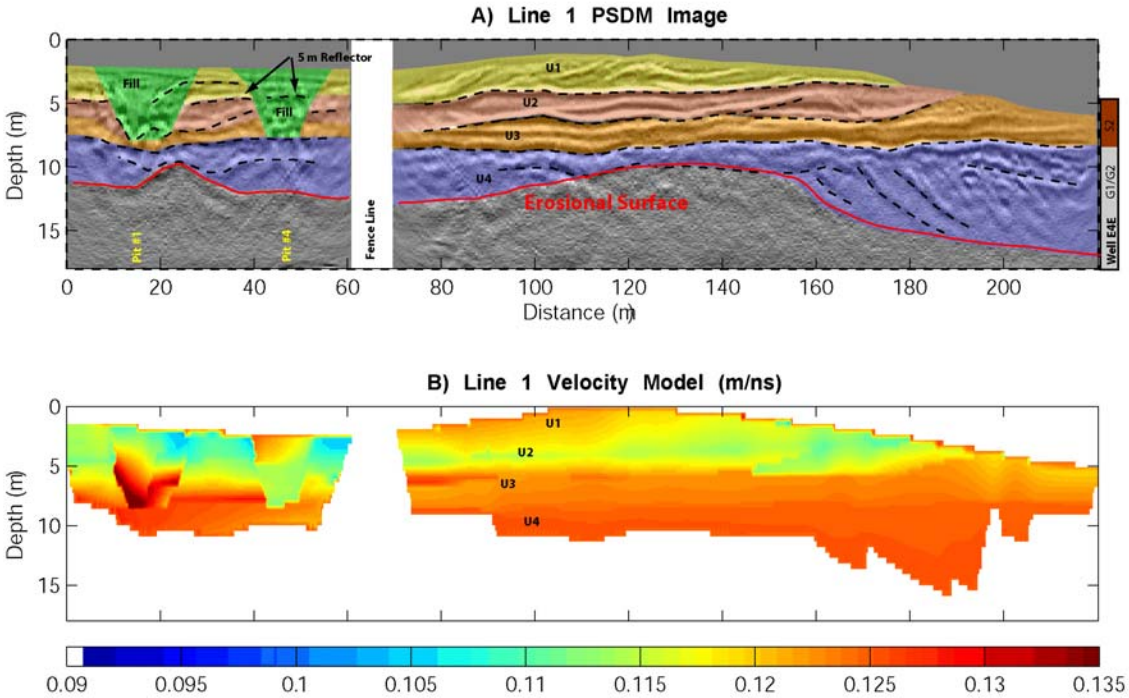

Figure 5. A) Interpreted PSDM image of Line 1 and B) tomographic velocity model. Horizons used for RMO analysis are indicated with dashed lines. The velocity model is only shown where there is ray coverage. The erosional surface at the base of U4 likely delineates a primary contaminant transport route. Pit 1 and Pit 4 are clearly evident in both the reflection image and velocity model.

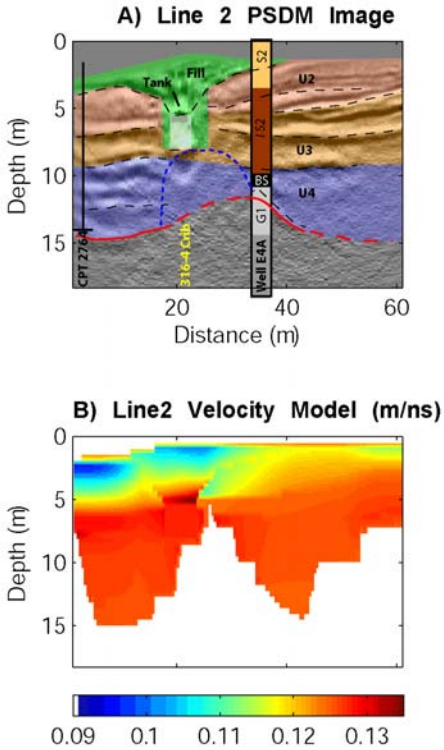

Figure 6. A) Interpreted PSDM image of Line 2 and B) tomographic velocity model. Horizons used for RMO analysis are indicated with dashed lines. The velocity model is only shown where there is ray coverage. One of the 316-4 Crib disposal tanks is clearly delineated in the reflection section, but not the velocity model. CPT B2764 indicates the depth of the cemented gravel unit.

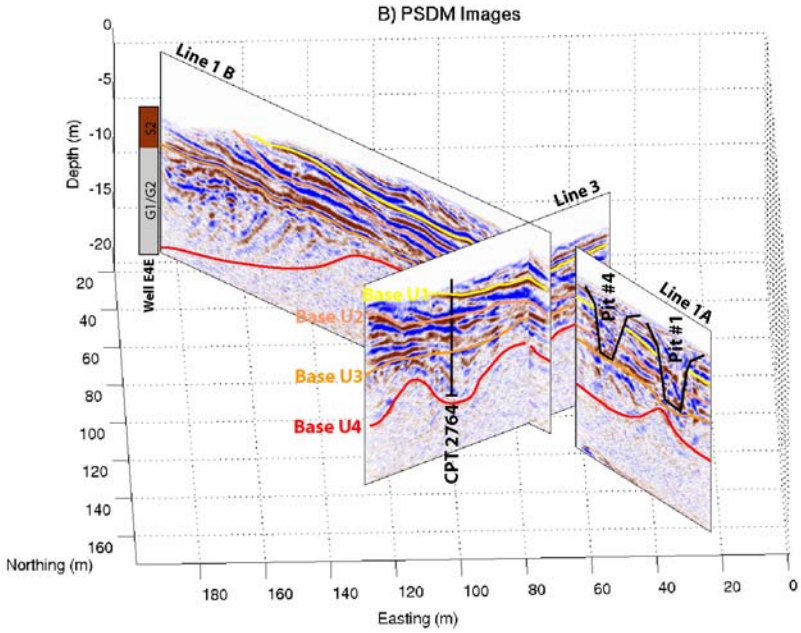

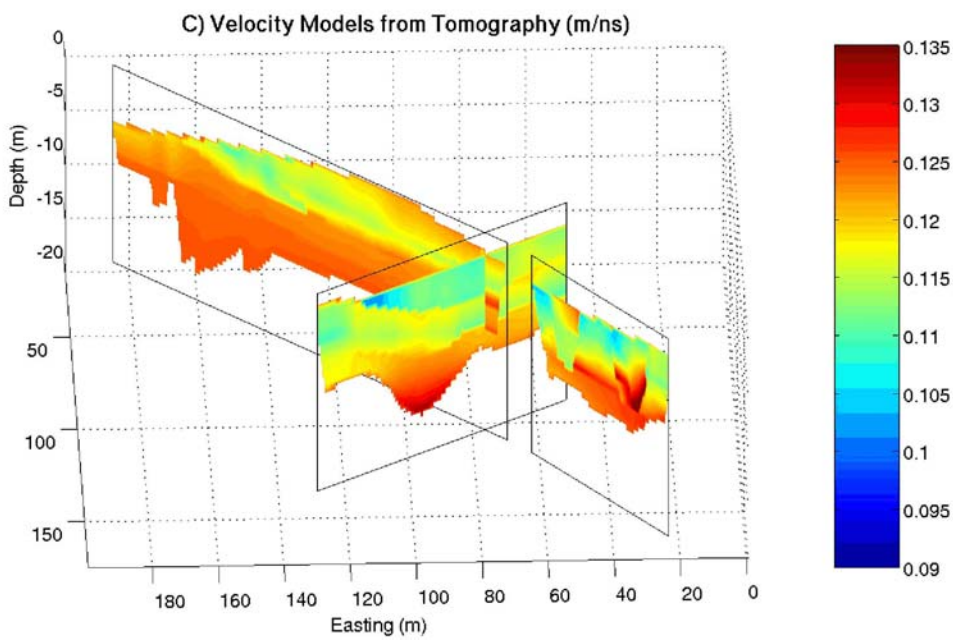

Figure 7. A) PSDM reflection images of Line 1 and Line 3, and B) tomographic velocity models. Based on high radar velocity and borehole observations, we interpret U4 to be comprised of relatively coarse grained and likely high permeability sandy gravels. The cemented gravel unit identified in CPT 2764 and Well E4E appears to lie at the base of U4 whichh defines a NW/SE trending paleochannel network that likely forms primary contaminant transport routes.

APPENDIX B: GROUND-PENETRATING RADAR THEORY AND APPLICATION OF THINBED OFFSET-DEPENDENT REFLECTIVITY

(Submitted to Geophysics)

Ground-penetrating radar theory and application of thinbed offset-dependent reflectivity

John H. Bradford[1] and Jacob C. Deeds[2]

[1] *Boise State University, Center for Geophysical Investigation of the Shallow Subsurface, 1910 University Dr., Boise, ID. 83703*

[2]*University of Wyoming, Department of Geology and Geophysics, 16th and Gibbon, Laramie, Wyoming, 82070*

ABSTRACT

Offset dependent reflectivity or amplitude variation with offset (AVO) analysis has significant potential to improve the detail and accuracy of estimating the subsurface electric permittivity distribution using ground-penetrating radar (GPR). The Fresnel equations serve as a starting point in understanding the GPR AVO response, but the assumptions needed to derive these equations are often violated under field conditions. One such complication is the thinbed problem where the target of interest is distributed in a layer that is thinner than a wavelength at the dominant frequency of the signal. Our approach to modeling the GPR thinbed response is a broadband, frequency dependent computation that utilizes an analytical solution to the three-layer reflectivity and is easy to implement for either transverse electric (TE) or transverse magnetic (TM) polarizations. In most cases, when the thin layer is greater than 0.5 to 0.75 as thick as the characteristic wavelength of the signal, the Fresnel Equations are a good approximation of the thinbed response. Below this limit thinbed analysis is necessary. In two field examples, taken from contaminated site characterization, we have found that quantitative thinbed modeling agrees well with the GPR field data and available characterization data.

INTRODUCTION

Over the past 20-25 years, the study of offset-dependent reflectivity, or amplitude variation with offset (AVO) analysis, of seismic data has been used successfully to associate shear and compressional wave properties with the presence of oil or natural gas (Allen and Peddy, 1993; Bradford et al., 1997; Castagna, 1993; Castagna et al., 1993; Ostrander, 1984). We submit that with careful consideration of the physics and material properties governing electromagnetic (EM) wave propagation, similar analysis methodologies may be applied to ground-penetrating radar (GPR) data to make detailed material property measurements of the shallow subsurface.

Over the past decade, several workers have investigated the potential for various applications of GPR AVO analysis. Lehmann (1996) discussed complex reflection coefficients and the effects of conductivity, Bergmann et al. (1998) briefly discussed AVO response in the context of a broader synthetic case study, Reppert et al. (2000) examined the potential for measuring the electric permittivity contrast at a boundary using Brewster's Angle, and Zeng et al. (2000) presented a detailed modeling study considering the effects of varying the Cole-Cole parameters on the AVO response.

The Fresnel reflection coefficient curves (Griffiths, 1989) serve as a starting point in understanding the GPR AVO response. This response depends strongly on the polarity of the incident electric field and the electric permittivity contrast at the reflecting boundary. The Fresnel equations are derived assuming a monochromatic EM plane-wave incident on a half space boundary separating two isotropic non-conducting media. In field studies, all of these assumptions are violated to some degree. In this study, we investigate the GPR AVO response to the presence of a thinbed, with thinbed defined as a layer having thickness less than a wavelength

(λ) at the dominant signal frequency. Typical GPR frequencies for groundwater contaminant studies are 50 - 100 MHz with corresponding wavelengths on the order of 1 m - 2.5 m. There are numerous potential GPR targets that may fall into the thinbed category. One example is at contaminated sites, where a hydrocarbon layer floating on the water table may be on the order of a few tenths of a meter thick.

Here we investigate the limits of the Fresnel equations in thinbed analysis and present an alternative analysis that utilizes a frequency dependent three-layer reflectivity model in a broadband signal computation. Further, we discuss practical considerations for AVO analysis of field data. Finally, we present two field examples taken from contaminated site characterization.

THE THIN BED PROBLEM IN GPR AVO ANALYSIS

Two common modes of GPR data acquisition are transverse magnetic (TM), or end-on, and transverse electric (TE), or broadside. In TM acquisition, the transmitting and receiving antennas are colinear, and oriented parallel to the survey profile (Figure 1). In TE acquisition the antennas are parallel, and oriented perpendicular to the survey profile (Figure 1). In TM mode the electric field is polarized parallel to the plane-of-reflection for a downgoing wave incident on a horizontal reflector (Figure 1), while in TE mode the electric field is polarized perpendicular to the plane-of-reflection. The plane-of-reflection is defined as the vertical plane that bisects the antennas. TE is the mode most commonly employed in GPR surveys, but because TE and TM modes have orthogonal polarizations the AVO responses are dramatically different.

For the following analysis, we assume the incident signal is a plane wave in non-conductive, isotropic media. Further, we assume the magnetic permeability is constant and equal to that of free-space ($\mu = \mu_0$) and that the electric permittivity (ε) is frequency independent.

While this is not the general case for earth materials, these are reasonable approximations for many media in which the GPR signal will propagate efficiently (Annan, 1996). Under these assumptions, the Fresnel equations for reflection can be written as

$$R_{TE} = \frac{\gamma_1 - \gamma_2}{\gamma_1 + \gamma_2} \tag{1}$$

$$R_{TM} = \frac{\gamma_1\varepsilon_2 - \gamma_2\varepsilon_1}{\gamma_1\varepsilon_2 + \gamma_2\varepsilon_1} \tag{2}$$

The layer parameter γ is given by the relationship

$$\gamma_n = \omega\sqrt{\varepsilon_n\mu}\ \cos\theta_n = \omega\sqrt{\varepsilon_n\mu}\left[1 - \frac{\varepsilon_1\sin^2\theta_1}{\varepsilon_n}\right]^{1/2} \tag{3}$$

where ω is the angular frequency, and θ_n is the angle made by the propagation vector in layer n with respect to vertical. Substituting Equation 3 into Equations 1 and 2 we find that the Fresnel equations are frequency independent. Further, we set $R_{TM} = 0$ in Equation 2 to find Brewster's Angle (θ_B) given by

$$\tan\theta_B = \sqrt{\frac{\varepsilon_2}{\varepsilon_1}} \tag{4}$$

As the incidence angle approaches θ_B the reflection amplitude goes to 0, and at incidence angles

greater than θ_B the reflected wave undergoes a 180° phase rotation. This is a significant GPR AVO effect that has the potential to be a robust indicator of the permittivity contrast at a reflecting boundary (Bradford, 1998; Reppert et al., 2000).

Now consider a three layer system consisting of an upper and lower half-space (layers 1 and 3) separated by a layer of finite thickness (layer 2). King (1992) derives the plane-wave reflection coefficients for the more general n-layered system which for the three-layer case reduce to

$$R_{TE} = \frac{\gamma_1 - \gamma_3 - i\left(\frac{\gamma_1\gamma_3}{\gamma_2} - \gamma_2\right)\tan(\gamma_2 l_2)}{\gamma_1 + \gamma_3 - i\left(\frac{\gamma_1\gamma_3}{\gamma_2} + \gamma_2\right)\tan(\gamma_2 l_2)} \tag{5}$$

$$R_{TM} = \frac{\gamma_1\varepsilon_3 - \gamma_3\varepsilon_1 - i\left(\frac{\gamma_1\gamma_3\varepsilon_2}{\gamma_2} - \frac{\gamma_2\varepsilon_1\varepsilon_3}{\varepsilon_2}\right)\tan(\gamma_2 l_2)}{\gamma_1\varepsilon_3 + \gamma_3\varepsilon_1 - i\left(\frac{\gamma_1\gamma_3\varepsilon_2}{\gamma_2} + \frac{\gamma_2\varepsilon_1\varepsilon_3}{\varepsilon_2}\right)\tan(\gamma_2 l_2)} \tag{6}$$

Where l_2 is the thickness of layer 2. Taking the limits as l_2 goes to either 0 or ∞ we find that Equations 5 and 6 reduce to Equations 1 and 2 for reflections from the Layer 1/Layer 3 boundary or the Layer 1/Layer 2 boundary respectively. For a finite thickness l_2, the reflected amplitude is frequency dependent via the $\tan(\gamma_2 l_2)$ term. This observation is consistent with our intuition since we expect the reflection from the boundary between layers 2 and 3 to interfere with the reflection from the boundary between Layers 1 and 2. This interference is the source of the thinbed

problem and gives rise to departure from Fresnel equation behavior.

Now consider a broad band source, typical of commercial GPR systems. In the limit of the infinite frequency spectrum, the source is a delta function and the reflections from the upper and lower boundaries do not interfere for any finite layer thickness. For a band limited signal the reflection amplitude is a function of the signal spectrum, layer thickness, and permittivity contrasts at the Layer1/Layer 2 and Layer 2/Layer 3 boundaries. When the layer thickness is greater than the total length of the source wavelet the reflections from the upper and lower boundaries will not interfere significantly. Note that the length of the source wavelet is not the same as the wavelength at the wavelets characteristic frequency, and it is often significantly larger as GPR signals tend to have significant side lobe cycles. As the layer thickness becomes less than the wavelet length and the reflected wavelets interfere we expect observed amplitudes to depart from Fresnel Equation behavior. To compute the reflected field for a broad band signal, we filter the source spectrum using Equation 5 or 6. The time domain response to the three-layer model is then given by the inverse Fourier transform of the filtered source spectrum.

As an example, we compute the thinbed AVO response at the Layer 1/Layer 2 boundary to a range of layer thicknesses (l_2) for a model with $\varepsilon_1/\varepsilon_0 = 7$, $\varepsilon_2/\varepsilon_0 = 5$, and $\varepsilon_3/\varepsilon_0 = 21$, and a Ricker source wavelet (Figure 2). Note that the measured amplitude is the amplitude at the centroid of the reflection from the Layer 1/Layer 2 boundary which is not well resolved when $l_2/\lambda < 0.25$. When $0 < l_2/\lambda < 0.25$, the Layer 1/Layer 2 reflection is not resolved and not surprisingly the amplitude vs angle of incidence (AVA) curves agree poorly with the Fresnel equations. However, when $l_2/\lambda \geq 0.5$ the curves are in relatively good agreement. The convergence of the thinbed and Fresnel curves is strongly case dependent. Computing the thinbed response over a

range of permittivity contrasts and layer thicknesses, we find that the agreement is poorest when $\varepsilon_1 = \varepsilon_2$. In this case, energy is not reflected from the Layer 1/Layer 2 boundary (Figure 3) and the measured amplitude is entirely a function of the Layer 2/Layer 3 permittivity contrast. The Fresnel approximation is exact when $\varepsilon_2 = \varepsilon_3$ where Equations 5 and 6 reduce to the Fresnel Equation for the Layer 1/Layer 2 boundary. The convergence of the thinbed curves with the Fresnel curves has a significant dependence on the sign of the $\varepsilon_1 - \varepsilon_2$ contrast (Figure 3). When $\varepsilon_1 > \varepsilon_2$, a critical angle exists, but the presence of a thinbed damps the amplitude build up at the critical angle and convergence with Fresnel behavior occurs at greater bed thickness. Additionally, the presence of a thinbed shifts and smooths the minima associated with Brewster's angle, so that convergence occurs with greater bed thickness in the TM mode. It is qualitatively evident in Figure 2 that the deviation from Fresnel behavior depends on the range of incidence angles used in the computation, with better agreement at small incidence angles. This occurs because the travel time curves for reflections from the top and bottom of the thinbed converge at large offsets resulting in a decrease in resolution with increasing offset. Computing the divergence from Fresnel behavior for various ranges of incidence angles and layer thicknesses, we find that there is a strong dependence on the incidence angles used in the computation. There is poorer agreement as the range of incidence angles increases. In field studies incidence angles are usually less than 45°. At incidence angles less than 45°, the Fresnel equations are a reasonable approximation of the thinbed reflection amplitudes when $l_2 > 0.5 - 0.75$ over a broad range of permittivity contrasts. The strong case dependence means that a generally applicable "rule-of-thumb" for the use of thinbed analysis does not exist. In most cases, we recommend using thinbed analysis when the layer thickness is less than than 0.75λ. However, when the Layer

1/Layer 2 contrast is small this limit should be increased to λ or greater.

AVO ANALYSIS OF FIELD DATA

Survey Design

AVO analysis requires multi-offset, CMP data. We believe that the method can be used most effectively if continuous multi-fold (CMF) data are acquired, analagous to CMP acquisition in reflection seismology. This is opposed to acquiring common offset data to identify anomalies for subsequent sparse CMP acquisition. We have reached this conclusion for two primary reasons. First there may be well defined AVO anomalies that do not appear as significant events in a common-offset section and may be missed entirely (see Hill Air Force Base example below). Second, we have found that the amplitude response, even in good quality field data, is relatively noisy. CMF data allow us to analyze several adjacent CMPs which statistically improves the permittivity estimates while at the same time provides an error estimate. The drawback to acquiring CMF data is that, currently, we must acquire the data with a single-channel system which is clearly more laborious and time consuming than acquiring conventional common-offset data. Using essentially the same acquisition methodology as that described by Fisher (1992), we have refined our field procedures so that we can acquire data at a rate of about 400-800 common source gathers per day with a three man crew. This is comparable to the rate of acquisition of a similar scale multi-channel seismic survey.

Several factors should be considered in designing AVO field studies. One of the most important of these is whether sufficient offset is achieved in the survey to observe the AVO effect of interest. Often the objective will require relatively large angles of incidence. The required offset is a function of the velocity in the overburden. In many cases the velocity decreases with

depth due to increasing moisture content, with a very large velocity decrease at the transition from the vadose zone to the saturated zone. This velocity decrease causes ray bending toward the vertical. For horizontal layers, this means that the incidence angle decreases with depth. Using Snell's law and geometrical arguments we derive the offset required to reach a given angle of incidence assuming a simple two layer model with the target at the base of the second layer. The offset (x) is given by

$$\frac{x}{2} = z_1 \tan\left[\sin^{-1}\left(\sqrt{\frac{\varepsilon_2}{\varepsilon_1}}\sin\theta_2\right)\right] + z_2 \tan\theta_2 \tag{7}$$

Note that in this case θ_2 is the incidence angle at the target depth. Additionally, we can derive the maximum angle of incidence that can be reached for a negative velocity gradient using Snell's law and setting θ_1 equal to zero. This yields

$$\theta_i = \sin^{-1}\sqrt{\frac{\varepsilon_s}{\varepsilon_d}} \tag{8}$$

where ε_s and ε_d are the permittivities at the surface and at the target depth respectively. Equations 7 and 8 are useful tools in survey design. In most cases a small preliminary study is necessary to estimate site parameters for full-scale survey design.

Amplitude Corrections

Ideally, we would like to process the GPR data so that the measured reflection amplitudes are a direct measure of the reflection coefficient curve. However, a number of factors affect the recorded amplitude that are unrelated to the reflection coefficient at the target boundary. The

recorded or observed amplitude, A_{obs}, can be represented as

$$A_{obs} = \frac{C_T C_R P_T P_R T}{G} R e^{-\alpha r} A_{sou} \tag{9}$$

where P_T and P_R are the transmitter and receiver antenna radiation patterns, T is the transmission loss across boundaries in the overburden, G is the geometric spreading factor, R is the reflection coefficient, A_{sou} is the source signal amplitude, α is the attenuation coefficient, and r is the length of the travel path. C_T and C_R are the transmitter and receiver coupling factors, which are a measure of energy loss at the antenna/earth interface. Each the parameters in Equation 9 may be functions of polarity, ray parameter, frequency, electric permittivity and conductivity, and magnetic permeability. Furthermore, the permittivity, conductivity and permeability are functions of frequency, and the coupling factors are functions of surface roughness. Clearly the measured amplitude is an extremely complicated function of many variables, most of which are difficult or impossible to determine. However, with a few simplifying assumptions and some understanding of the system we are investigating, we can reduce this complexity to a manageable problem.

First we assume frequency independent material properties which, as mentioned earlier, is a good first order approximation for many materials in which the GPR signal will propagate efficiently (Annan, 1996). Next, we assume the coupling factors do not vary significantly across a spread length and that the coupling factors and radiations patterns are the same for both the source and receiver. Finally, we assume that the transmission losses do not vary significantly with offset. Implicit in this third assumption is that strata in the overburden are flat lying. Using the Fresnel equation for transmission (Griffiths, 1989) to compute combined transmission losses

for the up and down going waves, we find that relative transmission losses are less than 5% for a wide range of subsurface models. For many realistic subsurface models, the 5% error is valid at angles that are up to 65% of the critical angle for permittivity decreases, and at angles from 35° to 55° for permittivity increases. These limits will not be violated for most GPR AVO investigations.

Now, using the above assumptions and taking the ratio of the observed amplitude at any given offset (A_x) to the amplitude at near offset (A_0) we find

$$\frac{A_x}{A_0} = \frac{P_x^2 G_0}{P_0^2 G_x} e^{-\alpha(r_x - r_0)} \frac{R_x}{R_0} \tag{10}$$

where $P^2 = P_T P_R$. Equation 10 shows that if we evaluate the relative amplitudes along a given reflection, we can eliminate many of the factors that affect the AVO response that are unrelated to the reflection coefficient. This leaves us computing corrections for the radiation patterns, geometric spreading, and attenuation. While in most cases some or all of the assumptions that go into the derivation of Equation 10 are violated, we have applied this methodology to several field data sets with good results (See field examples section below). Our findings suggest that Equation 10 provides a reasonable approximation in many cases. Moreover, this is essentially the same set of assumptions that go into a typical AVO processing scheme in seismic exploration (with the exception of the radiation pattern correction), where there is a long track record of successful AVO studies (Castagna, 1993).

Radiation pattern corrections are of particular importance in GPR studies. Many commercial GPR systems use linear dipole antennas and the radiation patterns have a strong

angular dependence. At infinite distance from the source, the antenna will appear as an infinitesimal dipole. Engheta and Papas (1982) derive the far field 3-D radiation pattern assuming an infinitesimal, horizontal dipole is placed at the boundary of a half-space, with the lower half-space consisting of a low-loss dielectric. The far-field radiation patterns have a sharp maxima and null at the critical angle of the earth-air interface for the TE and TM modes respectively (Figure 4). Several authors have reported significant deviations from the far-field patterns in the laboratory, even at relatively large distances from the antenna (Annan et al., 1975; Chew and Kong, 1981; Wensink et al., 1990). In particular, the sharp maxima and null points, at the critical angle for the earth-air interface, are absent or muted in the near field. Wensink et al. (1990) concluded that far field conditions had not been reached by a distance equivalent to 15λ. In GPR investigations the target is typically within 2λ - 20λ at the characteristic signal frequency. Thus, it is necessary to construct radiation pattern corrections that do not depend on the far-field approximation. We find that in the TE mode a semi-empirical radiation pattern that has the form $1/\cos\theta_{TO}$ at small take-off angles (θ_{TO}) then merges with the far-field approximation at large θ_{TO} (Figure 4) produces good results for our shielded and unshielded antennas (Figure 5). This radiation pattern has a form similar to laboratory measurements given by Annan (1975). We have found the TM radiation pattern more difficult to represent in a simple form. For shielded antennas, a radiation pattern with no angular dependence at small θ_{TO} that merges with the far-field pattern at large θ_{TO} (Figure 4) produces good results in some cases (Bradford, 1998; Bradford, 2004). In the case of unshielded antennas, we have found significant site and depth dependent variability (Figure 5). Thus, the radiation pattern correction remains a significant topic of research. At sites where a background AVO response at the target depth can be measured (i.e.

the water table reflection in an uncontaminated area), taking the ratio of the target AVO curve to the background AVO curve response cancels the radiation pattern contribution. We have used this approach successfully at several field sites (see the Wurtsmith AFB example below). Ultimately, a general solution may require case specific modeling of the antenna radiation.

The attenuation correction also requires careful consideration. It is difficult to measure the attenuation coefficient from the data because reflectivity, transmission loss, antenna coupling, and near surface effects are difficult to separate from intrinsic attenuation. Ideally, we compute the attenuation coefficient using either site specific lab or field conductivity measurements. However, these measurements are often unavailable and we are left with "typical" tabulated values from the literature. If the frequency independent attenuation assumption is approximately correct over the bandwidth of the signal, then a simple exponential gain correction can be applied. When significant frequency dependent attenuation occurs, the spectral ratio method holds promise for calculating a frequency dependent attenuation correction (Bradford and Wu, 1997). When significant heterogeneity exists in the attenuation structure, such as the transition from the vadose zone to the water saturated zone, a spatially dependent attenuation correction may be required. We find that for offset-to-depth ratios up to 2 and attenuation coefficients covering the range from dry to water saturated sands (0.01 to 0.5 dB/m), A_x/A_0 in Equation 10 is not strongly dependent on the attenuation correction.

Amplitude Extraction

When measuring field data amplitudes, it is important to consider the potential for processing artifacts. Typically surface noise, including the direct waves through the ground and air, travels at moveout velocities greater than that of subsurface reflections and little interference

occurs over a large range of incidence angles. The low frequency transient, or WOW, present at small times and near offsets has a significant effect on the AVO curve of shallow reflections, but is present at the lower end of the useable frequency spectrum. Often, only bandpass filtering and amplitude recovery corrections are required prior to performing AVO analysis, whereas seismic data typically require considerably more preparation (Resnick, 1993). In general, when soil conditions are such that reflections can be obtained from the target zone, GPR data have relatively high signal-to-noise ratios and are well suited for AVO analysis. However, the potential for processing or noise artifacts should be considered carefully on a case by case basis.

Although the simplifying assumptions presented in the preceeding section provide a first order approximation, we often observe some phase rotation and wavelet dispersion related to complex, frequency dependent material properties (Olhoeft, 1987). A detailed discussion of these effects is beyond the scope of this paper, but they are typically more prevalent in electromagnetic wave propagation than in seismic wave propagation (Greaves et al., 1996) and in general should not be ignored.

To eliminate the potential for amplitude artifacts associated with phase rotation, we extract wavelet amplitudes from the peak of the envelope function (Sheriff, 2002). Consider a set of Gabor wavelets (Gaussian modulated sine functions) that have the same amplitude but phase rotations varying from 0 to π (Figure 6a). The wavelets have identical power spectra. However, the peak value of the wavelets in the time domain shows a significant phase dependence (Figure 6b). The maximum amplitude of the envelope function is independent of phase and is equivalent to the maximum amplitude of the zero phase wavelet (Figure 6).

The amplitude we use for AVO analysis is the local maxima of the envelope function

within a time gate bounding a reflection event. To avoid NMO stretch artifacts, we extract amplitudes in the pre-NMO, CMP domain. Quantitive analysis of phase information has the potential to provide additional material property characterization, but is beyond the scope of this study.

FIELD EXAMPLES: DIRECT DETECTION OF NAPL

Of the many potential applications for GPR AVO analysis, detection of non-polar organic liquid contaminants has received particular attention (Baker, 1998; Bergmann et al., 1998; Bradford, 2003; Bradford, 2004; Deeds, 2002). These contaminants are collectively referred to as non-aqueous phase liquids (NAPL) due to their low solubility in water. NAPLs are subcategorized by their density relative to water; DNAPLs are denser than water and LNAPLs are lighter than water. It follows that DNAPLs tend to sink through the water column until they reach a low permeability layer, whereas LNAPLs tend to remain near the water table with free product floating on the water column and residual product present in a smear zone above and below the water table. Both LNAPLs and DNAPLs leave a zone of residual contamination along their migration routes. Chlorinated solvents (DNAPL) and fuel hydrocarbons (LNAPL) are common examples.

NAPLs typically have low relative permittivity ($\varepsilon/\varepsilon_0 \sim 2.5$) and low electric conductivity ($\sigma \sim 0.01 - 0.1$ mS/m) relative to fresh water ($\varepsilon/\varepsilon_0 \sim 80$, $\sigma \sim 0.5$ mS/m) which make them attractive targets for characterization using electrical geophysical methods. As the NAPL displaces water in the sediment pore space, a zone of anomalous electrical properties may be induced. An attractive first order conceptual model is based on the premise that NAPL contaminated zones will have low permittivity and low conductivity relative to the surrounding

formation. A number of controlled spill experiments have been consistent with this model (Bradford, 2004; Brewster and Annan, 1994; Campbell et al., 1995; DeRyck et al., 1993). This model has also proved effective in the interpretation of geophysical data acquired over a fresh LNAPL spill (Orlando, 2002) and over aged LNAPL and DNAPL spills at another field site (Deeds and Bradford, 2002; Lien and Enfield, 1998; Newmark et al., 1998). However, aged LNAPL spills at some sites have anomalously high electric conductivity (Atekwana et al., 2000; Monier-Williams, 1995; Sauck et al., 1998). This divergence stems from the incorrect assumption that the electric properties of the contaminated zone will be controlled by the electric properties of the unaltered LNAPL. Sauck (1998) proposed a conceptual model that explains the high conductivity LNAPL plume in terms of increased dissolved solid concentrations in the ground water related to biogenic activity. In either case, GPR AVO analysis can be a useful tool for contaminated zone characterization under the following two conditions: 1) A permittivity anomaly is associated with the contaminated zone, and 2) the zone boundary is sufficiently sharp relative to the signal wavelength to generate a reflection. Here we demonstrate quantitative thinbed AVO analysis at two LNAPL contaminated sites.

Hill Air Force Base

Field Setting. At Operable Unit 1 (OU-1), Hill Air Force Base (HAFB), Utah, disposal of a diverse mixture of contaminants from 1952 to 1973, including lubricating oils, fuels, and solvents, resulted in a large NAPL plume. This plume is currently estimated at 20,000 gallons covering about 7 acres. The plume is comprised almost entirely of LNAPL; the primary constituent is weathered jet fuel. The maximum thickness of free NAPL is around 0.3 m. Both free and residual phase NAPL are present in a roughly 1.5 m thick smear zone above the water

table. Annual fluctuations of the water-saturated zone control the smear zone thickness. As the water table rises, buoyant NAPL is smeared upward; as the water table falls, the contaminant pools under the effect of gravity.

Surficial sediments at the site are comprised of the Provo alluvium which consists of 6 to 10 meters of silt, sand and gravel in a cut and fill stratigraphy. The alluvium is underlain by the Alpine formation; a thick silty clay unit that acts as an aquitard about which the local water table fluctuates seasonally.

In previous work at HAFB, Lien and Enfield (1998) found that NAPL contaminated soils in the vadose zone at OU-1 had anomalously low electric conductivity. Their finding that NAPL at the site is associated with an electrical property anomaly coupled with favorable results of previous GPR imaging work at HAFB (Young and Sun, 1996; Young and Sun, 1998) led us to select OU-1 for a field research location.

Data Acquisition and Processing. In October, 2000, we acquired a 2973 m^2 3D survey at OU-1 designed to test the feasibility of detecting LNAPL contaminated zones using multi-offset GPR methodologies. The data consist of 20 parallel, multi-offset, TE GPR profiles acquired with the parameters listed in Table 1. We placed the survey area along the periphery of the known contaminant plume with the intention of surveying from contaminated to uncontaminated sediments.

Data quality is excellent with a well defined reflection from the surface of the Alpine Clay present throughout the survey area, as well as reflections within the Provo Alluvium (Figure 7). In the interpretation of the pre-stack, depth-migrated images and velocity model (Deeds and Bradford, 2002), we identified a high velocity anomaly at ~4.6 m depth located within a

topographic low along the alluvium/clay contact (Figure 7). The reflection originating from the upper surface of the velocity anomaly forms a dome shaped structure above the topographic low. The maximum thickness of the high velocity zone is about 1.5 m, which is 0.36 λ at data's dominant frequency of 35 MHz. In cores acquired subsequent to our GPR survey elevated levels of hydrocarbon (varying from 1% - 4% total volume) were found within the high velocity zone (Deeds and Bradford, 2002). Here we demonstrate that quantitative thin bed analysis of the reflection from the top of the high velocity anomaly is consistent with the field observations.

AVO analysis. For AVO preprocessing, we applied a geometric spreading correction, radiation pattern correction, and exponential attenuation correction. We computed path length, take off angle and incidence angle assuming straight rays. This computation gives incidence angles ranging from 11° - 45° for the reflection from the top of the high velocity anomaly. We applied the radiation pattern correction using the semi-empirical function shown in Figure 4. The input relative permittivity at the ground surface is 5.7 which we computed from the velocity of the direct ground wave (0.126 m/ns). For the attenuation correction, we used a frequency independent attenuation coefficient and adjusted the value to force the reflection amplitudes from the clay layer to remain approximately constant with increasing offset. We believe this approach is reasonable in this case because the signal is being reflected from the boundary between relatively high velocity vadose zone alluvium and very low velocity water saturated clay. Under these conditions, and given the range of incidence angles for the survey geometry, the Fresnel equations predict an approximately flat AVO curve. The computed attenuation coefficient is 3.1 dB/m which is at the low end of the range given for silts by Davis and Annan (1989).

The reflection amplitude from the top of the high velocity anomaly increases significantly

with increasing offset (Figures 7 and 8). This trend is qualitatively consistent with the Fresnel equation prediction for a signal reflected from a positive velocity contrast. Using the velocity model derived using pre-stack depth migration velocity analysis to compute both the Fresnel reflection coefficient curve and the thin bed amplitude response for the reflection from the top of the high velocity anomaly we find that the Fresnel equation agrees poorly with the observations (Figure 8). From our earlier analysis, this is expected since the layer thickness is only 0.36λ at the dominant frequency of 35 MHz (Figure 8). The thin bed computation produces a curve that is in good agreement with the field data.

In this field study we have derived a subsurface permittivity model using velocity analysis, then predicted the offset dependent reflectivity using thinbed analysis and found it to be in good agreement with the data. This supports the validity of the approach we took in AVO analysis and suggests that the method has potential as an exploratory tool.

Wurtsmith Air Force Base

Field Setting. This field site is a former fire training facility, designated FT-02, located on the now decommissioned Wurtsmith AFB in Oscoda, MI. In the early 1990s, a free NAPL plume was identified. The plume resulted from of incomplete burning of large quantities of jet fuel during training exercises. At that time, the free phase plume was up to 0.3 m thick and extended more than 180 m downgradient from FT-02 (Bermejo et al., 1997; Sauck et al., 1998).

The stratigraphy below the site consists of fine to medium grained sand and gravel deposits extending to a depth of approximately 20 m. Below this unit is a 6 - 30 m thick silty clay layer which is thought to be the lower boundary for contaminant migration. The surficial aquifer is unconfined, with the water table 3 - 5 m below the surface.

Central to the selection of this site for the current study are a series of geophysical investigations carried out by Sauck et al. (1998) and Bermejo et al. (1997). They found that the site provided excellent conditions for GPR with strong reflections well below the water table. Additionally, they found a well defined, high attenuation anomaly coincident with the LNAPL plume. Through resistivity and self potential measurements, and by inference from the GPR data, they concluded that high electrical conductivity was associated with both the LNAPL and the dissolved phase plume.

Note that by the time of our survey, remediation activities had resulted in a significant reduction in the total NAPL volume and free NAPL was no longer found in monitoring wells. We assume that residual phase NAPL remains in a zone above the water table with a distribution similar to that occupied by the previously existing free phase plume.

Data Acquisition and Processing. For this analysis, we present results from a representative 122 m profile taken from a larger 3D multi-offset survey acquired with the parameters given in Table 2. The profile extends well beyond the east and west boundaries of the attenuation anomaly, is roughly centered on the plume, and data were acquired in both TE and TM modes.

The stacked section is of excellent quality (Figure 9) and shows many of the same features noted by Sauck et al. (1998). In the off-plume areas, strong reflections are evident to greater than 500 ns. The most prominent reflection originates from the water table at a time of around 60 ns. Sauck et al. (1998) interpret the deep (> 150 ns) hummocky reflections as paleo-dunes.

Qualitatively, the attenuation anomaly appears as a zone of muted reflection amplitudes below the water table and extending to depth. A quantitative measure of this effect is the full trace amplitude (FTA) which is the sum of the envelope function (Sheriff, 2002) along a given

trace. The plume location is clearly delineated as a relatively sharp FTA trough (Figure 9). Detailed NMO velocity analysis reveals no apparent lateral velocity anomaly that correlates with the attenuation anomaly. The velocity structure is approximately 1D with a relatively high velocity vadose zone (~0.135 m/ns) and a sharp drop to water saturated sand velocity (~0.065 m/ns) across the water table (Figure 9). This indicates that the NAPL or biogeochemical process that produces an electric conductivity anomaly either does not produce a permittivity anomaly or that the permittivity anomaly is below the resolution of stacking velocity analysis. Our AVO analysis is consistent with the latter interpretation.

AVO Analysis. For this analysis, we focus on the water table reflection since it is the primary boundary controlling the NAPL distribution. The AVO pre-processing flow includes bandpass filtering (12-25-200-400 MHz), a geometric spreading correction, and a laterally variable attenuation correction.

To estimate the attenuation coefficients in the vadose zone, we first compute the root-mean-square (rms) values of vadose zone resistivity measured by Sauck et al. (1998) for the on-plume and off-plume areas. We then use the resistivity values to compute the attenuation coefficient with the equation for low-loss media given by Davis and Annan (1989). This gives attenuation coefficients of 0.26 dB/m and 0.066 dB/m for the on-plume and off-plume areas respectively. Because frequency dependence is not included, this approach gives the minimum attenuation coefficient, but the estimates are reasonably close to tabulated values for dry to water saturated sand (Davis and Annan, 1989).

Using the straight ray assumption to compute the offset to incidence angle transform, the acquisition geometry (Table 2) yields incidence angles at the water table ranging from 8° - 49° in

TE mode and 16° - 52° in TM mode.

After applying spreading and attenuation corrections, the data clearly show the antenna directivity with well developed lobate patterns that have the same shape in on-plume and off-plume areas (Figure 5). This suggests that the antenna directivity does not vary significantly along the profile. Given this observation and the fact that we have a good basis for computing the background water table amplitude response - a long section of high signal-to-noise data outside the plume boundaries - we avoid the radiation pattern correction problem by taking the ratio of the anomalous amplitudes to a background AVO curve. This computation cancels the radiation pattern contribution thereby minimizing the potential for radiation pattern artifacts. In this case we define the background AVO curve by taking the average AVO response of 112 adjacent CMPs from an area outside the plume attenuation anomaly (Figure 9).

When the velocity decreases across a reflecting boundary, the Fresnel Equations predict little variability in the AVO trend for both TE and TM modes over a large range of velocity contrasts (Bradford, 2003). This observation coupled with the lack of lateral variability in the long wavelength velocity structure at FT-02 suggests that a water table AVO anomaly is not likely a this site. However, we find significant TE and TM AVO anomalies that correlate with the plume attenuation anomaly (Figure 10 and 11). The anomalous zone correlates with a decrease in the near-offset water table reflection amplitude of as much as 40%. In TE mode, the water table reflection amplitude within the plume anomaly tends to decay more rapidly than the background amplitudes (Figure 11). A tempting explanation of this observation is that the AVO anomaly is an artifact resulting from an underestimate of the attenuation coefficient within the plume conductivity anomaly. However, this interpretation is not consistent with the TM data in

which the on-plume amplitudes grow larger with increasing offset relative to the background AVO curve. We demonstrate below that a thinbed model, derived from available characterization data, is consistent with all the observations.

For thin bed analysis, we compute the broad-band, offset-dependent reflectivity for a range of models using the measured thickness (Bermejo et al., 1997; Sauck et al., 1998) of the LNAPL zone above the water table (0.3 m) for the plume permittivity structure and a simple half-space model for the background permittivity structure. Here we've assumed that the transition from the vadose zone to water saturated zone occurs over an interval that is much less than the wavelength of the signal. Given that the signal wavelength is ~ 1.6 m at the dominant frequency of ~80 MHz and that the transition from the vadose zone to full saturation may occur over a few cm in coarse grained sands (Bedient et al., 1994), we believe the half-space background model is a reasonable approximation. We found that a model with an intermediate thin layer permittivity of $\varepsilon_{TB}/\varepsilon_0 = 8.5$ in the plume area produces amplitude curves that are in good agreement with both the TE and TM field data (Figure 11).

Two scenarios could result in a zone of intermediate permittivity: 1) The contaminant has low permittivity and a mixed LNAPL/water zone decreases the permittivity in the capillary fringe and upper part of the saturated zone, or 2) the LNAPL zone has anomalously high permittivity giving an increase in the vadose zone permittivity just above the water table. We favor the latter model which is more consistent with the high NAPL zone conductivities observed at the site (Bermejo et al., 1997; Sauck et al., 1998).

Two key points arise from from this field study. First, the 0.3 m thick NAPL impacted zone is below the resolution of a conventional reflection image. That is, the zone is thinner 1/4 λ

at the dominant signal frequency of 80 MHz. Yet, the presence of this layer produces significant, measurable amplitude effects that we may use to increase the detail in our subsurface characterization. Second, we found that including the TM amplitude response in our analysis was critical to constraining our interpretation. This illustrates that the polarity dependence of the GPR AVO response is a valuable attribute that we may use to improve the reliability of our subsurface characterizations.

CONCLUSIONS

Multi-fold GPR profiling coupled with quantitative analysis of GPR offset dependent reflectivity is a potentially valuable tool that can improve the detail and accuracy of GPR subsurface characterization. Thus far the method has seen limited application, probably in large part due to the difficulty of collecting continuous multi-fold data with commercially available single channel GPR systems. With future hardware advances we expect that multi-fold acquisition will become more efficient and more widely employed.

The Fresnel equations provide a starting point in understanding the GPR AVO response, but the assumptions that go into their derivation are violated in many field situations. Here we've presented an easily implemented broad-band formulation of the three-layer reflection coefficients to address the thinbed problem in GPR AVO analysis. In most cases when the thinbed is greater than 0.5λ - 0.75λ, the Fresnel equations are a reasonable approximation, but below this limit investigators should use thinbed modeling.

By making simplifying assumptions such as constant antenna coupling, constant radiation pattern, and frequency independent material properties, the GPR AVO response is reduced to a manageable problem. These assumptions, in some cases, appear to provide a reasonable

approximation of field subsurface conditions. We've also found that acquiring coincident TE and TM data allows us to take advantage of the polarity dependence of the reflection coefficients to limit the non-uniqueness in data interpretation. With careful processing, quantitative GPR AVO analysis of field data is possible and holds significant potential as an exploratory tool.

ACKNOWLEDGMENTS

The U.S. Department of Energy funded this work under the Environmental Management Science Program, Grant # DE-FG07-99ER15008.

REFERENCES

Allen, J.L., and Peddy, C.P., 1993, Amplitude variation with offset: Gulf Coast case studies, Geophys. Dev. Ser., **4**, Soc. Expl. Geophys.

Annan, A.P., 1996, Transmission dispersion and GPR: J. Env. Eng. Geophys., **0**, 125-136.

Annan, A.P., Waller, W.M., Strangway, D.W., Rossiter, J.R., Redman, J.D., and Watts, R.D., 1975, The electromagnetic response of a low-loss, 2-layer, dielectric earth for horizontal electric dipole excitation: Geophysics, **40**, 285-298.

Atekwana, E.A., Sauck, W.A., and Werkema Jr., D.D., 2000, Investigations of geoelectrical signatures at a hydrocarbon contaminated site: J. Appl. Geophys., **44**, 167-180.

Baker, G.S., 1998, Applying AVO analysis to GPR data: Geophys. Res. Let., **25**, 397-400.

Bedient, P.B., Rifai, H.S., and Newell, C.J., 1994, Ground water contamination: Transport and remediation, Prentice-Hall, Inc.

Bergmann, T., Robertsson, J.O.A., and Holliger, K., 1998, Finite-difference modeling of electromagnetic wave propagation in dispersive and attenuating media: Geophysics, **63**,

856-867.

Bermejo, J.L., Sauck, W.A., and Atekwana, E.A., 1997, Geophysical discovery of a new LNAPL plume at the former Wurtsmith AFB, Oscoda, Michigan: Groundwater Monitoring and Remediation, **17**, 131-137.

Bradford, J.H., 1998, Characterizing shallow aquifers with wave-propagation based geophysical techniques: Imaging and attribute analysis: Ph. D. thesis, Rice University.

Bradford, J.H., 2003, GPR offset-dependent reflectivity analysis for characterization of a high-conductivity LNAPL plume: SAGEEP 2003 Symposium on the Application of Geophysics to Environmental and Engineering Problems, Env. Eng. Geophys. Soc., 238-252.

Bradford, J.H., 2004, 3D Multi-offset, multi-polarization acquisition and processing of gpr data: a controlled DNAPL spill experiment: SAGEEP 2004 Symposium on the Application of Geophysics to Environmental and Engineering Problems, Env. Eng. Geophys. Soc.

Bradford, J.H., Sawyer, D.S., and Zelt, C.A., 1997, AVO analysis of low-velocity, shallow sands (<50m): 67th Ann. Internat. Mtg., Soc. Expl. Geophys., Expanded abstracts, 158-162.

Bradford, J.H., and Wu, Y., 1997, Time-frequency representation of seismic signals via matching pursuit decomposition with complex Ricker wavelets: AGU Fall meeting, Amer. Geophys. Union, EOS Supplement, 33.

Brewster, M.L., and Annan, A.P., 1994, Ground-penetrating radar monitoring of a controlled DNAPL release: 200 MHz radar: Geophysics, **59**, 1211-1221.

Campbell, D.L., Lucious, J.E., Ellefson, K.J., and Deszcz-Pan, M., 1995, Monitoring of a controlled LNAPL spill using ground-penetrating radar: SAGEEP '95: Symposium on the

Application of Geophysics to Environmental and Engineering Problems, Env. Eng. Geophys. Soc., Proceedings, 511-517.

Castagna, J.P., 1993, AVO Analysis - Tutorial and review, *in* Castagna, J.P., and Backus, M.M., Eds., Offset-dependent reflectivity - Theory and practice of AVO analysis: Soc. Expl. Geophys., Invest. Geophys. **8**, 3-36.

Castagna, J.P., Batzle, M.L., and Kan, T.K., 1993, Rock physics - the link between rock properties and AVO response, *in* Castagna, J.P., and Backus, M.M., Eds., Offset - dependent reflectivity - Theory and practice of AVO analysis: Soc. Expl. Geophys., Invest. Geophys. **8**, 135-171.

Chew, W.C., and Kong, J.A., 1981, Electromagnetic field of a dipole on a two-layer earth: Geophysics, **46**, 309-315.

Davis, J.L., and Annan, A.P., 1989, Ground-penetrating radar for high-resolution mapping of soil and rock stratigraphy: Geophysical Prospecting, **37**, 531-551.

Deeds, J.C., 2002, Amplitude variation with offset (AVO) of ground penetrating radar data for detection of non-aqueous phase liquids: M.S. thesis, University of Wyoming.

Deeds, J.C., and Bradford, J.H., 2002, Characterization of an aquitard and direct detection of LNAPL at Hill Air Force Base using GPR AVO and migration velocity analysis: GPR 2002, Ninth International Conference on Ground Penetrating Radar, Intl. Soc. for Optl. Eng., Proceedings, 323-329.

DeRyck, S.M., Redman, J.D., and Annan, A.P., 1993, Geophysical monitoring of a controlled kerosene spill: SAGEEP '93 Symposium on the Application of Geophysics to Environmental and Engineering Problems, Env. Eng. Geophys. Soc., Proceedings, 5-19.

Fisher, E., McMechan, G.A., and Annan, A.P., 1992, Acquisition and processing of wide-aperture ground-penetrating radar data: Geophysics, **57**, 495-504.

Greaves, R.J., Lesmes, D.P., Lee, J.M., and Toksoz, M.N., 1996, Velocity variation and water content estimated from multi-offset, ground-penetrating radar: Geophysics, **61**, 683-695.

Griffiths, D.J., 1989, Introduction to electrodynamics, Prentice-Hall.

King, R.W.P., and Owens, M., 1992, Lateral electromagetic waves: Theory and Applications to communications, geophysical exploration, and remote sensing, Springer-Verlag New York Inc.

Lehmann, F., 1996, Fresnel equations for reflection and transmission at boundaries between conductive media, with applications to georadar problems: GPR '96 6th International Conference on Ground-Penetrating Radar, Intl. Soc. Opt. Eng., Proceedings, 555-560.

Lien, B.K., and Enfield, C.G., 1998, Delineation of subsurface hydrocarbon contaminant distribution using a direct push resistivity method: J. Env. Eng. Geophys., **2**, 173-179.

Monier-Williams, M., 1995, Properties of light non-aqueous phase liquids and detection using commonly applied shallow sensing geophysical techniques: SAGEEP '95 Symposium on the Application of Geophysics to Environmental and Engineering Problems, Env. Eng. Geophys. Soc., Proceedings, 1-15.

Newmark, R.L., Daily, W.D., Kyle, K.R., and Ramirez, A.L., 1998, Monitoring DNAPL pumping using integrated geophysical techniques: J. Env. Eng. Geophys., **3**, 7-13.

Olhoeft, G.R., 1987, Electrical properties from 10^{-3} to 10^{9} Hz -- physics and chemistry: Proc. of the 2nd Int'l. Symp. on the Physics and Chemistry of Porous Media, AIP, Am. Inst. Phys. Conf. Proc., 281-298.

Orlando, L., 2002, Detection and analysis of LNAPL using the instantaneous amplitude and frequency of ground-penetrating radar data: Geophys. Prosp., **50**, 27-41.

Ostrander, W.J., 1984, Plane-wave reflection coefficients for gas sands at nonnormal angles of incidence: Geophysics, **49**, 1637-1648.

Reppert, P.M., Morgan, F.D., and Toksoz, M.N., 2000, Dielectric constant determination using ground-penetrating radar reflection coefficients: J. Appl. Geophys., **43**, 189-197.

Resnick, J.R., 1993, Seismic data processing for AVO and AVA analysis, *in* Castagna, J.P., and Backus, M.M., Eds., Offset - dependent reflectivity - Theory and practice of AVO analysis: Soc. Expl. Geophys., Invest. Geophys. **8**, 175-189.

Sauck, W.A., 1998, A conceptual model for the geoelectrical response of LNAPL plumes in granular sediments: SAGEEP '98 Symposium on the Application of Geophysics to Environmental and Engineering Problems, Env. Eng. Geophys. Soc., Proceedings, 805-817.

Sauck, W.A., Atekwana, E.A., and Nash, M.S., 1998, High conductivities associated with an LNAPL plume imaged by integrated geophysical techniques: J. Env. Eng. Geophys., **2**, 203-212.

Sheriff, R.E., 2002, Encyclopedic dictionary of applied geophysics, Soc. Expl. Geophys.

Wensink, W.A., Greeuw, G., Hofman, J., and Van Deen, J.K., 1990, Measured underwater near-field e-patterns of a pulsed, horizontal diplot antenna in air: Comparison with the theory of the continuous wave, infinitesimal dipole: Geophys. Pros., **38**, 805-830.

Zeng, X., McMechan, G.A., and Xu, T., 2000, Synthesis of amplitude versus offset variations in ground-penetrating radar data: Geophysics, **65**, 113-125.

TABLE CAPTIONS

Table 1. Data acquisition parameters at the Hill Air Force Base site.

Table 2. Data acquisition parameters at the former Wurtsmith Air Force Base site.

Table 1

Survey Type	TE, 3D, Constant Azimuth
GPR System	Sensors and Software PE 100A, 50 MHz Unshielded Antennas
Survey Size	61 m x 49 m (inline x crossline)
Min/Max Offset	1.8 m/9.1 m
Common source fold	25
Source Interval	0.61 m
Receiver Interval	0.30 m
Cross line spacing	2.4 m
Sampling Interval	1.6 ns
Recording time	500 ns
stacks/source	16

Table 2

Survey Type	TE, TM, 3D, Constant Azimuth
GPR System	Sensors and Software PE 100A, 100 MHz Unshielded Antennas
Survey Size	30 m x 30 m (inline x crossline)
Near/Maximum Offset (TE)	0.91 m/8.22 m
Near/Maximum Offset (TM)	2.1 m/9.44 m
Common source fold	25
Source Interval	0.61 m
Receiver Interval	0.30 m
Cross line spacing (TE)	0.91 m
Cross line spacing (TM)	3.66 m
Sampling Interval	0.8 ns
Recording time	750 ns
stacks/source	16

Figure 1

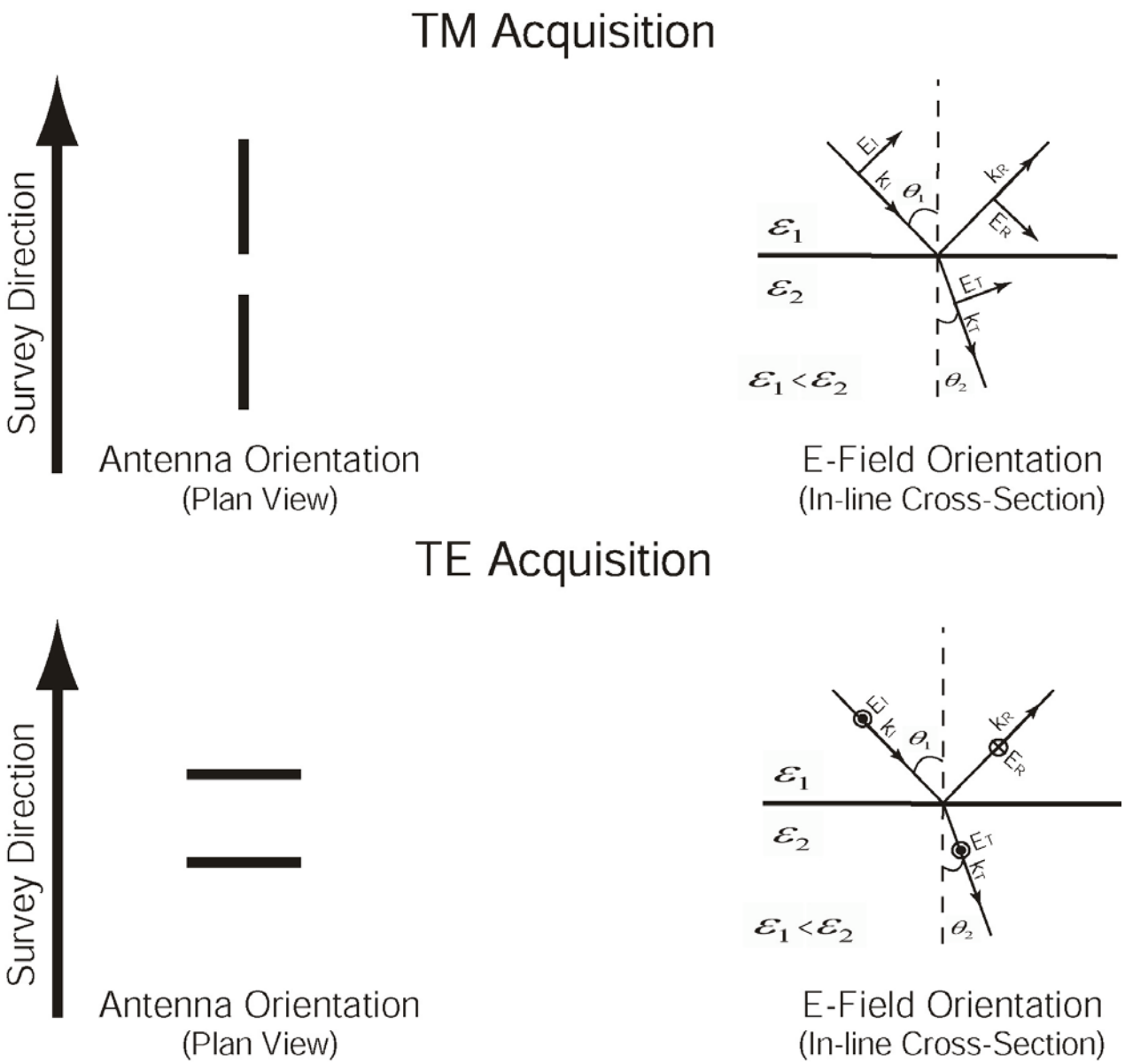

Figure 1. Linear dipole antenna configuration and wave propagation unit vectors where k is the wave vector and E is the electric field. The subscripts I, R, and T indicate incident, reflected, and transmitted fields respectively.

Figure 2

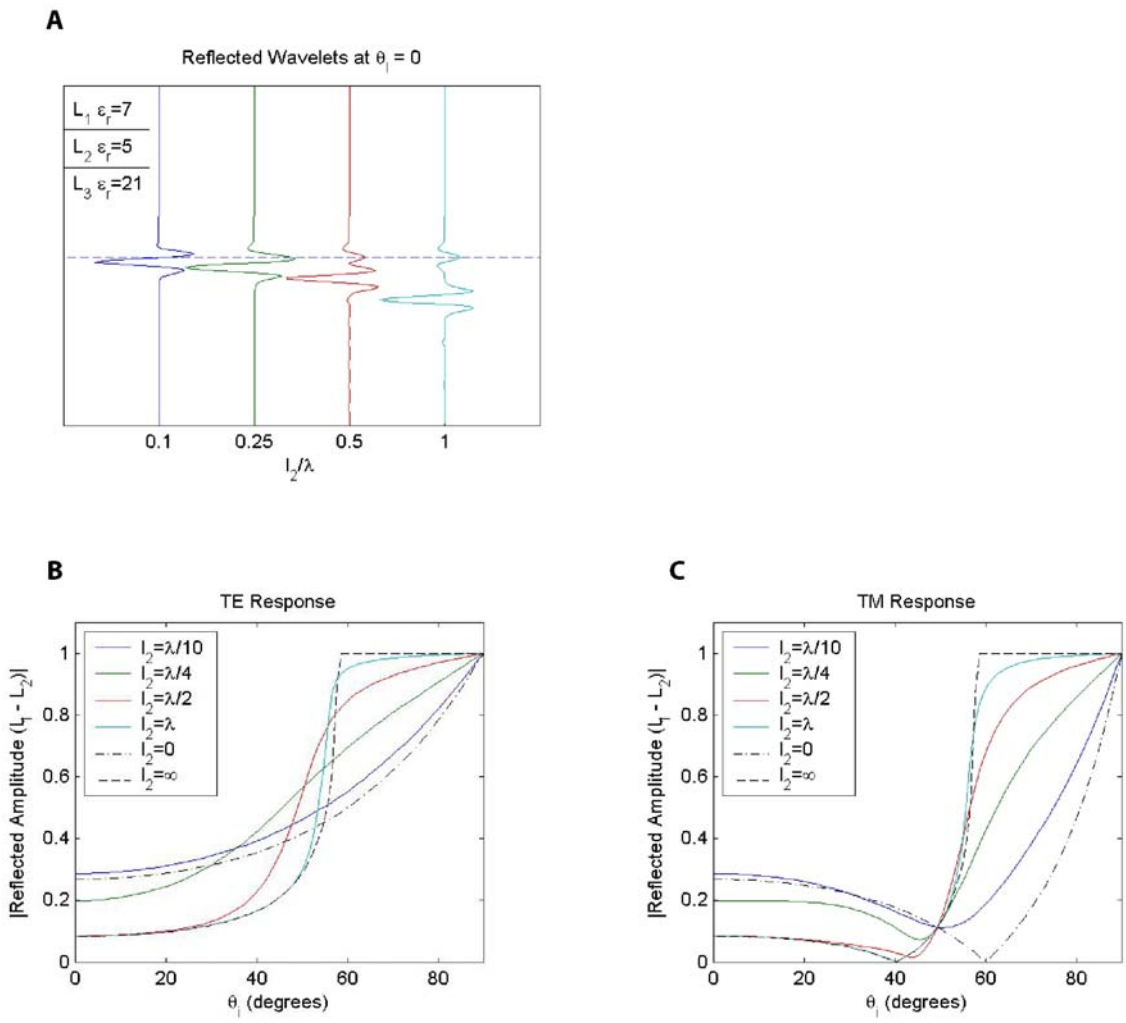

Figure 2. A) The reflected field from a three layer model at zero offset with the layer thickness varying from λ/10 to λ. B) TE reflection amplitude at the centroid of the reflection from the Layer 1/Layer 2 boundary (indicated with a dashed line in A) computed using the thinbed broadband computation, C) TM reflection amplitude using the thinbed broadband computation. The $l_2 = 0$ case is the Fresnel Equation for the Layer 1/Layer 3 boundary, and the $l_2 = \infty$ case is the Fresnel Equation for the Layer 1/Layer 2 boundary. The reflections from the upper and lower boundary are well resolved when $l_2/\lambda \geq 0.5$, and the Fresnel Equations are a fair approximation of the thinbed reflection amplitude beyond this limit.

Figure 3

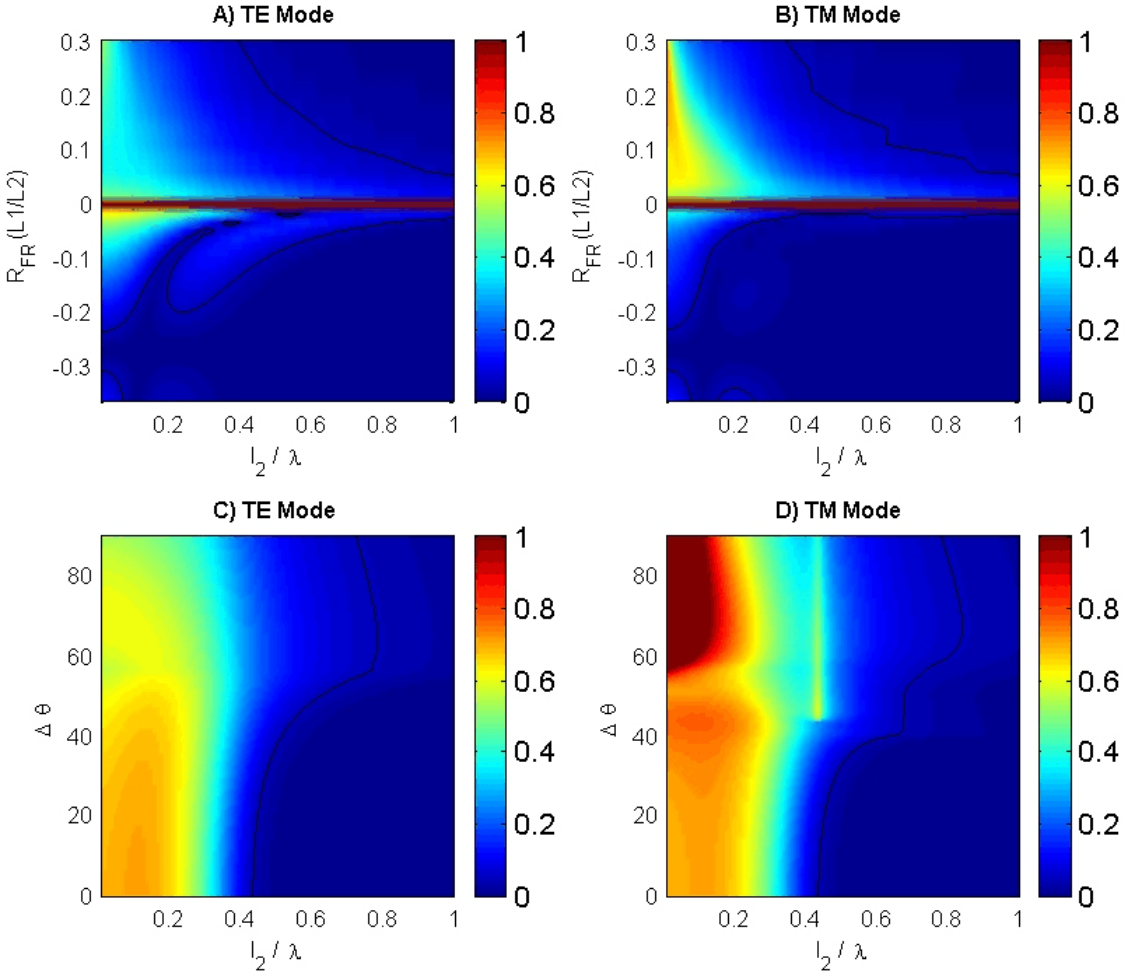

Figure 3. Plots showing the fractional deviation of the Fresnel reflection coefficients from the thinbed reflection amplitudes defined as the average of $(A_{TB} - R_{FR})/A_{TB}$. The 0.05 fractional deviation contour is shown in black. In A and B the permittivities of the first and third layer are held constant at $\varepsilon_1/\varepsilon_0 = 7$ and $\varepsilon_3/\varepsilon_0 = 21$, while varying the relative permittivity of the thinbed from 2 to 32. The vertical axis shows the Fresnel reflection coefficient for the Layer 1/Layer 2 boundary. Deviation depends strongly on the contrasts at the Layer 1/Layer 2 and Layer 2/Layer 3 boundaries which control the contribution of each boundary to the total reflection energy. A maximum deviation occurs when $\varepsilon_1 = \varepsilon_2$ the minimum occurs when $\varepsilon_2 = \varepsilon_3$. C and D show how deviation varies with the range of incidence angles used in the analysis. Generally, deviation increases as larger incidence angles are included because traveltime convergence causes greater interference with increasing offset.

Figure 4

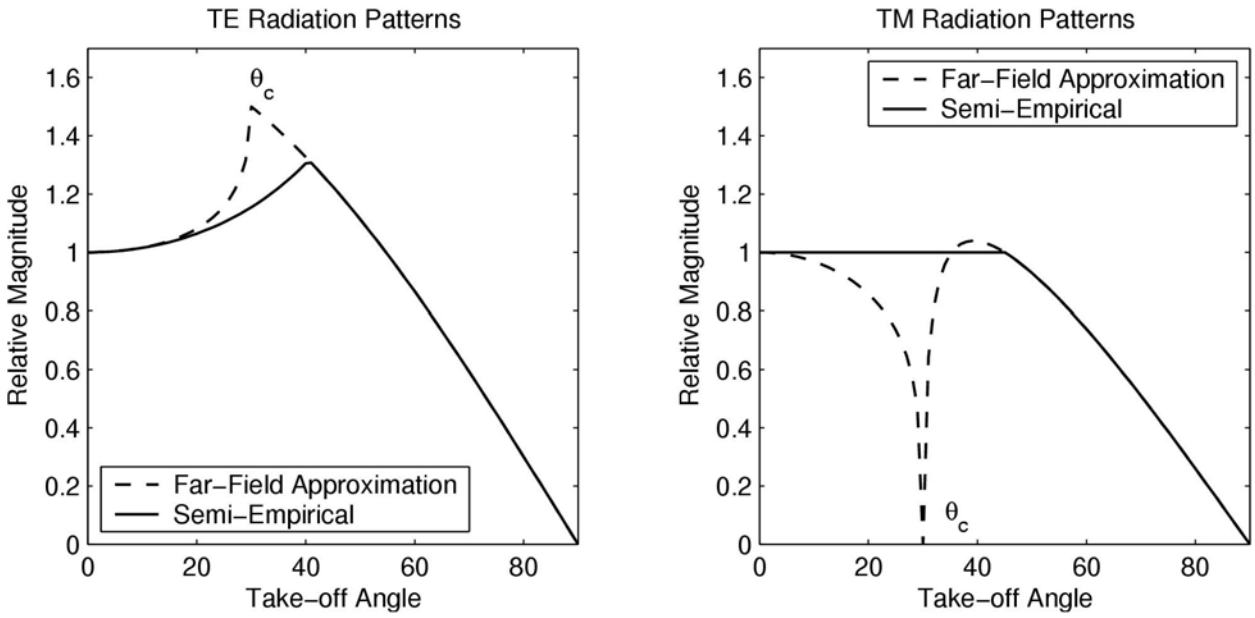

Figure 4. Radiation patterns for the infinitesimal dipole, or far field-approximation, and semi-empirical radiation patterns derived by Bradford (1998). The far-field approximation is typically not consistent with field observations, while the semi-empirical pattern for the TE mode has proven useful in several field and laboratory studies with both shielded and unshielded antennas. The semi-empirical pattern for the TM mode has only been consistent with data acquired using shielded antennas.

Figure 5

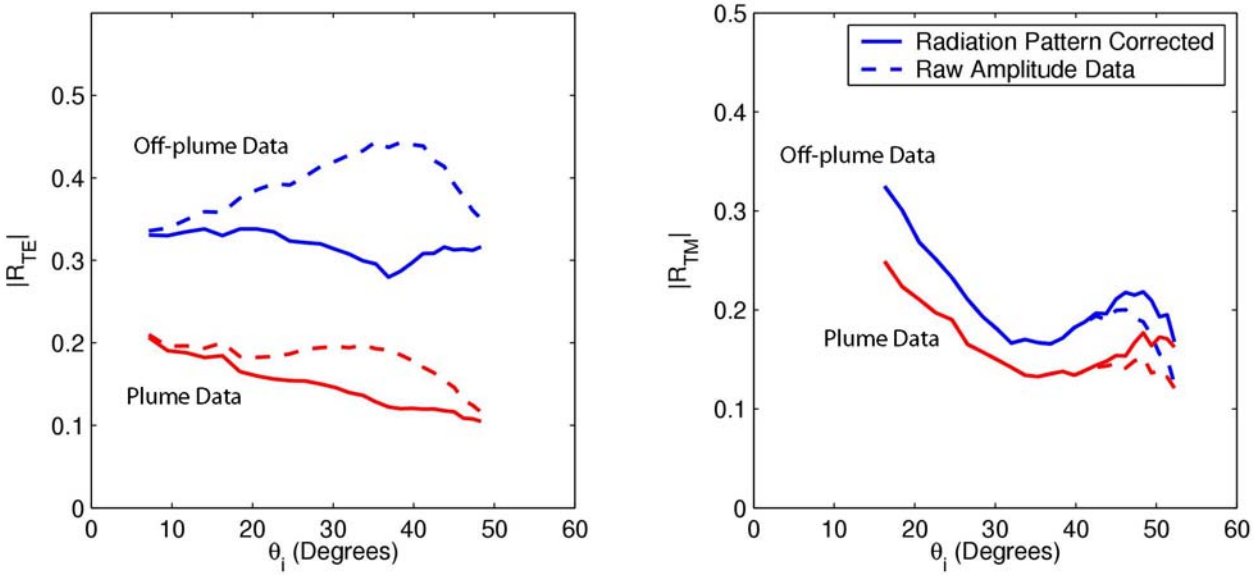

Figure 5. Amplitude curves taken from a field study at the former Wurtsmith Air Force Base. The amplitude curves are from the water table reflection with CMPs acquired over a hydrocarbon plume (low amplitude curves) and from an uncontaminated area (high amplitude curve). In the raw data, the radiation patterns are apparent with a consistent maxima (TE) or minima (TM) present in both the on-plume and off-plume reflections, despite having different reflection amplitudes and AVA curves. Applying a radiation pattern correction using the semi-empirical curves shown in Figure 4 effectively removes the radiation pattern contribution from the TE data, but is not effective for the TM data. Note that the infinitesimal dipole approximation is in very poor agreement with both the TE and TM data.

Figure 6

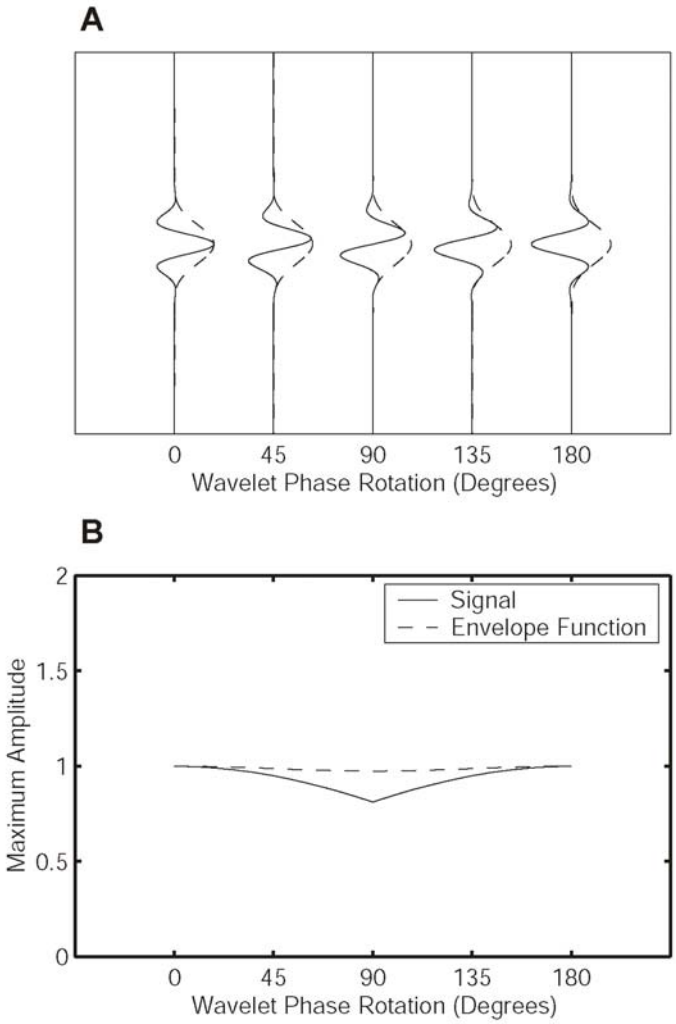

Figure 6. A) Wavelets with the same amplitude but variable phase rotation, and B) the peak wavelet value and peak value of the envelope function vs phase rotation. The envelope function is independent of phase rotation and therefore provides a good basis for AVO analysis.

Figure 7

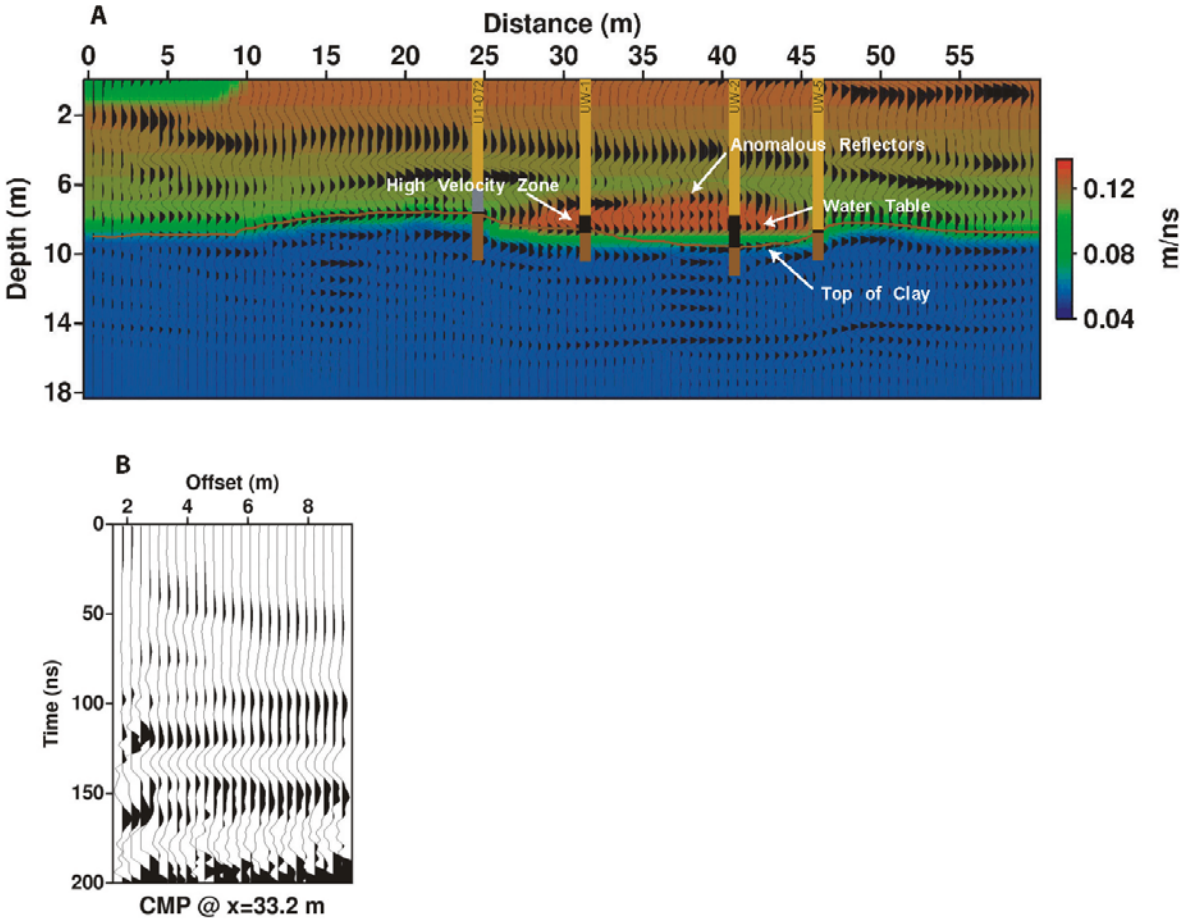

Figure 7. A) PSDM velocity model with migrated trace overlay. We identified a high velocity zone within a topographic low on the clay surface. In a subsequent coring effort, hydrocarbon contamination was found within this zone (the contaminated interval is indicated with black). B) The amplitude of the reflection from the top of the high velocity zone (~ 100 ns) in the CMP coincident with core UW-1 shows a clear increase in amplitude with increasing offset. This is qualitatively consistent with the Fresnel reflection coefficients. Note that we only used offsets of less than 8 m in the quantitative analysis (Figure 8) to minimize artifacts related to weak interference of the direct wave through the ground at far offsets.

Figure 8

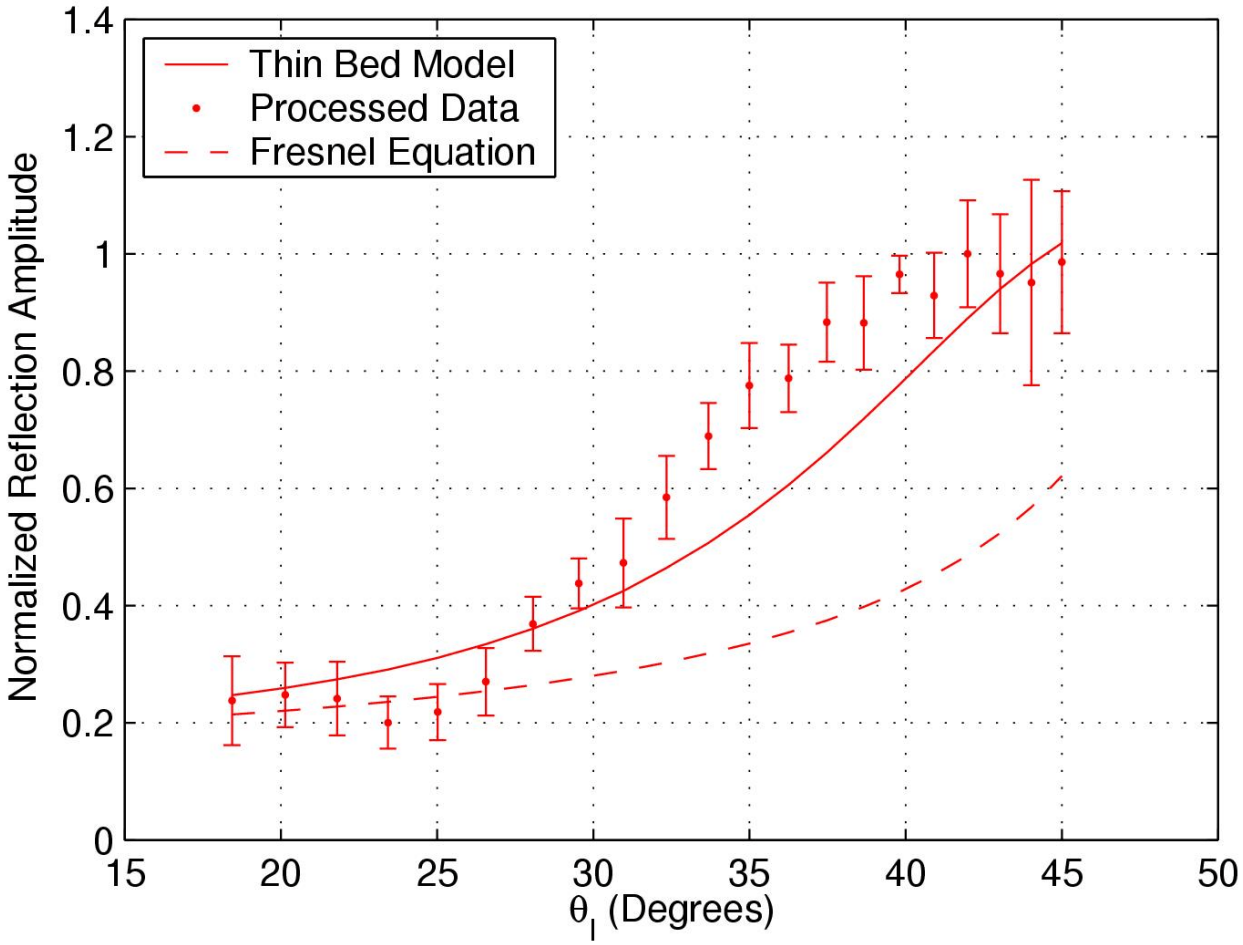

Figure 8. Reflection amplitudes taken from 20 CMPs centered on the core UW-1 (Figure 7). Although the Fresnel equation predicts the general trend of the data, the thinbed computation is in much closer agreement with the field observations.

Figure 9

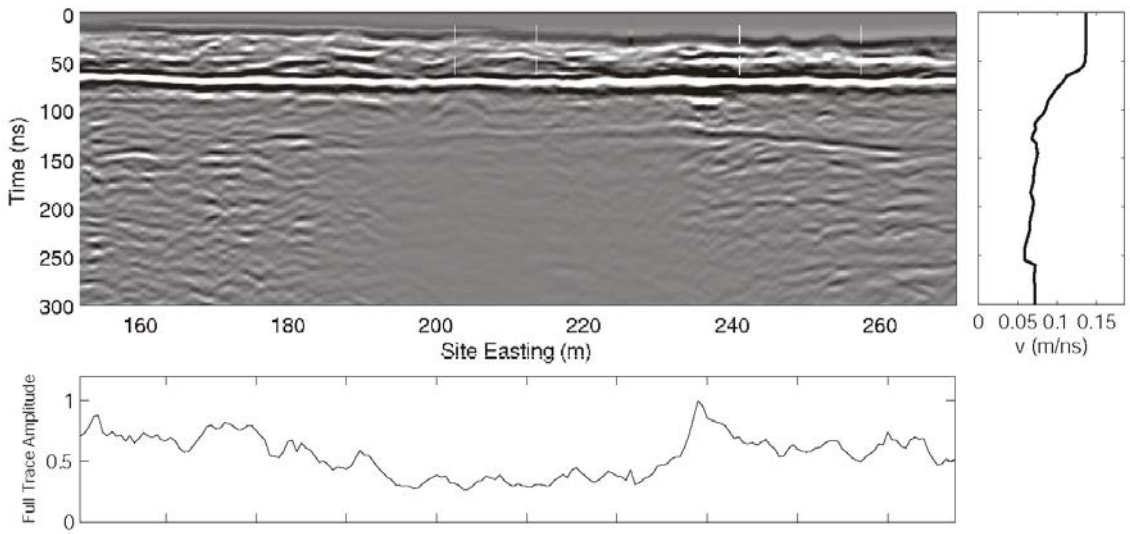

Figure 9. CMP stack, velocity model, and total trace amplitude curve taken from the former Wurtsmith AFB site study. The location of the hydrocarbon plume is evident where there is a decrease in total trace amplitude from 190 m - 235 m. The water table reflection is at ~ 60 ns. We used the interval from 245 m to 255 m to define the background AVO curve. CMPs from 205 m to 215 m were used in quantitative analysis of the plume AVO response (Figure 11).

Figure 10

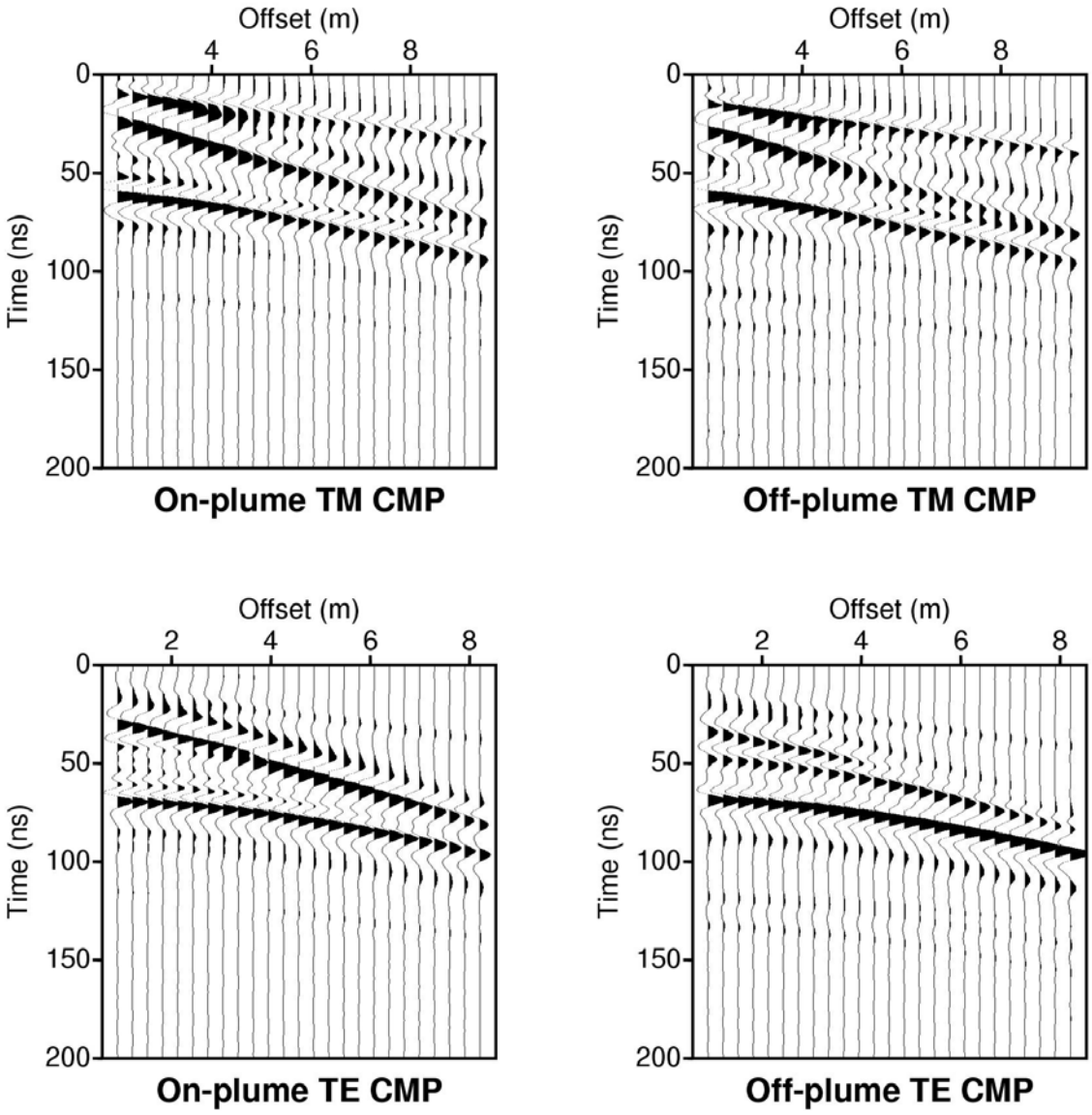

Figure 10. Representative gathers from the on-plume and off-plume areas (Figure 9). The water table reflection is at ~ 60 ns. There is no obvious AVO anomaly evident from qualitative inspection of the gathers.

Figure 11

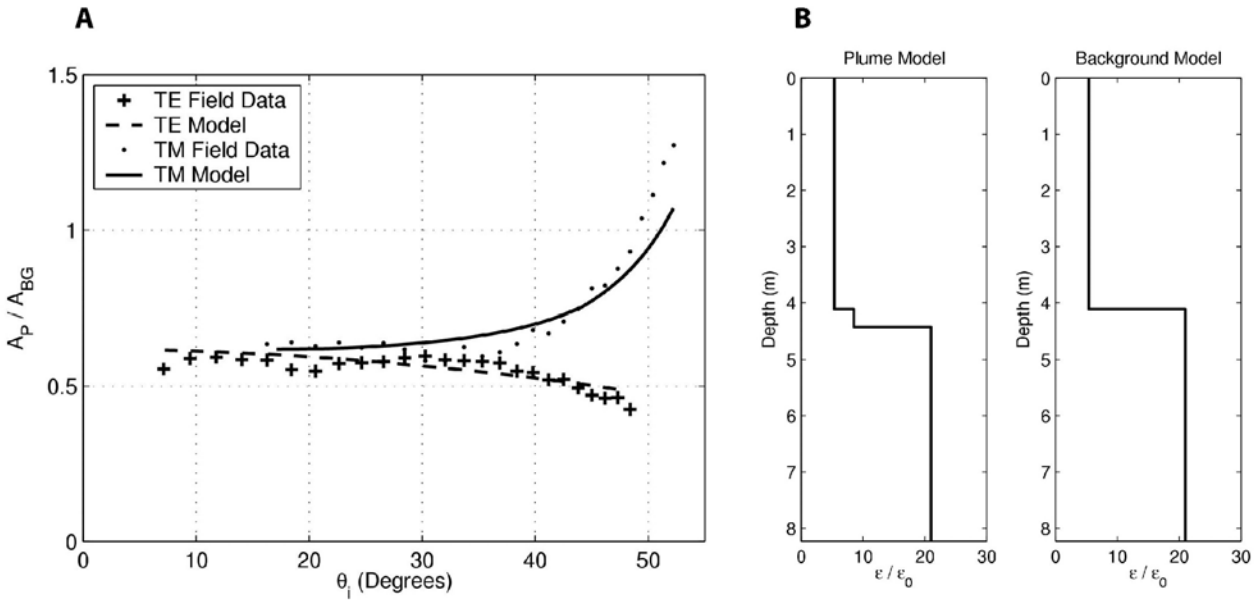

Figure 11. A) Plume anomaly (A_P) to background (A_{BG}) amplitude ratios for TE and TM modes. The plume amplitudes were computed by combining 76 adjacent CMPs approximately center on the hydrocarbon plume (Figure 9). Average standard deviations of the ratios are 0.12 and 0.13 for TM and TE modes respectively. B) Plume and background permittivity models used to compute the model ratios which are in good agreement with the field data.

APPENDIX C: ALGORITHM FOR GPR_RAY_MOD

For plane waves, the monochromatic propagating electric field is given by

$$\tilde{E}(r,t) = \tilde{E}_0 e^{i(\tilde{k}\hat{r} - \omega t)} \tag{1}$$

where the complex wavenumber k, is given by

$$\tilde{k} = k_+ + ik_- \tag{2}$$

and

$$k_\pm = \omega\left[\frac{\varepsilon\mu}{2}\left(\sqrt{1 + \left(\frac{\sigma}{\varepsilon\omega}\right)^2} \pm 1\right)\right]^{\frac{1}{2}} \tag{3}$$

The attenuation term is given by the complex part of the wavenumber ($A = A_0 e^{-k_-\hat{r}}$) , and the phase velocity is found from the real part of the wavenumber, ($v(\omega) = \omega/k_+$).

In general ε, μ, and σ are also complex quantities and Equation 3 is given in terms of effective permittivity, ε_e, and effective conductivity, σ_e, given by

$$\varepsilon_e = \varepsilon_r - \sigma_c/\omega \tag{5}$$

$$\sigma_e = \sigma_r + \varepsilon_c\omega \tag{6}$$

For many earth materials, the frequency dependence of the permittivity can be described using the Cole-Cole equation (Cole and Cole, 1941). The suitability of this parameterization for GPR studies is well documented and several workers have used Cole-Cole parameterization in numerical modeling (Powers and Olhoeft, 1996; Roberts and Daniels, 1992; Zeng et al., 2000). The Cole-Cole equation for permittivity has the form

$$\varepsilon_r - i\varepsilon_c = \varepsilon_\infty + \frac{\varepsilon_0 - \varepsilon_\infty}{1 + (i\omega\tau_\varepsilon)^\alpha} \tag{7}$$

Where ε_0 is the DC permittivity, ε_∞ is the permittivity at optical frequencies, ω is the frequency, and τ is a relaxation time. The permeability μ, for many earth materials can be described with

similar parameterization (Olhoeft and Capron, 1994; Olhoeft and Strangway, 1974)

$$\mu_r - i\mu_c = \mu_\infty + \frac{\mu_0 - \mu_\infty}{1 + (i\omega\tau_\mu)^\alpha} \tag{8}$$

In the frequency range typical for GPR studies, the conductivity is approximately frequency independent, and can be taken as the DC conductivity.

In terms of the wave number, the reflection and transmission coefficients for TE (R_{TE}, T_{TE}) and TM (R_{TM}, T_{TM}) fields are given by

$$R_{TE} = \frac{E_R}{E_I} = \frac{\mu_2 k_1 \cos\theta_1 - \mu_1 k_2 \cos\theta_2}{\mu_2 k_1 \cos\theta_1 + \mu_1 k_2 \cos\theta_2} \tag{9}$$

$$T_{TE} = \frac{E_T}{E_I} = \frac{2\mu_2 k_1 \cos\theta_1}{\mu_2 k_1 \cos\theta_1 + \mu_1 k_2 \cos\theta_2} \tag{10}$$

and

$$R_{TM} = \frac{E_R}{E_I} = \frac{\mu_2 k_1 \cos\theta_2 - \mu_1 k_2 \cos\theta_1}{\mu_2 k_1 \cos\theta_2 + \mu_1 k_2 \cos\theta_1} \tag{11}$$

$$T_{TM} = \frac{E_T}{E_I} = \frac{2\mu_2 k_1 \cos\theta_1}{\mu_1 k_2 \cos\theta_1 + \mu_2 k_1 \cos\theta_2} \tag{12}$$

where

$$\sin\theta_2 = \frac{k_1}{k_2} \sin\theta_1 \tag{13}$$

Where the subscripts 1 and 2 indicate the upper and lower medium respectively, the subscripts R and I indicate reflected and incident components respectively, μ is the magnetic permeability, k is the wavenumber, and θ_1 and θ_2 are the angle of incidence and transmission respectively (taken from the normal). Note that the reflection and transmission coefficients are frequency dependent

via k and μ.

For the TM mode there is a peculiar phenomena that has particular relevance and value for GPR AVO studies. There exists an angle of incidence at which all reflected energy is extinguished by the out of phase component of the incident field. The reflection coefficient (R_{TM}) goes to zero, and at greater angles there is a 180° phase rotation. The angle at which R_{TM} goes to zero is know as Brewster's angle (θ_B). For the zero conductivity case, θ_B is given by (Griffiths, 1989)

$$\tan\theta_B = \sqrt{\frac{\varepsilon_2}{\varepsilon_1}} \tag{14}$$

θ_B occurs at relatively small angles (< 45°) and is strongly dependent on $\varepsilon_2/\varepsilon_1$ when $\varepsilon_2/\varepsilon_1 < 1$. When $\varepsilon_2/\varepsilon_1 > 1$, θ_B occurs at relatively large angles and becomes weakly dependent on $\varepsilon_2/\varepsilon_1$. In a reflection survey, it is reasonable to achieve offsets corresponding to an angle of incidence in the 45° - 55° and therefore we may expect to observe θ_B for a decrease in permittivity across the reflecting boundary. Recall that this is the anomalous case associated with a NAPL rich zone at depth. If we consider a multi-chromatic signal, we see from Equation 14 that the amplitude of the wavelet only goes to zero for frequency independent ε (for frequency dependent ε, θ_B may be different for each frequency component). However, for a reasonably band limited wavelet, even when both materials have relatively large conductivities (0.1 S/m), there is a significant decrease in amplitude and a 180° phase rotation occurs, although the transition is diffuse rather than discreet.

Several workers have presented GPR modeling algorithms that are based in either ray theory (Cai and McMechan, 1995; Powers and Olhoeft, 1996), or wave equation formulations (Bergmann et al., 1998; Carcione, 1996; Casper and Kung, 1996; Roberts and Daniels, 1997; Wang and Tripp, 1996; Xu and McMechan, 1997; Zeng et al., 1995). However, with the exception of Roberts and Daniels (a full 3-D FDTD algorithm), none of these algorithms model both the transverse and parallel polarized electric fields. I present a ray based modeling algorithm that simultaneously models both transverse and parallel antenna polarization configurations, is implemented for arbitrary 2-D multi-offset acquisition geometries, and uses Cole-Cole parameterization to model the frequency dependent material properties. The algorithm consists of two components; 1) ray path computation, and 2) waveform modeling.

Ray path computation

For ray path computation, I use the method of Zelt and Smith (1992). Models are parameterized with constant velocity layers. The layer boundaries are of arbitrary geometry with the constraint that they are composed of a combination of straight line segments. The velocity within each layer is specified as the phase velocity at the peak frequency of the source wavelet. For each reflecting interface, two-point ray tracing is performed from the source to receiver. The length of each straight ray segment, transmitter take-off angle, angle of incidence and transmission at each layer boundary, and receiver reception angle are stored in a table.

Wavelet modeling

Several factors must be considered when modeling the reflected wavelet. These include source and receiver directivity, geometric spreading, the reflection coefficient, transmission losses, and attenuation and velocity dispersion due to propagation through a lossy medium. I carry out the computation in the frequency, calculating the amplitude and phase shift of each frequency component along the nth ray path. The time representation of the model data for ray n is then the real part of the inverse Fourier transform, given by

$$w_n(t) = Re\left[IFFT\left(\frac{D_{Sn}D_{Rn}\tilde{R}_n(\omega)}{G_n}\left(\prod \tilde{T}_i(\omega)e^{i\tilde{\phi}_i(\omega)}\right)A_0(\omega)\right)\right] \tag{15}$$

Where $w_n(t)$ is the time domain data, $A_0(\omega)$ is the spectrum of the source wavelet, D_{Sn} and D_{Rn} are the source and receiver radiation coefficients respectively, R_n is the reflection coefficient given by Equation 9 or 11, T_i is the transmission coefficient for each boundary the ray crosses given by Equation 10 or 12, and G_n is the 3-D geometric spreading term discussed by Cai and McMechan (1995). The variable ϕ_i includes a frequency dependent phase shift (corresponding to a velocity dependent time shift) and an attenuation component for the ith ray segment given by

$$\phi_i(\omega) = [k_{i+}(\omega) + ik_{i-}(\omega)]d_i \tag{16}$$

Where $k_{i\pm}$ are the real and complex parts of the wavenumber along the ith ray segment and d_i is the length of the ith ray segment. Summing $w_n(f)$ over all travel paths connecting a single source and receiver position gives the synthetic trace.

The source and receiver radiation coefficients depend strongly on both the azimuthal and radial angles and can significantly effect AVO measurements. Computation of the radiation patterns is not straightforward and requires approximation in ray based formulation. Most GPR antenna are designed to approximate an oscillating dipole. Engheta and Papas (1982) derive the far field (geometric optics approximation -GOA) 3-D radiation pattern for a dipole antenna assuming the antenna is placed at the boundary of a half-space, with the lower half consisting of a low-loss dielectric

$$\vec{S} \propto \left[-\sin^2\theta\cos\theta\frac{(1 - n^2\sin^2\theta)^{1/2} - n\cos\theta}{n(1 - n^2\sin^2\theta)^{1/2} + \cos\theta} - \frac{\cos^2\theta}{(1 - n^2\sin^2\theta)^{1/2} + n\cos\theta}\right]^2\cos^2\phi + \frac{\cos^2\theta\sin^2\phi}{\left[(1 - n^2\sin^2\theta)^{1/2} + n\cos\theta\right]^2}\hat{r} \tag{17}$$

, for $\theta < \theta_c$ and

$$\vec{S} \propto \left[\frac{(n^2 - 1)\sin^4\theta\cos^2\theta\cos^2\phi - 2\cos^2\theta\sin^2\theta\cos^4\theta}{n^2(n^2\sin^2\theta - 1) + \cos^2\theta} + \frac{\cos^4\theta\cos^2\phi + \sin^2\phi\cos^2\theta}{(n^2 - 1)} \right] \hat{r} \quad \textbf{(18)}$$

, for $\theta \geq \theta_c$, where S is the Poynting vector, θ is the vertical take-off angle measured from the vertical, ϕ is the azimuthal take off angle, and θ_c is the critical angle at the free surface. The source amplitude is proportional to the square root of the Poynting vector $\left(|\vec{E}| \propto |\vec{S}|^{1/2}\right)$ so the source and receiver radiation coefficients are the normalized square root of S with ϕ=0 for the case of parallel polarization, and $\phi = \pi/2$, for the case of transverse polarization. The coefficients have a lobate shape with a maximum and null at θ_c for the transverse and parallel polarizations respectively.

The far-field patterns have been discussed in considerable detail (Annan et al., 1975; Kong, 1972; Papas and Engheta, 1982; Smith, 1984; Tsang and Kong, 1973), and were used by Cai and McMechan (1995) to model the TE configuration. These are the radiation patterns for an infinitesimal dipole and are strictly only valid at infinite distance from the dipole. Several authors have reported significant deviations from the far-field patterns in the laboratory, even at relatively large distances from the antenna (Annan et al., 1975; Chew and Kong, 1981; Wensink et al., 1990). In particular, the sharp maxima and null points, at the critical angle for the earth-air interface, are absent or muted in the near field. Wensink et al. (1990) concluded that far field conditions had not been reached by a distance equivalent to 15λ. In GPR investigations the target is typically within 2λ - 20λ at the characteristic signal frequency. Thus, it is necessary to construct radiation pattern corrections that do not depend on the far-field approximation. An observation of data presented by Annan et.al. (1975) suggests that when the reflecting target is within 6λ, a transverse radiation pattern of the form $1/\cos\theta$ may be appropriate for near offsets. I use $[D_{ST}, D_{RT}] = 1/\cos\theta$ for $\theta < \theta_{CT}$, where Equation 18, evaluated at $\theta = \theta_{CT}$ and $\phi = \pi/2$, is equal to $1/\cos\theta_{CT}$. In the case of parallel polarization, I find that the assumption of spherical spreading at near offsets is a reasonable approximation in the near field. I use $[D_{SP}, D_{RP}] = 1$ for $\theta < \theta_{CP}$ where Equation 18, evaluated at $\theta = \theta_{CP}$ and $\phi = 0$, is equal to 1. I use Equation 18 where $\theta \geq \theta_{CT}$, and $\theta \geq \theta_{CP}$ for the transverse and parallel radiation patterns respectively. These modified radiation patterns result in an AVO response that in many cases is a significantly better representation of field data than the GOA approximation. The code is implemented to optionally use the semi-empirical approximations discussed above or the GOA approximation. While this provides reasonable approach for modeling either the near or far field, it remains somewhat unsatisfactory as there is a significant gray area in the transition from near to far-field conditions. The transition is dependent on the permittivity structure of the earth and not well defined, therefore some user intervention is required in determining which pattern to use. I see this as the main limitation of the code as currently implemented. Ultimately, explicit numerical computation of the radiation patterns is desirable. Nevertheless, in many cases the code provides a reasonable approximation of the reflected wavefield response with relatively little computational cost.

At this point, it is appropriate to point out some additional limitations of the code. In this implementation, the travel path is assumed frequency independent, which is only approximate for dispersive media. To evaluate the error introduced by this assumption, consider a horizontal two-layer model with each layer 3 m thick. The upper layer is non-dispersive with $\varepsilon/\varepsilon_0 = 6$. The

lower layer is strongly dispersive with 25% dispersion over the bandwidth of the signal with $\varepsilon_{fo/}\varepsilon_0$ = 29 where ε_{fo} is the permittivity at the peak frequency. Most materials through which a signal will efficiently propagate have much lower dispersion across the GPR frequency band (Annan, 1996), and this represents an extreme case for estimating maximum expected error. At zero offset, the frequency independent path length assumption is exact. The error increases as the offset increases. At an offset of 12 m (twice the depth to the target) the path length for the minimum and maximum phase velocities are 17.9 m (t = 223 ns) and 17.6 m (t = 193 ns) respectively; a difference in path length (Δr) of 1.7%. The difference in travel time is 13.5%. Accounting for traveltime differences due purely to velocity along a frequency independent traveltime path and since $\Delta t \propto \Delta r$ only 12.6% of the travel time difference is due to differing travel paths. The majority of dispersion is due purely to velocity differences and in most cases we can safely assume frequency independent travel paths.

A second problem arises if we consider the value of Brewster's angle. For a frequency dependent velocity field, the critical angle and Brewster's angle will occur at different angles of incidence for each frequency component. This has two primary effects. First, the computed wavelet phase will not be correct and second, since spatial dispersion is not properly accounted for, the assumption will introduce artificial time dispersion. As mentioned previously, dispersion in media that a GPR signal will propagate efficiently is relatively small, so that these errors are relatively small. The major problem I have observed, in a large number of model configurations, is the introduction of a non-causal, low-frequency precursor in the post-critical wavefield. In all cases the precursor has been relatively low amplitude and has not effected AVO computations in any noticeable way.

There are frequency dependent attenuation, reflection, transmission and dispersion effects, associated with thin layers, that are not treated properly with ray theory. In general, ray theory is assumed valid when the scale of the features being studied, d, is much larger than the wavelength λ, ($\lambda \ll d$). The maximum ratio of λ/d for which ray theory is still valid continues to be the subject of some debate, and active research continues in the seismological community. Mukerji et al. (1993) present laboratory data indicating the transition from ray theory to effective medium theory ($\lambda \sim d$) occurs between $\lambda/d = 1$ and $\lambda/d = 10$ for compressional waves. I find that the model response to short wavelength variations in permittivity is minimal to large angles of incidence (Figure 1).

For comparison to to field data, I have set up two models based on measurements acquired at Wurtsmith AFB. There are different permittivity and conductivity models for the on-plume and off-plume portions of the dataset. Synthetic data generated using the model described here is a close approximation of the field data (Figures 2 and 3).

REFERENCES

Annan, A.P., 1996, Transmission dispersion and GPR: J. Env. Eng. Geophys., **0**, 125-136.

Annan, A.P., Waller, W.M., Strangway, D.W., Rossiter, J.R., Redman, J.D., and Watts, R.D., 1975, The electromagnetic response of a low-loss, 2-layer, dielectric earth for horizontal electric dipole excitation: Geophysics, **40**, 285-298.

Bergmann, T., Robertsson, J.O.A., and Holliger, K., 1998, Finite-difference modeling of electromagnetic wave propagation in dispersive and attenuating media: Geophysics, **63**, 856-867.

Cai, J., and McMechan, G.A., 1995, Ray-based synthesis of bistatic ground-penetrating radar profiles: Geophysics, **60**, 87-96.
Carcione, J.M., 1996, Ground-penetrating radar: Wave theory and numerical simulation in lossy anisotropic media: Geophysics, **61**, 1664-1677.
Casper, D.A., and Kung, K.-J.S., 1996, Simulation of ground-penetrating radar waves in a 2-D soil model: Geophysics, **61**, 1034-1049.
Chew, W.C., and Kong, J.A., 1981, Electromagnetic field of a dipole on a two-layer earth: Geophysics, **46**, 309-315.
Cole, K.S., and Cole, R.S., 1941, Dispersion and absorption in dielectrics, I, alternating current characteristics: J. Chem. Phys., **9**, 341-351.
Griffiths, D.J., 1989, Introduction to electrodynamics, Prentice-Hall.
Kong, J.A., 1972, Electromagnetic fields due to dipole antennas over stratified anisotropic media: Geophysics, **37**, 985-996.
Mukerji, T., Mavko, and Marion, D., 1993, Velocity dispersion and scale effects in layered media: Modeling of experimental results, Stanford rock physics and borehole geophysics project **53**, A:1-A:12.
Olhoeft, G.R., and Capron, D.E., 1994, Petrophysical causes of electromagnetic dispersion: 5th Internat. Conf. GPR, Waterloo Center for Groundwater Research, Proceedings, 145-152.
Olhoeft, G.R., and Strangway, D.W., 1974, Magnetic relaxation and the electromagnetic response parameter: Geophysics, **39**, 302-311.
Papas, C.H., and Engheta, 1982, Radiation patterns of interfacial dipole antennas: Radio Science, **17**, 1557-1566.
Powers, M.H., and Olhoeft, G.R., 1996, Modeling the response of leaking, buried pipes: SAGEEP '95 Symposium on the Application of Geophysics to Environmental and Engineering Problems, Soc. Appl. Geophys. Env. Eng., Proceedings, 525-534.
Roberts, R.L., and Daniels, J.J., 1992, 3-D data collection and analysis for high-resolution GPR studies: 62nd Ann. Internat. Mtg., Soc. Expl. Geophys., Expanded abstracts, 360-363.
Roberts, R.L., and Daniels, J.J., 1997, Modeling near-field GPR in three dimensions using the FDTD method: Geophysics, **62**, 1114-1126.
Smith, G.S., 1984, Directive properties of antennas for transmission into a material half-space: IEEE transactions on antennas and propagation, **AP-32**, 232-246.
Tsang, L., and Kong, J.A., 1973, Interference patterns of a horizontal electric dipole over layered dielectric media: J. Geophys. Res., **78**, 3287-3300.
Wang, T., and Tripp, A.C., 1996, FDTD simulation of EM wave propragation in 3-D media: Geophysics, **61**, 110-120.
Wensink, W.A., Greeuw, G., Hofman, J., and Van Deen, J.K., 1990, Measured underwater near-field e-patterns of a pulsed, horizontal diplot antenna in air: Comparison with the theory of the continuous wave, infinitesimal dipole: Geophys. Pros., **38**, 805-830.
Xu, T., and McMechan, G.A., 1997, GPR attenuation and its numerical simulation in 2.5 dimensions: Geophysics, **62**, 403-414.
Zeng, X., McMechan, G.A., Cai, J., and Chens, H.-W., 1995, Comparison of ray and Fourier methods for modeling monostatic ground-penetrating radar profiles: Geophysics, **60**, 1727-1734.
Zeng, X., McMechan, G.A., and Xu, T., 2000, Synthesis of amplitude versus offset variations in

ground-penetrating radar data: Geophysics, **65**, 113-125.

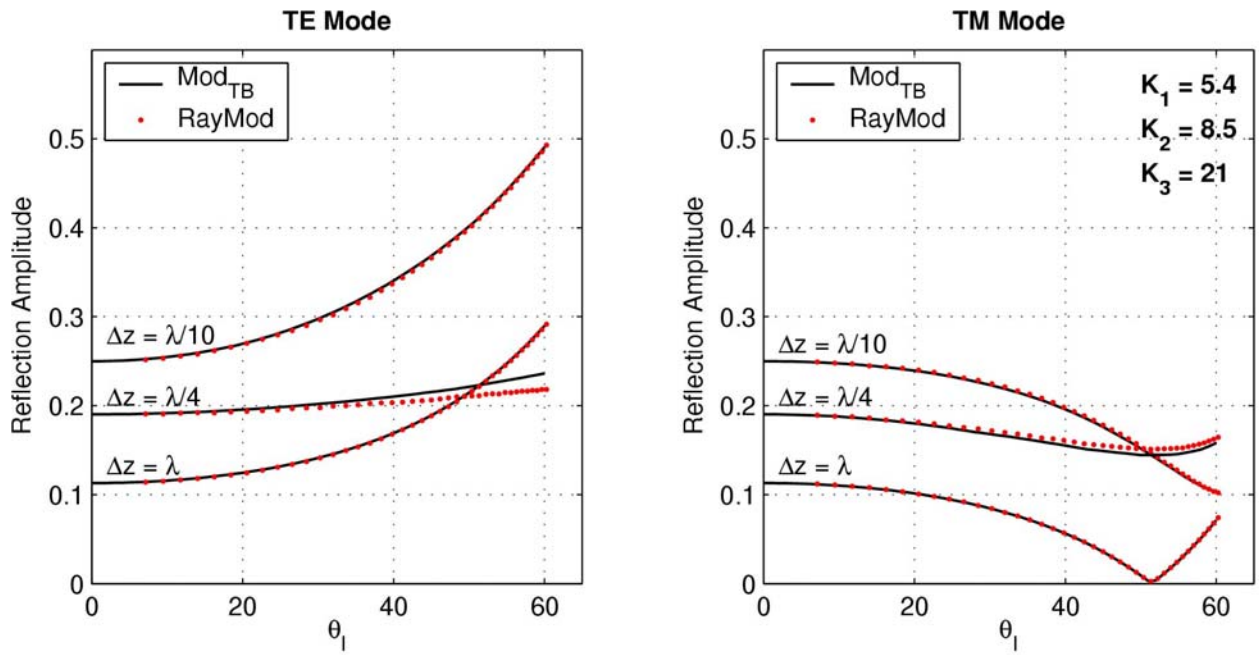

Figure 1. Comparison of the thinbed reflectivity response computed using GPR_RAY_MOD and the broadband analytical solution (Mod_{TB}). The comparison assumes zero conductivity, and frequency independent permittivity with relative permittivity values shown in the upper right. The curves are computed using a Ricker wavelet for both models with a thinbed thickness varying as a fraction of the wavlength at the dominant signal frequency. GPR_RAY_MOD is an excellent approximation of the analytical solution to large incidence angles.

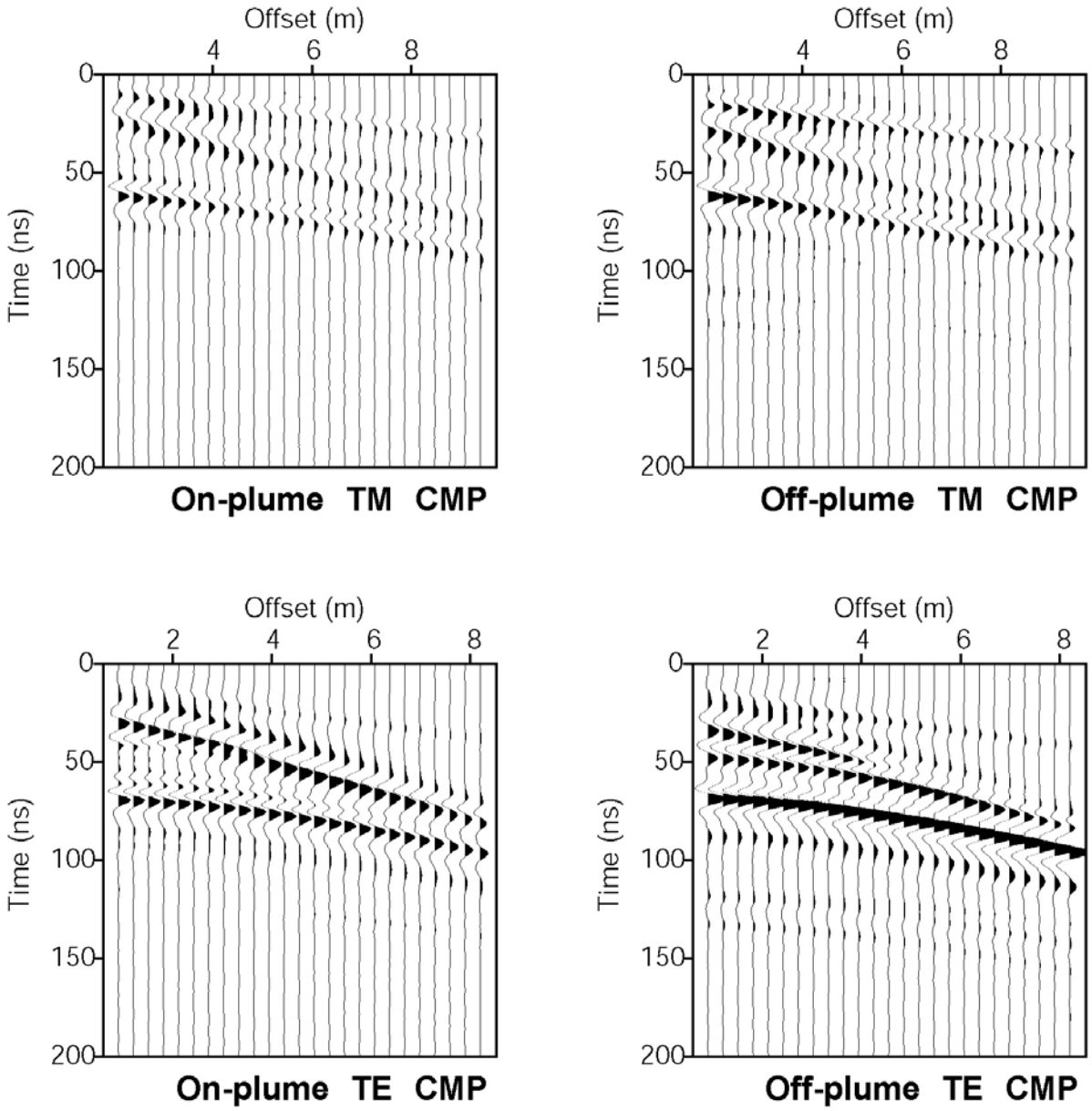

Figure 2. Representative field data from the Wurtsmith AFB. Compare to synthetic data in Figure 3.

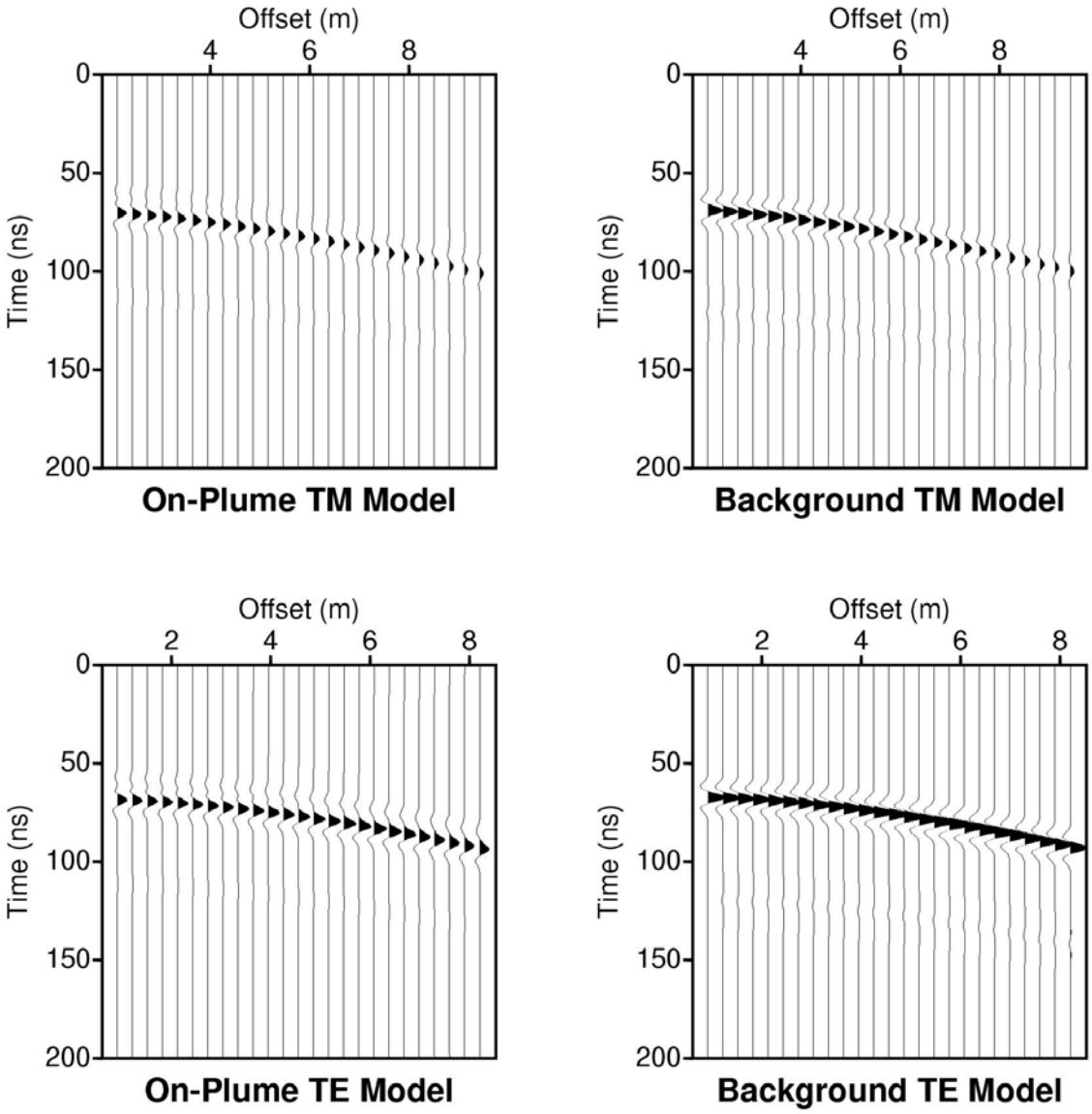

Figure 3. Synthetic data generated using GPR_RAY_MOD. The model is based on measurements and GPR field data from Wurtsmith AFB. The synthetic data are a good approximation to the field data shown in Figure 2. Note that the direct air wave and air coupled ground wave are not modeled. The dominate reflection is from the water table. Subsurface property models are shown in Figure 4.

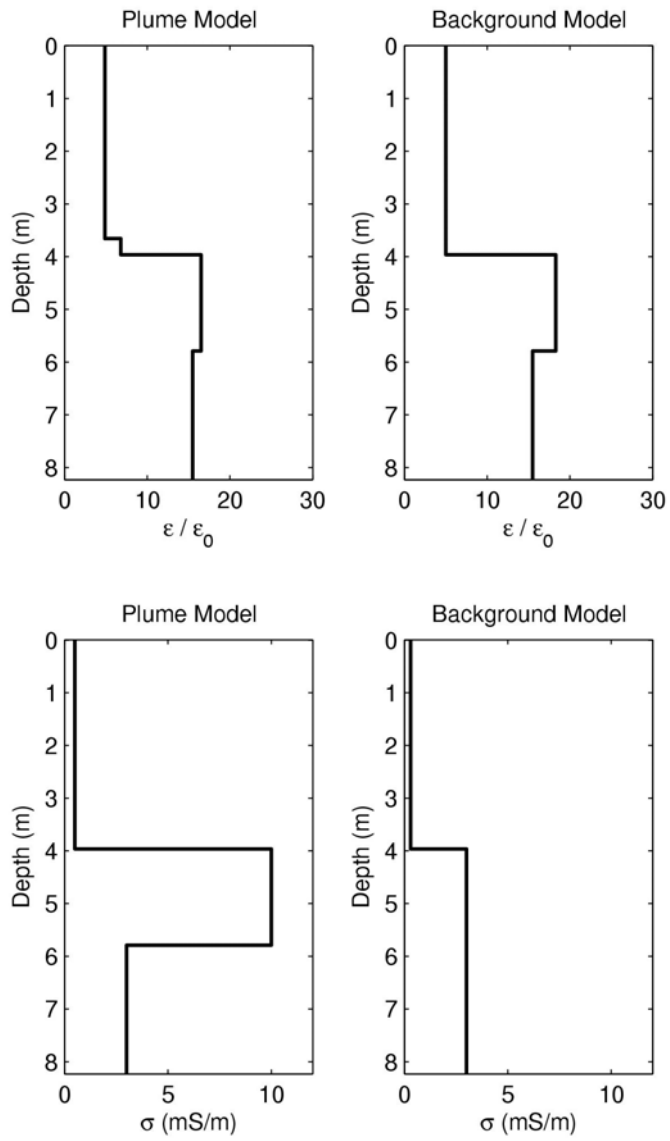

Figure 4. Electric property models used to compute the synthetic data shown in Figure 3.

APPENDIX D: CALCULATING ATTENUATION ATTRIBUTES

Time-frequency (t-f) analysis is a valuable tool for evaluating frequency dependent wave attributes attributes such as attenuation, dispersion, etc. The windowed Fourier transform and the Wigner distribution are commonly used to obtain the t-f distribution. However, the windowed Fourier transform is time-resolution limited because the window length is fixed, and the Wigner distribution suffers from cross-term interference (Boudreaux-Bartels, 1985). To reduce unwanted cross term interference, signals are commonly decomposed into wavelet atoms that are used to construct a t-f distribution (Daubechies, 1991).

Propagating electromagnetic waves are subject to frequency dependent attenuation which depends primarily on conductivity. Typically, over the bandwidth of a ground-penetrating-radar (GPR) pulse, the attenuation can be approximated with the following equation (Turner and Siggins, 1994):

$$\alpha = \alpha_0 + \frac{\omega}{2cQ^*} \tag{1}$$

where α_0 is controlled by the DC electrical conductivity and Q^* is a parameter that is derived assuming that the frequency dependent component of attenuation is a linear function of frequency across the GPR signal band. There is an inherent non-uniqueness between reflectivity and the DC component of attenuation α_0 which means that we cannot measure α_0 from surface GPR data without additional geophysical or borehole measurements such as DC resisitivity. However, by measuring the change in the signal spectrum through time using time-frequency analysis we can measure Q*. As we show below, with a few simplifying assumptions, Q* is independent of reflectivity and therefore has the potential to provide a reliable estimate of one component of GPR signal attenuation that is altered by the presence of NAPL in the subsurface. Note that in the low conductivity case, which covers all conditions under which GPR will operate efficiently, Q^* can be shown to be a function of the complex permittivity given by

$$Q^* = \frac{\varepsilon'}{\varepsilon''} \tag{2}$$

where ε' is the real part of the permittivity and ε'' is the complex part of the permittivity.

Given a frequency independent $Q^*(z)$, in a layered earth model, the amplitude spectra varies according to the following equation

$$A_n(f) = A_0(f) e^{-\alpha_0 t_n} e^{\frac{-\pi f t_n}{Q^* eff_n}} K_n \tag{3}$$

where f is the frequency, K_n is a constant at any specified time which accounts for source directivity, geometric spreading, transmission, and reflection losses (this of course assumes that these parameters are frequency independent), A_o is the source spectrum or reference spectrum, and t_n is the traveltime to the base of the layer of interest. Q^*_{eff} is an effective Q^* value which

accounts for the cumulate intrinsic attenuation of all layers above the time of interest, and is given by

$$\frac{1}{Q^{*}eff_n} = \frac{\sum(\Delta t_i / Q^{*}{}_i)}{t_n} \tag{4}$$

where Δt_i and Q_i are the interval traveltime and Q for each layer, and t_n is the total traveltime.

The spectral ratio method is commonly used for estimating seismic Q values in laboratory measurements or sonic logs, but can also be applied to GPR reflection data, given an accurate t-f distribution. It is an attractive method because, ideally, it allows one to separate frequency dependent attenuation due to complex permittivity from attenuation due to reflection and transmission losses, spherical spreading and source and receiver effects, which are assumed frequency independent. Taking the natural log of both sides of Equation 3, we derive the following equation:

$$\ln\frac{A_0(f)}{A_n(f)} = \frac{\pi t_n}{Qeff_n} f - \ln(K_n) \tag{5}$$

Q_{eff} can then be estimated from the slope of a plot of $\ln(A_0/A_n)$ vs. f. Given Q_{eff}, the interval Q value can be estimated from the following equation

$$\frac{1}{Q_n} = \left(\frac{t_n}{Qeff_n} - \frac{t_{n-1}}{Qeff_{n-1}} \right) \frac{1}{\Delta t_n} \tag{6}$$

We see from Equation 6 that our estimate of $1/Q^{*}_n$ is most sensitive to small values of Q^{*}_{eff} or alternatively from Equation 4, that Q_{eff} is sensitive to small interval Q values. It is apparent from this observation that $1/Q^{*}_n$ is most sensitive to zones of high attenuation (low Q^{*}). In field data, it is often difficult to estimate the source spectra and certain assumptions such as frequency independent reflection and transmission may not be valid. In this case, extracting the true Q^{*} value may be difficult, or even impossible. However, as with other attributes, we are searching for anomalies, and is not necessary to determine the absolute value.

A second method of estimating Q^{*} is the frequency shift method. As the signal undergoes frequency dependent attenuation, high frequencies are attenuated more rapidly and the dominant frequency of the signal shifts toward the lower end of the spectrum. It can be shown that Q^{*} is a function of the shift and is given by (Quan and Harris, 1997)

$$\frac{1}{Q^{*}eff_n} \propto f_0 - f_n \tag{7}$$

where f_0 is the centroid frequency of the reference wavelet, and f_n is the centroid frequency at reflection n. We've found that the frequency shift method and the spectral ratio method give comparable results in high signal-to-noise data, but that the frequency shift method is more robust in low signal-to-noise data.

To extract Q^*_{eff} from field data we must first choose a reference spectrum $A_0(f)$. Ideally, we would always use the source spectrum, but this is not always trivial in field data. With the Sensor's and Software™ system, we find that a Ricker source wavelet, with peak frequency corresponding to about 80% of the dominant frequency of the antenna produces good results. Alternatively, from Equation 5, we see that the spectrum of any wavelet along the trace will produce the correct result. We typically choose the first clean event that is laterally coherent and is isolated in time. GPR data typically have a very consistent, high amplitude direct wave that can be isolated and used as the reference wavelet.

Second, we must choose which events to use for attenuation analysis. We cannot simply carry out the analysis at every time sample, since there will only be noise or no data at some locations, which would produce erroneous results. Thresholding is one method (i.e. every event with amplitude above a certain threshold are deemed significant and used in the analysis). But this method is quite sensitive to noise even in good quality data. We currently interpret significant events manually. A time gate is chosen that spans the event of interest. The maximum amplitude of the envelope function within this gate is specified as t_0 for the corresponding event. Choosing amplitudes from the envelope function avoids the problem of incorrect placement of t_0 due to phase rotation.

REFERENCES

Boudreaux-Bartels, G.F., 1985, Time-varying signal processing using the Wigner-Distribution time-frequency signal representation, Advances in geophysical data processing: JAI Press Inc. **2**, 33-79.

Daubechies, I., 1991, Ten lectures on wavelets, SIAM.

Quan, Y., and Harris, J.M., 1997, Seismic attenuation tomography using the frequency shift method: Geophysics, **62**, 895-905.

Turner, G., and Siggins, A.F., 1994, Constant Q attenuation of subsurface radar pulses: Geophysics, **59**, 1192-1200.

APPENDIX E: 3D MULTI-OFFSET, MULTI-POLARIZATION ACQUISITION AND PROCESSING OF GPR DATA: A CONTROLLED DNAPL SPILL EXPERIMENT

Bradford, J.H., 2004, 3D Multi-offset, multi-polarization acquisition and processing of gpr data: a controlled DNAPL spill experiment: SAGEEP 2004 Symposium on the Application of Geophysics to Environmental and Engineering Problems, Env. Eng. Geophys. Soc., 514-527.

3D MULTI-OFFSET, MULTI-POLARIZATION ACQUISITION AND PROCESSING OF GPR DATA: A CONTROLLED DNAPL SPILL EXPERIMENT

John H. Bradford, *CGISS, Boise State University, Boise, ID*

Abstract

Dense non-aqueous phase liquid contaminants (DNAPL) typically have much lower electric conductivity and electric permittivity than water. The bulk electric properties of the subsurface can be significantly altered when these contaminants replace water in the pore space. Ground-penetrating radar (GPR) is sensitive to permittivity contrasts and provides the potential to identify zones of low permittivity associated with the presence of DNAPL. To test 3D multi-fold GPR techniques for quantifying DNAPL induced permittivity anomalies, my research team conducted a small (107 cm x 122 cm), controlled DNAPL spill experiment. The model was confined within a cylindrical polyethylene tank; model material consisted of medium to coarse grained sand with a thin gravel layer near the base. My team injected twenty liters of a chlorinated solvent solution into the vadose zone just below the surface, and monitored contaminant migration into and through the water saturated zone to the bottom of the tank. I compiled a comprehensive dataset for testing a variety of data processing and analysis techniques including 900 MHz, multi-offset, 3D surface datasets in both TE and TM polarizations, 2D GPR transmission data, downhole TDR probe data, and post-injection soil samples for chemical analysis. Both reflection tomography from TE polarized surface data and crosswell tomography from transmission data reveal significant velocity anomalies associated with pooled DNAPL that approaches a saturation of 40%. Further, thinbed offset-dependent reflectivity analysis of TM surface data suggests the formation of a thin, highly saturated (80-100%) DNAPL zone at the top of the main DNAPL pool. This work demonstrates that detailed analysis of multi-offset, multi-polarization GPR data can significantly improve our ability to quantify subsurface permittivity anomalies.

Introduction

Chlorinated solvents are common groundwater contaminants that are linked to a number of health problems and are suspected carcinogens. These chemicals are non-polar and denser than water and are thus classified as dense, non-aqueous phase liquids (DNAPL). Previous workers have shown that introducing chlorinated solvents into the subsurface can significantly alter the bulk electric properties (Brewster and Annan, 1994; Newmark et al., 1998; Powers and Olhoeft, 1996; Redman and DeRyck, 1994). The primary mechanism of this alteration is the displacement of high electric permittivity pore water ($\varepsilon_w/\varepsilon_o$=80) with low permittivity DNAPL ($\varepsilon_D/\varepsilon_o \approx 2$), where ε_w, ε_D, and ε_o are the permittivity of water, DNAPL, and free space respectively. In the water saturated zone, the bulk permittivity is primarily controlled by the pore fluid, and is therefore a function of porosity (ϕ). Ground penetrating radar is sensitive to variations in subsurface permittivity. This leads to the potential for detecting DNAPL induced permittivity anomalies using GPR. More specifically, assuming frequency independent material properties, and that magnetic permeability does not vary significantly, GPR velocity is related to permittivity by the relationship,

$$v = c\sqrt{\frac{\varepsilon_o}{\varepsilon}} \qquad (1)$$

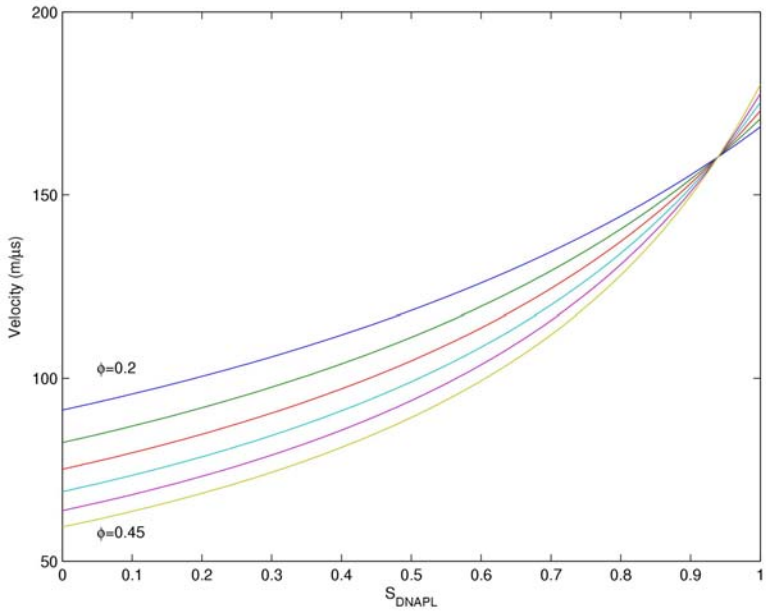

Figure 1. GPR velocity vs DNAPL saturation for porosity (ϕ) varying from 0.2 to 0.45. I computed the curves using the CRIM equation assuming a 3-phase system consisting of a quartz matrix ($\varepsilon/\varepsilon_o$=3.5), water ($\varepsilon/\varepsilon_o$=80), and DNAPL ($\varepsilon/\varepsilon_o$=2).

where v is the GPR velocity, c is the speed of light in free space, ε_o is the permittivity of free space, and ε is the permittivity of the material through which the signal is propagating. This approximation holds to first order in most materials in which GPR operates efficiently (Annan, 1996) and means that a DNAPL rich zone may have anomalously high radar velocities (Figure 1). GPR velocity is the material property most often measured, typically through traveltime analysis of multi-offset data. It may be possible to gain additional constraint on the subsurface properties by considering how the amplitude of a signal varies with offset. A signal reflected from a low permittivity anomaly, such as DNAPL pool, will lead to offset-dependent reflectivity anomalies (Figure 2). In particular, in TE mode the amplitude will increase more rapidly as the incident angle (θ_i) approaches the critical angle θ_c. In TM mode, the amplitude will initially decay more rapidly as θ_i approaches Brewster's angle (θ_B) where the reflection coefficient goes to zero and the signal undergoes a 180° phase shift. Beyond θ_B, the TM amplitude builds (but with opposite polarity) as θ_i approaches θ_c.

Most GPR data are acquired with constant transmitter-receiver offset which can provide a map of permittivity contrasts in the subsurface. Making quantitative permittivity estimates from constant offset data requires reflectivity inversion using GPR amplitude data. This inversion is extremely difficult due to the many factors that affect recorded amplitude, and has not yet proven reliable. Thus, GPR investigators often acquire a sparse sampling of multi-offset data within a larger survey area to provide a rough permittivity calibration. While this approach provides acceptable results in many cases, it fails to account for lateral variations in the permittivity structure .

In multi-offset data acquisition, we acquire data with multiple transmitter-receiver offsets for any given sampling location. Multi-offset data enable measurement of propagation velocity and offset dependent reflectivity. Continuous multi-offset data or multi-fold data acquisition is analogous to common-midpoint (CMP) data acquisition in seismic reflection (Yilmaz, 2001). While these acquisition and processing methodologies are more labor intensive and time consuming, the advantages in improving the quality of GPR images are well documented (Bradford, 1998; Fisher et al., 1992a; Fisher et al., 1992b; Greaves et al., 1996; Loughridge, 1998). Additionally, multi-fold data enable detailed measurement of both lateral and vertical permittivity variations using velocity analysis (Bradford, 2003a; Bradford, 2003b; Deeds and Bradford, 2002). This capability is critical in identifiying laterally discontinuous concentrated DNAPL zones. Multi-offset data acquisition also enables investigation of the offset-dependent reflectivity (ODR). This is often referred to amplitude vs offset analysis (AVO) or amplitude vs angle analysis (AVA) in the angle of incidence domain. For electromagnetic wave propagation, the amplitude of the reflection coefficient varies significantly with increasing angle of incidence. This response depends strongly on the polarity of the electric field and the contrast of permittivity (ε) between the incident and reflecting fields

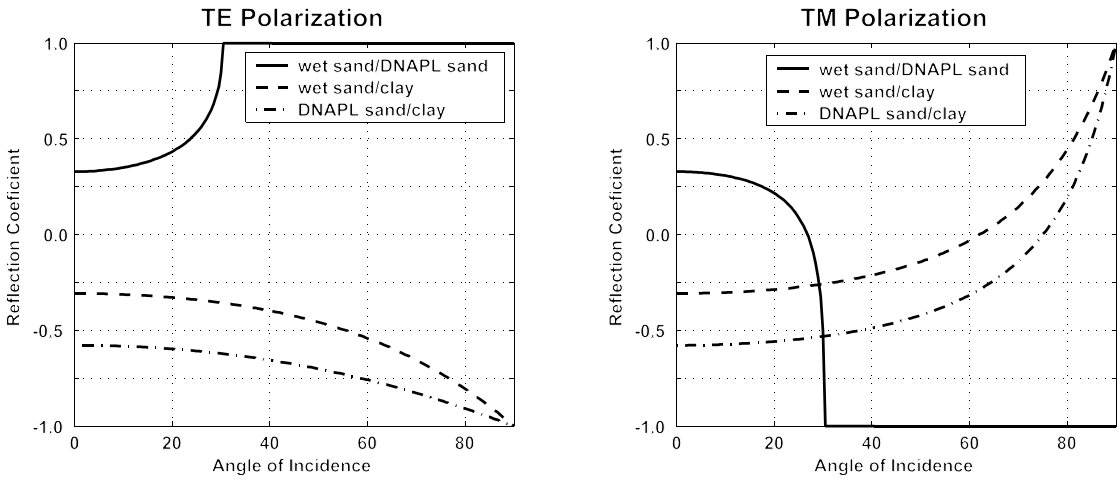

Figure 2. . Reflection coefficients at 900 MHz, for various interfaces that might be imaged in a DNAPL contaminated aquifer. The model uses a porosity of 0.4 and DNAPL saturation of 0.8.

(Figure 2). Lehmann (1996) discusses complex reflection coefficients and the effects of conductivity, Bergmann et al. (1998) briefly discuss AVO response in the context of a broader synthetic case study. Baker (1998) presents a modeling study indicating the potential for detecting LNAPLs based on the transverse AVO response. Zeng et al. (2000) present a detailed modeling study considering the effects of varying the Cole-Cole parameters on the AVO response. With the exception of Bergmann et al. and Baker, these studies are general in nature, and Zeng et al., Bergmann et al., and Baker focus only on the response for the TE field. Most recently, my research group has successfully used offset dependent reflectivity analysis to measure permittivity anomalies associated with hydrocarbon contamination at two field sites (Bradford, 2003a; Deeds and Bradford, 2002). The analysis is significantly more robust when both TE and TM polarized data are evaluated. Because the reflection coefficient curves for the two polarizations are significantly different, they provide essentially two independent measures of the permittivity contrast at a reflecting boundary.

To test multi-offset methods for identifying DNAPL induced permittivity anomalies, my research team constructed a physical model for a controlled DNAPL spill experiment. The experiment is similar to a controlled DNAPL spill detailed by Brewster and Annan (1994), Redman and DeRyck (1994), and Kueper et al (1993) at the Canadian Air Force Base Borden. Brewster and Annan (1994) found significant GPR reflectivity anomalies in common-offset data associated with pooled DNAPL. Additionally, they measured a significant increase in radar velocity using normal moveout (NMO) analysis at a single CMP location. My objective here is to further Brewster and Annan's earlier efforts by focusing on detailed processing and analysis of 3D multi-offset data including data acquired in both TE and TM polarizations. Additionally, I also investigate DNAPL migration through both the vadose and saturated zones as opposed to the Borden experiment in which only fully water saturated conditions were investigated.

My primary objective is to demonstrate the use of modern processing techniques to maximize the amount and accuracy of the measured subsurface properties. To this end, I focus on pre-stack processing methodologies including reflection tomography coupled with prestack depth migration for velocity analysis (Stork, 1992). In previous work, my research group has demonstrated the of use pre-stack migration velocity analysis in identifying lateral and vertical velocity heterogeneity at contaminated sites (Bradford, 2003b; Deeds and Bradford, 2002). Additionally, I investigate the offset dependent reflectivity response to the DNAPL induced permittivity anomaly.

Experiment Configuration and Data Acquisition

The physical model was contained within a cylindrical polyethylene tank that was 122 cm in diameter and 107 cm deep (Figure 3). A bowl shaped bentonite layer lined the base of the tank. I used this configuration to route migrating DNAPL to the valved drain at the center of the tank. Above the clay, the tank fill consisted primarily of a medium to coarse grained sand ($\phi = 0.41$) with the exception of an 11 cm thick gravel layer ($\phi = 0.46$) 32 cm above the bottom of the tank. Although originally uniform and flat lying, the gravel layer deformed as the tank was filled, with the final configuration being an asymmetric bowl shape (Figure 4). While this 3D geometry was not the original design, I felt the structure would prove beneficial in demonstrating the processing techniques without being overly complex. Thus no attempt was made to reconfigure the tank with flat lying stratigraphy. My team covered the top of the tank with plexiglass and placed permanent GPR survey markers on the plexiglass.

For an independent measure of electric permittivity variations, my team installed two sealed 2" PVC access tubes for a commercial downhole TDR probe (Figure 3). Redman and DeRyck (1994) successfully used TDR to measure permittivity anomalies in the Borden experiment. In this case, using a downhole probe allowed me to remove all metal hardware during GPR data acquisition. The TDR access ports were placed at the periphery of the target zone to avoid interference with radar reflections at the center of the tank where I expected DNAPL concentrations to be the highest. I felt this was a reasonable compromise that would provide a measure of in-situ experiment control while avoiding interference in the primary target

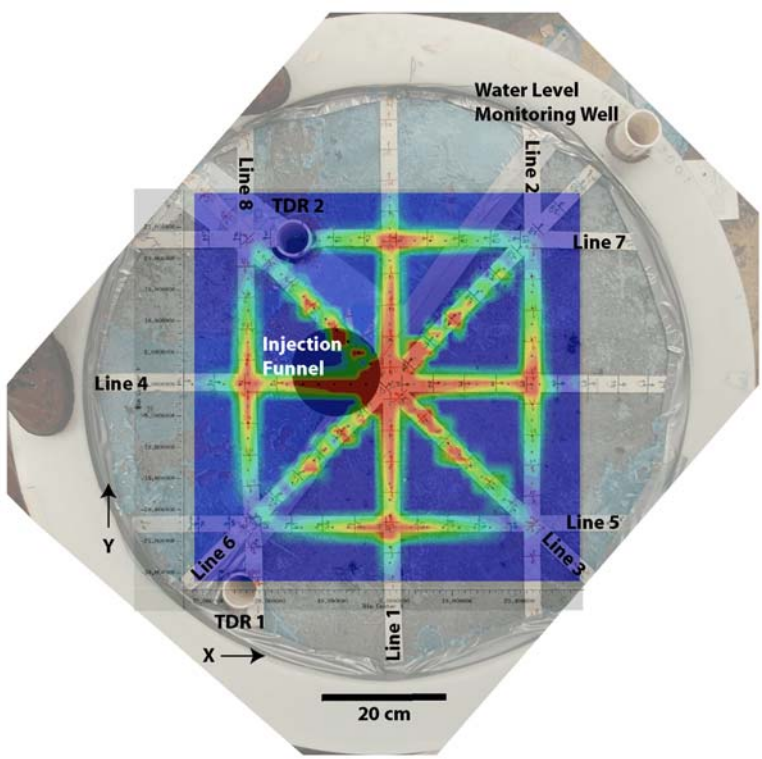

Figure 3. . Overhead photo of the experiment tank with the CMP fold map overlain. Fold greater than 6 is shown in red.

zone. The TDR probe waveguides are 20 cm long and the manufacturers specifications state an approximate 15 cm radius of influence; the measured permittivity is an average over this volume.

Prior to all data acquisition, I raised the water level in the tank to the surface, then allowed the water level to equilibrate at 53 cm below the surface. In subsequent TDR probe and GPR measurements I found that the top of the water saturated zone was 40 cm below the surface, indicating a 13 cm thick capillary fringe.

The DNAPL consisted of a mixture of 4 liters of 1,1,1-carbon trichloroethane (specific gravity =1.4, $\varepsilon/\varepsilon_o$ =7.3), and 16 liters of tetrachloroethylene (specific gravity=1.6, $\varepsilon/\varepsilon_o$ =2.3). I added red Sudan IV dye to the DNAPL mixture so that I could visually detect DNAPL during post-injection tank excavation. I injected the DNAPL mixture into the tank via gravity feed through a small, perforated funnel inserted 15.25 cm below the surface. DNAPL flow into the tank was rapid and all liquid drained from the funnel in less than 2 minutes.

I acquired surface GPR data in a wagon wheel geometry with 5.08 cm source and receiver intervals. For each common source point, I acquired a trace with the receiver at each available position along the same line as the source (Figure 3) with a minimum offset of 16 cm and maximum offset of 77 cm. This resulted in a symmetric split spread geometry in the center of the tank, and off-end geometry at the periphery. This geometry yields high CMP fold in the center of the tank (Figure 3) where I wanted the highest signal-to-noise ratio for detailed amplitude analysis. I acquired TE data along lines 1-8. Since I planned to use the TM data primarily for ODR analysis, TM data were only acquired along the full offset lines 1, 3, 4 and 6. I acquired GPR transmission data across the Line 4 plane with source and receiver positions every 5.08 cm across the top and down the sides of the tank. This geometry provided 32-fold common-source gathers with with wide aperture and near vertical raypaths. I acquired all data using a Sensors and Software PulseEKKO 1000 system using 900 MHz antennas. For both surface and transmission data, I used a 60 ns recording time, 0.1 ns sampling rate and stacked 16 pulses/trace. I acquired a full round of data prior to injection and 48 hr after injection when no further changes were evident in the TDR data. I also acquired time lapse and 450 MHz data but for brevity am not presenting these data here.

Data Processing

The data processing flow for all surface GPR data is the same. Pre-processing for velocity and ODR analyses consists of bandpass filtering (225-450-1800-3600) to attenuate the low frequency transient and high frequency random noise, a time zero correction, and a non-spherical spreading correction based on a 1D NMO velocity model. I estimate the 1D velocity model using normal-moveout analysis (NMO) of the high-fold CMP at the center of the tank, then use Dix inversion to compute the interval velocity model. NMO analysis is not applicable at the clay reflection due to the complex reflection moveout along the bowl shaped sand/clay interface. Thus, I limit NMO analysis to times less than that corresponding to the gravel reflections (~20 ns). I migrate the data using a Kirchhoff 3D pre-stack time migration algorithm using the 1D model and get very good results in all cases. This is an accurate method of interpolating the data onto a uniform grid for 3D interpretation (Figure 4). To compute the detailed depth velocity model, I apply pre-stack depth migration (PSDM) velocity analysis in the following sequence. I first migrate the data, line by line using a 2D Kirchhoff PSDM algorithm with the 1D velocity model from NMO analysis and Dix inversion. I update this model using a layer stripping approach to minimize residual moveout in the post-migration common image point (CIP) gathers. Next, I apply PSDM using the updated velocity model and

pick residual moveout on the post-migrated CIPs. The final velocity model is computed by tomographic

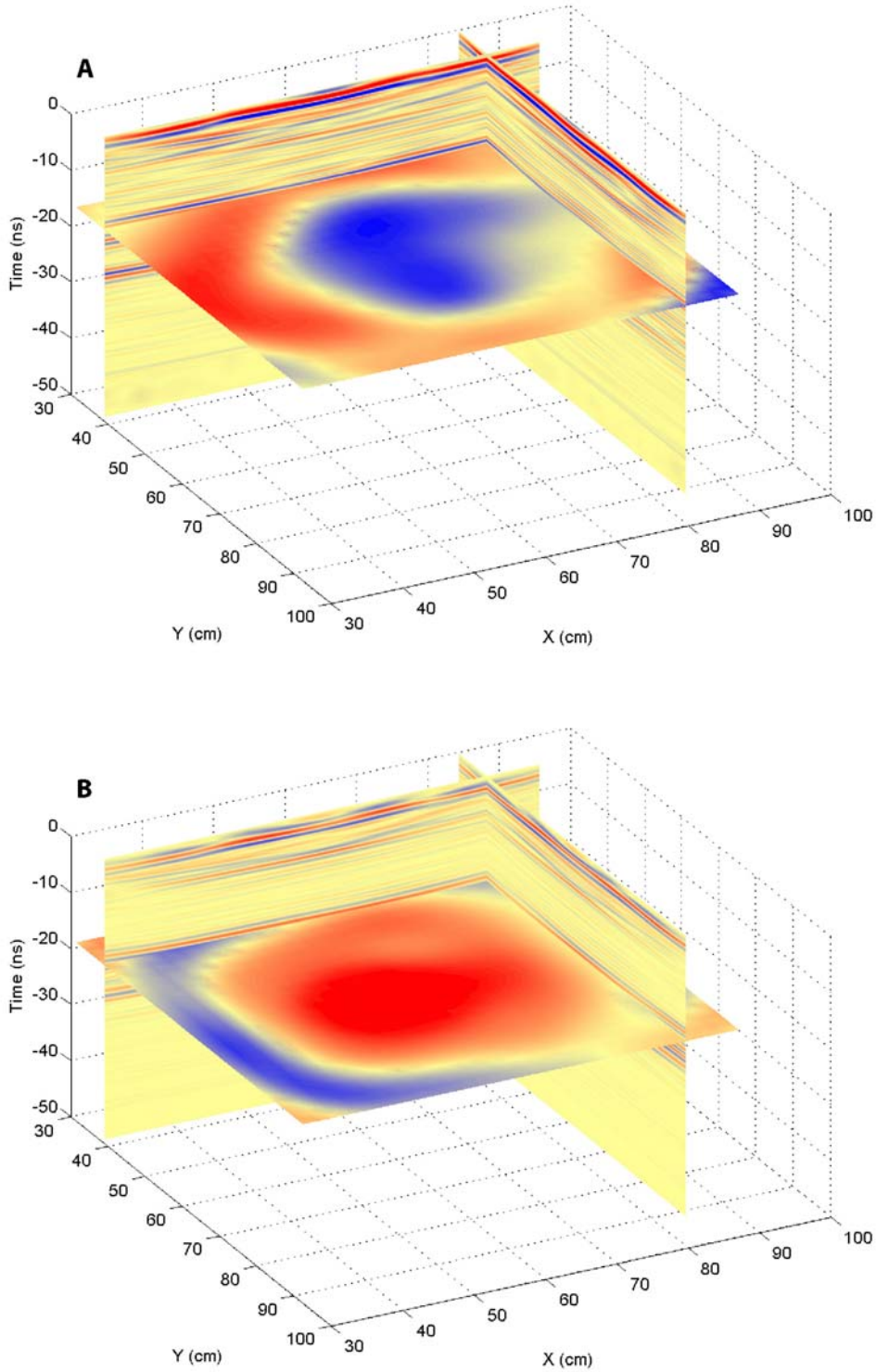

Figure 4. . 3D pre-stack time migrated images of A) the tank prior to injection and B) 48 hr after the injection. The time slices are through the A) top of gravel and B) top of DNAPL reflections. Note the asymmetric distribution of gravel and DNAPL.

inversion of the residual moveout picks using the method of Stork (1992). The migration velocity analysis tool available with Promax™ was conveniently configured for this task, and for all lines, one iteration of this process produced excellent PSDM results and required only 0.5 - 1 hr per line.

For ODR analysis, I first compute the offset to angle of incidence transform by ray tracing through the 1D average velocity model for each dataset. I then generate CMP supergathers for pre- and post injection TE and TM datasets by combining all the data within a 4x4 CMP bin area at the center of the tank (Figure 3). Data amplitudes used in the analysis are picked using an automated picking algorithm and are the maxima of the envelope function along a given reflection. Using the envelope function for the analysis eliminates the potential for amplitude artifacts caused by phase rotation of the wavelet (Bradford, 1998). I make no detailed attenuation or radiation pattern corrections, and instead carry out detailed analysis relative to a background amplitude curve. In principle this method cancels any ODR artifacts caused by radiation pattern effects or attenuation in the overburden. In practice, I have found this method to be relatively robust, but have only applied it to a few datasets (e.g. (Bradford, 2003a)). In this case I focus on the reflection from the primary DNAPL pool and use the top-of-gravel reflection from the pre-injection data for the background ODR trend. The angle of incidence in the experiment was limited to a relatively small aperture due to the spatial confines of the tank and the large negative velocity gradient across the water table. The maximum angle of incidence at the primary target depth (~ 40 cm below the water table) was less than 17°.

The porosities of the tank materials are well constrained and I use the CRIM equation (Greaves et al., 1996) for petrophysical analysis. This is a simple time-average equation and is easily formulated for velocity or relative permittivity. The equation for bulk formation velocity is given by the expression

$$v = \left(\frac{1}{v_M}(1-\phi) + \frac{1}{v_W}\phi(1 - S_{DNAPL}) + \frac{1}{v_{DNAPL}}\phi S_{DNAPL} \right)^{-1} \quad (2)$$

where v_M, v_W, and v_{DNAPL} are the matrix velocity, water velocity and DNAPL velocity respectively, ϕ is the porosity, and S_{DNAPL} is the DNAPL saturation or volume fraction of DNAPL in the pore fluid. In this experiment, this formula predicts GPR velocities comparable to velocities measured with the TDR probe, and I consider it a reasonable approximation.

Results and Discussion

In the pre-injection data, reflections from the water saturated zone (SZ), top and bottom of the gravel layer, and the clay are evident (Figures 6 and 7). Within 30 min after the injection, a significant DNAPL pool formed in the gravel layer (Figure 5) producing a strong, well defined GPR reflection (Figures 6 and 7). There was no clear evidence in the GPR or probe data for pooling between the injection point and gravel layer, although in the subsequent excavation residual DNAPL was present throughout much of the vadose zone and all of the saturated zone, and DNAPL pools were present at the top of the saturated zone. Between 24 and 48 hours after the injection, TDR Probe 1 showed a significant velocity increase as DNAPL drained rapidly from the gravel layer and formed a pool in the sand at the bottom of the tank. There was no evidence of further DNAPL migration during the following 48 hrs at which time I stopped the GPR acquisition phase of the experiment.

At 48 hrs after injection, the SZ reflection is significantly higher amplitude than in the pre-injection data (Figures 6 and 7). The water table, as measured in the monitoring well, rose 5.0 cm during this time. The added volume of pore fluid required to raise water table by 5 cm is 24 liters which is greater than the total amount of DNAPL added to the system. I interpret these observations as indicating a partial collapse of the capillary fringe as DNAPL accumulated transition from vadose zone to SZ .

The top-of-DNAPL pool reflection is at approximately the same depth as the top of the gravel layer, but has opposite polarity. The polarity reversal occurs because the upper saturated sand/gravel interface is a negative impedance contrast due to the higher water content of the gravel while the top of the DNAPL pool is a positive impedance contrast due to the low permittivity of the DNAPL rich zone. The DNAPL reflection was evident 30 min after the injection and did not change significantly in character throughout the remainder of the experiment. The high amplitude DNAPL reflection masks the reflections from the top and bottom of the gravel layer because of the ~400-500% increase in amplitude coupled with decreased resolution due to a longer wavelength in the high velocity DNAPL pool. Asymmetry of the DNAPL reflection and a dramatic shift of the underlying clay reflection in the post injection data suggest a non-uniform DNAPL distribution (Figures 4 and 6). PSDM sections along Line 4 are consistent with the above observations and much of the clay reflection distortion is removed, although there appears to be a slight misplacement on the right side of the profile (Figure 7). Comparison of the pre and post injection reflection tomography models show generally similar velocity structure with the exception of the large velocity increase associated with the DNAPL pool near the base of the tank. Rearranging Equation 2, and using the average measured DNAPL pool velocity of 8.3 cm/ns, I estimate the pooled DNAPL saturation at 0.39. This is in good agreement with the measured saturation of 0.37 in a soil sample extracted from the pooled zone. Minor increases in velocity are found in the saturated zone above the gravel layer that are likely related to residual DNAPL contamination. However, the magnitude of the measured velocity increase is lower than expected. Soil sample analysis reveals a residual saturation of around 14% in both the vadose and saturated zones. This is consistent with vadose zone measurements in TDR Probe 2 and should lead to a velocity increase of around 16%. The results of transmission tomography are similar, but the vertical resolution is not as good as the reflection tomography models because reflector positions are used to constrain the reflection tomography. However transmission tomography reveals a significant increase in velocity around the injection point. Apparently the reflection tomography lacked the lateral resolution to detect this velocity increase. The small aperture of the experiment decreases the velocity resolution of the surface data, and with greater aperture the analysis could reveal more subtle details. Nevertheless, the primary DNAPL pool is clearly delineated, and both reflection tomography and transmission tomography measure similar velocity distributions.

For analysis of the ODR response I focus on the top-of-DNAPL reflection (Figure 9). In the absence of significant differences in the overburden, dividing the DNAPL reflection amplitudes by the pre-injection, top-of-gravel amplitudes will approximately cancel the radiation pattern and attenuation contributions to the amplitudes. These are difficult parameters to measure directly from the data, and the following observations indicate that this is a reasonable approach. Both

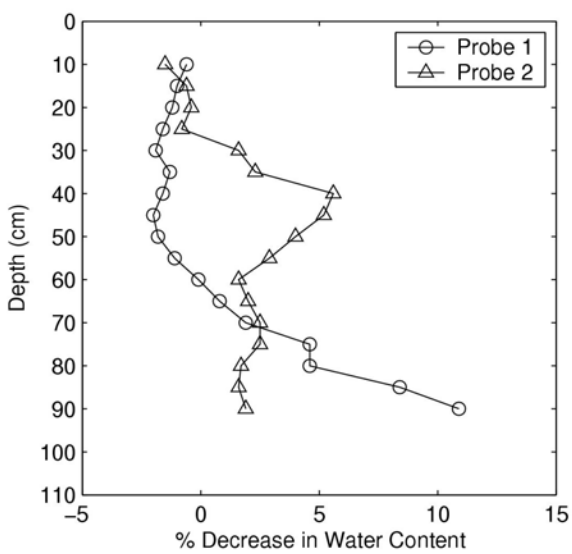

Figure 5. . The change in water content 48 hr after the injection as measured with the downhole TDR probes. The decrease in water content is approximately equal to the increase DNAPL concentration. Probe 2, near the injection point, shows a large vadose zone DNAPL concentration, but a deeper pool is not observed at this location. At Probe 1, little change is observed in the vadose zone, but deep pool development is evident.

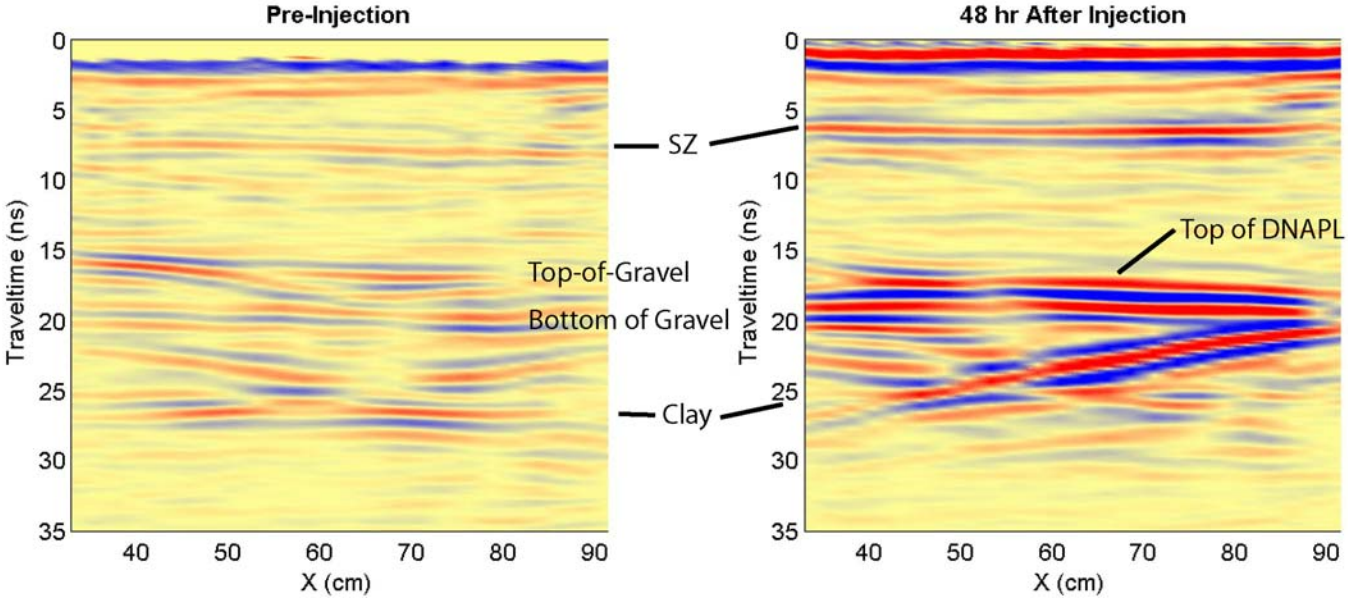

Figure 6. . Unmigrated stacks before and after the injection. The plots have the same amplitude scaling for comparison. 48 hr after the injection, the DNAPL has formed a pool within the gravel layer. Note the significant distortion of the clay reflection due to asymmetric distribution of the DNAPL. Also the saturated zone reflection is higher amplitude and shallower after the injection.

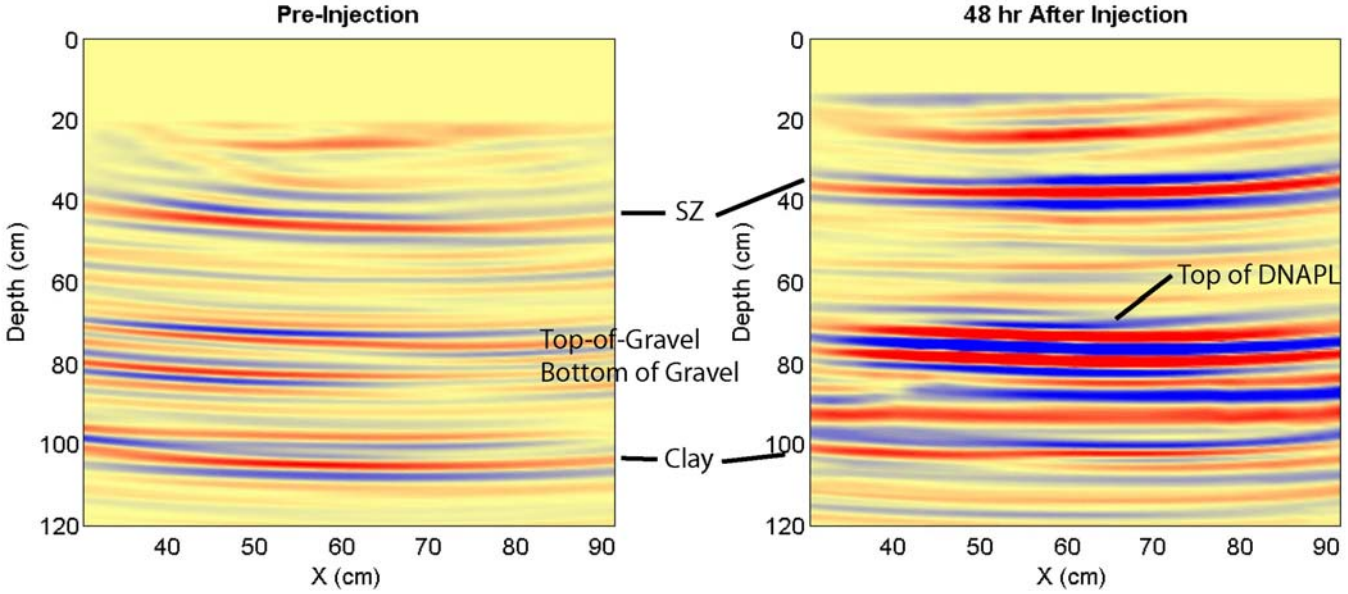

Figure 7. . PSDM images before and after the DNAPL injection. Amplitude scaling of the two plots is the same for comparison. The clay reflection has been migrated to the approximate spatial position using the reflection tomography models in Figure 8, although the distortion in the post injection data has not been completely eliminated. The gravel layer is not well resolved after formation of the DNAPL pool due to the velocity increase (leading to a longer wavelength) and masking by the high amplitude DNAPL reflection.

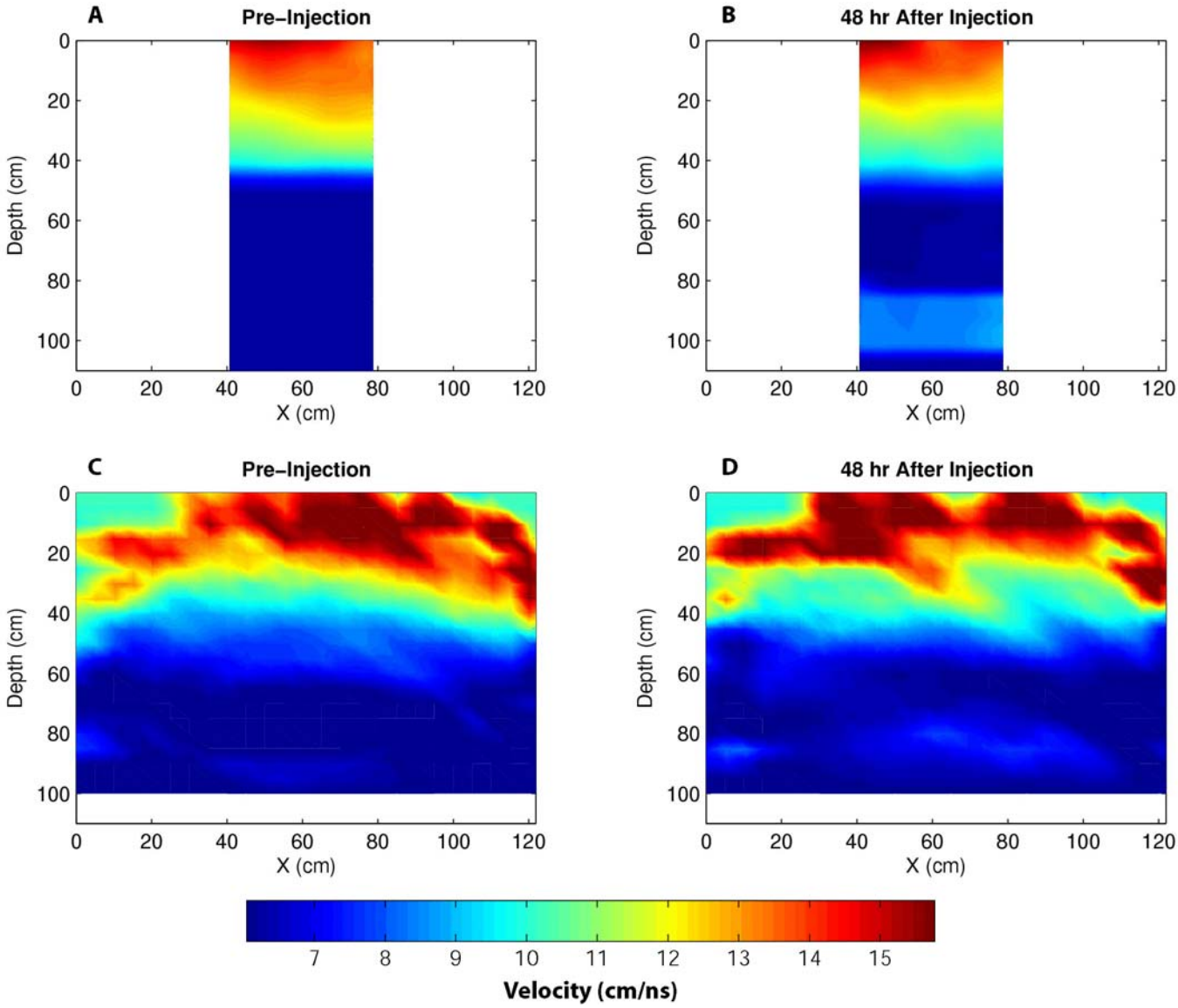

Figure 8. . Pre and post injection velocity models along Line 4 derived through reflection tomography of surface data (A & B), and transmission tomography of transmission data (C & D). Surface data coverage is limited to the center of the tank while transmission data cover the full width. Both methods measure similar velocity distribution, with a comparable increase in velocity within the pooled DNAPL zone. Only transmission tomography measures a significant velocity increase in the vadose zone near the injection point. Both methods measure slight velocity increases associated with residual saturation above the DNAPL pool in the saturated zone.

the TM and TE models show a nearly 500% increase in near offset amplitude for the DNAPL reflection relative to the gravel reflection (Figure 9). This is consistent with the increase in the reflection coefficient computed for a simple half space reflection using the velocity derived through PSDM analysis for the DNAPL pool and lab measured values for the water saturated sand and gravel (Figure 10). In the TE data, both the gravel and DNAPL reflections show a slight decay of amplitude with increasing angle of incidence and the amplitude ratio shows very little relative variation which is consistent with the half space model. Additionally, this observation indicates that the assumption of no significant changes in the radiation pattern

or overburden attenuation is reasonable. The TM ODR curves provide a significantly different picture. There

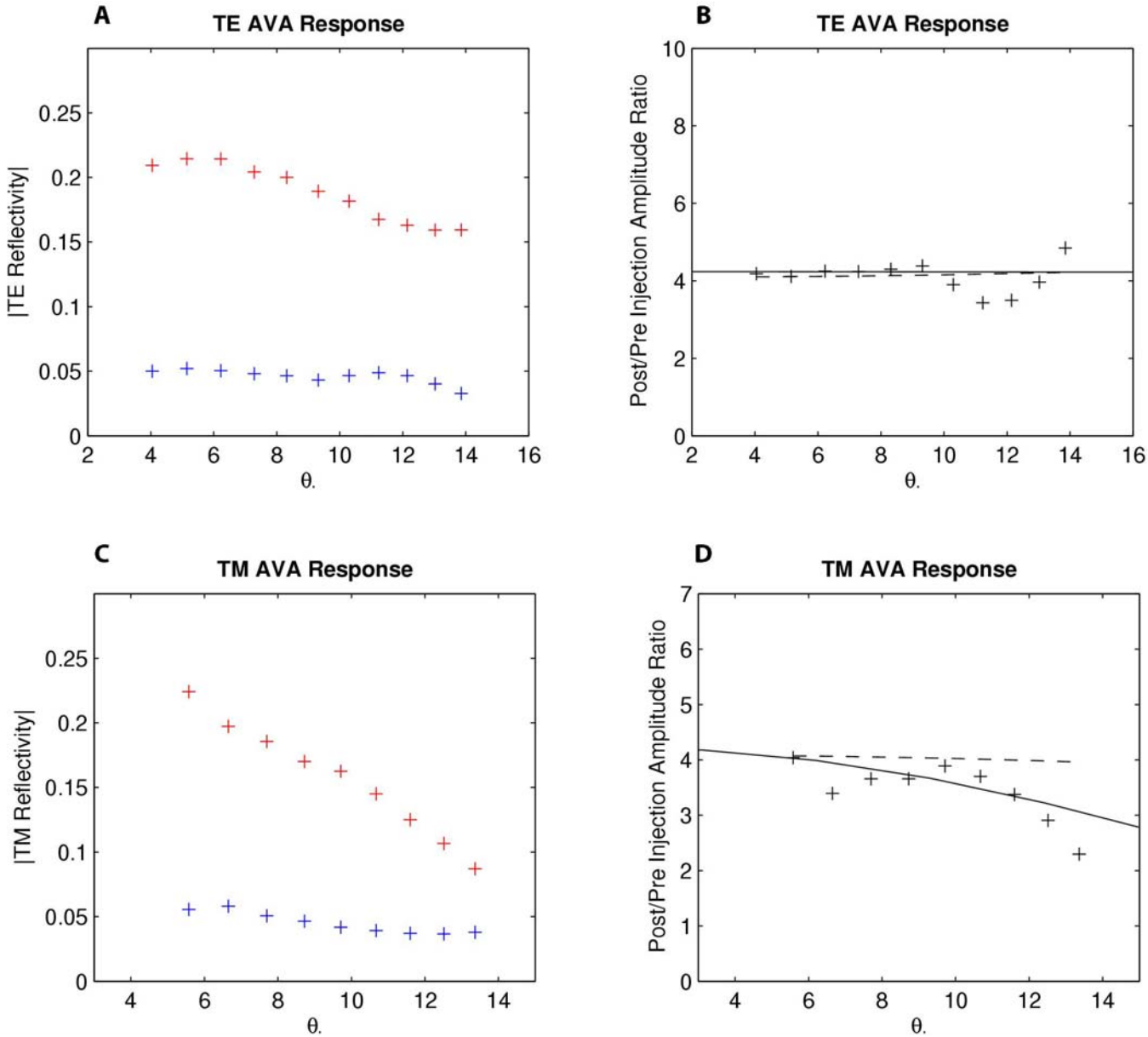

Figure 9. . AVA response for the top of gravel reflection (+), and the top of DNAPL pool reflection (+). There is a well developed trend in the TM data. A simple half space model (dashed line) does not agree well with the measured amplitude ratios (+). A model that includes a 5.5 mm thick layer of near 100 % DNAPL saturation at the top of the pool (solid line) agrees with the observed trend.

is a well developed trend in the top-of-DNAPL reflection showing significant amplitude decay with increasing angle-of-incidence. This is in contrast to the top-of-gravel curve which decays very little. The simple boundary model, over this range of angles, predicts little variation in either ODR curve, similar to what is observed in the TE mode. In fact, the TE and TM observations cannot be explained using a simple half-space model. However, I can reproduce the observed trend with a thin bed model. Using the analytical solution for a three layer model (King and Owens, 1992) and the method described by Deeds (2002) to compute the frequency dependent reflection coefficients for a broadband signal, I calculate that a 5.5 mm thick, 98% DNAPL saturation zone at the top of the primary DNAPL pool produces an amplitude response that is consistent with both the TE and TM ODR curves (Figures 9 and 10). This requires decreasing the velocity in the primary DNAPL pool by 10% (S_{DNAPL}=0.27) which is close to the maximum value computed

using the transmission tomography velocity model (S_{DNAPL}=0.29).

Conclusions

Using detailed surface GPR velocity analysis, including reflection tomography, I constructed a detailed velocity distribution both prior to, and 48 hr after the injection of 20 liters of a chlorinated solvent solution into a small test tank. I found an average 33% increase in velocity associated with a DNAPL pool that formed near the bottom of the tank. Using the CRIM equation, I estimated that 39% DNAPL saturation was required to cause this velocity increase. The DNAPL saturation measured in the pooled area during post injection chemical sampling was 37%. This suggests that these methods can be used to make accurate, quantitative estimates of subsurface electrical properties, and that relatively simple petrophysical models can, in some cases, be used to estimate fluid concentrations. The results in the residually saturated vadose and saturated zones were not as favorable. Although I did measure a slight increase in velocity, the value was significantly lower than that which was measured with TDR probes or which is predicted considering the 14% residual saturation measured in soil samples. The limited aperture of the experiment limited the velocity

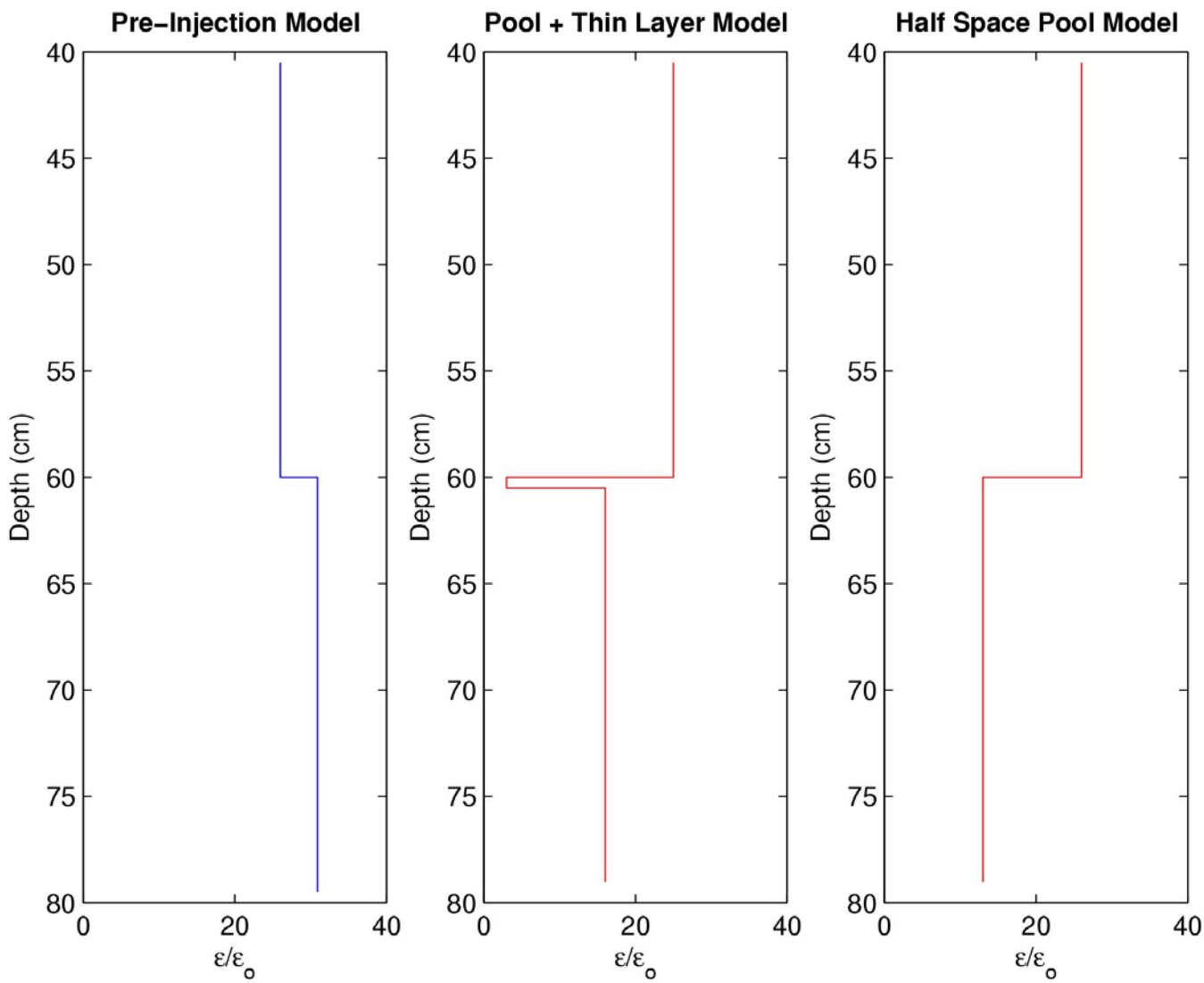

Figure 10. . Different permittivity models used in ODR analysis. The thin bed model produces a trend similar to what I observed in the data, while the simple half space model is not consistent with the data.

resolution, and with greater aperture, one could expect to measure more subtle velocity variations.

Using thin bed analysis, I found that a DNAPL pool model (S_{DNAPL}=0.27) with a 5.5 mm thick zone of 98% DNAPL saturation along the upper boundary produces an ODR response consistent with both the TE and TM data. Unfortunately, I could confirm or reject the presence of the thin, high DNAPL saturation zone through direct sampling. Multi-phase fluid flow modeling may provide some additional insight as to the viability of this interpretation, but has not yet been completed. As with previous field studies, I found that combined analysis of the TE and TM data was necessary to produce a consistent subsurface model. The results suggest that ODR analysis has significant potential to reveal subsurface details that are not resolved with conventional imaging methods or velocity analysis alone.

Acknowledgments

The US Department of Energy funded this work under the EMSP Groundwater/Vadose Zone Integration Project, Grant # DE-FG07-99ER15008. I would like to thank Mark Nell for helping construct the experiment and collect the data.

References

Annan, A.P., 1996, Transmission dispersion and GPR: J. Env. Eng. Geophys., **0**, 125-136.

Baker, G.S., 1998, Applying AVO analysis to GPR data: Geophys. Res. Let., **25**, 397-400.

Bergmann, T., Robertsson, J.O.A., and Holliger, K., 1998, Finite-difference modeling of electromagnetic wave propagation in dispersive and attenuating media: Geophysics, **63**, 856-867.

Bradford, J.H., 1998, Characterizing shallow aquifers with wave-propagation based geophysical techniques: Imaging and attribute analysis: Ph. D. thesis, Rice University.

Bradford, J.H., 2003a, GPR offset-dependent reflectivity analysis for characterization of a high-conductivity LNAPL plume: SAGEEP 2003 Symposium on the Application of Geophysics to Environmental and Engineering Problems, Env. Eng. Geophys. Soc., 238-252.

Bradford, J.H., 2003b, Using GPR to estimate water content at the Hanford Site: Acquisition and Processing Methodologies: 2003 GSA Ann. Mtg., Geol. Soc. Amer., GSA Abstracts with Programs.

Brewster, M.L., and Annan, A.P., 1994, Ground-penetrating radar monitoring of a controlled DNAPL release: 200 MHz radar: Geophysics, **59**, 1211-1221.

Deeds, J.C., 2002, Amplitude variation with offset (AVO) of ground penetrating radar data for detection of non-aqueous phase liquids: M.S. thesis, University of Wyoming.

Deeds, J.C., and Bradford, J.H., 2002, Characterization of an aquitard and direct detection of LNAPL at Hill Air Force Base using GPR AVO and migration velocity analysis: GPR 2002, Ninth International Conference on Ground Penetrating Radar, Intl. Soc. for Optl. Eng., Proceedings, 323-329.

Fisher, E., McMechan, G.A., and Annan, A.P., 1992a, Acquisition and processing of wide-aperture ground-penetrating radar data: Geophysics, **57**, 495-504.

Fisher, E., McMechan, G.A., Annan, A.P., and Cosway, S.W., 1992b, Examples of reverse-time migration of single channel ground-penetrating radar profiles: Geophysics, **57**, 577-586.

Greaves, R.J., Lesmes, D.P., Lee, J.M., and Toksoz, M.N., 1996, Velocity variation and water content estimated from multi-offset, ground-penetrating radar: Geophysics, **61**, 683-695.

King, R.W.P., and Owens, M., 1992, Lateral electromagetic waves: Theory and Applications to communications, geophysical exploration, and remote sensing, Springer-Verlag New York Inc.

Kueper, B.H., Redman, D., Starr, R.C., Reitsma, S., and Mah, M., 1993, A field experiment to study the

behavior of tetrachloroethylene below the water table: Spatial distribution of residual and pooled DNAPL: Ground Water, **31**, 756-766.

Lehmann, F., 1996, Fresnel equations for reflection and transmission at boundaries between conductive media, with applications to georadar problems: GPR '96 6th International Conference on Ground-Penetrating Radar, Intl. Soc. Opt. Eng., Proceedings, 555-560.

Loughridge, J., 1998, Application of seismic tools and techniques to ground-penetrating radar (GPR) studies: M.A. thesis, Rice University.

Newmark, R.L., Daily, W.D., Kyle, K.R., and Ramirez, A.L., 1998, Monitoring DNAPL pumping using integrated geophysical techniques: J. Env. Eng. Geophys., **3**, 7-13.

Powers, M.H., and Olhoeft, G.R., 1996, Modeling the response of leaking, buried pipes: SAGEEP '95 Symposium on the Application of Geophysics to Environmental and Engineering Problems, Soc. Appl. Geophys. Env. Eng., Proceedings, 525-534.

Redman, J.D., and DeRyck, S.M., 1994, Monitoring non-aqueous phase liquids in the subsurface with multilevel time domain reflectometry probes: Proceedings of the symposium and workshop on time domain reflectometry in environmental, infrastructure and mining applications, United States Bureau of Mines, Special Publication, 207 - 214.

Stork, C., 1992, Reflection tomography in the postmigrated domain: Geophysics, **57**, 680-692.

Yilmaz, O., 2001, Seismic data analysis, Soc. Expl. Geophys.

Zeng, X., McMechan, G.A., and Xu, T., 2000, Synthesis of amplitude versus offset variations in ground-penetrating radar data: Geophysics, **65**, 113-125.

APPENDIX F: COMPLETE TECHNICAL REPORT OF GPR EXPLORATION ACTIVITIES AT HILL AIR FORCE BASE

1. Introduction

This report summarizes field activities for the GPR work component detailed in "Source Zone Remediation Design Data Collection For OU-1, Hill Air Force Base, Utah: Task 1 - GPR Site Investigation". Proposed work for this project included a two phase field effort with a division of work as follows:

- Phase 1: Acquisition and analysis of 50,000 linear ft of common offset GPR data covering approximately 1,000,000 sq ft in the vicinity of the OU1 source zone. Primary objectives were imaging the upper surface of the Alpine clay aquitard, constructing a detailed map of the clay surface based on the GPR data analysis, identifying areas not suitable for GPR investigation, and identifying topographic or GPR reflectivity anomalies for more detailed investigation in the second phase of the GPR investigation.
- Phase 2: Acquisition and analysis of 4,000 linear ft of targeted, dense, multi-offset GPR data. This field effort had two primary objectives: 1) to investigate anomalies found in Phase 1 for detection of NAPL rich zones, and 2) to use noise reduction benefits of multi-offset data acquisition and processing to improve the image of the clay surface in high-noise areas.

2. Background

2.1. Principles of GPR Investigation

In GPR studies, an oscillating electric field is transmitted into the earth and is reflected at boundaries separating materials with differing electric properties (dielectric permittivity, magnetic permeability, and conductivity). The reflected wavefield is recorded and used to produce a subsurface representation similar to a cross-section of the earth. For most earth materials in which the GPR signal will propagate efficiently, the magnetic permeability is roughly constant and the conductivity is low, so we primarily image contrasts in dielectric permittivity. Conductivity controls attenuation of electromagnetic waves, with signal attenuation increasing with increasing conductivity. Conductivity is the primary parameter controlling the success of GPR studies, with

essentially no signal penetration in highly conductive soils. Clays are typically relatively good conductors whereas sandy, coarse grained materials have relatively low conductivity and generally provide a suitable sedimentary environment for GPR investigation. High conductivity materials in the earth such as a clay aquitard, metal objects, or highly mineralized ground water, produce a strong reflection at the upper boundary, but also act as a barrier to GPR signal penetration.

GPR operates in the frequency band from 10 MHZ - 1 GHZ, with a peak frequency of 50 - 225 MHZ typical for groundwater studies. Lower frequencies correspond to greater depth of penetration and lower resolution whereas high frequencies correlate with shallow penetration at higher resolution. Velocities in dry and water saturated sands are on the order of 0.15 m/ns and 0.05 m/ns respectively. Thus we can expect to resolve features on the order of 10 - 40 cm in the water saturated zone and 30 - 120 cm in the vadose zone. Depth of penetration varies from ~ 0 m under the worst conditions to as much as 50 m under ideal conditions. The best results in GPR studies are obtained in dry sandy environments (low conductivity), but excellent results have been obtained with variable sediment composition and well below the water saturated zone (Haeni, 1996; Loughridge, 1998).

2.2. Multi-offset vs. Common-offset Data Acquisition and Velocity Estimation

Most GPR surveys are acquired with a constant transmitter-receiver offset (bi-static mode) and little or no processing is employed in generating the final image. This can provide useful information and is valuable as a rapid reconnaissance tool. However, as the complexity of the EM velocity structure increases, the ability to produce useful images using this simple acquisition geometry diminishes. EM velocity estimates cannot be made from common-offset data, therefore reflector depth estimates must be based on rough guesses of material velocity or correlation of interpreted reflectors with known material boundaries.

In multi-offset data acquisition, several traces are recorded at various source-receiver separations at each point along the survey, as opposed to a single trace at each point for a constant-offset survey. The data are typically sorted into common-midpoint (CMP) gathers which contain

traces representing several transmitter-receiver offsets with coincident transmitter-receiver midpoint. Multi-offset acquisition, while more labor intensive and time consuming, significantly improves our ability to accurately predict the subsurface. This improvement arises from three primary features;

1) Multi-offset data provide traveltime vs. offset curves, which enable one to estimate propagation velocity. Velocity estimation is necessary for making depth estimates and is used to estimate electric permittivity, an important material property in NAPL detection.

2) Dramatic attenuation of random noise and/or coherent noise such as scatter from surface objects is achieved through a process known as stacking. To produce a stacked image, all reflected events are shifted to their equivalent zero-offset traveltime by applying a normal-moveout (NMO) correction, which in effect flattens the travel time curve of a given reflector. All traces in the CMP are then vertically summed to produce a stacked trace. Coherent or flattened reflections stack constructively, while noise events are attenuated. A profile of stacked traces is analogous to the common-offset profile, but with significantly reduced noise levels. This type of processing can lead to dramatically improved image quality and therefore improve our ability to predict the subsurface.

3) Multi-offset data acquisition allows one to observe reflected wave behavior for various travel paths and angles of incidence at a common reflection point . Quantification of this behavior can be a valuable tool in material property estimation.

One of the most valuable material properties that can be extracted from GPR data is EM propagation velocity which leads directly to estimates of effective permittivity (Griffiths, 1989). It is typical to acquire a single CMP gather within a broader survey area to obtain a 1-D velocity structure for interpreting a bi-static survey. An RMS velocity is estimated for each reflection using normal moveout analysis (Bradford et al., 1996; Campbell et al., 1995; Young and Sun, 1996). Typically, the RMS velocity structure is used to estimate effective interval velocities using Dix inversion. There are two primary problems associated with this methodology. First, the 1-D

velocity estimate does not account for lateral velocity (or equivalently, dielectric permittivity) heterogeneity. This results in significant problems for advanced velocity dependent processing methodologies such as migration. More importantly for purposes of this proposal, 1-D velocity analysis does not allow one to identify lateral velocity variation that may be associated with NAPL rich sediments.

The second problem, which requires significantly greater processing sophistication to treat properly, is that the underlying assumptions of NMO velocity analysis and Dix inversion are often violated within the zone of GPR investigation. A fundamental assumption of NMO velocity analysis/Dix inversion is that vertical and horizontal velocity gradients are relatively small resulting in an approximately straight ray path (Dix, 1955). It is typical for velocities in the GPR zone of investigation to decrease by a factor three or more as the sediments grade from dry to fully water saturated. This results in severe departure from normal moveout and leads to very large overestimates of interval velocity. We refer to the amount of overestimate as NMO bias. NMO bias is a complicated function that depends on velocity heterogeneity in the overburden, maximum and minimum transmitter-receiver offset, and the thickness of all layers through which the signal propagates.

When conventional velocity analysis fails, we must resort to more sophisticated methods. A number of these methods have been developed for seismic reflection data such as pre-stack depth migration (PSDM) velocity analysis (Lafond and Levander, 1993) or travel time inversion (Zelt and Smith, 1992). Inverse methods can provide an accurate description of the gross velocity structure, but lack detail since only a few key interfaces are used in the analysis. PSDM is the most accurate and detailed imaging method available. In a complex subsurface setting, PSDM focuses scattered energy and moves dipping events to the correct location. PSDM treats severe lateral and vertical velocity gradients correctly, which cannot be done with the post-stack migration methods typically applied.

2.3. Principles of NAPL Detection with GPR

The relative dielectric permittivity (K) and conductivity (σ) depend strongly on material type. The amplitude of a GPR reflection is dependent on the contrast of permittivity and conductivity at material boundaries, and attenuation of the signal is dependent on the conductivity of the material through which the signal is propagating (Davis and Annan, 1989). Water has very high permittivity (K~80), whereas common NAPLs such as light hydrocarbons and chlorinated solvents have very low permittivity (K~2) and are very poor conductors. Most dry earth materials, through which the GPR signal will propagate efficiently, have relatively low permittivity (4 - 16) so that introduction of water into the pore space results in a significant increase in bulk permittivity of the three phase system (air, water, earth material). Additionally, the presence of water can significantly increase bulk conductivity, particularly in the presence of clay.

Anomalous displacement of naturally occurring water with low permittivity NAPL leads to lower bulk permittivity and conductivity than the surrounding sediments. The amount of the contrast depends on the wetting phase and relative concentrations of water and NAPL. Several modeling and laboratory studies have illustrated that when the organic is the wetting phase, the conductivity and dielectric permittivity drop sharply with very low concentrations of NAPL, whereas the change is more gradual when water is the wetting phase (Endres and Redman, 1996; Santamarina and Fam, 1997). In a cross-well ERT field study, Newmark et. al.(1998) recorded significant decreases in conductivity associated with pooled and residual TCE in water wet sediments at Hill, AFB, Utah. We expect a significant decrease in dielectric permittivity to correlate with the decrease in conductivity.

We expect the GPR signature associated with the presence of NAPL to be manifest in essentially three ways. First, the decrease in dielectric permittivity results in increased EM propagation velocity. Secondly, the decrease in permittivity can significantly change reflectivity. If the NAPL is in a discreet pool or plume, we expect increased reflectivity or variations in the AVO response associated with the NAPL boundaries. If the NAPL is smeared vertically or has diffuse boundaries, as is the case for residual saturation, we may observe decreased reflectivity in the sediment column due to homogenization of the permittivity profile. This occurs because decreased bulk water content reduces porosity dependence (Olhoeft, 1986). Finally, the decrease in

conductivity leads to decreased levels of signal attenuation.

Our approach to NAPL detection with GPR is to combine detailed velocity analysis and imaging with reflected waveform attribute analysis to produce detailed, quantitative subsurface images and material property maps that can be used to predict the location of subsurface contaminants.

2.4. History of GPR Investigation at OU-1

Young and Sun (1996) reported the results of a 20,000 sq. ft. GPR survey acquired just north of CDP 1. The data were of excellent quality, providing a good image of both the contact between the Provo alluvium/Alpine clay contact and the major stratigraphic boundaries within the alluvium. The data were acquired primarily in common offset mode, with some sparse multi-offset sampling for course velocity control. Based only on NMO velocity analysis at a few locations, Young and Sun concluded that the presence of NAPL would not introduce sufficient contrast in electrical properties for detection using GPR.

Although Young and Sun conducted a quality survey and achieved excellent results, their conclusion that NAPL detection potential was low was based on an incorrect assumption about the information provided by NMO velocity analysis. Namely that NMO velocity analysis provides a good estimate of actual propagation velocity which, for the reasons discussed in the previous section, is incorrect.

Based on the excellent data quality presented by Young and Sun, and on the recognition that their conclusions concerning NAPL detection potential were likely incorrect, we chose OU-1 at Hill AFB for a NAPL detection feasibility study. In August of 1999 we acquired two 2-D, multi-offset surveys at OU-1. The first was oriented north-south and crossed the western edge of CDP 1. The second was located approximately 350 ft west of CDP 1, was oriented northeast-southwest, and spanned the northern boundary of the LNAPL plume. This study provided several significant insights. First, while overall, GPR data quality was good, there was significant variability within

OU-1. This ranged from excellent north and south of CDP 1, to extremely poor directly over CDP 1, to poor but adequate along the western line. Second, we found that there was significantly greater radar velocity heterogeneity than was assumed by Young and Sun. Additionally, we identified an anomaly just northwest of CDP 1 as a potential NAPL source that was previously unidentified.

Based on the results of our feasibility study, we conducted a research scale, 3-D, multi-offset GPR survey in October, 2000. Survey parameters were designed to target the anomaly identified in the feasibility study. The survey covered 32,000 sq. ft. and produced an excellent quality dataset with resolution on the order of 1 - 2 ft vertically and 2 - 4 ft horizontally. From these data, we identified a topographic low on the clay surface. Using PSDM velocity analysis we found a zone of anomalously high radar velocity just above the low in the clay surface. Thus, we have identified both a stratigraphic trap and physical properties consistent with a NAPL rich zone. This interpretation was verified in a subsequent soil sampling and NAPL characterization study (Appendix B) where NAPL saturation up to 4% was found within the anomalous zone.

In addition to the 3-D survey, nine 2-D common-offset profiles were acquired to evaluate data quality variations in large area west of CDPs 1 and 2 spanning most of the free LNAPL plume as currently mapped. We conclude that data quality is generally good in the area. The old artificial cap that is present over much of the site has an adverse effect on data quality due to increased surface conductivity associated with the higher clay fraction. However, the data quality in these areas is adequate for identifying the Alpine clay/Provo alluvium contact. Very poor data quality is found directly over CDPs 1 and 2 as currently mapped and data acquired in these areas is of limited value. The reason for this is not well understood, but is likely related to increased electric conductivity of artificial fill material or to buried metal debris. Where the old cap is not present, both immediately adjacent to the CDPs and elsewhere, the data quality is excellent.

3. Completed Objectives

Between May 6 and May 19, 2002, a total of 62,622 linear ft of common offset GPR data were acquired exceeding the specification in the original workplan by over 25% (Figure 1). These data have been interpreted, cross checked with available control points, and gridded to produce a detailed map of the clay surface topography at OU-1 (Figure 2). Additionally, topographic and reflectivity anomalies were identified for detailed multi-offset GPR data acquisition and analysis. Between June 10 and June 15, 2002 4,000 linear ft of targeted multi-offset GPR data were acquired. Detailed processing was applied to these data with an emphasis on noise reduction and velocity analysis to identify electric property anomalies potentially associated with NAPL contamination. Improved clay surface interpretations from the multi-offset data were incorporated into the the site aquitard map, and locations considered likely to hold NAPL contaminated zones were passed on to personnel from INTERA, Inc. This information was subsequently incorporated into the site coring plan.

4. Phase 1

4.1. Data Acquisition Parameters and Survey Design

Data were acquired with a Sensors and Software Pulse Ekko100A system using 50 MHz antennas, a 1.6 ns sampling rate and 400 ns total recording time. Traces were recorded at 1ft increments along 87 profiles.

The original work plan called for GPR data acquisition within a 1,000,000 sq ft area (Figure 1) however access to the western portion of this area was limited as it lies within the restricted flight line area. Prior to GPR data acquisition a survey grid was established outside the restricted area with 100 ft grid nodes coincident with the Utah State plane coordinate system. Within the survey grid, 49 north-south profiles were acquired with a 25 ft spacing between profiles, and every fourth profile coincident with 100 ft grid nodes. Additionally, 12 east-west profiles were acquired along lines defined by 100 ft grid nodes. An additional 12 profiles were collected within the restricted flight line area. These profiles were parallel and separated by 25 ft in the east west direction. Orientation of the flight line profiles followed the trend of the access control fence. The survey area was also extended northwest of the survey grid with acquisition of fourteen 300 ft profiles. Seven of these

profiles were oriented east west along 50 ft centers, and seven oriented northwest/southeast along 50 centers.

Subsequent to data acquisition, we attempted to survey coordinates at 100 ft nodes for all lines outside the established survey grid. SVERDUP arranged for use of the Hill AFB EMR GPS unit for this purpose. After surveying, the GPS data were processed for a differential correction by EMR personnel. Significant problems were encountered during this surveying effort. The GPS unit was apparently malfunctioning and only a few points could be established. These included the 12 100 ft line nodes just inside the flight line control fence, and the four southern and western most nodes. In the extended area to the north, four nodes on the eastern edge of the survey area were established. While suboptimal, the limited number of survey points, combined with our efforts to establish GPR profile positions relative to the survey grid, provide an estimated ± 5 ft accuracy in horizontal positioning in the areas outside the survey grid.

The survey covered the full area defined in the workplan and significantly extended the data coverage area to the north and west. With the exception of the newly constructed fence isolating the OU-1 capped area and the control fence for the flight line area, surface obstructions were minimal and allowed for relatively free movement around the site. Occasional deviation from the profile line was necessary to avoid well head casings, however this typically required less than a 3 ft deviation from the profile line. This is approximately ½ the signal wavelength which is below the lateral resolution of the signal in 2D mode and therefore not significant. Maneuvering around the fences required gaps in data coverage which are evident in the coverage map (Figure 1). We do not believe these gaps significantly alter our qualitative understanding of the geometry of the aquitard surface, but do prevent us from making definitive interpretations of depth to clay near the fences.

Perhaps more problematic is noise related to the power line that trends northwest/southeast across the site. Coherent noise from the power line prevented us from imaging the aquitard within 50 - 100 ft of the power line across most of the site. A second significant gap in data coverage is evident in the vicinity directly over and just south and west of CDPs 1 and 2. In these areas GPR data quality

is poor due to little to no subsurface signal penetration. This is caused by increased electric conductivity of the shallow subsurface in these areas. This was identified as a problem in previous work and was discussed in the proposal for this project. Previous GPR coverage was not adequate to delineate the boundaries of this high conductivity area, but the current survey clearly establishes these bounds (Figure 1) which was a secondary objective of the proposed work. The source of this increased conductivity is not clear. It may be due to buried metal debris, backfill with non-native clay rich material, or variations in the clay content of the old cap material. Variation in GPR response in locations covered by the old cap indicate significant variability in the clay content, however this is the only large area where the aquitard cannot be imaged. In any case this area is not suitable for GPR investigation. As discussed in the proposal for this work, electric resistivity or seismic reflection/refraction (as long as the site is fully dewatered) may be suitable geophysical alternatives for imaging the clay surface in this area, but the resolution potential will be significantly diminished relative to GPR.

4.2. Data Processing and Interpretation

All data were processed with the following sequence:

1) Time-zero delay correction
2) Dewow (high pass filter - to remove low frequency transient)
3) Automatic gain control
4) Low pass filter (1-4-70-140, to attenuate high frequency random noise)
5) F-X decon (Coherency filter)
6) Elevation statics
7) Depth conversion (assume constant velocity of 390 ft/μs)

Additionally, an F-K filter was applied locally to attenuate air velocity coherent noise related to scattering from surface objects (fences, powerline, pumphouse etc.)

Along most profiles the clay surface is easily identified as a high amplitude coherent event that is

subhorizontal and continuous across the entire profile. Exceptions occur when the clay surface dips below the water table in the deeper channels, and where the reflection is obscured by coherent noise. Where the surface lies below the water table, the amplitude decreases significantly due to increased signal attenuation in the water saturated sediments. However, in most locations the surface is relatively easy to identify (Figure 3). Where the reflection is obscured by surface scatter such as the fence reflection, it was often impossible to interpret depth to clay. As discussed previously, a significant region in the vicinity of CDPs 1 and 2 was not interpretable due to increased electric conductivity of the sediment column. These data regions are dominated by surface scatter (Figure 4).

The wavelength of the signal is approximately 8 - 10 ft, and due to processing distortions and velocity uncertainty, it is not clear which point on the reflected wavelet corresponds to the sand/clay interface. Since there are a large number of control points at the site, we can significantly improve the accuracy of our depth-to-clay estimate in the following way. We first identify a relative depth to the aquitard surface by picking an arbitrary, but easily identified, point on the wavelet reflected from the sand/clay interface. In this case, I picked the first large negative peak, and only made picks where I could identify the aquitard reflection to roughly an 80% confidence level. Estimating the confidence level is subjective and based on the previous experience at this site. Post-interpretation cross-checking with control points supports this interpretation strategy (see error analysis below). In this phase of processing it is most important that the same point on the reflection is picked consistently on all the profiles resulting in an accurate relative depth, while the absolute depth is later refined by comparison to available control. This is relatively straightforward where the clay reflection is well resolved. In some cases other reflections, such as that from the water table, interfere with the clay reflection. This decreases the resolution potential and we can do no better than the theoretical 1/4 wavelength resolution limit. Interpretation in these areas requires a level of subjective interpolation by the interpreter.

With all clay picks compiled, the surface is estimated on a uniform 5 ft grid using a linear 2d interpolation algorithm. This process gives a reasonable first pass estimate of the clay surface geometry. The computed surface is then compared to 87 control points that lie within the GPR

survey area. The control points are compiled from depth-to-clay picks from soil borings and CPT logs which were previously provided by Hill AFB EMR personnel. To adjust the GPR picks from the relative depth estimate to an absolute depth, data are first analyzed for a systematic deviation from the control points. This analysis indicates that the original depths interpreted from the GPR data were, on average, 1.94 ft lower than the control points. A DC shift of 1.94 ft was then applied to the GPR picks. With this correction applied, the standard deviation of the interpreted surface from the 87 control points is 2.09 ft. Note that this analysis includes 7 wells that are in poor data quality area where a reliable GPR pick could not be made. Excluding these 7 wells, the standard deviation is reduced to 1.70 ft and is a more realistic indicator of the precision of the GPR interpretation. Figure 5 shows the deviation from the control points. Wells that deviate from the interpreted surface by more than 3 ft are labeled. Note that all but two of these lie in areas where data quality was too poor to image the clay surface. The two exceptions are U1-857 and U1-149. I could make no reasonable resolution between the GPR and well data at these locations and suspect there may be some error in the log coordinates or logs themselves. Another notable deviation occurs at U1-882. The log indicates that there are two thin, shallow clays starting at around 23 ft and thick clay is not reached until about 5 - 6 ft deeper. The thin shallow clays have been used in the past as the top-of-aquitard, but the deeper clay better correlates with the GPR data so that is what I'm using for control at that point. Whether the shallow clays are lenses or laterally extensive may be important in understanding the significance of the deep channel to the south. I suspect they are lenses. Overall there is excellent correlation of the GPR data with the available control, and of course, the most accurate estimate of aquitard surface geometry will be made by combining the GPR interpretation with direct sampling data.

4.3. Discussion of Results

The data indicate three to four primary paleo-channel systems that appear to be hydraulically connected to the area around CDPs 1 and 2 (Figure 2). The deepest and most clearly connected of these channels trends west to southwest from the CDP area. Two shallower broad channel systems trend west to northwest. The northern most of these branches into a northeast trending depression. Overall there is a deepening of the aquitard toward the west which is consistent with previous

characterization results, but the aquitard surface is relatively complex which may have significant implications for contaminate transport and groundwater flow. At least four routes for transport away from OU-1 are evident with the significance of each route likely dependent on temporal water table fluctuations.

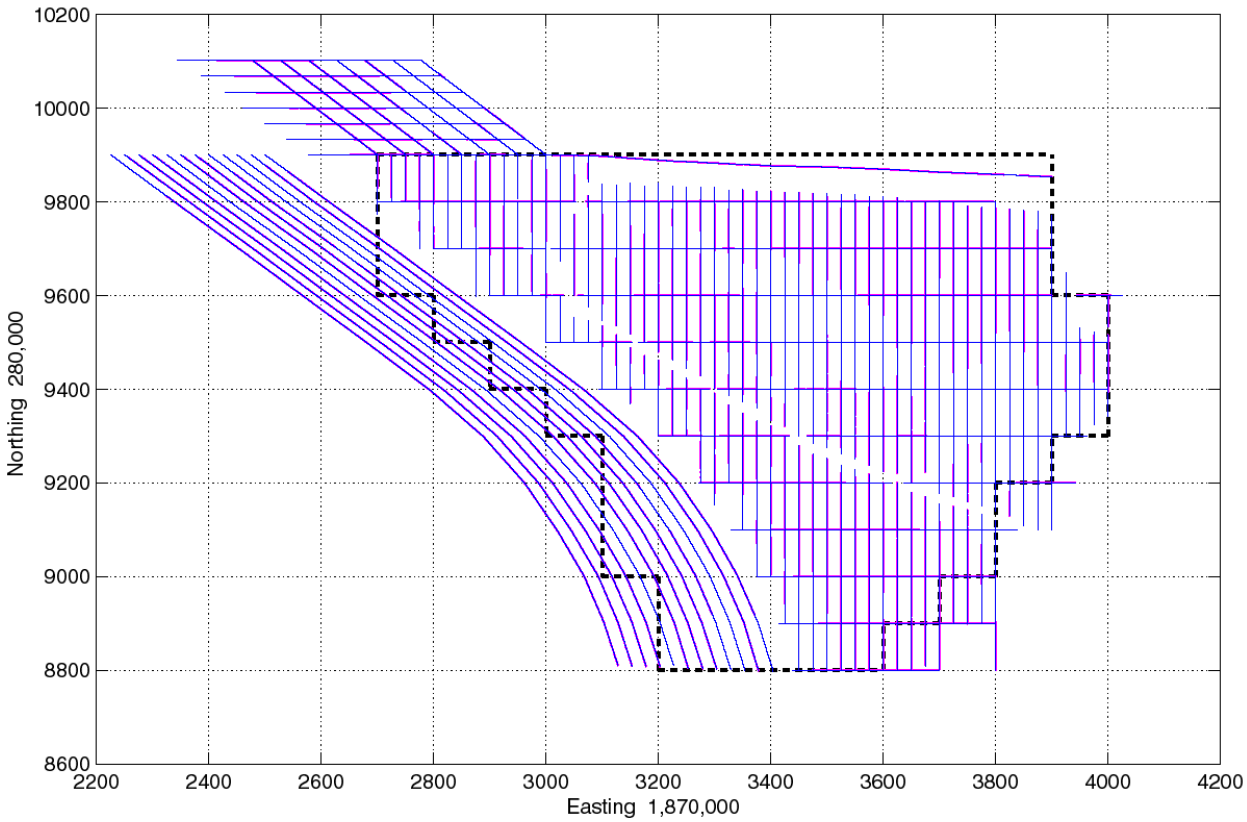

Figure 1. Map showing GPR survey area identified in the original workplan (dashed black line), GPR coverage (blue lines), and location of GPR picks (purple). Significant gaps in pick coverage are evident along the northwest trending line corresponding to the power line and in an area around CDPs 1 and 2. GPR coverage gaps are evident at fence locations.

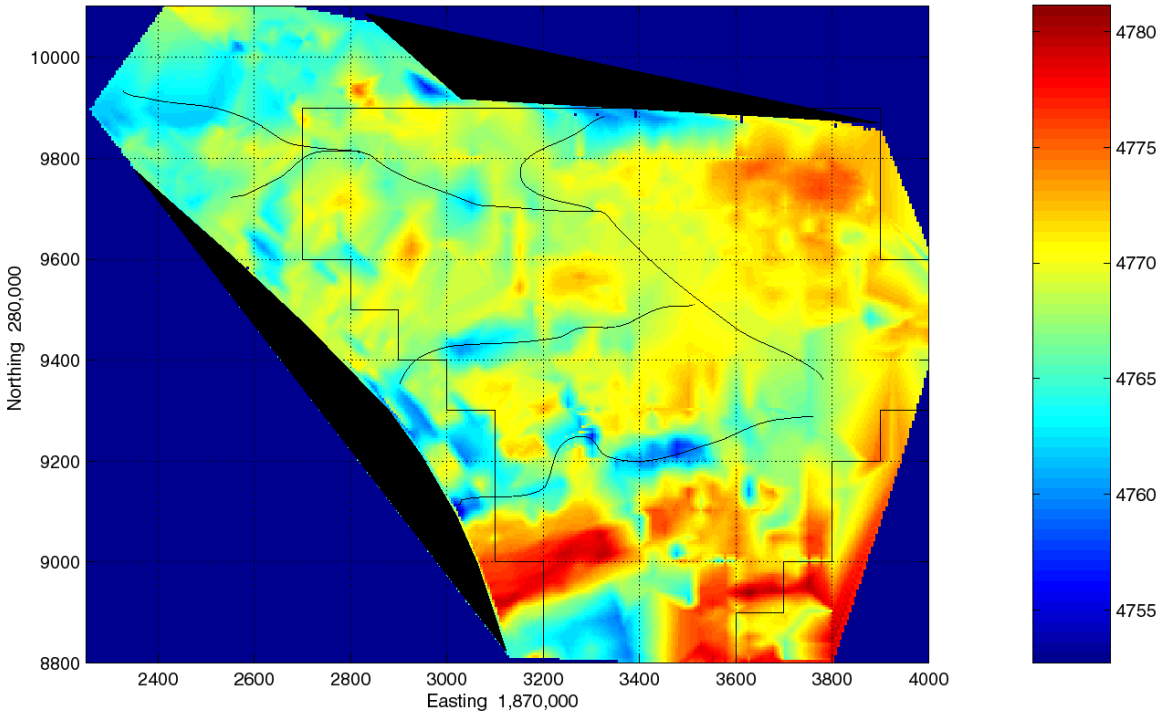

Figure 2. Clay surface elevation interpreted from GPR data. Black lines indicate significant paleo-channel systems. Standard deviation of this surface from the 87 control points located within the survey area is 2.09 ft. Standard deviation from the 80 control points located in areas of good GPR pick coverage is 1.70 ft.

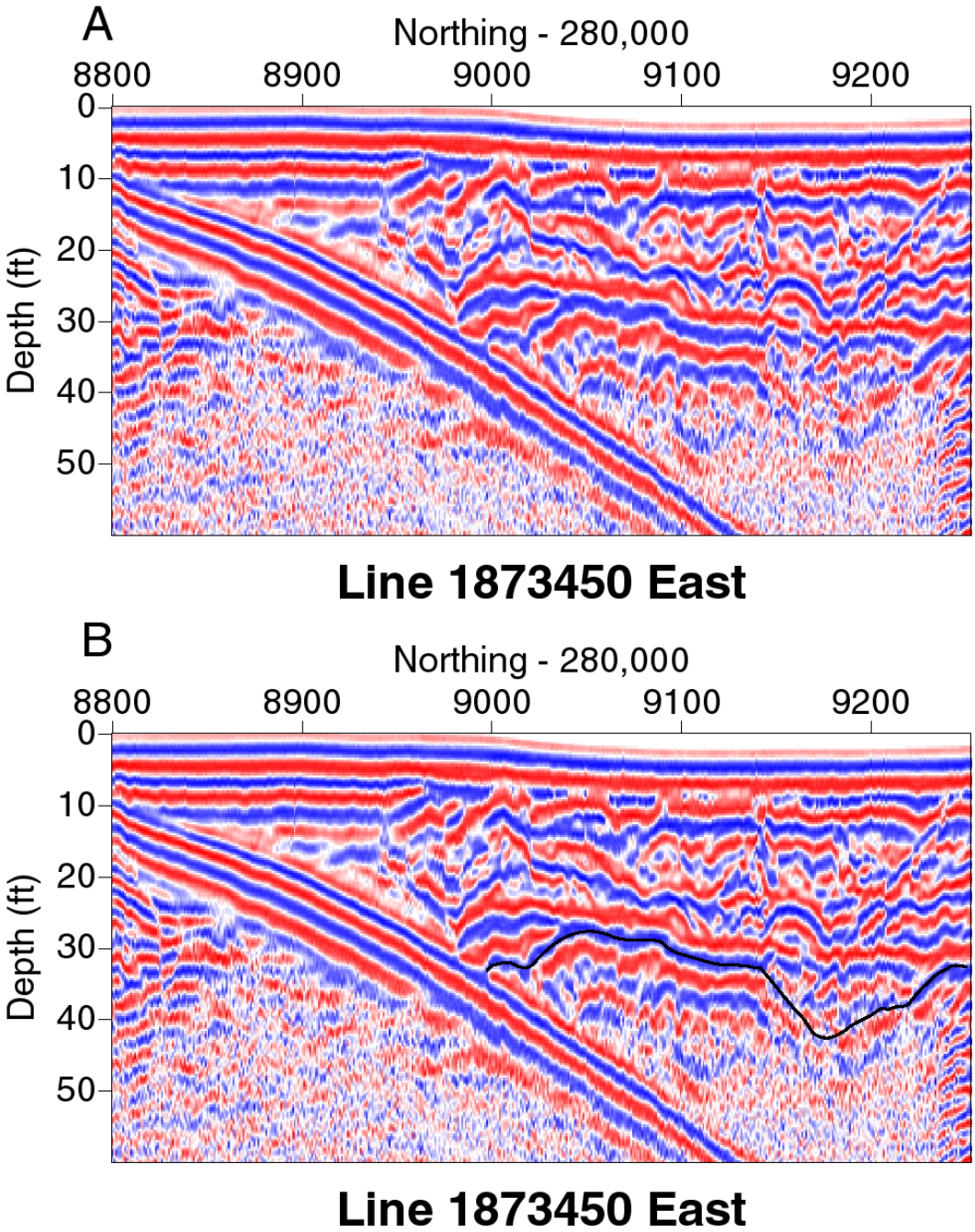

Figure 3. A) Uninterpreted and B) interpreted profile showing the deep west/southwest trending channel and high amplitude coherent noise (dipping from left to right) that is the reflection from the flight line access control fence. Interpreted clay surface is indicated with a black line.

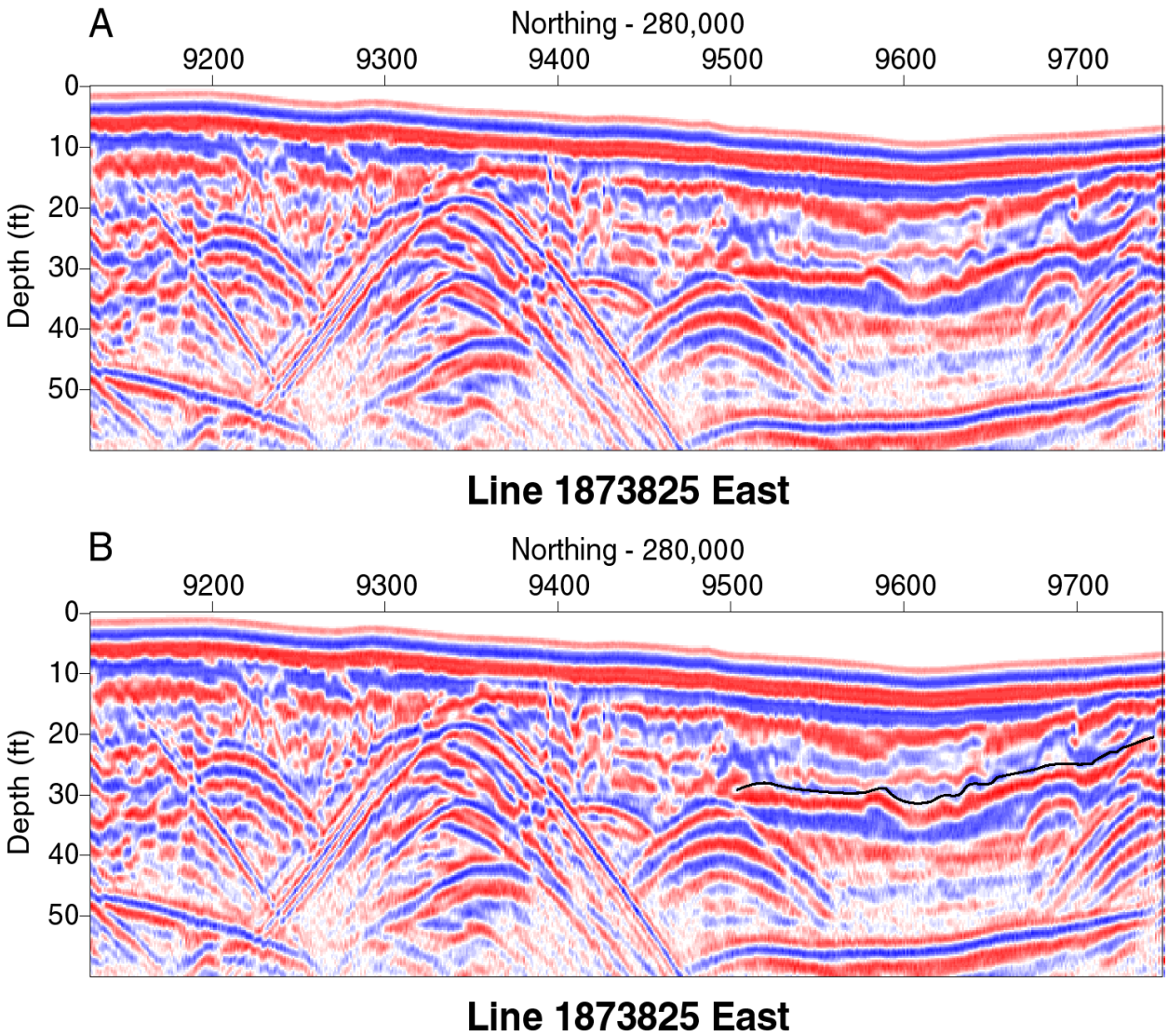

Figure 4. A) uninterpreted and B) interpreted GPR profile showing excellent data quality to the north and poor data quality to the south. Poor data quality at the southern end of the profile is in the vicinity of CDPs 1 and 2, and is entirely dominated by surface scatter. The subhorizontal event at an apparent depth of 50 ft is the OU-1 fence reflection. The hyperbolic event centered at 289340 North is the power line reflection. Interpreted clay surface is shown with a black line.

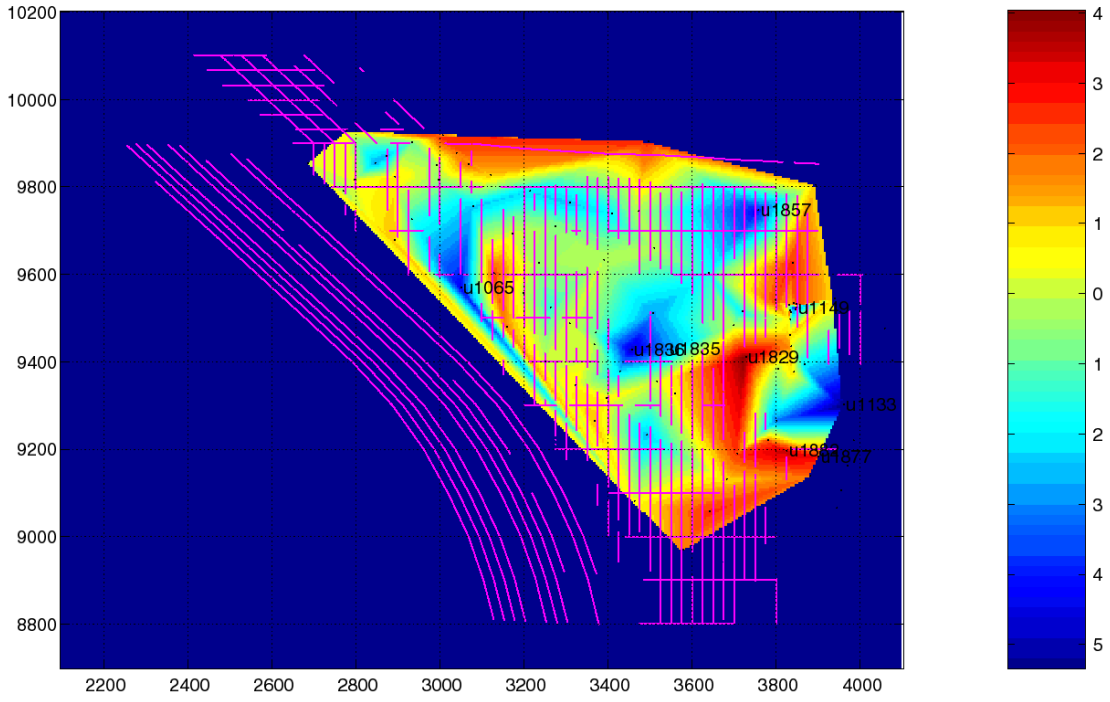

Figure 5. Image showing deviation of the surface interpreted from GPR from the 87 control points located within the survey area (Control - GPR surface). Control points that deviate by more than 3 ft are labeled. Purple lines indicate GPR pick coverage. Note that all but two of these lie in areas of poor GPR data quality where no picks were made. Also note the lack of control for the western and northern expanded areas.

5. Phase 2

5.1. Survey Site Selection

In consultation with INTERA, Inc. personnel, four zones were identified for multi-offset investigation in Phase 2 (Figure 6). Two objectives were identified for this effort; 1) to locate electric property anomalies potentially associated with NAPL contamination, and 2) to improve the clay surface interpretation in high noise areas. Zones were prioritized based on the expected potential for NAPL contamination, lack of preexisting well control, and potential for successful imaging based on previous experience at the site. Zone 1 targets the northeast trending depression which may be an important offsite contaminate transport route. There is little control on the geometry of this depression and Zone 1 was given the highest priority. Zone 2 targets the poor data quality area in the vicinity of the power line. and the primary objective for Zone 2 was improved image quality for interpretation of the clay surface. Zone 3 targets the deep channel that trends west/southwest. Little control is available for this potentially important transport pathway. Zone 4 targets the poor data quality area in the vicinity of the CDPs. Given the poor results of previous efforts in this area, we felt our chances of success were low and this area was given the lowest priority. Additionally, three reflectivity anomalies were identified north of 289600 North and east of 1873400 East. Each of these areas were investigated in Phase 2 with a series of dense, multi-offset 2D lines (Figure 7).

5.2. Data Acquisition and Processing Sequence

Table 1. Acquisition parameters for multi-offset surveying

Source Interval	2 ft
Receiver Interval	1 ft
Source Fold	25
Near Offset	6 ft
Recording Time	500 ns
Sampling Interval	1.6 ns
Stacks/Trace	32

All data were acquired with a Sensors and Software PulseEKKO 100A system with 50 MHz antennas. Acquisition parameters are listed in Table 1. The data were acquired in off-end common-source point gathers by holding the source position constant while moving the receiver to each of 25 receiver positions with the first position 6 ft from the source. The source antenna was then moved up one position and the process repeated. The

following processing sequence was applied to all data:

- Time zero correction
- Bandpass filter (12 - 25 - 100 - 200 Mhz)
- Automatic Gain Control (40 ns window)
- Semblance velocity analysis
- Sort in to common-midpoint gathers
- Normal moveout correction and stacking
- Elevation statics correction
- Depth conversion

Noteable exceptions to the processing sequence include Freqency-Wavenumber (F-K) domain filtering to remove air velocity noise events from some profiles and pre-stack depth migration (PSDM) velocity analysis and imaging applied to Zone 3 and Anomaly profiles. The effect of these additional processing steps will be discussed in greater detail below.

5.3. Results and Interpretation

Representative profiles from each line are given below for detailed discussion. All processed profiles and raw data are included in the CD that accompanies this report. Overall, the data are of good quality and adequate to meet the survey objectives. Coherent noise related to surface scatter was significantly attenuated through multi-offset processing techniques. There were three apparent NAPL responses observed in the data. These responses are distinct and very different, with the variation in response likely due to contaminant heterogeneity and transport and/or weathering history. First, zones of decreased electric permittivity (increased velocity) near the aquitard boundary were identified (Anomaly lines). This is consistent with results of the October 2000 survey, and will be referred to as a Type 1 anomaly. Second, zones of increased signal attenuation were observed in areas thought to have significant potential for NAPL accumulation (Zones 1 and 4). This response is consistent with a zone of increased electric conductivity in the NAPL zone as has been observed at other LNAPL sites (Atekwana et al., 2000; Bradford, in press; Sauck, 1998;

Sauck et al., 1998) and will be referred to as a Type 2 anomaly. This increase in conductivity may be related to biodegradation of the LNAPL. The third response, is actually a null response. In some areas that were later found to have relatively high NAPL levels, there was no clear, quantitative GPR response (Zone 3). This will be referred to as a Type 3 response. Examples of each type response are presented below.

5.3.a. Zone 1

The field team acquired 6 profiles in Zone 1 (Figure 7). The objective was to better delineate the topography of the clay surface along the broad channel that runs through this zone extending off-site to the north. Additionally, data were analyzed for NAPL related anomalies. Lines 1 and 2 were merged to provide a continuous profile just over 500 ft in length trending west to east. This profile is presented here for discussion (Figure 9).

Coherent noise, related to fence reflections, reflections from a pump-house, and off-end reflections from a telephone pole to the west, was effectively removed using pre-stack F-K filtering. Additionally, the process of stacking significantly reduces the level of random noise. The broad channel is evident as the clay surface dips from a depth of about 22 ft at x=190 ft to a depth of about 32 ft at x=300 ft. At distances greater than 300 ft the clay reflection is significantly attenuated. From the common-offset survey the clay reflection is again clear and well defined further to the east where it again rises to a depth of between 20 and 25 ft (See Appendix A). This attenuated response within the channel is observed along other profiles collected in Zone 1. The favored current interpretation is that this is due to increased electric conductivity in the NAPL zone, however surface heterogeneity is an alternative explanation. The fact that in Zone 1, the attenuated zone correlates clearly with the channel where NAPL is likely to have accumulated favors the former interpretation.

5.3.b. Zone 2

In Zone 2, the field team acquired 3 profiles spanning the zone of poor data quality caused by coherent noise related to scatter from the powerline (Figures 8 and 10). The primary objective in

Zone 2 was to improve the clay surface interpretation near the powerline. Multi-offset processing was effective at attenuating scatter from the powerline, and the clay surface was interpreted in these data where interpretation was not possible from the Phase 1 survey (Figures 8 and 10). Due to the low signal to noise ratio, it was not possible to identify quantitative NAPL related anomalies in this zone.

5.3.c. Zone 3

During the October 2000 study, a deep paleo-channel was identified in this zone. The presence of this channel was verified during Phase 1, and it became apparent that the channel is likely hydraulically connected to the CDPs. This channel is the deepest portion of the aquitard surface in the vicinity of west of the CDPs, and given its position relative to the CDPs, is a likely contaminant transport route, particularly during low water table conditions. Given the high probability of locating NAPL along this transport route, a 100 ft section of the channel was targeted for multi-offset investigation. Multi-offset analysis and imaging provided an excellent image of the channel (Figure 11), and the interpreted depth-to-clay at the base of the channel (38 ft b.d.) is within 2 ft of depth found during the later CPT investigation (36 ft b.d.). There is a large decrease in velocity at the transition from the vadose to saturated zone. Normal-moveout velocity analysis fails under these conditions and pre-stack depth migration was used to derive an accurate velocity model. From the derived velocity model, the water filled portion of the paleo-channel is clearly evident (Figure 11), and the interpreted depth to the water table is consistent with depths measured in nearby wells (OU1-064).

Although no quantitative anomalies were evident that suggest the presence of NAPL, the area was investigated in the subsequent INTERA CPT investigation. A LIF probe log acquired along Line 3 suggested the presence of a significant NAPL accumulation just above the water table (Figure 11). This was later verified through analysis of core samples, where NAPL saturations of around 5% were found. This represents a Type 3 response. Post-coring analysis suggests that there is a reflectivity anomaly associated with NAPL zone. This indicates that there is a permittivity anomaly associated with the NAPL, but that it is below the resolution of PSDM velocity analysis. Although

the thickness of the anomaly is similar to that found in other areas (See Appendix A), the velocity contrast is likely lower.

5.3.d. Zone 4

Zone 4 consists of a large area containing part of CDP 1 and all of CDP 2 where poor results were obtained in all previous data acquisition efforts due to very low signal to noise ratios. It is unclear if the poor data quality is due to significant alteration of the surface material and/or near surface buried debris, or if the GPR response is related to a Type 2 contaminant reponse. It is potentially a combination of the two, but analysis of the direct ground wave indicates a significant near surface increase in the ground conductivity suggesting surface alteration as the primary inhibitor.

This is one of the most important areas of investigation given the proximity to CDPs 1 and 2, and in consultation with INTERA personnel, it was determined that some additional effort should be expended in an attempt to characterize this area with GPR. Two ~ 400 ft multi-offset profiles were acquired in Zone 4 (Figure 8). The profiles were oriented to span a significant portion of Zone 4, and to cross the projected axis of the paleo-channel found in Zone 3.

The common-offset profiles are heavily contaminated with noise, and no clay reflection is evident (Figure 12). Pre-stack F-K filtering reveals an event along the western end of the profiles that is at the approximate depth-to-clay, but the data quality is too poor to allow a confident interpretation. Thus, we conclude that data acquired in Zone 4 is not useable and recommend against further Zone 4 GPR investigation. If future geophysical characterization is undertaken in this area, other electric methods such as resistivity or TDEM may prove useful.

5.3.e. Anomaly Lines

During the Phase 1 investigation, three anomalies were identified with similar character to that investigated in the October 2000 investigation (Appendix A). These anomalies are topographic lows in the clay surface with a weaker reflection arching over the low. The anomaly studied in

October 2000 was found to have low electric permittivity (high velocity), and the presence of NAPL was later verified through coring. These represent the Type 1 response.

Multi-offset data were acquired over each of the three anomalies, and pre-stack depth migration velocity analysis was applied to look for the presence of a high velocity anomaly. Along Lines 2 and 4, a high velocity anomaly was present within the topographic low. During the INTERA CPT investigation a LIF probe log was acquired in the Line 4 anomaly. A LIF anomaly was found and was consistent with the velocity anomaly. However, the LIF anomaly is very small, potentially below the noise level, and suggests a maximum concentration of only around 1%. No core samples were taken from this site. It is possible that the NAPL is not uniformly distrbuted in the anomalous zone, and that the CPT simply missed a concentrated area. This would not be too surprising, as significant variation in NAPL concentration was observed in the October 2000 anomaly where four cores were taken from within the anomalous zone. However, it is not likely that high NAPL saturations exist within the anomalous zone.

As in the October 2000 investigation, this leaves the problem of explaining a large velocity anomaly with a relatively small NAPL saturation. The interpretation favored currently is that a small amount of highly viscous NAPL is clogging the pore throats in the anomalous zone. This results in a zone of low hydraulic conductivity that has lower water saturation than the surrounding sediements. This leads to high GPR velocity. This explanation is purely speculative, but could easily be tested by measuring water content in samples taken from within and around the anomalous zone.

5.4 Results of CPT/LIF verification

Based on the results of both common- and multi-offset profiling, four specific sites were recommended for verification analysis using CPT/LIF probing. The objective of this effort was to verifiy the presence of NAPL in locations where GPR anomalies were present. The locations and results are given in Table 2. Note that CPT numbers are internal INTERA sampling locations (See INTERA report for Hill AFB location numbers).

At Location 3 there is a significant deviation from background in the LIF log from CPT-014 at a depth consistent with the velocity anomaly from GPR profiling. The amplitude of the LIF anomaly is less than 0.1 V which may be below the noise level of the system, and this is therefore listed as possible low level NAPL saturation. It should be noted that in some locations, deviations less than 0.1 V were shown to be associated with NAPL saturations of around 1% (ie CPT-057)

5.5 Discussion and Conclusions

Table 2. Summary of CPT/LIF verification results.

Location /Line	Easting	Northing	Type of GPR anomaly	CPT/LIF probe location? (y/n)	NAPL present? (y/n)
1/A3L3	1873474	2892331	Deep paleo-channel, anomalous reflectivity	y (CPT-011B)	y
2/ANL2	1873729	289796	Topographic low, anomalous reflectivity, high-velocity	n	NA
3/ANL4	1873825	289638	Topographic low, anomalous reflectivity, high-velocity	y (CPT-014)	possible low level
4/A1L1	1873321	289860	Paleo-channel, high attenuation	n	NA

This site was particularly challenging for three primary reasons:

- Significant heterogeneity in the surface material related to variations in fill material associated with capping and landfill activities.
- Significant heterogeneity at the target depth. The NAPL is present near the sand/clay boundary. Variable topograpy along this surface had a significant impact on contaminant migration. This was further complicated by seasonal water table fluctuations about the sand/clay interface.

• A highly heterogeneous NAPL resulting in variable electric properties and heterogeneous contaminant migration and distribution.

In spite of these difficulties, data quality was generally good and study objectives were met successfully. This is particularly true for mapping the clay surface. The clay topography was imaged to within about 1 ft over most of the site. The most significant exception to this is in the southeast of the site in the vicinity of CDP 2 where poor data quality made it impossible to interpret the clay surface with confidence. The poor data quality is due to increased near surface electric conductivity. The source of this increased conductivity is not known.

Through multi-offset profiling we were able to overcome some of the difficulties noted above and were able to improve imaging of the clay surface in high noise areas in the vicinity of the powerline. Attribute analyses for detection of NAPL are more sensitive to noise and heterogeneity than simple clay surface imaging. Sites selected for attribute analyses were specifically selected for the quality of data in those areas. Of the four locations recommended as likely to have NAPL, two were sampled in the subsequent CPT effort. LIF probing indicated that both of these sites potentially had NAPL accumulations. Only one of these was selected for soil sampling - along A3L3. This location was found to have significant NAPL accumulation above the water table.

There appears to be at least three types of GPR response to NAPL contamination at the site:

Type 1: High GPR velocity associated with reflectivity anomalies

Type 2: High GPR signal attenuation.

Type 3: No apparent response.

The variation in response is likely due to a complex combination of factors that may include contaminant heterogeneity to include phase separation along the migration route and a migration dependent, variable weathering history.

The results of this study, as with all geophysical studies, are “soft” and ultimately the product of subjective data interpretation. As such, absolute verification of any results presented here requires direct sampling. However, error analysis indicates that these results are relatively accurate and provide valuable input in the overall understanding of the hydrogeologic system at OU-1.

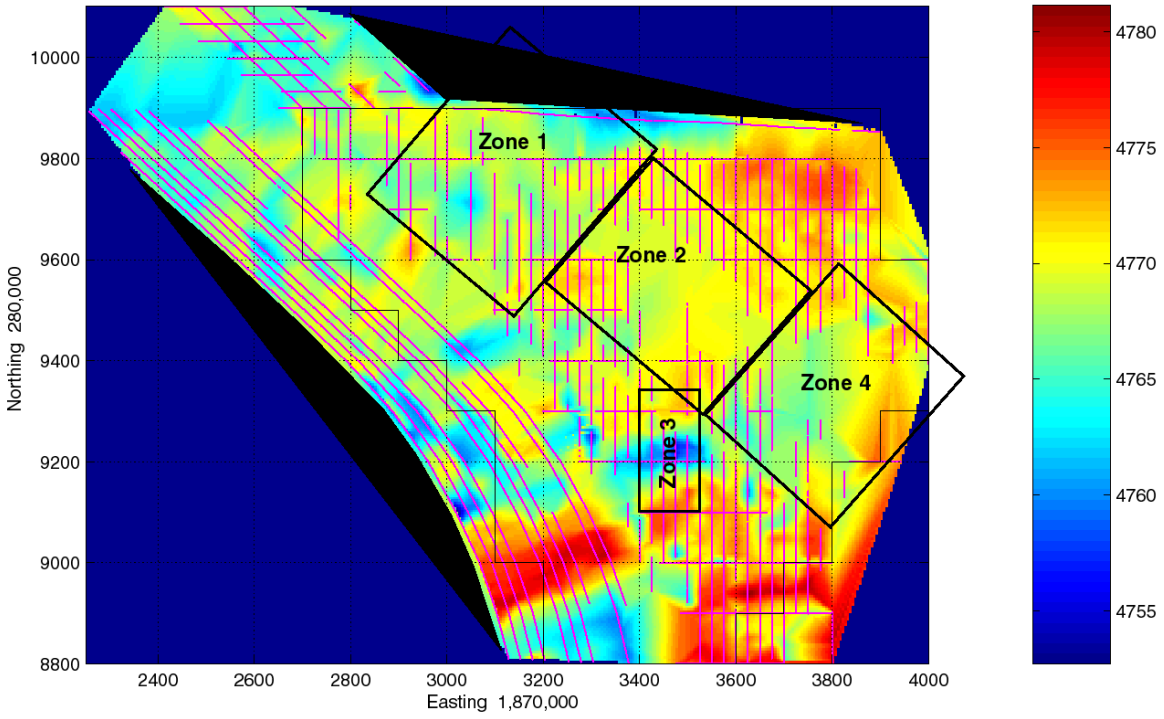

Figure 6. Map showing the four zones identified for investigation in Phase 2. See Figure 7 for specific line locations.

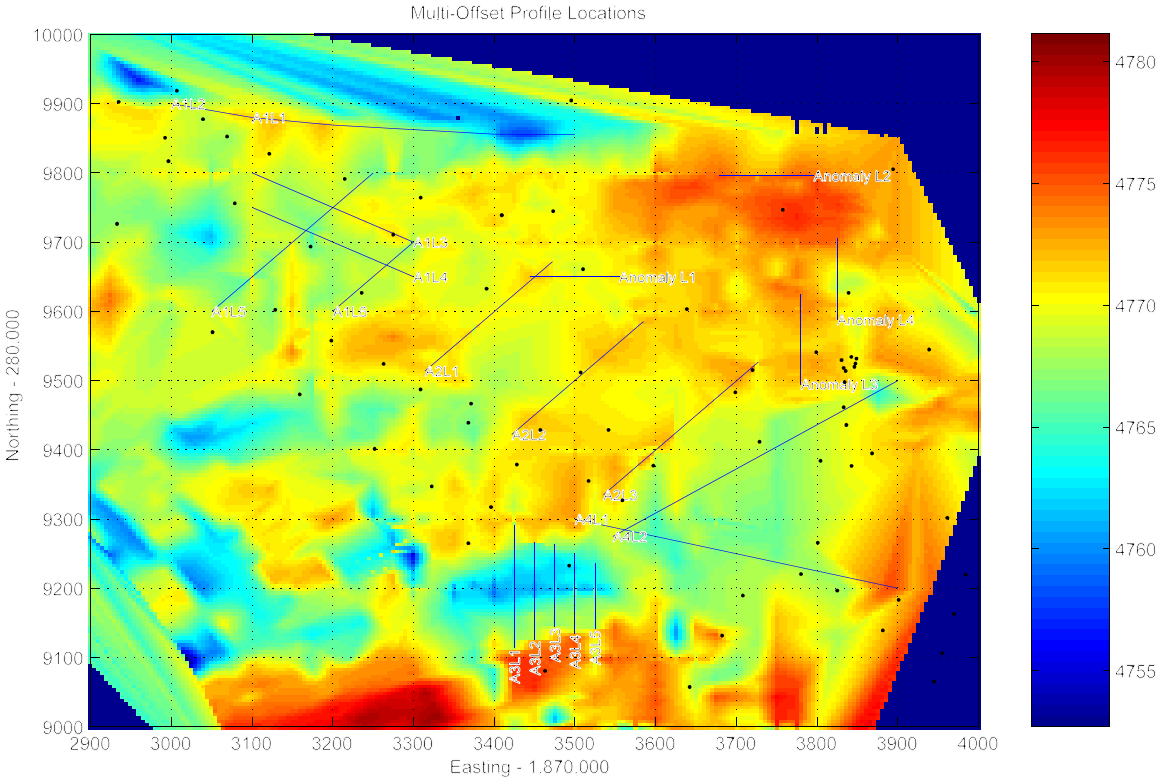

Figure 7. Multi-offset profile locations. Each line is designated by *AxLy* with *x* denoting the zone and *y* denoting the line number within the zone. Lines located to investigate specific anomalies are simply denoted Anomaly L*y*.

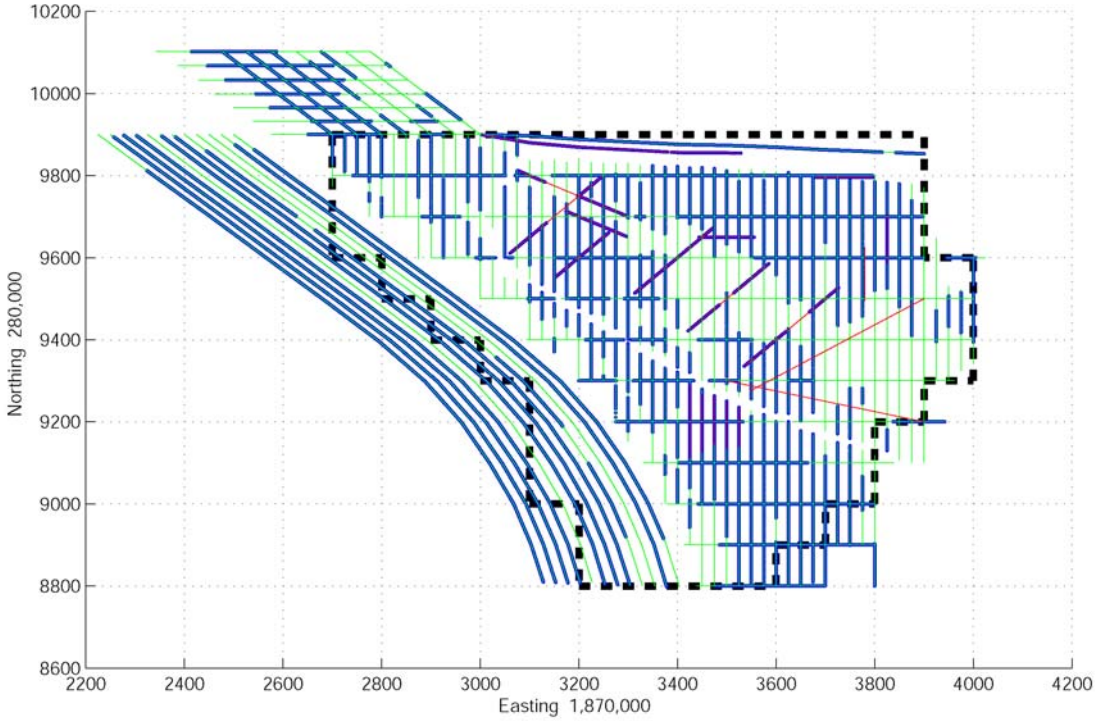

Figure 8. GPR survey coverage for Phases 1 and 2. Green indicates common-offset profiles, red indicates multi-offset profiles, and blue indicates locations where the clay surface could be interpreted with confidence.

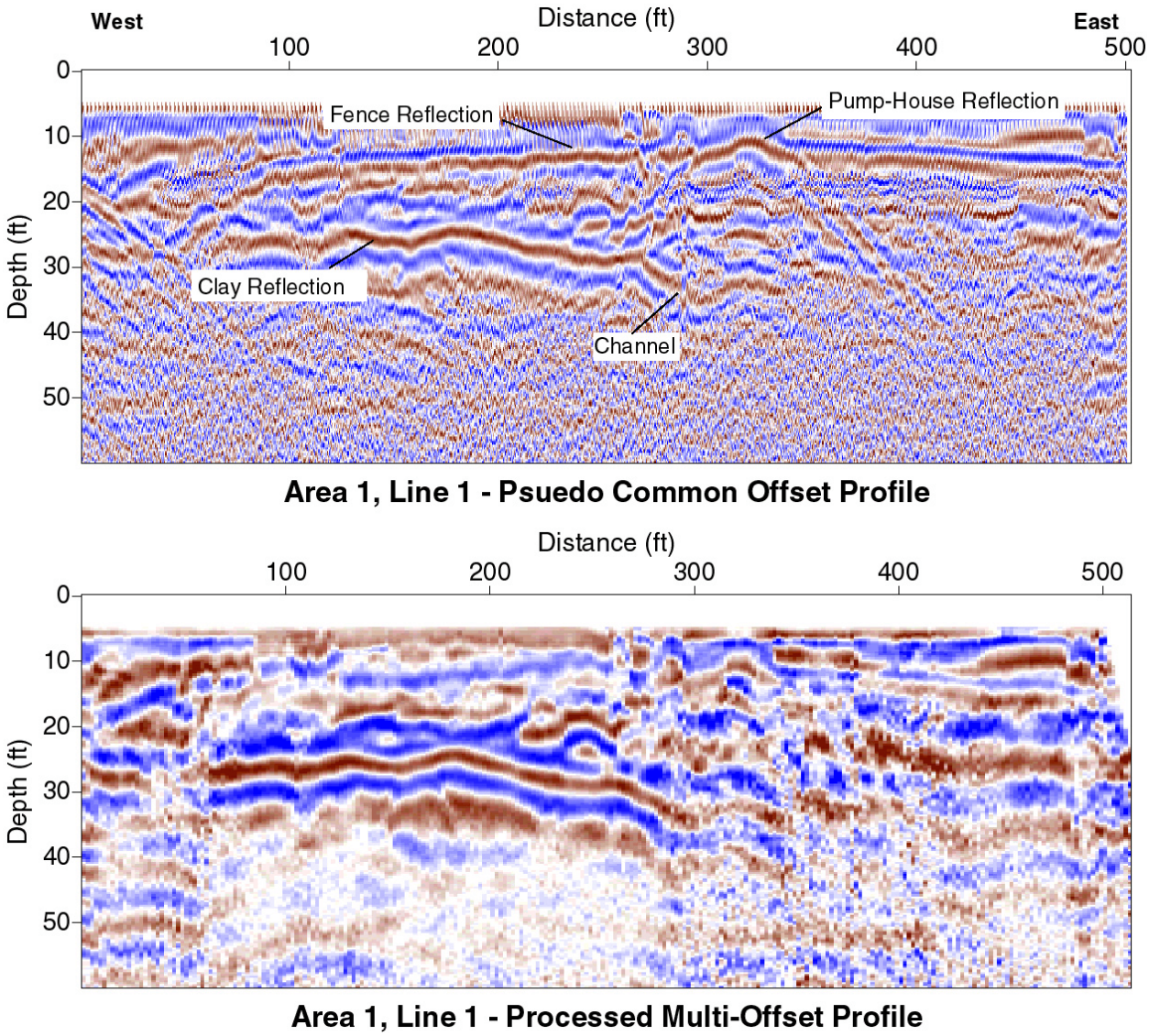

Figure 9. Conventional (common-offset) and full processed multi-offset profiles along Line 1 in Zone 1. Pre-stack F-K filtering effectively removes all surface scatter noise and improves interpretability of the section. Note the attenuated clay reflection amplitude toward the east. This may be due to a zone of high electric conductivity in the NAPL contaminated zone.

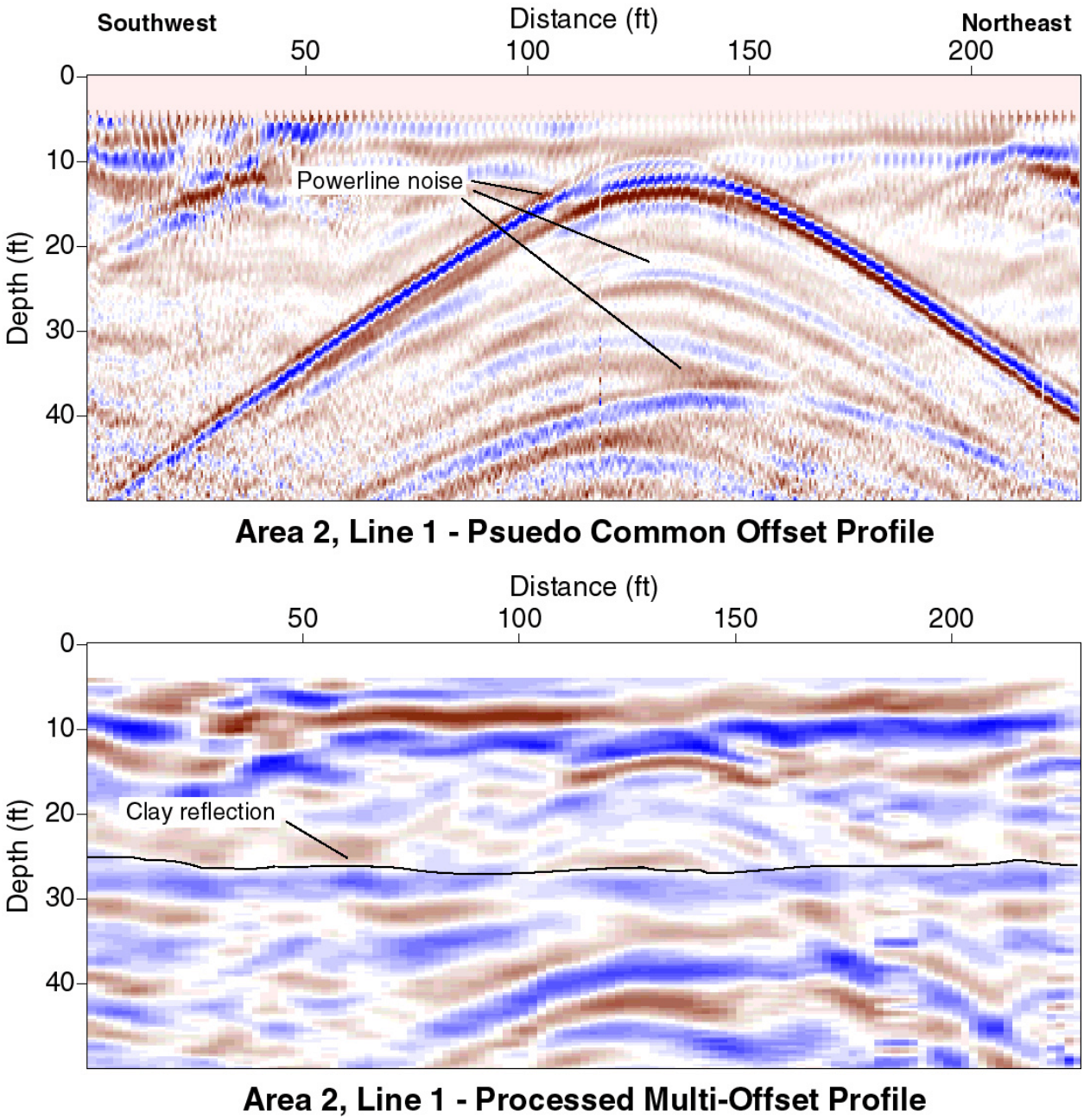

Figure 10. Conventional (common-offset) and fully processed multi-offset profile. In the conventional profile, the clay reflection cannot be identified across much of the profile. Pre-stack F-K filtering effectively attenuates scatter from the powerline, and the clay reflection is easily identified across the entire section.

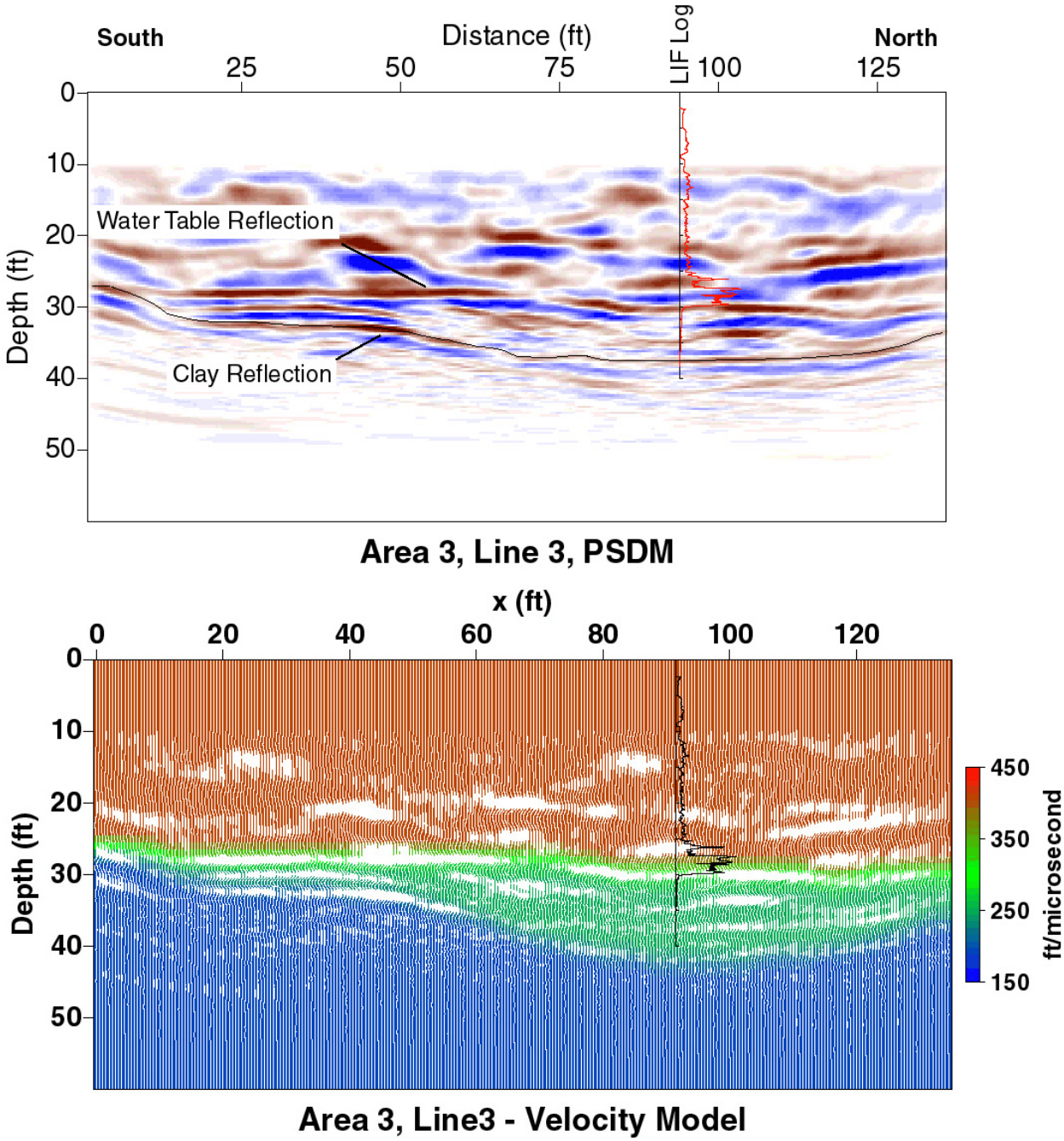

Figure 11. Line 3, Zone 3 showing the deep paleo-channel south of the existing slurry wall. The clay surface is clearly imaged in the PSDM profile, and the water filled channel is evident in the velocity model as a low-velocity zone. LIF probe data show a high concentration of LNAPL just above the water table at x=92.5 ft. There appears to be a reflectivity anomaly, identified qualitatively, associated with the NAPL, but we have not identified a quantitative anomaly.

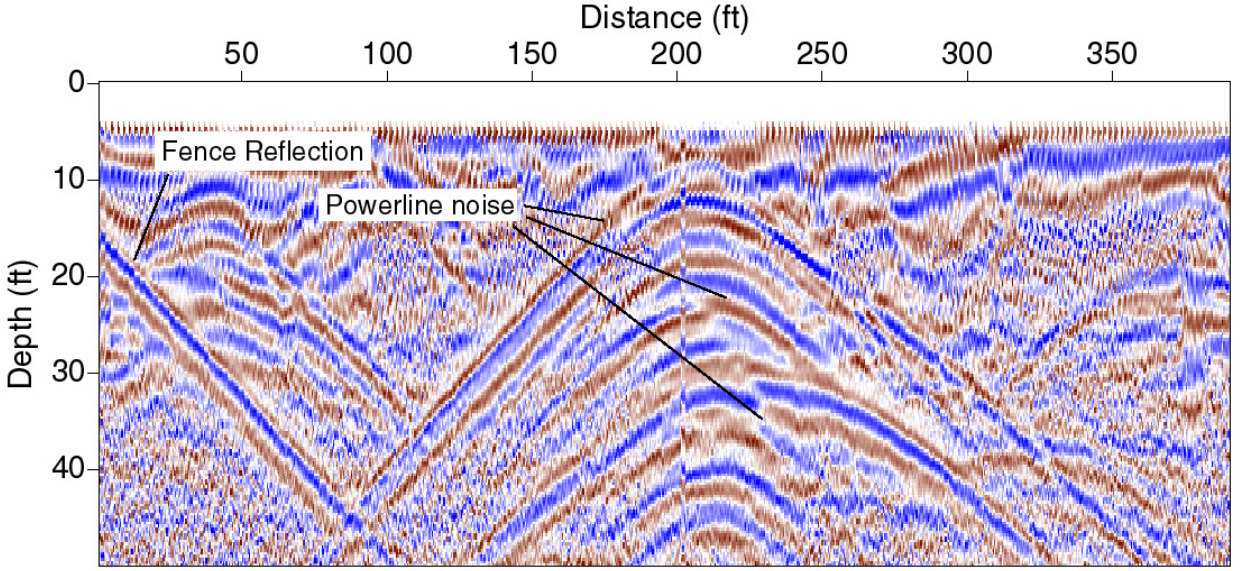

Area 4, Line 2 - Psuedo Common Offset Profile

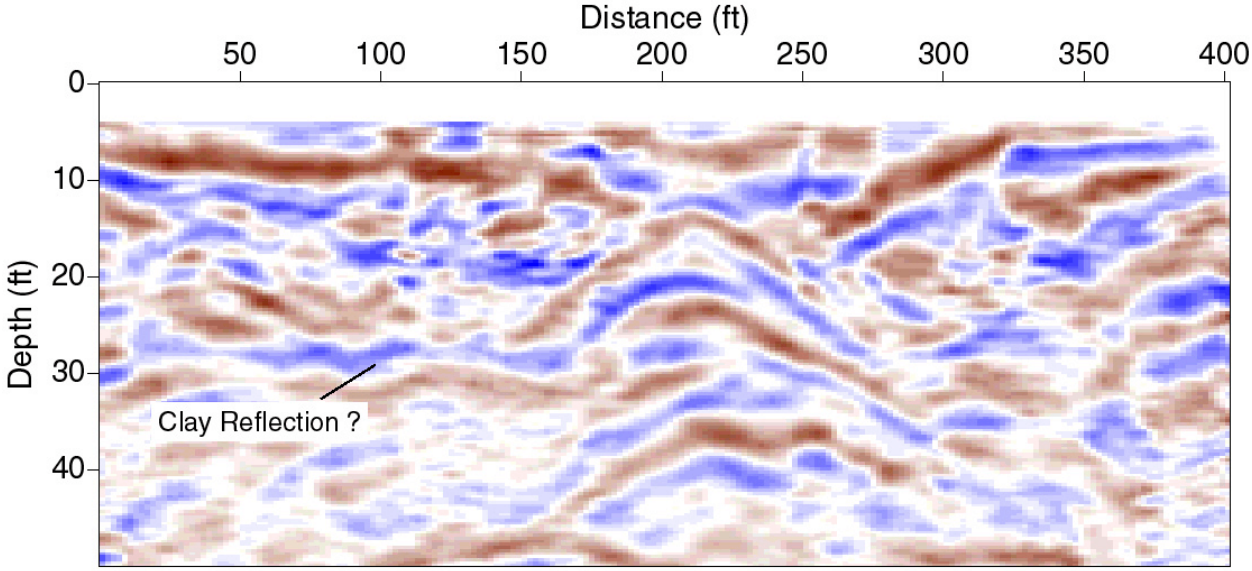

Area 4, Line 2 - Processed Multi-Offset Profile

Figure 12. Line 2, Zone 4 is heavily contaminated with noise. Pre-stack F-K filtering appears to reveal a clay reflection along the western portion of the line, but the data quality is too poor to make a confident interpretation.

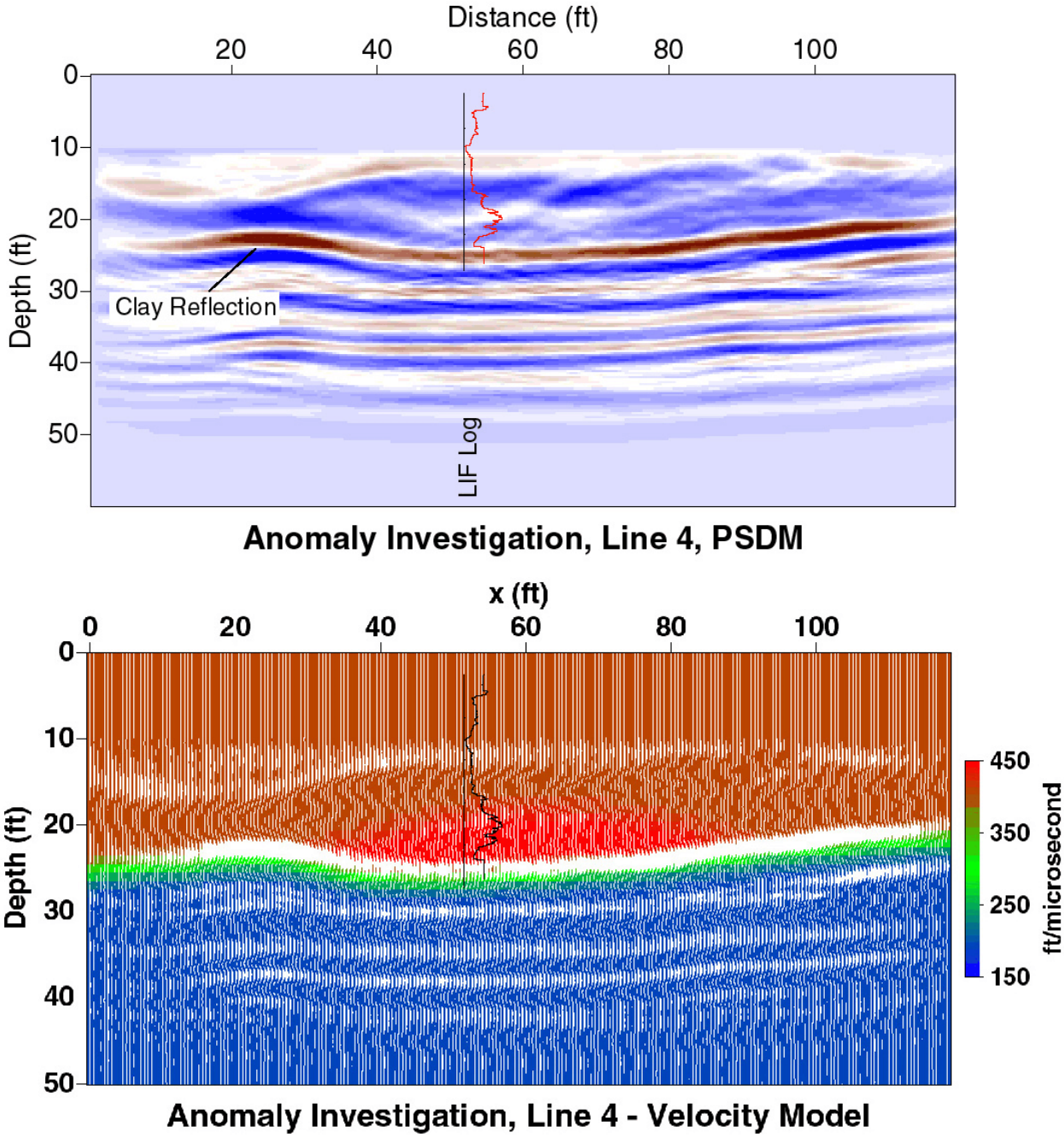

Figure 13. Pre-stack depth migrated image of Anomaly Line 4 and velocity model with wiggle trace overlay. A topopgraphic low with over-arching reflector was identified along this profile, and a high velocity anomaly was found within this zone. This is analagous to the anomaly found in the October 2000 study. LIF probe data suggest that a small amount of NAPL may be present in the anomaly, but no large concentrations are present.

8. References

Atekwana, E.A., Sauck, W.A., and Werkema Jr., D.D., 2000, Investigations of geoelectrical signatures at a hydrocarbon contaminated site: J. Appl. Geophys., v. 44, p. 167-180.

Bradford, J., Ramaswami, M., and Peddy, C., 1996, Imaging PVC gas pipes using 3-D GPR, SAGEEP '95: Expanded Abstracts: Keystone, CO, Soc. Appl. Geophys. Env. Eng., p. 519-524.

Bradford, J.H., in press, GPR offset-dependent reflectivity analysis for characterization of a high-conductivity LNAPL plume, SAGEEP 2003 Symposium on the Application of Geophysics to Environmental and Engineering Problems: San Antonio, TX, Env. Eng. Geophys. Soc.

Campbell, D.L., Lucious, J.E., Ellefson, K.J., and Deszcz-Pan, M., 1995, Monitoring of a controlled LNAPL spill using ground-penetrating radar, SAGEEP '95: Symposium on the Application of Geophysics to Environmental and Engineering Problems: Proceedings: Keystone, CO, Env. Eng. Geophys. Soc., p. 511-517.

Davis, J.L., and Annan, A.P., 1989, Ground-penetrating radar for high-resolution mapping of soil and rock stratigraphy: Geophysical Prospecting, v. 37, p. 531-551.

Dix, C.H., 1955, Seismic velocities from surface measurements: Geophysics, v. 34, p. 180-195.

Endres, A.L., and Redman, J.D., 1996, Modeling the electrical properties of porous rocks and soils containing immiscible contaminants: J. Env. Eng. Geophys., v. 0, p. 105-112.

Griffiths, D.J., 1989, Introduction to electrodynamics: Englewood Cliffs, NJ, Prentice-Hall, 532 p.

Haeni, F.P., 1996, Use of ground-penetrating radar and continuous seismic-reflection profiling on surface-water bodies in environmental and engineering studies.: J. Env. Eng. Geophys., v. 1, p. 27-35.

Lafond, C.F., and Levander, A.R., 1993, Migration moveout analysis and depth focusing: Geophysics, v. 58, p. 91-100.

Lien, B.K., and Enfield, C.G., 1998, Delineation of subsurface hydrocarbon contaminant distribution using a direct push resistivity method: J. Env. Eng. Geophys., v. 2, p. 173-179.

Loughridge, J., 1998, Application of seismic tools and techniques to ground-penetrating radar (GPR) studies [M.A. thesis]: Houston, Rice University.

Montgomery-Watson, 1995, Hill Air Force Base, Utah: Comprehensive remedial investigation

report for Operable Unit 1 - Volume 1: Salt Lake City, Montgomery Watson.

Newmark, R.L., Daily, W.D., Kyle, K.R., and Ramirez, A.L., 1998, Monitoring DNAPL pumping using integrated geophysical techniques: J. Env. Eng. Geophys., v. 3.

Olhoeft, G.R., 1986, Direct detection of hydrocarbon and organic chemicals with ground-penetrating radar and complex resistivity, NWWA/API Conference on petroleum and hydrocarbons and organic chemicals in groundwater -- Prevention, detection, and restoration: Houston, NWWA, p. 284-305.

Santamarina, J.C., and Fam, M., 1997, Dielectric permittivity of soils mixed with organic and inorganic fluids (0.02 GHz to 1.30 GHz): J. Env. Eng. Geophys., v. 2, p. 37-51.

Sauck, W.A., 1998, A conceptual model for the geoelectrical response of LNAPL plumes in granular sediments, SAGEEP '98 Symposium on the Application of Geophysics to Environmental and Engineering Problems: Proceedings: Chicago, IL, Env. Eng. Geophys. Soc., p. 805-817.

Sauck, W.A., Atekwana, E.A., and Nash, M.S., 1998, High conductivities associated with an LNAPL plume imaged by integrated geophysical techniques: J. Env. Eng. Geophys., v. 2, p. 203-212.

Young, R.A., and Sun, J., 1996, 3D ground penetrating radar imaging of a shallow aquifer at Hill Air Force Base, Utah: J. Env. Eng. Geophys., v. 1, p. 97-108.

—, 1998, Extracting a radar reflection from a cluttered environment using 3-D interpretation: J. Env. Eng. Geophys., v. 3, p. 121-131.

Zelt, C.A., and Smith, R.B., 1992, Seismic traveltime inversion for 2-D crustal velocity structure: Geophys. J. Internat., v. 108, p. 16-34.

APPENDIX A: OCTOBER 2000 REPORT

METHODOLOGY

Principles of GPR Investigation

In GPR studies, an oscillating electric field is transmitted into the earth and is reflected at boundaries separating materials with differing electric properties (dielectric permittivity, magnetic permeability, and conductivity). The reflected wavefield is recorded and used to produce a subsurface representation similar to a cross-section of the earth. For most earth materials in which the GPR signal will propagate efficiently, the magnetic permeability is roughly constant and the conductivity is low, so we primarily image contrasts in dielectric permittivity. Conductivity controls attenuation of electromagnetic waves, with signal attenuation increasing with increasing conductivity. Conductivity is the primary parameter controlling the success of GPR studies, with essentially no signal penetration in highly conductive soils. Clays are typically relatively good conductors whereas sandy, coarse grained materials have relatively low conductivity and generally provide a suitable sedimentary environment for GPR investigation. High conductivity materials in the earth such as a clay aquitard, metal objects, or highly mineralized ground water, produce a strong reflection at the upper boundary, but also act as a barrier to GPR signal penetration.

GPR operates in the frequency band from 10 MHZ - 1 GHZ, with a peak frequency of 50 - 225 MHZ typical for groundwater studies. Lower frequencies correspond to greater depth of penetration and lower resolution whereas high frequencies correlate with shallow penetration at higher resolution. Velocities in dry and water saturated sands are on the order of 0.15 m/ns and 0.05 m/ns respectively. Thus we can expect to resolve features on the order of 10 - 40 cm in the water saturated zone and 30 - 120 cm in the vadose zone. Depth of penetration varies from ~ 0 m under the worst conditions to as much as 50 m under ideal conditions. The best results in GPR studies are obtained in dry sandy environments (low conductivity), but excellent results have been obtained with variable sediment composition and well below the water saturated zone (Haeni, 1996; Loughridge, 1998).

Multi-offset vs. Common-offset Data Acquisition and Velocity Estimation

Most GPR surveys are acquired with a constant transmitter-receiver offset (bi-static mode) and little or no processing is employed in generating the final image. This can provide useful information and is valuable as a rapid reconnaissance tool. However, as the complexity of the EM velocity structure increases, the ability to produce useful images using this simple acquisition geometry diminishes. EM velocity estimates cannot be made from common-offset data, therefore reflector depth estimates must be based on rough guesses of material velocity or correlation of interpreted reflectors with known material boundaries.

In multi-offset data acquisition, several traces are recorded at various source-receiver separations at each point along the survey, as opposed to a single trace at each point for a constant-offset survey. The data are typically sorted into common-midpoint (CMP) gathers which contain traces representing several transmitter-receiver offsets with coincident transmitter-receiver midpoint. Multi-offset acquisition, while more labor intensive and time consuming, significantly improves our ability to accurately predict the subsurface. This improvement arises from three primary features;

1) Multi-offset data provide traveltime vs. offset curves, which enable one to estimate propagation velocity. Velocity estimation is necessary for making depth estimates and is used to estimate electric permittivity, an important material property in NAPL detection.

2) Dramatic attenuation of random noise and/or coherent noise such as scatter from surface objects is achieved through a process known as stacking. To produce a stacked image, all reflected events are shifted to their equivalent zero-offset traveltime by applying a normal-moveout (NMO) correction, which in effect flattens the travel time curve of a given reflector. All traces in the CMP are then vertically summed to produce a stacked trace. Coherent or flattened reflections stack constructively, while noise events are attenuated. A profile of stacked traces is analogous to the common-offset profile, but with significantly reduced noise levels. This type of processing can lead to dramatically

improved image quality and therefore improve our ability to predict the subsurface.

3) Multi-offset data acquisition allows one to observe reflected wave behavior for various travel paths and angles of incidence at a common reflection point . Quantification of this behavior can be a valuable tool in material property estimation.

One of the most valuable material properties that can be extracted from GPR data is EM propagation velocity which leads directly to estimates of effective permittivity (Griffiths, 1989). It is typical to acquire a single CMP gather within a broader survey area to obtain a 1-D velocity structure for interpreting a bi-static survey. An RMS velocity is estimated for each reflection using normal moveout analysis (Bradford et al., 1996; Campbell et al., 1995; Young and Sun, 1996). Typically, the RMS velocity structure is used to estimate effective interval velocities using Dix inversion. There are two primary problems associated with this methodology. First, the 1-D velocity estimate does not account for lateral velocity (or equivalently, dielectric permittivity) heterogeneity. This results in significant problems for advanced velocity dependent processing methodologies such as migration, and can lead to inaccurate depth estimates. Additionally, 1-D velocity analysis does not allow one to identify lateral velocity variation that may be associated with NAPL rich sediments.

The second problem, which requires significantly greater processing sophistication to treat properly, is that the underlying assumptions of NMO velocity analysis and Dix inversion are often violated within the zone of GPR investigation. A fundamental assumption of NMO velocity analysis/Dix inversion is that vertical and horizontal velocity gradients are relatively small resulting in an approximately straight ray path (Dix, 1955). It is typical for velocities in the GPR zone of investigation to decrease by a factor three or more as the sediments grade from dry to fully water saturated. This results in severe departure from normal moveout and leads to very large overestimates of interval velocity. We refer to the amount of overestimate as NMO bias. NMO bias is a complicated function that depends on velocity heterogeneity in the overburden, maximum and minimum transmitter-receiver offset, and the thickness of all layers through which the signal propagates.

When conventional velocity analysis fails, we must resort to more sophisticated methods. A number of these methods have been developed for seismic reflection data such as pre-stack depth migration (PSDM) velocity analysis (Lafond and Levander, 1993) or travel time inversion (Zelt and Smith, 1992). Inverse methods can provide an accurate description of the gross velocity structure, but lack detail since only a few key interfaces are used in the analysis. PSDM is the most accurate and detailed imaging method available. In a complex subsurface setting, PSDM focuses scattered energy and moves dipping events to the correct location. PSDM treats severe lateral and vertical velocity gradients correctly, which cannot be done with the post-stack migration methods typically applied.

PSDM velocity analysis follows an iterative approach in which the data are first migrated using a starting velocity model that may be obtained using a variety of methods including NMO velocity analysis or travel time inversion. The data are then checked for "focusing" ; the data are visually inspected to see if all reflected energy from a common subsurface point is migrated to the same depth independent of offset. The velocity model is then updated from the top down until all reflected energy is "focused".

Principles of NAPL Detection with GPR

The relative dielectric permittivity (K) and conductivity (σ) depend strongly on material type. The amplitude of a GPR reflection is dependent on the contrast of permittivity and conductivity at material boundaries, and attenuation of the signal is dependent on the conductivity of the material through which the signal is propagating (Davis and Annan, 1989). Water has very high permittivity ($K \sim 80$), whereas common NAPLs such as light hydrocarbons and chlorinated solvents have very low permittivity ($K \sim 2$) and are very poor conductors. Most dry earth materials, through which the GPR signal will propagate efficiently, have relatively low permittivity (4 - 16) so that introduction of water into the pore space results in a significant increase in bulk permittivity of the three phase system (air, water, earth material). Additionally, the presence of water can significantly increase bulk conductivity, particularly in the presence of clay.

Anomalous displacement of naturally occurring water with low permittivity NAPL leads to lower bulk permittivity and conductivity than the surrounding sediments. The amount of the contrast depends on the wetting phase and relative concentrations of water and NAPL. Several modeling and laboratory studies have illustrated that when the organic is the wetting phase, the conductivity and dielectric permittivity drop sharply with very low concentrations of NAPL, whereas the change is more gradual when water is the wetting phase (Endres and Redman, 1996; Santamarina and Fam, 1997). In a cross-well ERT field study, Newmark et. al.(1998) recorded significant decreases in conductivity associated with pooled and residual TCE in water wet sediments at OU-2, and Lien and Enfield (1998) found low conductivity associated with residual LNAPL contamination at OU1. We expect a significant decrease in dielectric permittivity to correlate with the decrease in conductivity.

We expect the GPR signature associated with the presence of NAPL to be manifest in essentially three ways. First, the decrease in dielectric permittivity results in increased EM propagation velocity. Secondly, the decrease in permittivity can significantly change reflectivity. If the NAPL is in a discreet pool or plume, we expect increased reflectivity or variations in the AVO response associated with the NAPL boundaries. If the NAPL is smeared vertically or has diffuse boundaries, as is the case for residual saturation, we may observe decreased reflectivity in the sediment column due to homogenization of the permittivity profile. This occurs because decreased bulk water content reduces porosity dependence (Olhoeft, 1986). Finally, the decrease in conductivity leads to decreased levels of signal attenuation.

Our approach to NAPL detection with GPR is to combine detailed velocity analysis and imaging with reflected waveform attribute analysis to produce detailed, quantitative subsurface images and material property maps that can be used to predict the location of subsurface contaminants.

HISTORY OF GPR INVESTIGATION AT OU-1

Young and Sun reported the results of two 20,000 sq. ft. 3D GPR surveys, one acquired

just north of CDP 1 (Young and Sun, 1996) and the other spanning CDP 2 and extending to the south (Young and Sun, 1998). The data north of CDP 1 were of excellent quality, providing a good image of both the contact between the Provo alluvium/Alpine clay contact and the major stratigraphic boundaries within the alluvium. The data acquired around CDP 2 were contaminated with coherent noise scattered from surface objects, but provided some useful subsurface relection information. The data were acquired primarily in common-offset mode, with some sparse multi-offset sampling for coarse velocity control. Based only on NMO velocity analysis at a few locations, Young and Sun concluded that the presence of NAPL would not introduce sufficient contrast in electrical properties for detection using GPR.

Although Young and Sun conducted a quality survey and achieved excellent results, their conclusions that NAPL detection potential was low was based on an incorrect assumption about the information provided by NMO velocity analysis. Namely that NMO velocity analysis provides a good estimate of actual propagation velocity which, for the reasons stated in the previous section, is incorrect.

Based on the excellent data quality presented by Young and Sun, and on the recognition that their conclusion that NAPL detection potential was low was potentially incorrect, we chose OU-1 at Hill AFB for a NAPL detection feasibility study. In August of 1999, we acquired two, 2-D, multi-offset surveys at OU-1. The first was oriented north-south and crossed the western edge of CDP 1. The second was located approximately 350 ft west of CDP 1, was oriented northeast-southwest, and spanned the northern boundary of the LNAPL plume. This study provided several significant insights. First, while overall, GPR data quality was good, there was significant variability within OU-1. This ranged from excellent north and south of CDP 1, to extremely poor directly over CDP 1, to poor but adequate along the western line. Second, we found that there was significantly greater radar velocity heterogeneity that was assumed by Young and Sun. Additionally, we identified an anomaly just northwest of CDP 1 as a potential NAPL source that was previously unidentified.

2000 OU-1 GPR SURVEY

In October of 2000, we conducted a research scale GPR survey at OU-1. The survey covered approximately 1,000,000 sq. ft. west of CDPs 1 and 2 (Figure 2). The objectives were twofold:

1) Acquisition of site scale 2D common-offset profiles to investigate variations in GPR signal quality and determine potential for mapping the clay surface in the area covering the known free LNAPL plume west of CDP 1.

2) Acquisition of a dense, 3D multi-offset survey designed to investigate the radar

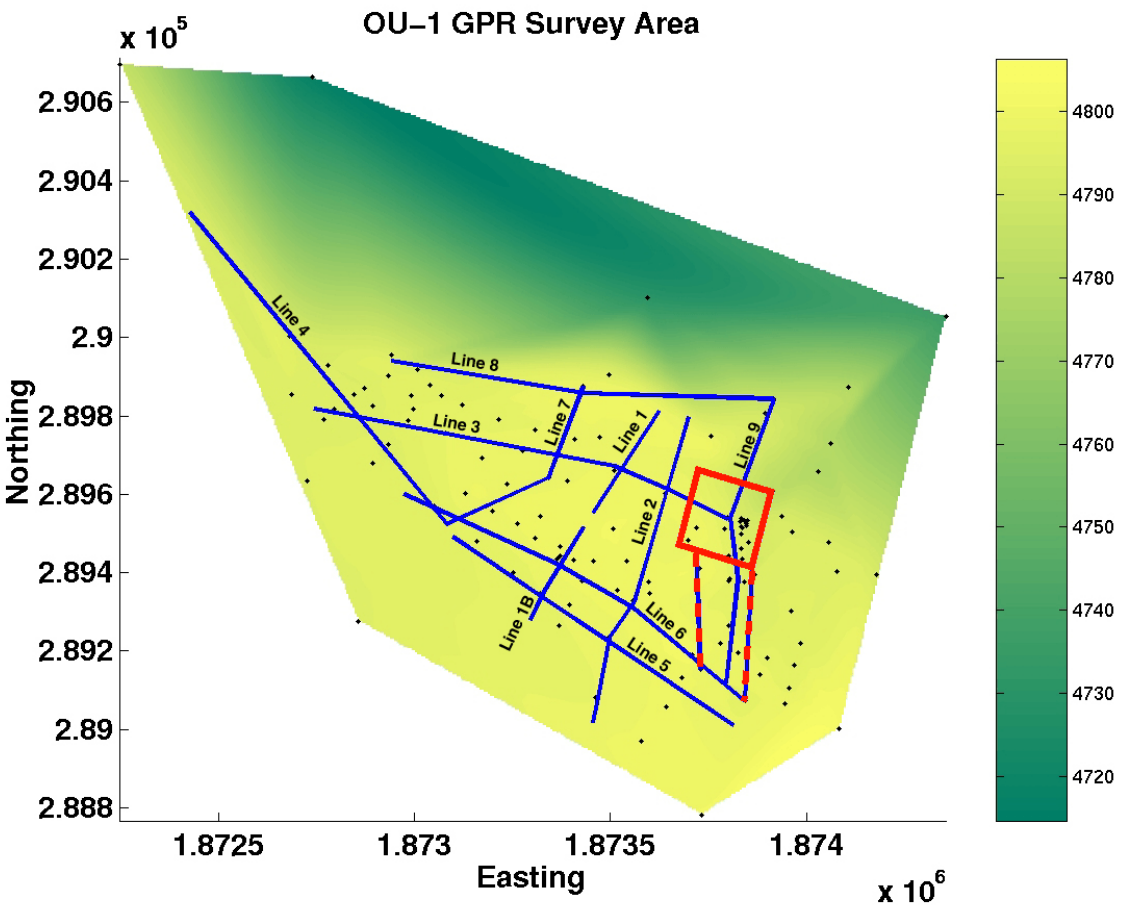

Figure 1. GPR profiles and 3D survey area. Blue lines indicate 2-D profiles, red dash indicates multi-offset lines, and the red box shows the 3-D survey area. Color scale image shows surface elevation and control points (CPT and boring locations) are shown in black.

anomaly identified in the feasibility study as a potential NAPL rich zone. Additionally, two long multi-offset profiles were acquired extending approximately 350 ft. south of the 3D survey area.

All data were acquired with a Sensors and Software PulseEkko1000 system using 50 Mhz antennas. Selection of the antenna frequency was based on results of the feasibility study. Although 100 Mhz antennas could be used in some locations, giving better resolution, the 100 Mhz signal could not penetrate to the clay aquitard in much of the area due to variations in soil conductivity. The 50 MHz antennas were selected to ensure that the signal would reach the clay surface in all locations.

The field work was carried out while the site was actively under construction (Figure 2). Construction activities included completion of the LNAPL extraction trenches with associated facilities and preparation for installation of a bentonite cap. Since the radar signal would be severely degraded after the cap was in place, it was imperative to complete the radar survey prior to installation of the cap. This required us to conduct night operations using a generator and halogen lights. Equipment related to construction activities during the day, and lighting equipment at night produced variable but significant surface scatter that degraded data quality. Additional sources of surface noise included the power line oriented east-west, the fence that lies just east of our survey area, permanent structures, and a variety of debris and temporary items related to the construction. Additionally, construction activities would periodically result in destruction of our survey markers and it was necessary to re-survey the area several times. In spite of these problems, we were able acquire a dataset with excellent quality in most places.

Figure 2. Photos illustrating construction activities, data acquisition and night operations.

The most significant exceptions to this are the two 2D, multi-offset profiles acquired south of the 3D patch. During acquisition, this area was heavily cluttered with both moving and stationary vehicles, construction materials and debris, and structures. This clutter was a significant source of coherent noise and no useful information could be extracted along the two multi-offset profiles. A portion of common-offset line 10 was also acquired in this area and while the data quality was poor, a 120 ft section of the clay surface was imaged in this area.

Common-offset survey

Acquisition parameters for the common-offset survey are shown in Table 1.

Table 1. Acquisition parameters for the common-offset survey

Antenna frequency	50 MHz
Offset	6 ft
Trace spacing	1 ft
Sampling interval	1.6 ns
Recording time	500 ns

Data Processing. The first step in processing is correcting for the time zero lag. This is a systematic delay between the start of recording and the generation of the source pulse. The time delay can be accurately computed by first dividing the known antenna separation distance by the speed of light ($3x10^8$ m/s). This value is then subtracted from the near offset arrival time of the direct air wave (the event traveling directly from the transmitter to the receiver through the air) to compute the lag time. The lag time is then subtracted from all records. Next we apply automatic gain control followed by a 10-20-100-200 MHz bandpass filter.

Some care is taken to attenuate coherent noise related to scattering from surface objects. When this energy originates off-end or from point scatterers it is easy to identify as it travels with moveout at the speed of light in air. Off-end energy and the tails of point diffractors are effectively removed using an F-K filter. When the energy is reflected from a planar interface that is subparallel to the profile orientation, it may be difficult or impossible to differentiate in 2D data, so some care is required in interpretation to ensure that interpreted events do not have a surface origin. Along the long 2D profiles collected in this study, this is trivial since any subparallel surface reflectors are present over only small sections of any profile and thus are easily identified.

After F-K filtering adjacent traces are stacked to reduce the level of random noise. The data are then converted to the depth domain using a velocity of 400 ft/μs. This is believed to be a reasonable velocity estimate for the Provo alluvium and is based on velocities computed from the multi-offset surveys. Using this velocity, depth-to-clay estimates from the radar data are

within ± 2ft of the depth determined from core or CPT data over most of the survey area.

Finally a topographic correction is applied. we estimated site topography using a cubic data gridding algorithm with 123 previously surveyed well and CPT locations as control points.

Data Interpretation. Overall, interpretation of the alluvium/clay interface is relatively straightforward, and an estimate of depth-to-clay can be made from manual picks of the radar data to within about ± 2 ft. The following procedure is used. First, the strongest, laterally continuous event is identified. Where the boundary is well defined, this event appears in a couplet pattern. This means that there are two light bands separated by a strong dark band that correspond to the reflection from the alluvium clay interface. Distortion of the reflected wavelet during processing, and uncertainty in the velocity estimate used for depth conversion make it difficult to choose an exact point on the reflected event that corresponds to the alluvium/clay interface. Therefore, to accurately estimate depth-to-clay, we define a pick "template" using one of the control points. Taking the known depth-to-clay from a boring that lies along one profile, we identify which point on the reflection corresponds to the clay contact. This horizon is then picked throughout the survey. The accuracy is checked by comparing to know depth-to-clay at other control points within the survey. In this case, we use the depth-to-clay at OU1-072 as the control point, and find that the alluvium/clay contact corresponds to the top of the strong dark band within the couplet. Extending this horizon throughout the survey results in a very accurate estimate of depth-to-clay (verified by control points) in most areas.

However, there are a few exceptions. In general, uncertainty in depth-to-clay can be attributed to a variety of factors. These include coherent noise from energy scattered at the surface, poor resolution of the saturated zone boundary (SZ) and clay interface where the clay is below but close to the SZ, and lateral velocity heterogeneity not accounted for in depth conversion. Additionally, inaccurate information contained in some boring descriptions makes verification of the radar interpretation difficult. Complicating the interpretation is the proximity of the SZ. In most areas the SZ is very close to, or coincident with the clay interface. Where the clay dips significantly below the SZ, both boundaries can be identified in the radar data. Where

the SZ lies less than 3 - 4 ft above the clay interface, neither boundary is well resolved and accuracy of the depth-to-clay estimate is degraded. In most areas, this is not a problem since the SZ is either below the clay or is within our picking accuracy, but it is a potential pitfall to be aware of. Specific problems are identified in the detailed discussion of each line below.

In the following discussion, each line is shown both in relatively raw form and in a fully processed and interpreted format. Picks of the clay interface are shown with a blue line and depth-to-clay at control points are shown in red, with the depth-to-clay indicated by the length of the line. All depths are referenced to an elevation datum of 4800 ft. Control points typically lie within 10 ft of the profile but are greater than this in a few rare cases where no other control was available.

Line 1. It was necessary to acquire Line 1 in two sections due to debris piles related to construction of the main extraction trench. The two sections are labeled Line 1 and Line 1B (Figure 2). Along most of Line 1 (Figure 3) the clay boundary is clearly defined and interpretation is straightforward. Strong scattering from the power line to the south and from a pump truck to the north interfered with the signal making interpretation at either end of the profile difficult. F-K filtering is effective for removing much of the power line scattering and increases the segment of the clay boundary that can be identified. Depth-to-clay correlated well with OU1-073. The clay boundary in Line 1B (Figure 4) is less clearly defined and interpretation is based heavily on control points OU1-139 and OU1-041. The most poorly defined section lies between the power line and the southern slurry wall. Degraded data quality in this area was observed on several lines and is typical of the site.

Line 2. Along this line we see excellent data quality along most of the line with the exception of the area around the power line from 350 ft to 550 ft (Figure 5). Again F-K filtering increases the section of the clay boundary we can identify. Along this profile two relatively deep, steep walled channels are identified south of the slurry wall. These channels are not identified in any previous reports we have seen, and could have a significant impact on groundwater flow and contaminant transport at the site. The channel that lies 200 ft from the southern end of the line is

relatively well defined and depth-to-clay of around 43 ft is confirmed in OU1-064. A potentially deeper channel drops off the end of the line toward the south. The SZ is clearly observed in this area as a relatively flat horizon at a depth of about 25 ft. Again, relatively poor data quality is observed between the southern slurry wall and the power line. No interpretation is possible from about 400 ft to 550 ft. The central extraction trench is evident between about 390 ft and 430 ft. Unfortunately, the clay boundary is not well imaged below the extraction trench. Again, the clay boundary is clearly defined north of the power line.

Line 3. Line 3 (Figure 6) has the best well control of the survey and shows excellent radar data quality with good depth-to-clay correlation at all six control points. There is some uncertainty between 550 ft. and 750 ft. due to strong scattering from telephone poles located near the profile. Additionally, a definitive interpretation is not possible between 900 ft. and 980 ft. due to ringing associated with a road crossing.

Line 4. Data quality along Line 4 (Figure 7) varies significantly and some conflicting information obtained from boring descriptions adds to uncertainty in this profile. There is a good image of the clay surface from 0 ft to 220 ft and from 500 ft to the end of the profile. Significant surface scattering significantly decreases data quality from 200 ft to 400 ft. F-K filtering improves the interpretation potential for the clay surface but the depth estimate in this region is admittedly a "best guess". Unfortunately no control was available for this portion of the profile. There is good correlation at OU1-801 and OU1-807. The correlation at OU1-103 is very poor. Depth-to-clay is estimated at 29 ft in the 1995 RI report (Montgomery-Watson, 1995). It is difficult to make a reasonable correlation with the radar data at this depth. A look at the core log shows that a thick clay is not reached in the full thickness of the log which reaches 40 ft. The radar data support an interpretation that would put depth-to-clay at around 40 ft. suggesting that the original interpretation of depth-to-clay from the core log may be in error. A second conflict arises between OU1-841 and OU1-065. Depth-to-clay in the control logs correlate with two different reflectors. At OU1-841, the log corresponds to a deeper reflector that dips toward the south. At OU1-065, the log correlates with a relatively flat lying shallower horizon. We pick the shallower event as the clay boundary, in both Lines 4 and 6 as this is

consistent with data presented in the 1995 RI, but the deeper event may be a more accurate interpretation. Data along Line 6 (Figure 9) suggest that this may be a channel that has cut into the clay. There is no strong evidence in the original OU1-065 log that supports placing the clay boundary at the shallower horizon at a depth of 35 ft. Unfortunately the event is near the end of both Lines 4 and 6 which limits the interpretation. Additional radar and/or coring data are needed to solve this problem definitively.

Line 5. This profile runs from west to east just outside the southern slurry wall and shows excellent data quality with the exception of a region between 550 ft and 680 ft that is heavily contaminated with surface noise (Figure 8). This noise was surface scatter from a large steel tank trailer located near the profile. And although it is not as well defined here, the same deep channel imaged in Line 2 is imaged in this profile extending from 400 ft. to 650 ft. It appears that Line 2 crossed approximately perpendicular to the channel and that Line 4 crosses oblique to the channel axis. Depth-to-clay cannot be interpreted between 530 ft and 650 ft. Again, the SZ appears as a relatively flat horizon above the channel depression.

Line 6. Line 6 runs east to west and is roughly parallel to Line 5, but lies just inside the slurry wall. This area had generally the poorest data quality at the site, but a reasonable interpretation of the clay surface is still possible along most of the profile. A depression adjacent to the channel imaged along Line 5 is evident, although the shape of the channel is not well defined. The coherent noise from the large trailer is even more prevalent in this area than in Line 5 and makes interpretation of the clay surface impossible between 100 and 300 ft which is where we would guess the channel is located. A high amplitude event dips steeply downward toward the east from 370 ft to 280 ft. While this event appears to be the western bank of the channel, it is actually a surface scatter event. Elsewhere along the profile, the interpretation is relatively straightforward. It is now time to revisit our discussion of depth-to-clay in OU1-065. As in Line 4 we find that at the location of OU1-065 there two reflections close to the depth-to-clay reported in OU1-065. We favor the interpretation that the deeper reflection corresponds to an event dipping toward the west that forms the eastern edge of a channel. Again further radar or core data is needed to define the clay surface in this area.

Line 7. This profile takes a roughly 45° bend near the center but generally runs from southwest to northeast. Data quality along the entire profile is excellent and interpretation of the clay surface is straightforward (Figure 10). Scatter from the power line is effectively attenuated with F-K filtering making it possible to identify the clay surface along the entire profile. There is poor correlation with depth-to-clay from the log at OU1-850. The radar data are of excellent quality in this location and do not support a significantly shallower interpretation of depth-to-clay. We submit the following possible explanations for the discrepancy - 1) OU1-850 is approximately 50 ft offline in this location. It is clear that topography of the clay surface at the site can vary significantly over 50 ft and that the control point is just too far from the line, or 2) that the log was interpreted incorrectly. Either explanation is plausible given evidence from other locations around the site.

Line 8. Line 8 runs from west to east along the road on the north side of the site. Data are of excellent quality and the clay surface is well defined along nearly the entire profile (Figure 11). One exception is between 380 and 450 ft. In this area a relatively deep channel is evident, however surface scatter from a pump truck at a nearby sump obscures part of the base of the channel. There is good correlation with the two control points along this profile.

Line 9. Data quality is excellent on the north end of the line but is significantly degraded near the southern end (Figure 12). This is partially due to surface scatter from the power line, but the signal strength decreases significantly in this area. This may be due to increased surface conductivity. Beyond 500 ft, the interpretation must be considered a best guess.

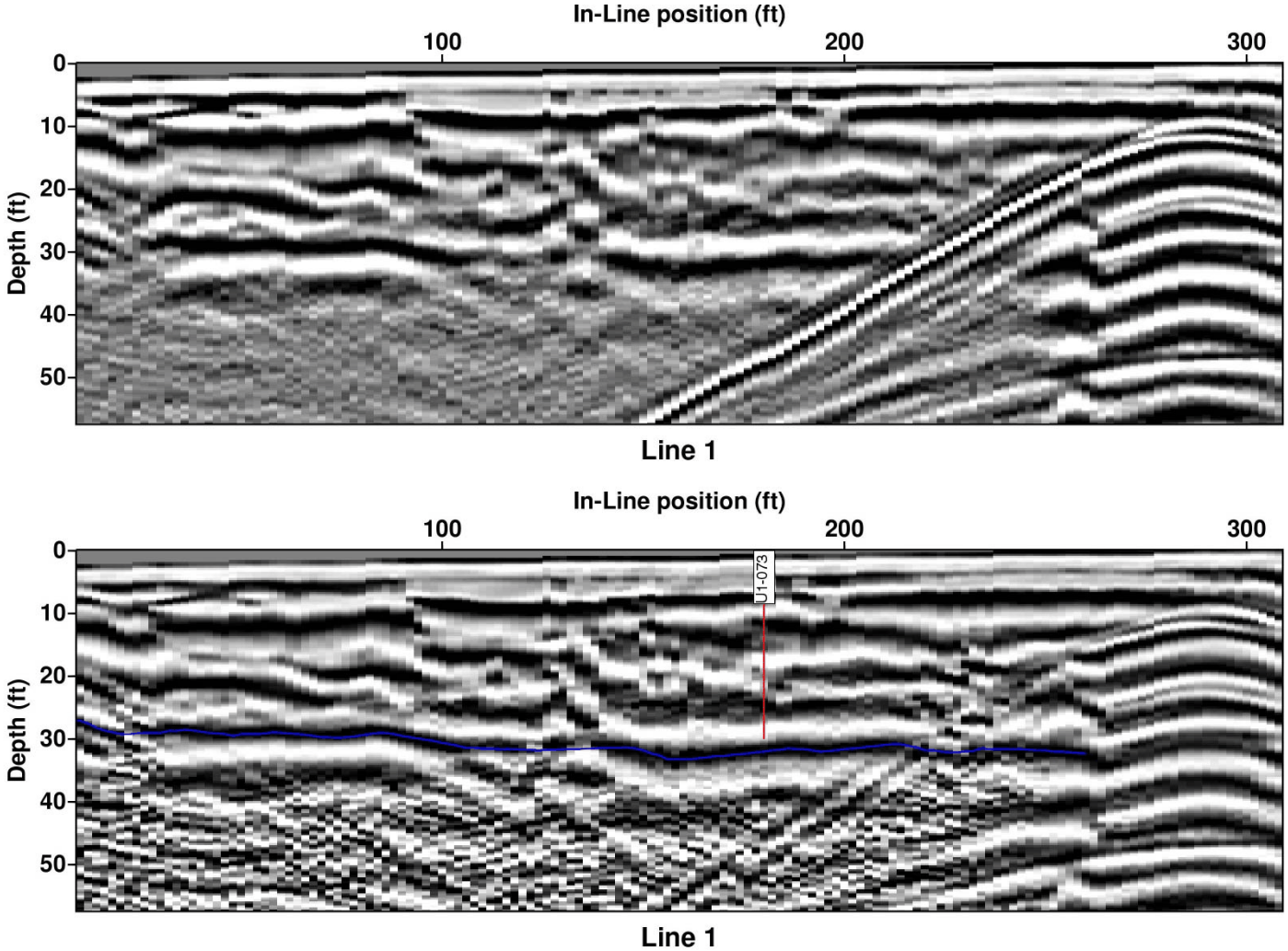

Figure 3. South is to the right in this profile. The clay boundary is well defined in this section. Scattering from the power line to the right and from truck on the left interfere with the signal. F-K filtering attenuates the power line noise significantly.

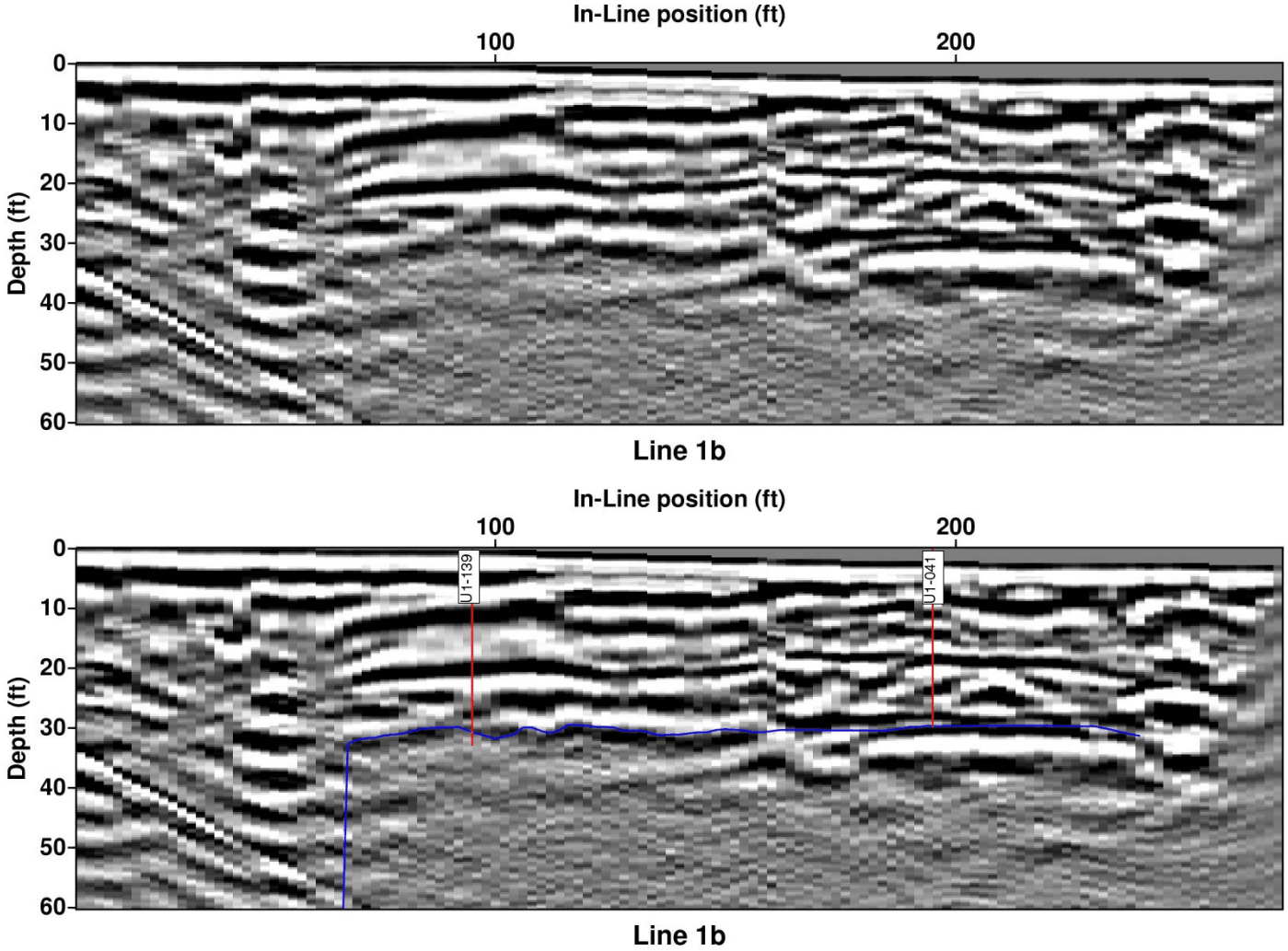

Figure 4. South is to the right on this profile. The clay boundary is not as well defined as in Line 1, and interpretation was based heavily on control points.

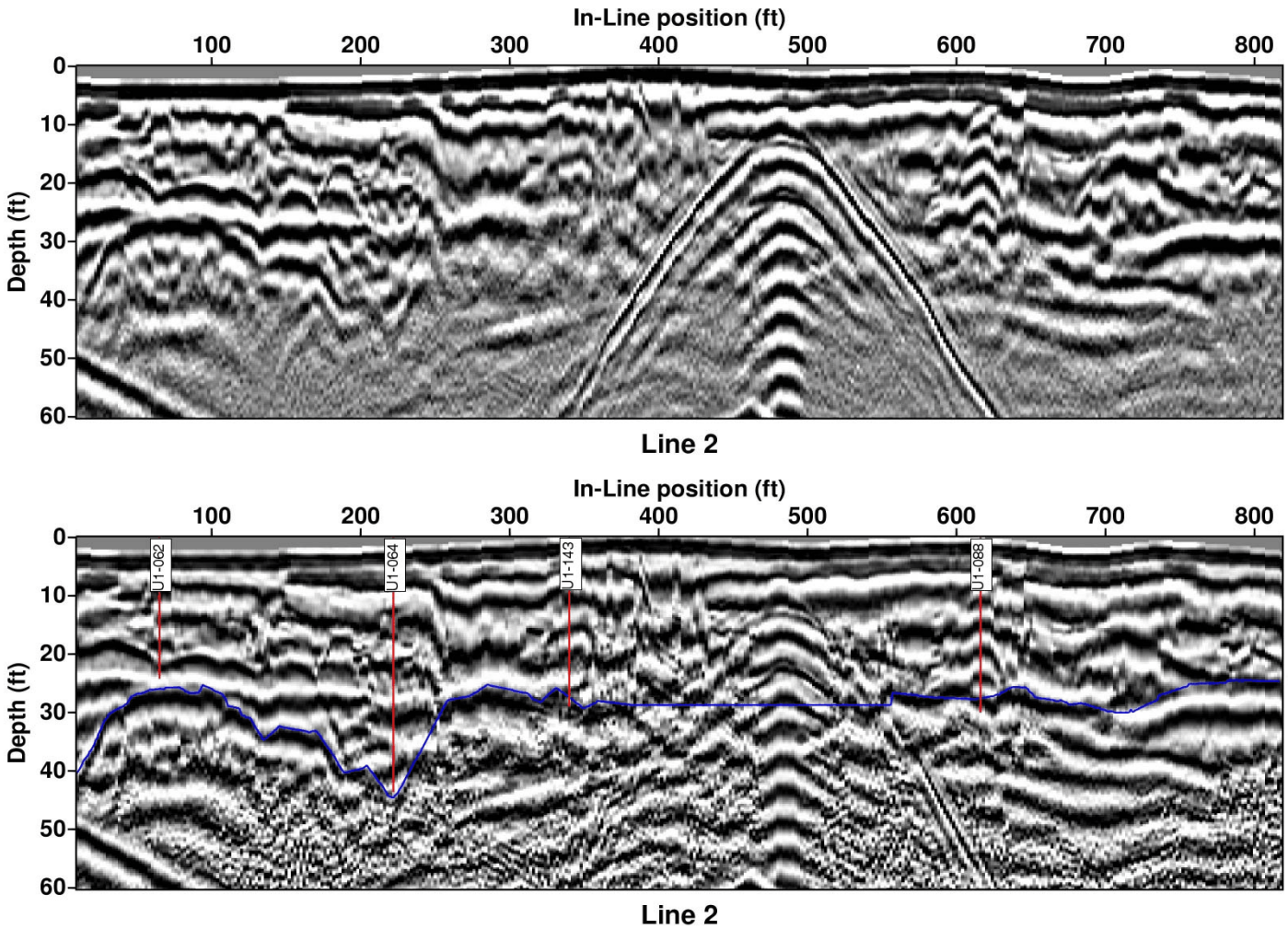

Figure 5. North is to the right along this profile. The most interesting feature seen here are the two deep channels imaged near the southern end of the profile. Depth-to-clay in the channel between 100 ft and 250 ft is confirmed in OU1-064. The central extraction trench is evident between 390 ft and 430 ft as a break in the shallow strata.

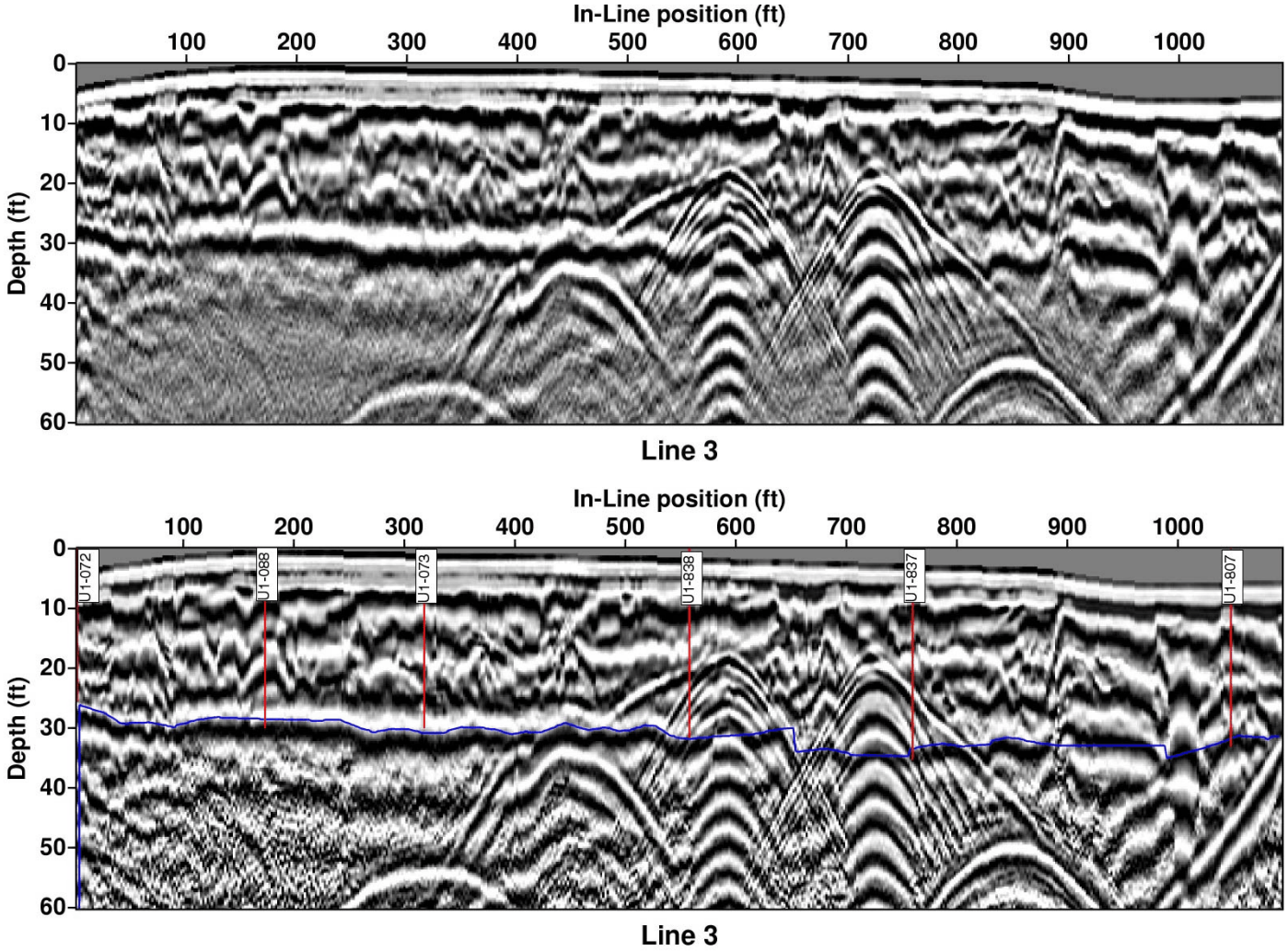

Figure 6. North is to the right along Line 3. Interpreted depth-to-clay is in excellent agreement with all control points along this profile.

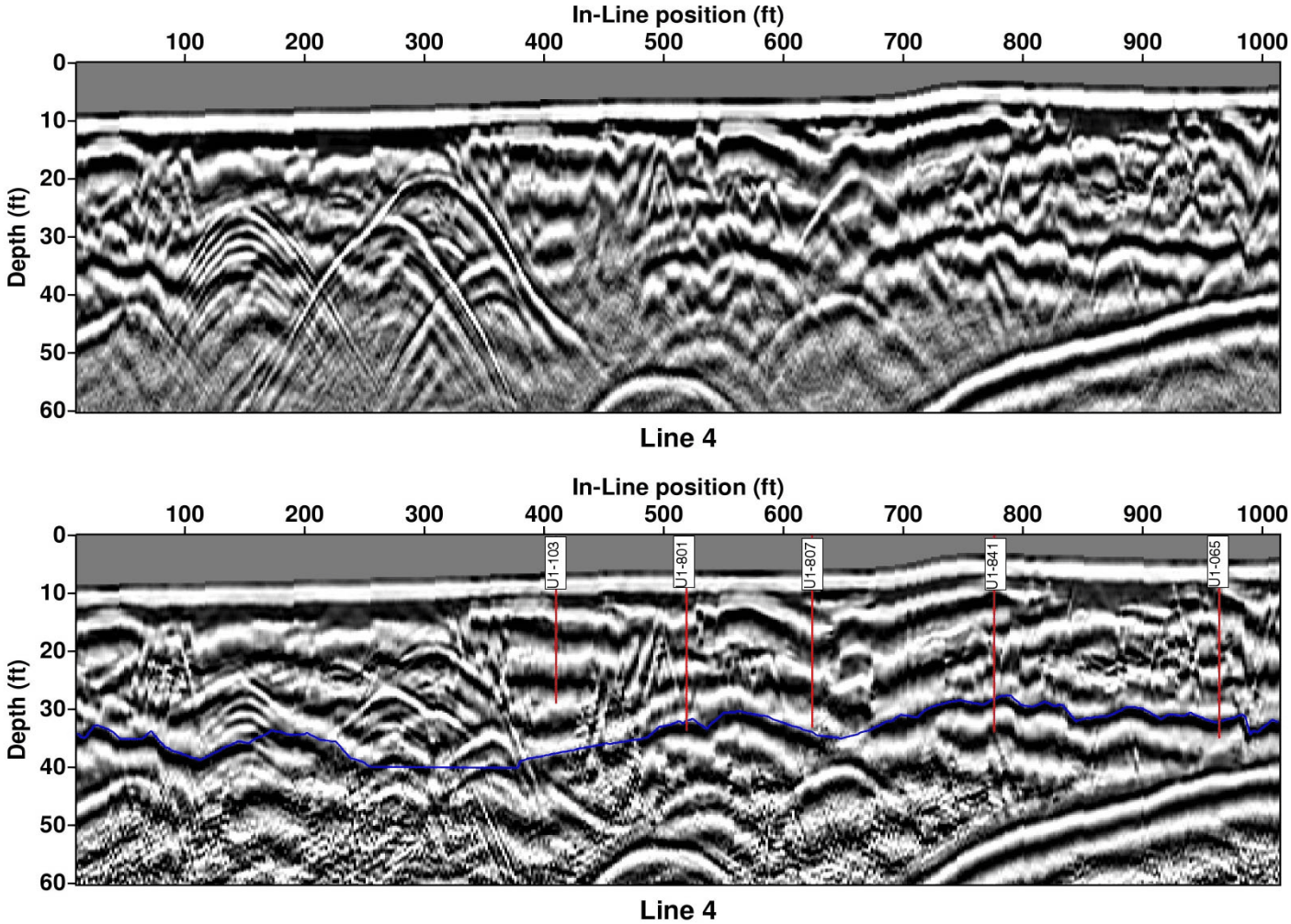

Figure 7. South is to the right. Data quality varies significantly along this profile and there are some conflicts with control data. The interpretation between 200 ft and 400 ft is only a best guess due to poor data quality. It is suspected that depth-to-clay estimates from logs at OU1-103 and OU1-065 are in error.

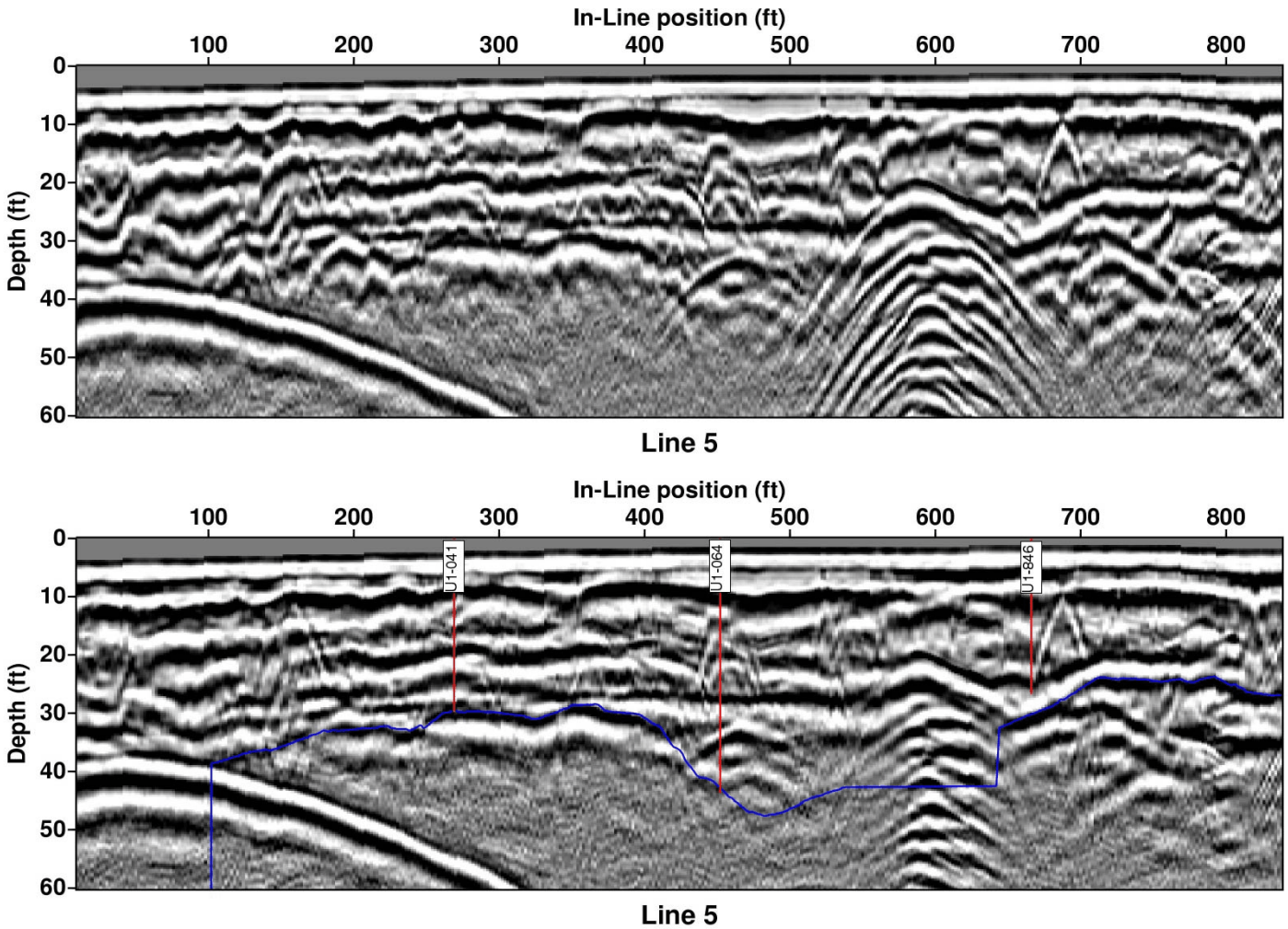

Figure 8. East is to the right. The clay surface is not imaged left of 100 ft. due to surface scatter from the air field fence. The deep channel is also image in Line 2 (Figure 5), although these data suggest the channel may reach depths of close to 50 ft. Interpretation between 550 and 630 ft is not possible due to surface scatter from a large trailer.

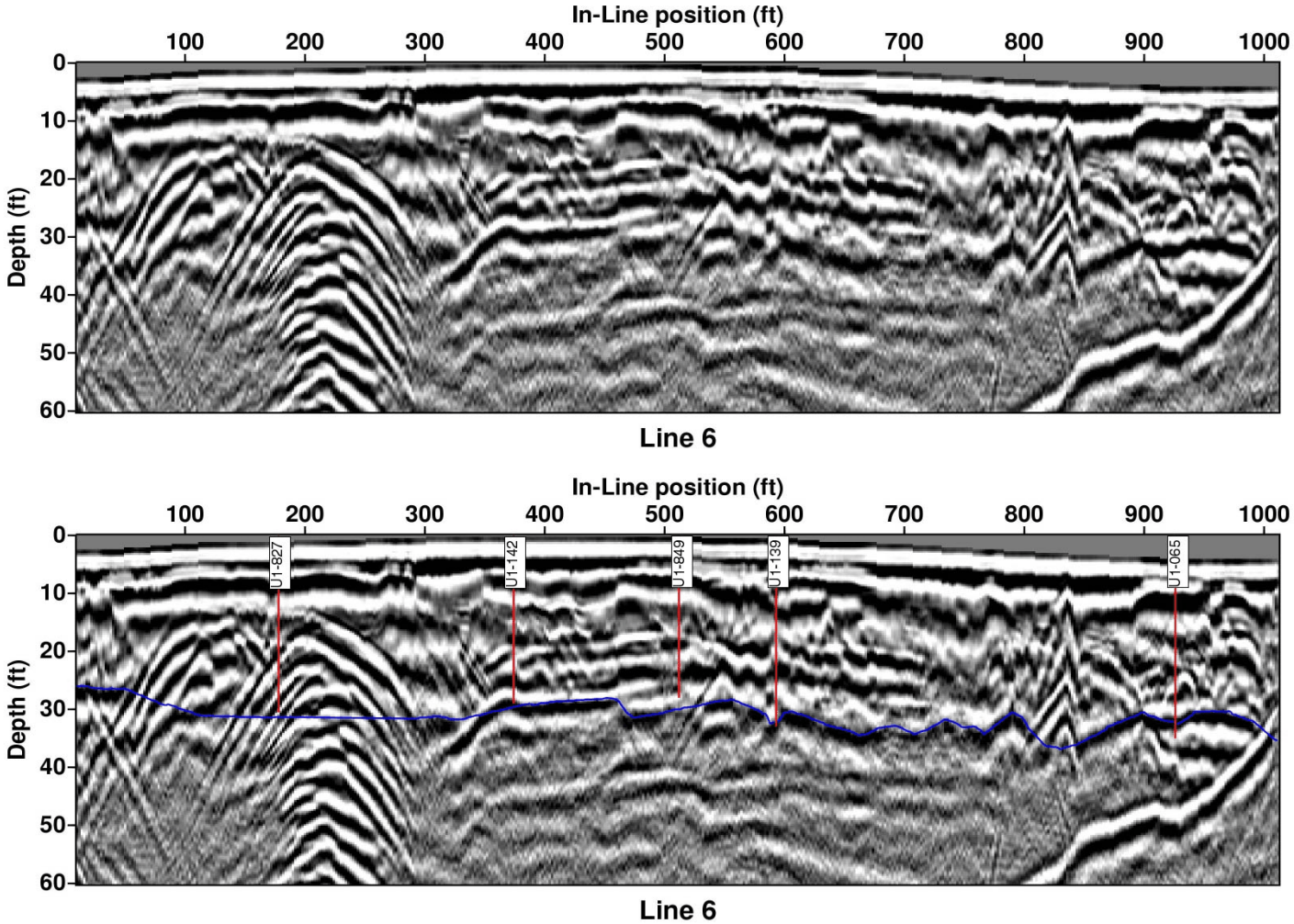

Figure 9. This line runs east to west between the slurry wall and the power line. Although data quality in this area is generally poor relative to the rest of the survey area, a reasonable interpretation of the clay surface is still possible. The high noise area between 50 and 320 ft is an exception and interpretation here is difficult.

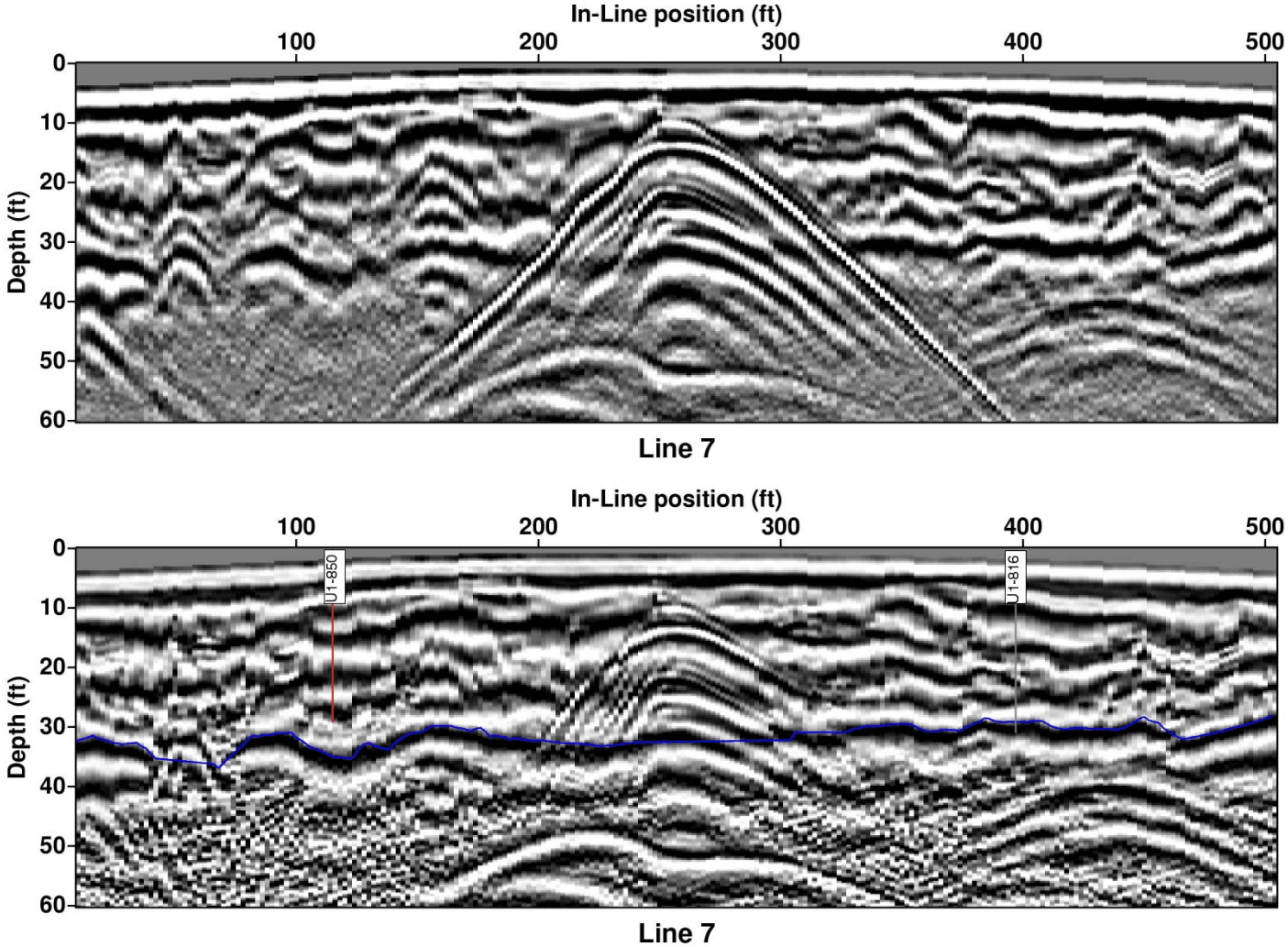

Figure 10. The profile runs generally southwest to northeast. Excellent data quality provides a well defined clay reflection along the entire profile. Poor correlation with OU1-850 may be due to lateral topographic variation or incorrect interpretation of the log.

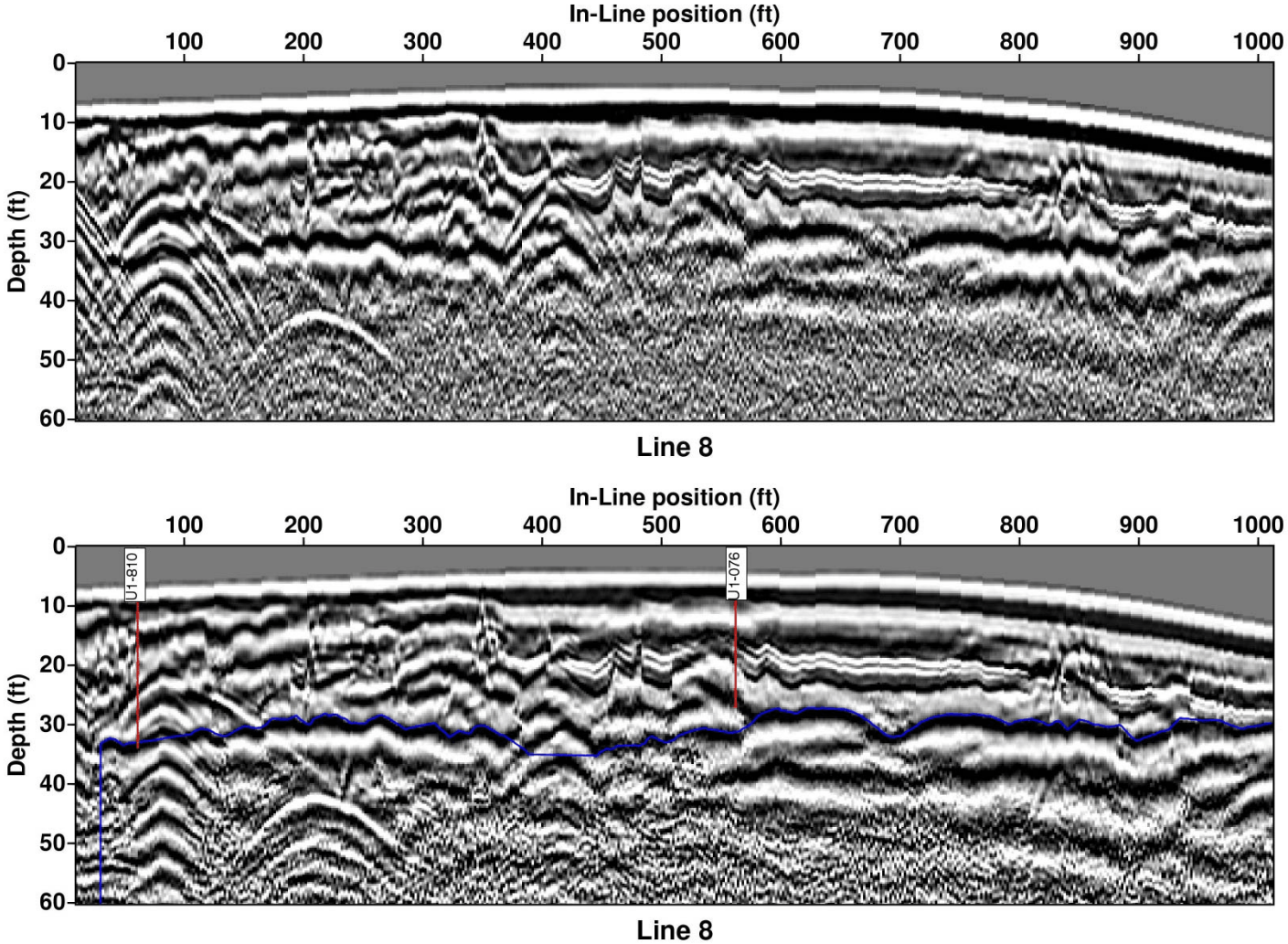

Figure 11. This profile runs west to east along the road on the north side of the site. The clay surface is well defined everywhere except the portion around 400 ft which is obscured by surface scatter.

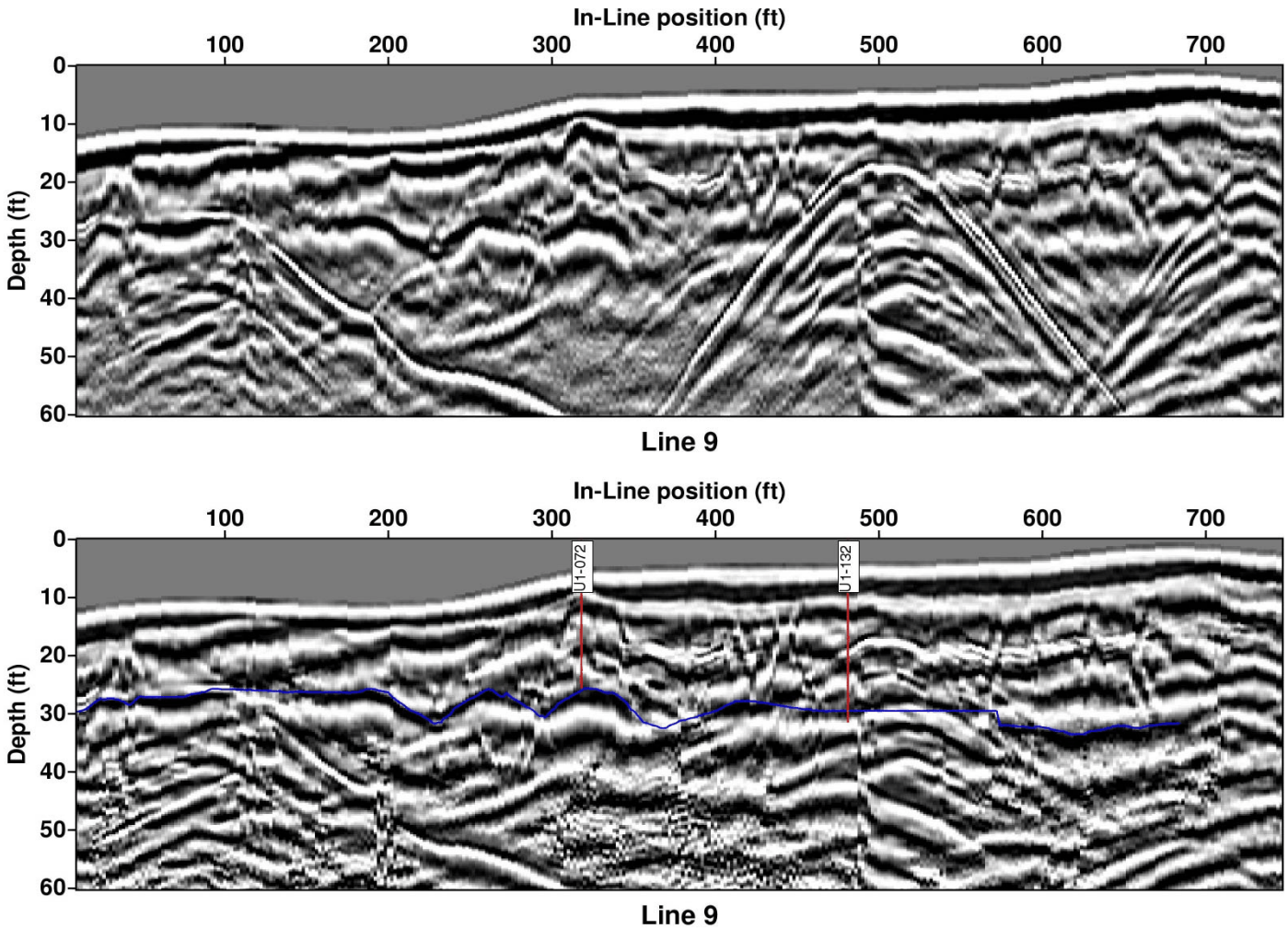

Figure 12. South is toward the right. Data quality is excellent to around 450 ft. Beyond this location the clay reflection is obscured by surface scatter, and the signal strength decreases significantly. Additionally, the SZ and clay boundary are not well resolved on the southern end of the profile.

Discussion of Common-Offset Survey Results. Subject to the specific uncertainties presented in the interpretation section and the limited uncertainty inherent to all geophysical tools, it is clear that GPR provides a good estimate of depth-to-clay over most of the site. Although the radar data does not stand alone, it provides continuity between core locations which can significantly improve our characterization of the near surface groundwater system at the site leading to a better understanding of contaminant transport. When we include the radar data in mapping the clay surface across the site, a significantly more detailed topography begins to emerge (Figure 13). A particularly striking feature is the deep depression in the southeast section of the survey area. This is likely a significant channel, although there isn't sufficient

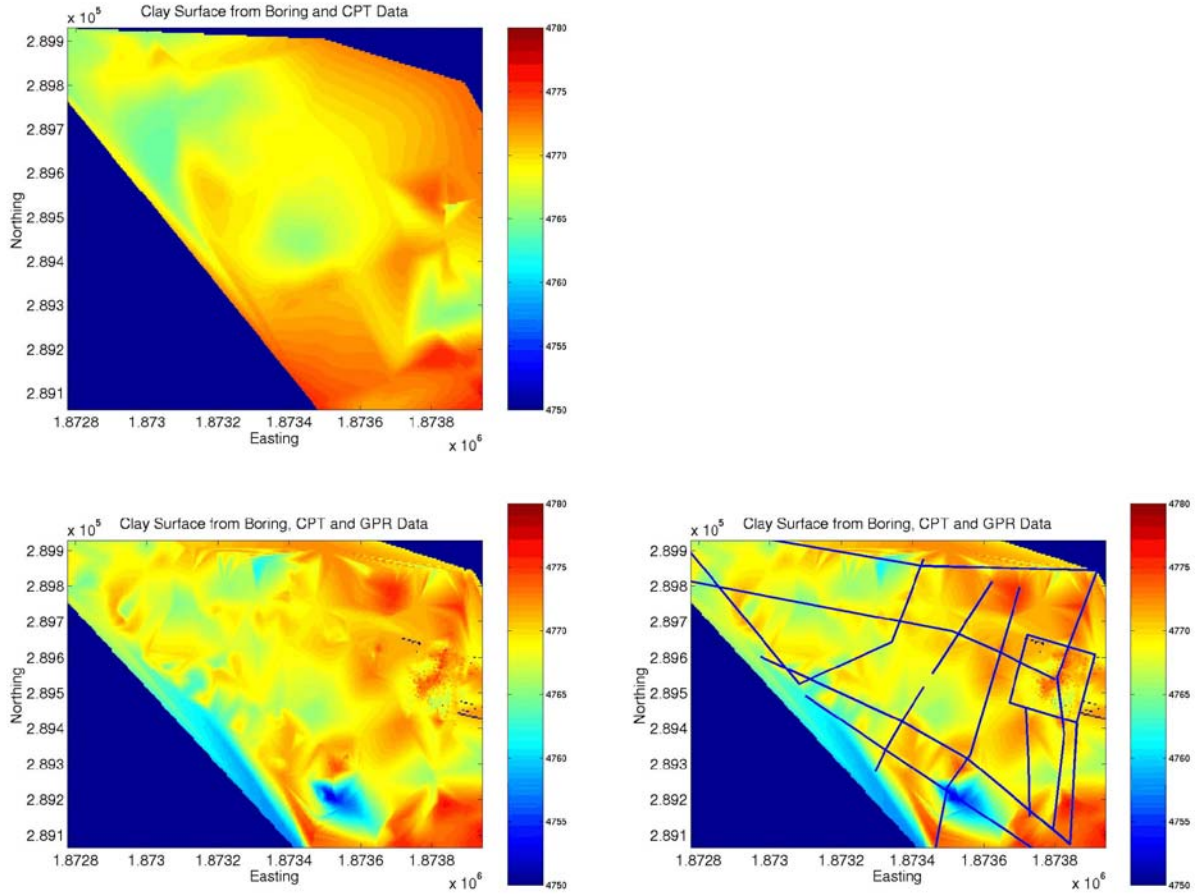

Figure 13. Maps showing clay surface elevations interpreted from boring and CPT data only, and including the GPR data interpretations. GPR provides continuity between direct sampling locations and a significantly more detailed image begins to emerge. The most significant feature not previously identified is the deep depression in the southeast portion of the survey area. This is likely a significant channel, but there isn't sufficient data to determine its trend. Smaller scale channels throughout the site may have a significant impact on contaminant transport.

data to determine its trend. It is the deepest part of the clay surface in this portion of OU-1, and depending on the trend, the channel may have a significant impact on contaminant transport from the source areas. Additionally, smaller scale channels are prevalent throughout the site, and may play an important role in the groundwater shallow groundwater system. A denser grid of GPR data is necessary to gain a complete understanding of the primary and secondary channel system. We recommend that such a study be undertaken in future site investigation. Although we recognize it was not possible during our field study, the data set can be improved significantly in the future by removing all unnecessary surface objects (such as trailers, trucks, debris etc.) and limiting site access during data acquisition. Additionally, multi-offset acquisition and processing techniques can be used to improve data quality in some areas such as in the vicinity of the power line.

The common-offset portion of the study was originally envisioned as a feasibility study designed to identify areas within the site suitable for GPR investigation. We conclude that GPR is suitable for virtually the entire site and that the dataset we acquired may be useful beyond the feasibility stage in building a greater understanding of the shallow subsurface at OU-1.

Table 2. Acquisition parameters for the multi-offset survey

Antenna frequency	50 MHz
Near offset	6 ft
Maximum offset	30 ft
# receivers/common source point	24
source interval	2 ft
receiver interval	1 ft
Sampling interval	1.6 ns
Recording time	500 ns
Line spacing	8 ft
Antenna polarity	Transverse

3-D Multi-offset Survey

Our 3-D survey was designed to bound CDP 1 on the east, west and north sides and to extend to the north beyond the known boundary of the free LNAPL plume. Survey objectives included imaging the sand/clay interface and direct detection of the LNAPL plume.

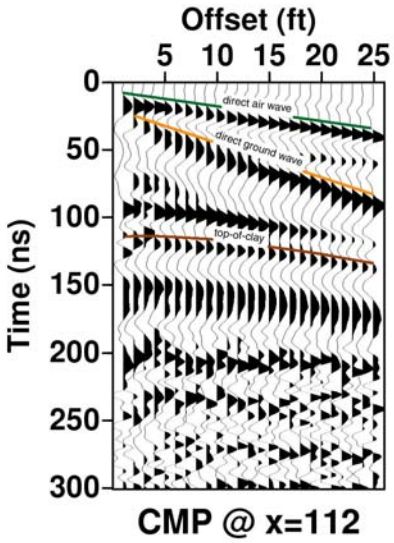

Figure 14. This CMP is along Line 14 which lies about 12 ft west of OU1-072.

Multi-offset data were acquired with off-end geometry with the parameters listed in Table 2. The data were acquired south to north along 20 parallel profiles covering 32,000 sq. ft. Interference with the ongoing construction project prevented us from collecting the full 25 lines called for in the work plan.

Collecting data along parallel lines provides true 3D sampling of the wavefield but not the velocity field. Building a 3D velocity model requires interpolation between 2D velocity profiles determined along each line. This procedure results in an accurate subsurface image as long as no severe cross-line velocity gradients are present.

Data processing. The initial processing steps are identical to those followed for the zero-offset survey including a time lag correction, agc and bandpass filtering. As discussed in the methodology section, multi-offset data acquisition allows for velocity estimation based on the variation of arrival time with offset. In most of the 3D survey area, a very clean reflection from the clay surface is observed over the full offset range (Figure 14). This allows us to make very detailed and precise velocity estimates.

For direct detection of LNAPL we are interested in locating lateral and vertical velocity anomalies with great accuracy. To accomplish this we apply iterative PSDM velocity analysis along each line. The data are migrated in the common-offset domain using a Kirchhoff migration algorithm that accounts for topography. A constant velocity of 400 ft/ns was assumed for the starting model. While this appears to be a reasonable bulk velocity, a better migration result is obtained using a background velocity profile with a negative linear gradient. Including a negative velocity gradient roughly accounts for the increase in moisture content with depth, although this relationship is likely not linear. A number of deviations from the background

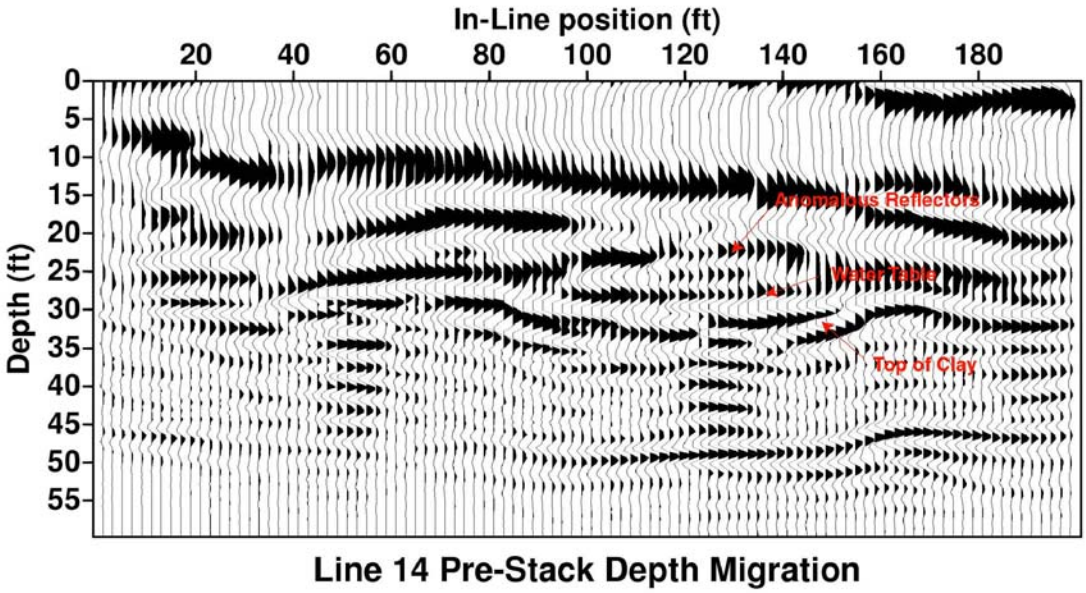

Figure 15. Line 14 lies just west of OU1-072. Along this profile the clay surface dips into a channel between 80 and 160 ft. The top of the SZ is clearly imaged within this depression. Additionally, an anomalous set of reflections is imaged that appear in a dome-like feature above the trough. There is no clear geologic explanation for this anomalous zone.

velocity are identified and included in the velocity model. A very large velocity anomaly, that does not appear to be of geologic origin, is identified just above the water table in the northwest portion of the 3-D patch and may be associated with an accumulation of LNAPL.

After completion of the velocity analysis, all data are pre-stack depth migrated in 2D then sorted into common image point gathers and stacked to attenuate random noise and processing artifacts. The stacked profiles are then combined for 3D interpretation. Data are generally of excellent quality, with a strong reflection clearly evident from the clay surface. Surface scatter from a standing fence, fence debris and construction equipment degrade the data in the southeast portion of the survey. Both pre-stack migration and post-migration stacking act as velocity filters and strongly suppress surface scatter traveling at air velocity. The fully processed profiles are relatively clean, and the clay surface is identified throughout the entire 3D survey. This is subject to the caveat that clay surface estimates in the southeast portion of the survey are not as accurate due to degraded data quality.

3D Data Interpretation and Discussion. The procedure for assigning picking criteria is identical to that followed for the common-offset survey, and again OU1-072 is the seed control point. All other wells within the survey are used only as verification and to judge accuracy of

the interpretation. Since PSDM processing of multi-offset data allows for highly accurate estimates of lateral and vertical changes in velocity, depth estimate uncertainty is significantly reduced in the 3D survey.

Data quality in the processed sections is superb and interpretation straightforward throughout the entire survey (Figure 16). The radar data provide a relatively detailed image of the clay surface (Figure 16). Twelve core logs were available within the active 3D patch providing excellent stratigraphic control (Figure 17). Taking the difference between the clay topography mapped using radar data, and the topography mapped using core information alone, we find that

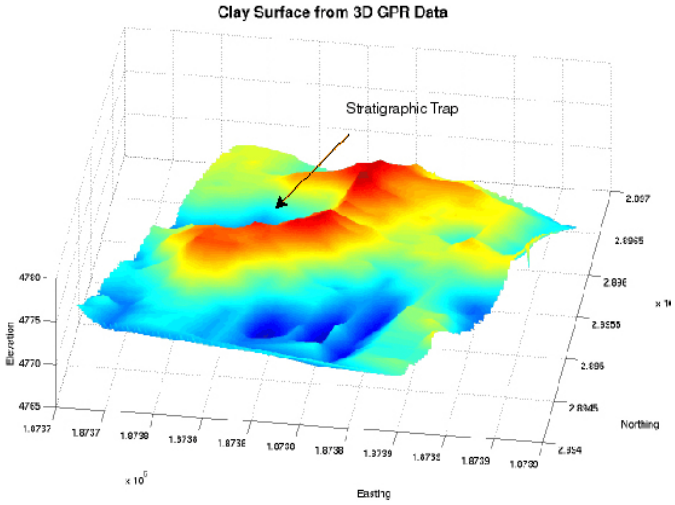

Figure 16. The radar data provide a relatively detailed image of the clay surface. The most striking feature is the ridge and trough located in the northwest portion of the survey with a total relief of about 10 ft. This feature may form a stratigraphic trap in which LNAPL has accumulated.

there is excellent agreement at the wells, but that the two maps diverge significantly away from the wells (Figure 18). In fact, the agreement is within ± 1 ft at most well locations. With this in mind, we can think of the difference map as showing how poor the clay surface characterization is when it is based on core information alone.

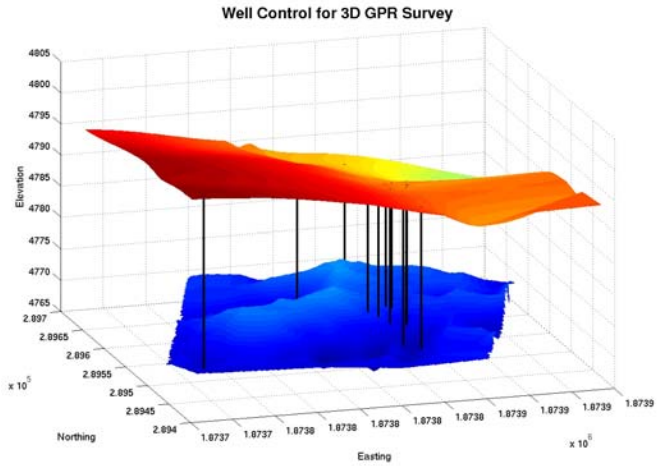

Figure 17. Surface topography, clay topography from radar data, and well control within the 3D patch. Twelve core logs provide stratigraphic control.

The primary objective of the 3D survey is to test methods for direct detection of free NAPL. We found a significant ridge and trough on the clay surface that was not previously identified. The trough lies beyond the known location of the free LNAPL plume, but may act as a stratigraphic trap (Figure 16). Sediment within the trough was not previously sampled so it is not currently known if it contains elevated NAPL concentrations. Our data show a zone of anomalous reflectivity directly above the trough that does not appear geologic in nature (Figure 16). Additionally, velocity analysis indicates that the zone of anomalous reflectivity is associated with a very large velocity anomaly (Figures 19 and 20). Both of these effects are consistent with an accumulation of low permittivity LNAPL.

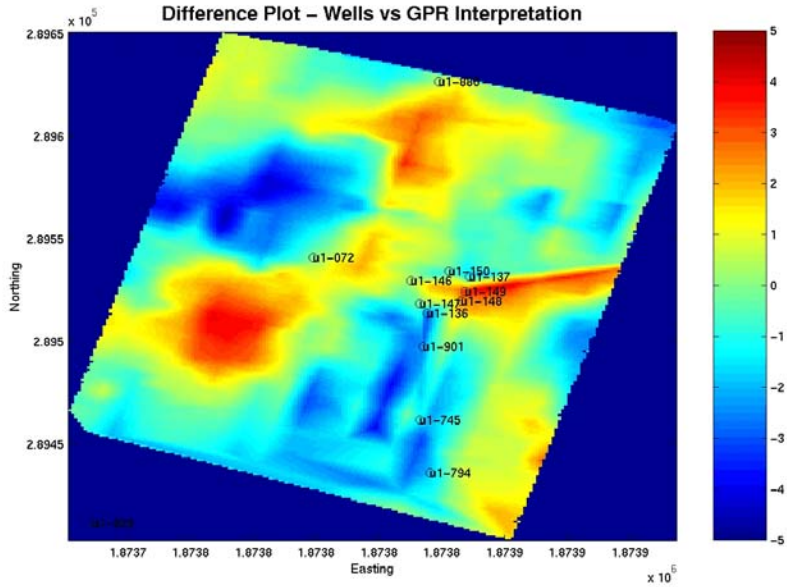

Figure 18. Difference (in ft) between the clay surface estimated from radar data and clay surface estimated from core logs only. The difference is less than a 1 ft at most core locations but varies significantly elsewhere. Radar picks up much of the detail between wells.

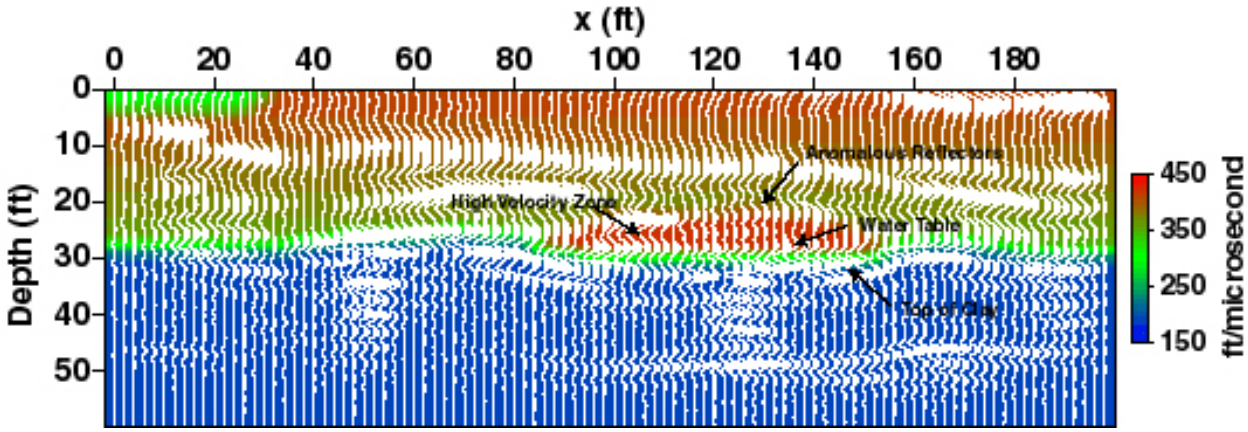

Figure 19. Velocity model and wiggle trace image overlay at Line 14. The high velocity zone is a dramatic velocity anomaly particularly given its position just above the water table where we expect a large decrease in velocity related to an increase in water saturation. A possible explanation is that there is an accumulation of LNAPL within the trough/channel feature.

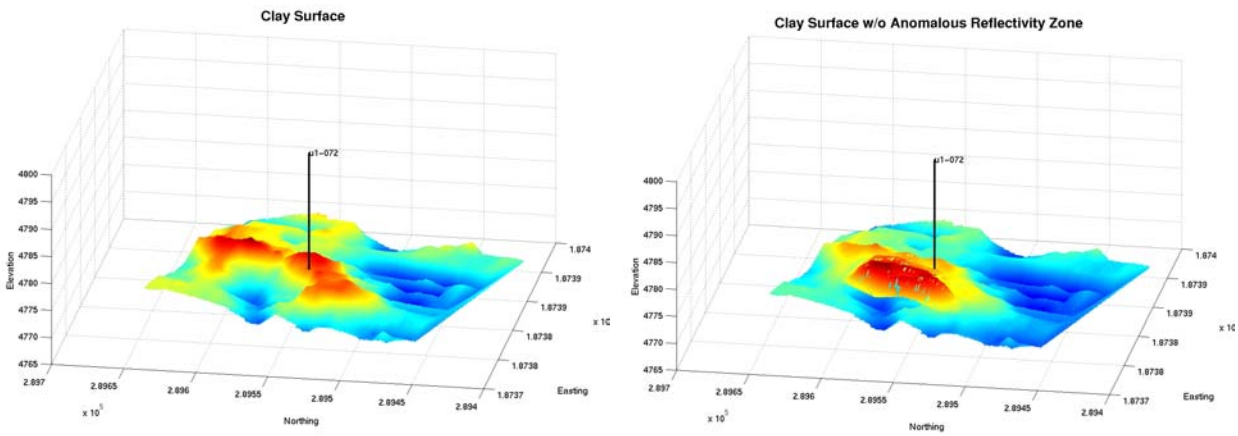

Figure 20. Depression in the clay surface and the upper surface of the overlying zone of anomalous reflectivity. The closest core log, OU1-072, did not sample the anomaly. It lies just outside the zone and hits the clay at a topographic high.

Additionally, preliminary AVO analysis indicates that the anomalous reflectors have a large AVO gradient. This is consistent with the velocity analysis results.

A puzzling feature of the anomaly is that its thickness is about 5 ft. The greatest thickness of free NAPL measured in any well at the site is on the order of 1 ft so it is not likely a floating NAPL pool. Also the domelike shape of the anomaly is not what we expected for a free NAPL pool. We offer two potential explanations. First, the anomaly may be residual LNAPL forming the smear zone. The LNAPL concentration in the smear zone above the trough may be

higher than in adjacent areas because there is a thicker pool within the trough that is not well resolved in the radar data. A second possible explanation is that the anomaly may be related to a vapor transport effect from a relatively thick floating pool. It is also possible that there is a geologic explanation for the anomaly. The anomaly meets our general expectations for a anomalous accumulation of LNAPL and we feel that this interpretation is more plausible. Direct sampling is necessary to verify this interpretation and to identify the transport mechanism responsible for the geometry of the anomaly.

This was the most obvious radar anomaly we found within the survey area, but we know, from previous direct sampling efforts, that there is significant and varied contaminant accumulation beneath the site. Continued research efforts will focus on correlating more subtle radar anomalies with known contaminant accumulations, and attempting to identify the northern boundary of the free NAPL plume. Our data suggest that plume migration is more strongly controlled by the secondary channel system than previously thought and that accurate characterization of the NAPL plume will require detailed delineation of these features.

CONCLUSIONS AND RECOMMENDATIONS

Overall, the GPR study was very successful. With few exceptions the goals of the work plan were met or exceeded. The radar data provides a detailed image of the clay surface over much of the survey area and a there is strong evidence that a previously unidentified contaminant rich zone has been found near CDP 1. Given the success of the radar study we make the following recommendations.

1) Additional sampling or geophysical work should be carried out to define the orientation of the deep channel in the southeast section of the survey area.
2) A denser grid of common-offset data should be acquired to delineate the secondary channel system on a site wide basis.
3) Direct detection of an LNAPL rich zone in the 3D survey area should be verified through direct sampling.

4) Assuming detection of LNAPL is verified, additional areas for detailed 3D multi-offset acquisition and analysis should be identified.

Meeting these recommendations will significantly improve the site characterization.

REFERENCES

Bradford, J., Ramaswami, M., and Peddy, C., 1996, Imaging PVC gas pipes using 3-D GPR: SAGEEP '95, Soc. Appl. Geophys. Env. Eng., Expanded Abstracts, 519-524.

Campbell, D.L., Lucious, J.E., Ellefson, K.J., and Deszcz-Pan, M., 1995, Monitoring of a controlled LNAPL spill using ground-penetrating radar: SAGEEP '95 Symposium on the application of geophysics to environmental and engineering geophysics, Soc. Appl. Geophys. Env. Eng., Proceedings, 511-517.

Davis, J.L., and Annan, A.P., 1989, Ground-penetrating radar for high-resolution mapping of soil and rock stratigraphy: Geophysical Prospecting, **37**, 531-551.

Dix, C.H., 1955, Seismic velocities from surface measurements: Geophysics, **34**, 180-195.

Endres, A.L., and Redman, J.D., 1996, Modeling the electrical properties of porous rocks and soils containing immiscible contaminants: J. Env. Eng. Geophys., **0**, 105-112.

Griffiths, D.J., 1989, Introduction to electrodynamics, Prentice-Hall.

Haeni, F.P., 1996, Use of ground-penetrating radar and continuous seismic-reflection profiling on surface-water bodies in environmental and engineering studies.: J. Env. Eng. Geophys., **1**, 27-35.

Lafond, C.F., and Levander, A.R., 1993, Migration moveout analysis and depth focusing: Geophysics, **58**, 91-100.

Lien, B.K., and Enfield, C.G., 1998, Delineation of subsurface hydrocarbon contaminant distribution using a direct push resistivity method: J. Env. Eng. Geophys., **2**, 173-179.

Loughridge, J., 1998, Application of seismic tools and techniques to ground-penetrating radar (GPR) studies: M.A. thesis, Rice University.

Newmark, R.L., Daily, W.D., Kyle, K.R., and Ramirez, A.L., 1998, Monitoring DNAPL pumping using integrated geophysical techniques: J. Env. Eng. Geophys., **3**.

Olhoeft, G.R., 1986, Direct detection of hydrocarbon and organic chemicals with ground-penetrating radar and complex resistivity: NWWA/API Conference on petroleum and hydrocarbons and organic chemicals in groundwater -- Prevention, detection, and restoration, NWWA, 284-305.

Santamarina, J.C., and Fam, M., 1997, Dielectric permittivity of soils mixed with organic and inorganic fluids (0.02 GHz to 1.30 GHz: J. Env. Eng. Geophys., **2**, 37-51.

Montgomery Watson, 1995, Hill Air Force Base, Utah: Comprehensive remedial investigation report for Operable Unit 1 - Volume 1:, Montgomery Watson.

Young, R.A., and Sun, J., 1996, 3D ground penetrating radar imaging of a shallow aquifer at Hill Air Force Base, Utah: J. Env. Eng. Geophys., **1**, 97-108.

Young, R.A., and Sun, J., 1998, Extracting a radar reflection from a cluttered environment using 3-D interpretation: J. Env. Eng. Geophys., **3**, 121-131.

Zelt, C.A., and Smith, R.B., 1992, Seismic traveltime inversion for 2-D crustal velocity structure: Geophys. J. Internat., **108**, 16-34.

APPENDIX G: GPR OFFSET DEPENDENT REFLECTIVITY ANALYSIS FOR CHARACTERIZATION OF A HIGH-CONDUCTIVITY LNAPL PLUME

Bradford, J.H., 2003, GPR offset-dependent reflectivity analysis for characterization of a high-conductivity LNAPL plume: SAGEEP 2003 Symposium on the Application of Geophysics to Environmental and Engineering Problems, Env. Eng. Geophys. Soc., 238-252.

GPR OFFSET DEPENDENT REFLECTIVITY ANALYSIS FOR CHARACTERIZATION OF A HIGH-CONDUCTIVITY LNAPL PLUME

John H. Bradford
Center for Geophysical Investigation of the Shallow Subsurface
Boise State University
Boise, ID

Abstract

In July, 2002 my field team collected a 10,000 sq ft 3D ground-penetrating radar (GPR) survey consisting of over 4000 linear ft. of dense, multi-fold data. The field site is located over a known LNAPL plume associated with a former fire training facility. Previous workers have shown that hydrocarbon contamination, within the saturated zone, is associated with anomalously high electric conductivity at this site. Regions of high conductivity result in zones of increased GPR signal attenuation. These high conductivity areas manifest as "shadow zones" below the water table reflection (10 - 15 ft b.g.s) and are readily identified on GPR profiles. The purpose of the current study is to evaluate the efficacy of GPR amplitude vs. offset (AVO) analysis in the characterization of conductive contaminant plumes. Amplitude analysis reveals that a clear AVO gradient anomaly is associated with the LNAPL plume. The lateral extent of the anomaly is roughly coincident with the shadow zone. This study demonstrates the utility of multi-offset data acquisition, and suggests that GPR AVO analysis may be another valuable tool in contaminated site characterization.

Introduction

Non-polar organic liquids are collectively referred to as as non-aqueous phase liquids (NAPL) due to their low solubility in water. NAPLs are subcategorized by their density relative to water with DNAPL being denser than water and LNAPL being lighter than water. It follows that DNAPLs tend to sink through the water column until they reach a low permeability layer, while LNAPLs tend to remain near the water table with free product floating on the water column and residual product present in a smear zone above and below the water table. Both LNAPL and DNAPL leave a zone of residual contamination along their migration routes. Chlorinated solvents (DNAPL) and fuel hydrocarbons (LNAPL) are examples that commonly found at contaminated sites.

NAPLs typically have low relative permittivity ($K \sim 2.5$) and high electric resistivity ($\sim 10^4$- 10^5 ohm-m) relative to water which make them attractive targets for characterization using electric geophysical methods. As the NAPL displaces water in the sediment pore space, a zone of anomalous electric properties may be induced. An attractive first order conceptual model is based on the premise that NAPL contaminated zones will have low permittivity and low conductivity relative to the surrounding formation. A number of controlled spill experiments have been consistent with this model (Brewster and Annan, 1994; Campbell et al., 1995; DeRyck et al., 1993), and this has proved to be an effective working model in the interpretation of geophysical data acquired over a fresh LNAPL spill (Orlando, 2002), and over aged LNAPL and DNAPL spills at one field site (Deeds and Bradford, 2002; Lien and Enfield, 1998; Newmark et al., 1998). However, it is now well established that aged hydrocarbon spills at some sites, have anomalously high electric conductivity in direct contrast to the simple conceptual model stated above (Atekwana et al., 2000; Monier-Williams, 1995; Sauck et al., 1998). This divergence stems from the

incorrect assumption that the electric properties of the contaminated zone will be controlled by the electric properties of the unaltered LNAPL. Sauck (1998) proposes a conceptual model that explains the high conductivity LNAPL plume in terms of increased dissolved solid concentrations in the ground water related to biogenic activity. The relatively low number of LNAPL plumes documented as having low electric conductivity and low electric permittivity suggests that the conductive LNAPL plume model may be more widely applicable.

Most GPR data are acquired with a constant transmitter-receiver offset. While in many cases this provides an adequate image of the subsurface, significantly more information can be obtained when multi-fold data are acquired, where at each sampling location, traces are recorded at several source-receiver offsets. Not only does multi-fold acquisition allow us to improve image quality using seismic reflection processing methodologies (Fisher et al., 1992; Fisher et al., 1996; Loughridge, 1998), but also allows us to measure variations in offset dependent reflectivity which is the basis for amplitude vs offset (AVO) analysis (Castagna, 1993). Since AVO analysis depends only on energy reflected from the upper surface of a target boundary, we can determine the permittivity of the zone just below the boundary, even if no energy penetrates the boundary. This is in contrast to velocity analysis which requires a reflection originating below the zone of interest. Although little work has previously been published in this area, AVO analysis is receiving greater attention. Lehmann (1996) discusses complex reflection coefficients and the effects of conductivity, Bergmann et al. (1998) briefly discuss AVO response in the context of a broader synthetic case study. Baker (1998) presents a modeling study indicating potential for detecting LNAPLs based on the transverse AVO response. Zeng et al. (2000) present a detailed modeling study considering the effects of varying the Cole-Cole parameters on the AVO response. Deeds and Bradford (2002) show that the technique can be effective in the characterization of a low permittivity anomaly associated with LNAPL contamination at Hill Air Force Base, UT. The purpose of the current study is to investigate the utility of AVO analysis in a conductive plume environment.

The field site is a former fire training facility, designated FT-02, located on the now decommissioned Wurtsmith AFB, in Oscoda, MI (Figure 1). Over a period of about 24 years, large quantities of fuel were burned on open ground during weekly training exercises. A significant volume of hydrocarbons did not burn and seeped into the underlying aquifer. In 1982 a concrete catch basin was constructed to minimize the amount of contaminant reaching the subsurface. By the early 1990s, the free product plume was up to 1 ft thick, and extended more than 600 ft downgradient from FT-02 (Bermejo et al., 1997; Sauck et al., 1998).

The stratigraphy below the site consists of fine to medium grained sand and gravel deposits extending to a depth of approximately 65 ft. Below this is a 20 - 100 ft thick silty clay layer which is thought to be the lower boundary for contaminant migration. The surficial aquifer is unconfined, with the water table present 10 - 15 ft below the surface. The site was formerly a National Environmental Technology Test Site (NETTS), and was the site of a long term natural bioremediation investigation. Although no longer an active NETTS site, the wealth of characterization data available make this an excellent location for a semi-controlled GPR field experiment. More recently a soil vapor extraction system was installed, and is currently operating continuously.

Central to the selection of this site for the current study are a series of geophysical investigations carried out by Sauck et al. (1998) and Bermejo et al. (1997). They found that the site provided excellent conditions for GPR with strong reflections well below the water table. Additionally, they found that there was a well defined, high attenuation anomaly coincident with the LNAPL plume. Through resistivity and self potential measurements, and by inference from the GPR data, they concluded that high electric conductivity was associated with both the LNAPL and the dissolved phase plume.

Through a comprehensive 3D, multi-offset, multi-polarization data set, I demonstrate that AVO

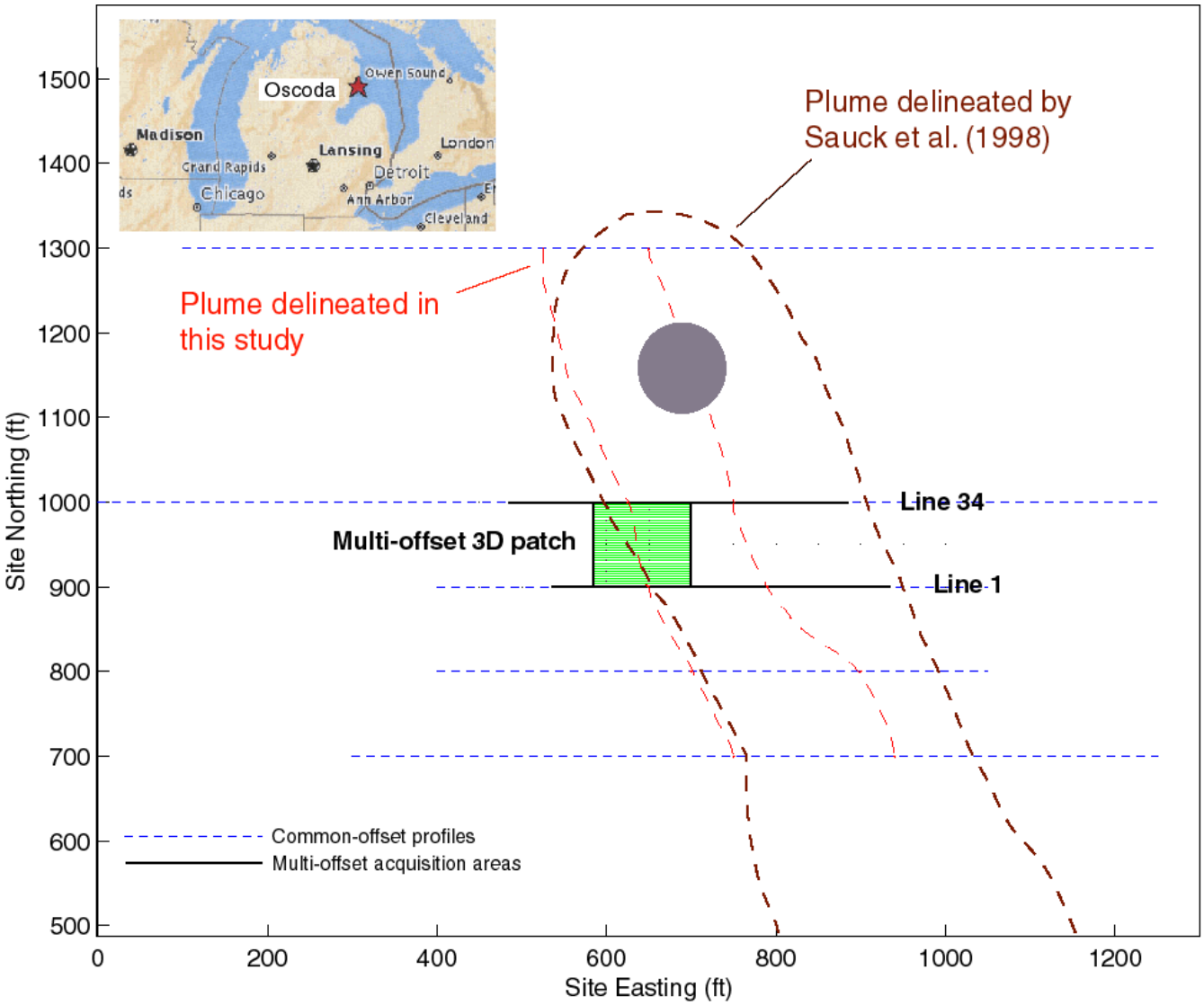

Figure 1. . Field site location and survey layout.

analysis is effective in delineating the zone of contamination, and that careful analysis may reveal details in plume geometry that are not readily evident from qualitative image interpretation or other multi-fold methodologies such as velocity analysis. Critical to this success was acquisition and analysis of continuous multi-fold profiles in both TE and TM polarizations.

AVO Processing for LNAPL Detection

I begin by defining two orientations for linear dipole antennas. The first is transverse electric (TE), in which the transmitting and receiving antennas are parallel, and oriented perpendicular to the survey profile. The electric field in this mode is polarized transverse to the vertical plane oriented along the survey direction. This plane is called the plane of reflection (Griffiths, 1989). The second orientation is transverse magnetic (TM), in which the antennas are in-line, and oriented parallel to the survey direction. In this mode, the electric field is polarized parallel to the plane of reflection. TE is the mode most commonly used in both common-offset and multi-offset GPR surveys, but the AVO responses for transverse and parallel polarization are dramatically different. The reflection coefficients for TE and TM fields incident on a single reflecting interface are

$$R_{TE} = \frac{ER_{TE}}{EI_{TE}} = \frac{\cos\theta_1 - \sqrt{K_2/K_1}\cos\theta_2}{\cos\theta_1 + \sqrt{K_2/K_1}\cos\theta_2} \quad (1)$$

$$R_{TM} = \frac{ER_{TM}}{EI_{TM}} = \frac{\cos\theta_2 - \sqrt{K_2/K_1}\cos\theta_1}{\cos\theta_2 + \sqrt{K_2/K_1}\cos\theta_1} \quad (2)$$

EI and ER are the incident and reflected fields, θ_1 and θ_2 are the angle of incidence and transmission, and and K_1 and K_2 are the relative electric permittivites for the upper and lower boundaries. These, of course, are the Fresnel equations with the assumption that the magnetic permeability is constant. The equations are valid for plane waves in isotropic media and can be reformulated in terms of the wave number to give expressions for conductive, frequency dependent media.

In theTM mode there exists an angle of incidence at which all reflected energy is extinguished by the out of phase component of the incident field. At this angle, R_{TM} goes to zero and there is a 180° phase rotation. The angle at which R_{TM} goes to zero is known as Brewster's Angle (θ_B). For the zero conductivity case, θ_B is given by

$$\tan\theta_B = \sqrt{\frac{K_2}{K_1}} \quad (3)$$

which is easily derived by setting Equation 2 equal to zero.

The Fresnel equations are only valid for a simple interface, but LNAPL typically forms a thin pool floating at the top of the water table. This pool may only be a few cm thick which will be below the image resolution in most cases, but this does not mean we can't detect it. The presence of a thin layer can cause a significant deviation in the reflection coefficient curve. Consider the FT-02 site. Sauck et al. report as much as 1 ft of free product at the top of the water table. The velocity in the vadose zone is about 450 ft/µs which gives a wavelength of 4.5 ft at 100 MHz. Thus, the LNAPL layer is below the 1/4 wavelength image resolution limit, which only means that the top and bottom of the layer cannot be differentiated. King et al. (1992) derive the three layer reflection coefficients for TE and TM plane waves, showing that for multiple layers, the reflection coefficient is frequency dependent. Using the three layer plane wave reflection coefficients given by King et al., and the method described by Deeds (2002) to compute reflection amplitudes for a broad band signal, I estimate the water table reflection coefficient curves for a 100 MHz Ricker wavelet. This wavelet is close to the recorded GPR signal for the Sensors and Software PE 100 system used in this study. I consider three cases: 1) a 1 ft thick intermediate permittivity (K_{TL}=8.5) NAPL layer, 2) a 1 ft thick low permittivity (K_{TL}=3.4) NAPL layer, and 3) no NAPL layer (Figure 2). It is important to note that the reflection coefficient curve is for a composite reflection that includes the contribution of the thin bed. The zero offset reflection coefficient is higher for the low permittivity NAPL

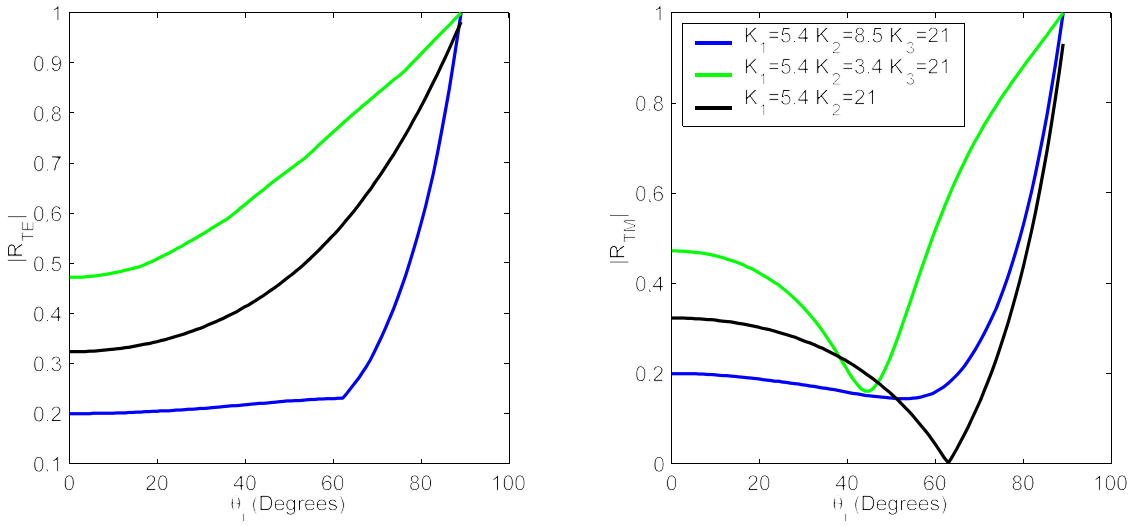

Figure 2. . TE and TM water table reflection coefficient curves for a 100 MHz Ricker wavelet with: — a 1 ft thick intermediate permittivity NAPL layer: — a 1 ft thick low permittivity NAPL layer: — no NAPL layer. Both the presence and permittivity of a thin layer have a significant impact on the reflection coefficient curves.

case, with a smaller gradient in the TE mode and a larger gradient at near offsets in the TM mode. Additionally there is a significant shift in the amplitude minima related to Brewster's angle, although the amplitude does not reach zero. For the case of an intermediate permittivity NAPL layer, the zero offset reflection coefficient is decreased and the near offset amplitude gradient is significantly lower for both TE and TM modes. Again the minima associated with Brewster's angle is shifted and significantly muted.

The reflection coefficients are only a starting point in understanding the AVO response in field data. There are many factors that impact the amplitude of the reflected signal that are unrelated to the reflection coefficient. These include geometric spreading, signal attenuation, heterogeneity in the overburden, and source and receiver directivity patterns. Castagna (1993) gives a detailed discussion of factors affecting seismic amplitudes, which are also relevant GPR AVO studies.

Of particular importance in GPR studies are source and receiver directivity. Many GPR antennas are designed to behave approximately like an oscillating dipole and the source and receiver radiation patterns have a strong angular dependence. These patterns have been discussed extensively in the literature (Papas and Engheta, 1982; Tsang and Kong, 1973). Engheta and Papas (1982) derive the far field 3-D radiation pattern assuming an infinitesimal, horizontal dipole is placed at the boundary of a half-space, with the lower half consisting of a low-loss dielectric. The radiation patterns have a lobate shape, and there is a sharp maxima and null at the critical angle of the earth-air interface for the TE and TM polarizations respectively (Figure 3). Other workers have recorded significant deviations from these patterns in

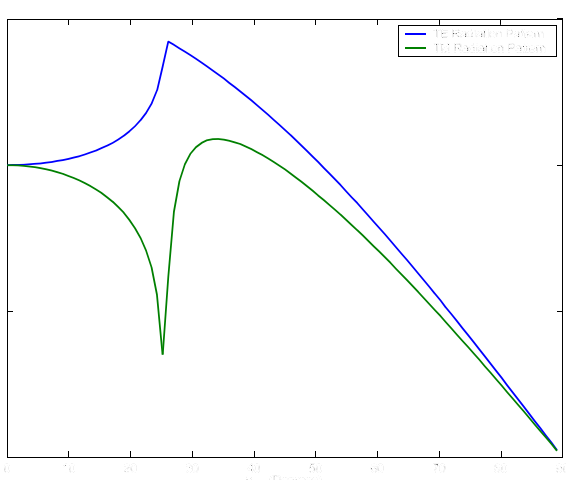

Figure 3. . TE and TM radiation patterns for an infinitesimal dipole at the air/earth interface assuming $K_E = 5.4$. θ_{TO} is the take-off angle measured from vertical.

the laboratory, even at relatively large distances from the antenna (Annan et al., 1975; Chew and Kong, 1981; Wensink et al., 1990). In particular, the sharp maxima and null points, at the critical angle for the earth-air interface, are absent or muted in the near field. Wensink et. al. (1990) concluded that far field conditions had not been reached by a distance equivalent to 15 wavelengths (λ). In many cases in GPR, particularly for buried object detection or shallow contaminant studies, the reflecting target may be within 10λ.

Data Acquisition and Analysis

Data Acquisition

The field team conducted the site investigation in July, 2002. The first objective was to reproduce the results of Sauck et al. (1998). During the earlier characterization of the site, permanent survey markers were established on a 50 ft grid. This enabled us to revisit precisely the same profiles recorded during the Sauck et al. investigation. We acquired 9000 ft of common-offset GPR data coincident with 5 of Sauck et al.'s profiles. Acquisition parameters are noted in Table 1.

We found the same type of attenuation anomaly noted by the previous investigators. This is most evident as an area of low reflection amplitudes, or "shadow zone", beginning just below the water table and extending to depth (Figure 4). Attempting to follow the same criteria used by Sauck et al., I mapped the spatial extent of the attenuation anomaly. This was not entirely straightforward as the anomaly has a transitional character along some lines (ie Line 1). Therefore, the mapped anomaly is the zone of maximum attenuation which appears to be consistent with Sauck et al.'s criteria. Although the character of the attenuation anomaly is the same, the geometry of the LNAPL plume appears to have changed significantly in the 8 years since Sauck et al.'s initial investigation. Most notably, the width of the plume has decreased significantly, being only about half as wide as that measured by Sauck et al. (Figure 1). Additionally, the plume axis appears to have shifted toward the west.

Table 1. Acquisition parameters

GPR System	Sensors and Software PE100 w/ 100 MHz antennas
Common-offset Acquisition:	
trace spacing	1 ft
recording time	500 ns
stacks/trace	32
Multi-offset Acquisition:	
TE Mode	34 lines - 3 ft line interval
TM Mode	9 lines - 12 ft line interval
Source Interval	2 ft
Receiver Interval	1 ft
TE near offset	3 ft
TM near offset	7 ft
recording time	750 ns
stacks/shot record	16
sampling interval	0.8 ns (for all)

Based on the results of the common-offset survey, the location for the 3D multi-offset survey was chosen such that the western most boundary of the plume would cross diagonally through the 3D patch (Figure 1). This layout gave significant coverage of both on- and off-plume areas. Multi-offset 3D data were acquired along parallel, 100 ft profiles spaced 3 ft apart. Additionally, two, 400 ft long east/west profiles were acquired along the northern and southern boundaries of the 3D patch. These profiles extend well beyond the east and west boundaries of the attenuation anomaly, and are roughly centered on the plume (Figure 1). Continuous multi-fold data were acquired in both TE and TM modes with the acquisition parameters noted in

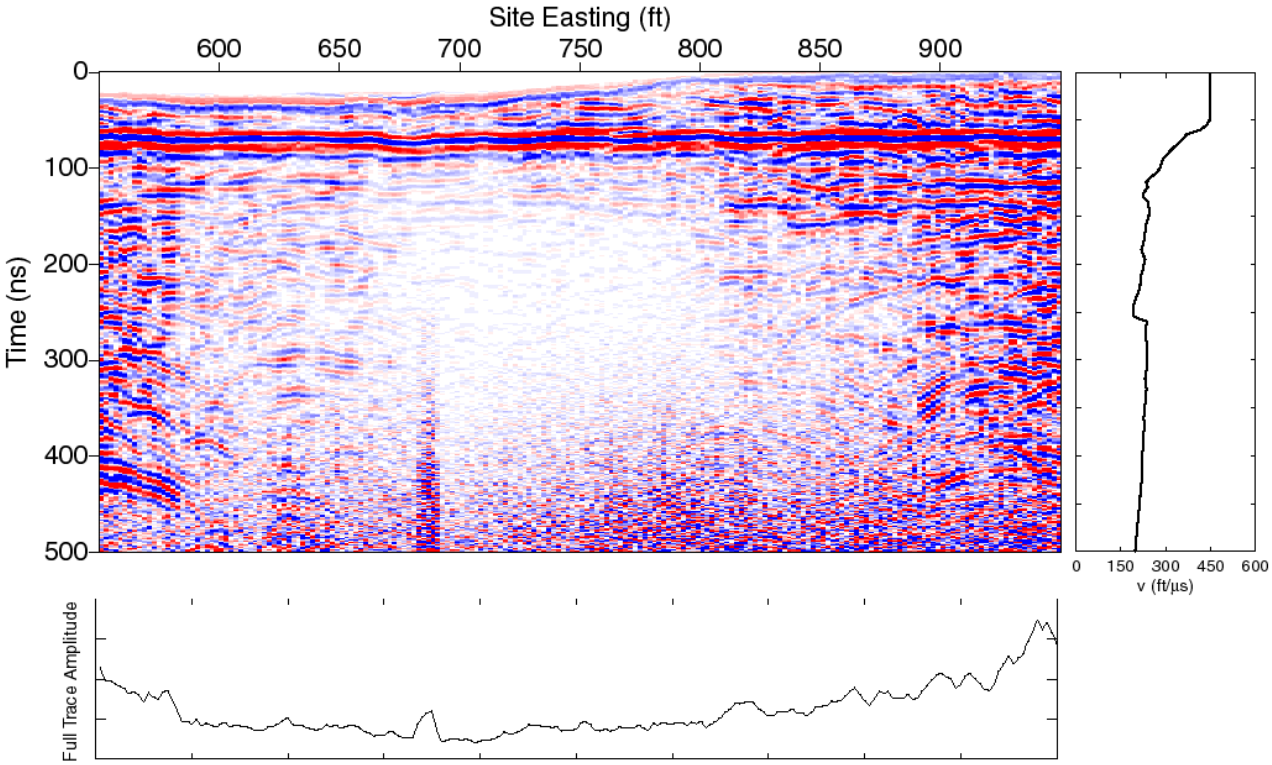

Figure 4. . Line 1 stack with average interval velocity model and full trace amplitude plot. The attenuation anomaly associated with the LNAPL plume extends from about 590 ft to 890 ft. The full trace amplitude plot suggests a gradational plume boundary with the attenuation gradually increasing toward the center with the highest attenuation at around 700 ft.

Table 1.

General Processing and Interpretation

The initial processing stream consists of a t_0 shift to correct for the start time delay and instrument drift. This is followed by a spherical spreading correction and exponential gain correction with an attenuation coefficient of 100 dB/µs. For imaging purposes, this coefficient is selected by trial and error to give the data a balanced appearance through the full range of recording time in the off-plume areas, but has no quantitative significance. Spreading and attenuation corrections are followed by a bandpass filter (25-50-200-400 MHz) to attenuate the low frequency transient signal at small times and high frequency random noise. The velocity structure is then determined through semblance velocity analysis. Finally, the data are stacked and corrected for elevation statics.

I determined the average interval velocity by first averaging the stacking velocities over the full 3D patch, then converted to interval velocity using a smoothed gradient Dix inversion (Figure 4). Maximum lateral velocity variations are only around 10%, so the 1D velocity model is a reasonable representation of the subsurface. Velocity in the vadose zone is very high at around 450 ft/µs, which is consistent with clean sand and low residual water saturation. Below the water table the velocity drops to 220 - 190 ft/µs which is consistent with clean water saturated sand.

The stacked sections are of excellent quality, and show many of the same features noted by Sauck et al. (Figure 4). In the off-plume areas, strong reflections are evident to greater than 500 ns. The most prominent reflection originates from the water table at a time of around 60 ns. Sauck et al. interpret the deep (> 150 ns) hummocky reflections as paleo-dunes.

The most relevant feature is the high attenuation anomaly associated with the contaminant plume. Qualitatively, the attenuation anomaly appears as a zone of muted reflection amplitude below the water table

and extending to depth. This can be represented quantitatively, by computing the trace envelope function (the absolute value of the Hilbert transform) then summing along the trace. This representation clearly shows decreased reflection energy in the zone of high attenuation (Figure 4). Additionally, the amplitude shows a gradual decay toward the center that is not readily evident from qualitative interpretation of the profile. This may indicate a diffuse plume boundary. There is no apparent lateral velocity anomaly that correlates with the attenuation anomaly. This indicates that either the process resulting in NAPL related conductivity changes does not produce a permittivity anomaly, or that the permittivity anomaly is below the resolution of stacking velocity analysis. The analysis below suggests that the latter is the case.

AVO Analysis

In the following discussion I focus only on the water table reflection. There are two reasons for this. First, the water table reflection is the highest amplitude and most laterally coherent event in the dataset, and thus presents the most reliable target for analysis. Second, the analysis yields an unexpected, but important result.

In this study, I use two levels of AVO analysis which vary from primarily qualitative for rapid scanning of large data volumes to very detailed analysis to develop a quantitative understanding of the AVO response. For first pass analysis, I fit a curve of the form $D_t(\theta) = A + B\sin^2\theta$ to the data along constant time horizons. D_t are the NMO corrected data sorted into CMP gathers and θ is the angle of incidence at the reflecting boundary. The angle of incidence is computed using the equation (Walden, 1991)

$$\sin^2\theta_1 = \frac{x^2 v_N^2}{v_{stk}^2\left[v_{stk}^2 t^2(0) + x^2\right]} \tag{4}$$

This equation is valid as long as the assumptions of NMO velocity analysis are not violated which is reasonable in this case. The fit parameters A and B are the intercept and gradient attributes respectively. A approximates the zero offset reflection amplitude and B is the referred to as the AVO gradient. It should be noted that I applied no radiation pattern corrections or detailed attenuation corrections prior to this analysis. While not quantitatively rigorous, this analysis provides a basis for relative comparison along laterally coherent horizons.

Plots of the AVO gradient show a clear, well defined anomaly, in both TE and TM modes, that roughly coincides with the attenuation anomaly (Figure 5). This correlation is not exact, but I will return to this point later in the discussion. I also find that water table reflection amplitude decreases by as much as 40% over the attenuation anomaly. This decrease in amplitude correlates with the AVO gradient anomaly. Lets first consider only the TE AVO response. In off-plume areas, the TE AVO gradient is large indicating that the amplitude is increasing significantly with increasing offset. In on-plume areas, the TE AVO gradient is very small indicating that the amplitude remains roughly constant across the offset range.

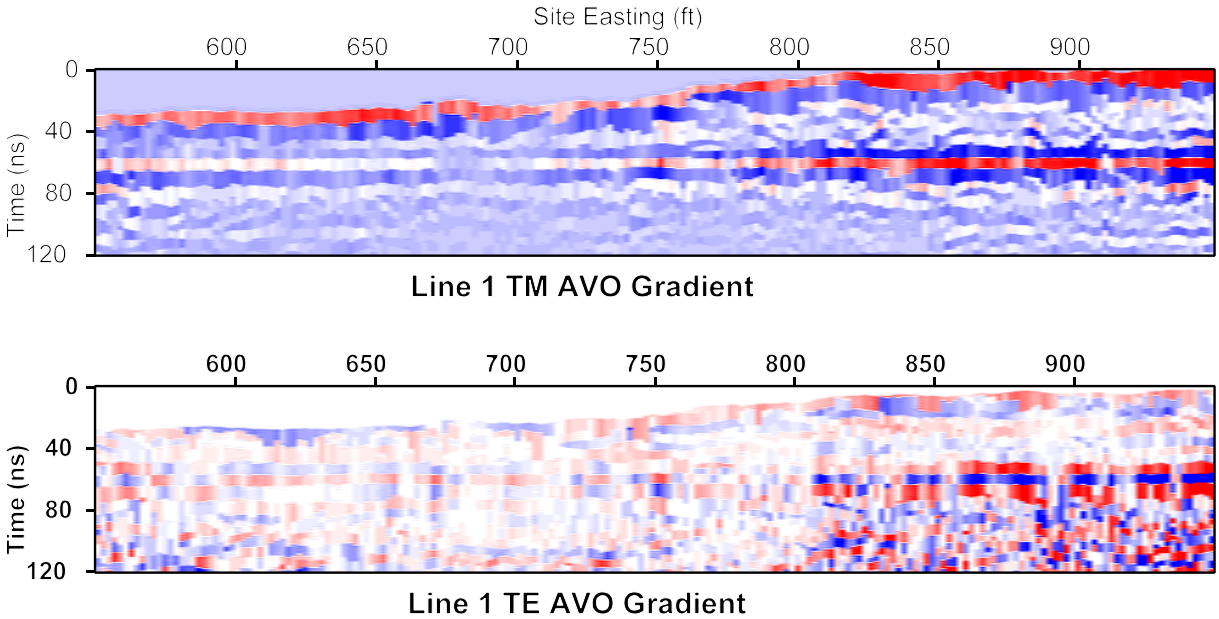

Figure 5. . Plots of the TE and TM AVO gradient along Line 1. The water table reflection is at 60 ns. The gradient is estimated from a $\sin^2\theta$ fit to the data. Note that the water table horizon has been flattened.

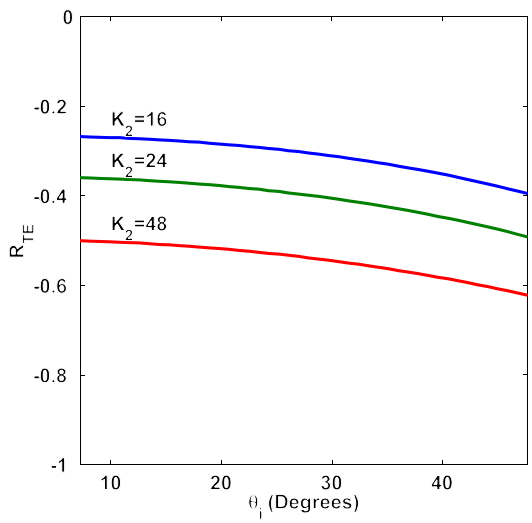

Figure 6. . Fresnel reflection coefficients for a range of saturated zone permittivities. Although the near offset amplitudes vary significantly, the AVO gradient is nearly identical for the three curves.

This is coupled with decreased near offset amplitudes. There are many reasonable explanations for this response, and a careful evaluation of several alternatives is warranted. First consider a simple change in dielectric permittivity across the water table boundary. Results of the velocity analysis indicate that the in the vadose zone $K_1 \approx 5.4$, while in the water saturated zone $K_2 \approx 21$. Guessing that there might be a permittivity anomaly in the vadose or saturated zones associated with the plume, I compute reflection coefficients for a range of permittivity contrasts using the TE Fresnel Equations. The computation is limited to angles-of-incidence (θ_i) observed for the acquisition geometry. This analysis demonstrates that for a simple boundary with an increase in permittivity, the zero-offset reflection coefficient changes significantly, but the AVO gradient is very insensitive to the permittivity contrast (Figure 6).

Some readers might note that there is an apparent correlation of the AVO attributes with topography along Line 1 suggesting a processing artifact. When the distance between the reflector and surface decreases, the angle-of-incidence increases, and the travel path decreases resulting in lower spreading and attenuation losses. These effects would combine to increase the AVO gradient and near offset amplitude which is exactly the opposite of what is observed along Line 1. So there is no solid basis for attributing the effect to topography, and I find no evidence for topographic correlation in the 3D data.

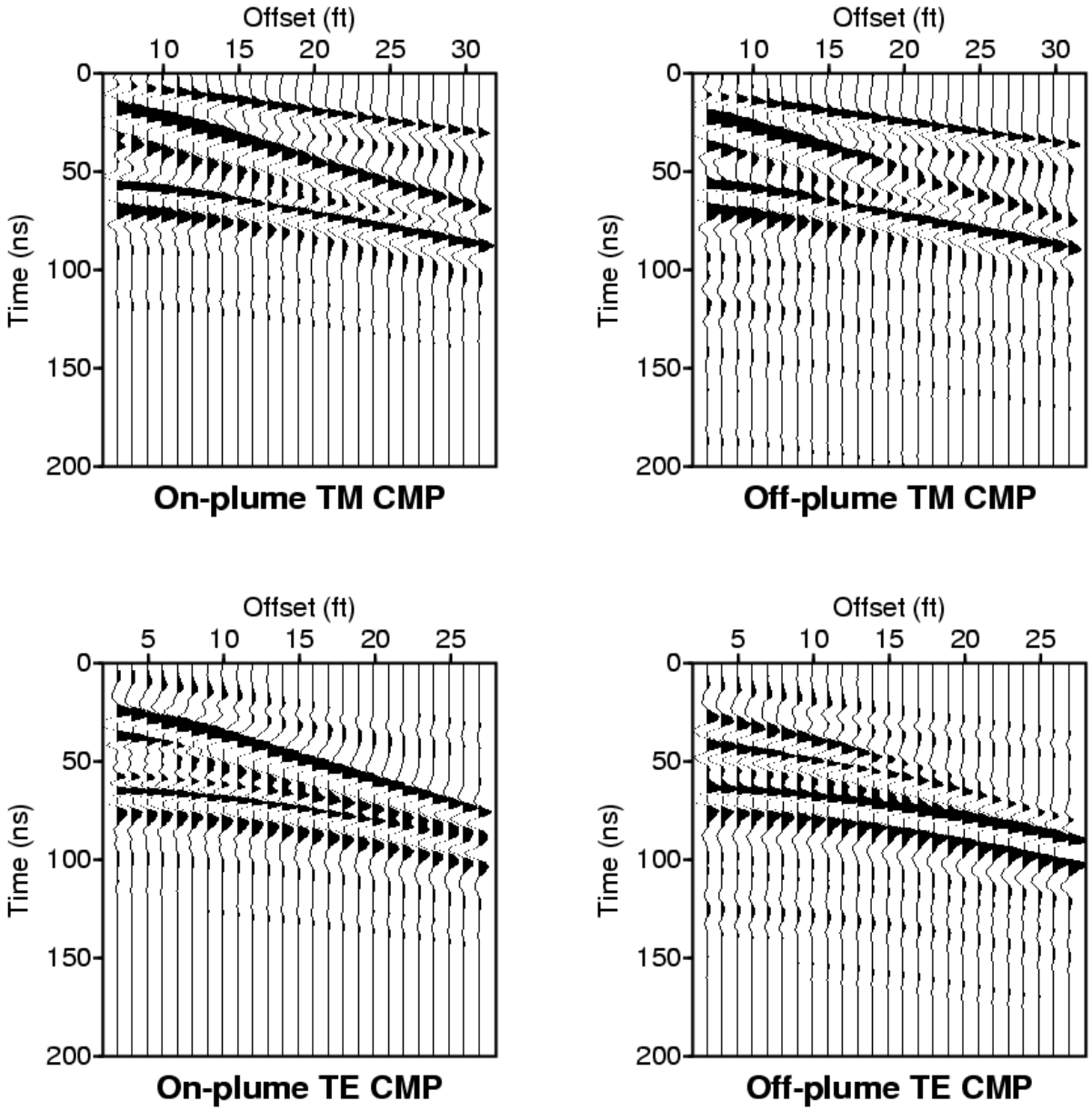

Figure 7. . CMP supergathers created by combining 20 adjacent CMPs from the on-plume and off-plume areas along Line 34.

For a more detailed level of analysis, I first extract representative CMP gathers from the dataset. To minimize errors associated with the radiation pattern, I first select a section of Line 34 where there is little topographic relief. In this area, the water table reflection remains at approximately the same depth b.g.s. across both the on-plume and off-plume sections. With no topographic variation, and little lateral surface heterogeneity, the take-off angles for the water table reflection in the on-plume and off-plume areas

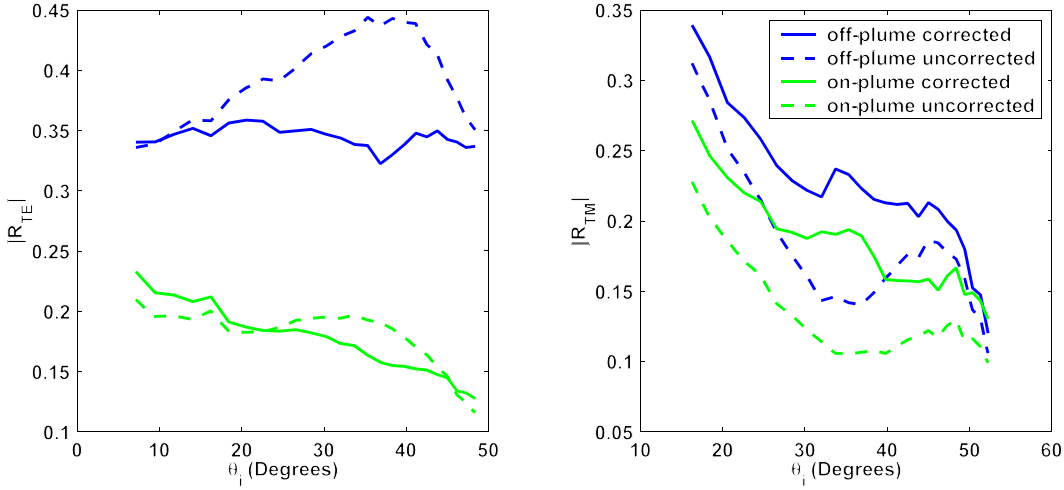

Figure 8. . Corrected and uncorrected amplitude curves extracted from the CMP supergathers shown in Figure 7). Note the lobate pattern characteristic of the source receiver directivity in the uncorrected curves.

are approximately equal. Consequently, the contribution of the radiation pattern to the AVO response will be approximately the same. Next, I create two sets of CMP supergathers. Each set consists of a TE and TM gather with 20 adjacent CMPs combined and summed into 1 ft offset bins. One set is generated for the on-plume area and one for the off-plume area (Figure 7). Carrying out the analysis on supergathers minimizes the effects of random noise and lateral heterogeneity in the overburden, thereby making the results more reliable.

The objective of this calculation is to extract an amplitude that is approximately proportional to the reflection coefficient curve, then test various models against the observed data in an attempt to match the AVO response. To accomplish this, we must attempt to remove all factors effecting amplitude that are independent of the reflection coefficient. This includes geometric spreading (S), source and receiver radiation patterns (P), and signal attenuation. Assuming there is little lateral heterogeneity in the overburden the amplitude correction has the form

$$A_c = \frac{1}{S(\theta)}\frac{1}{P(\theta)}e^{-\alpha d(\theta)}A_m \qquad (5)$$

where A_m is the measured amplitude, A_c is the corrected amplitude, d is the length of the travel path from the source to receiver, α is the attenuation coefficient, and θ is the angle of incidence.

The amplitudes are the maxima of the envelope function along the water table reflection. This eliminates the potential for any distortion due to phase rotation. Note that NMO corrections are not applied so NMO distortions are not a concern. Geometric spreading is assumed spherical, which is reasonable due to the relative homogeneity in the vadose zone. To estimate the attenuation coefficients, I first

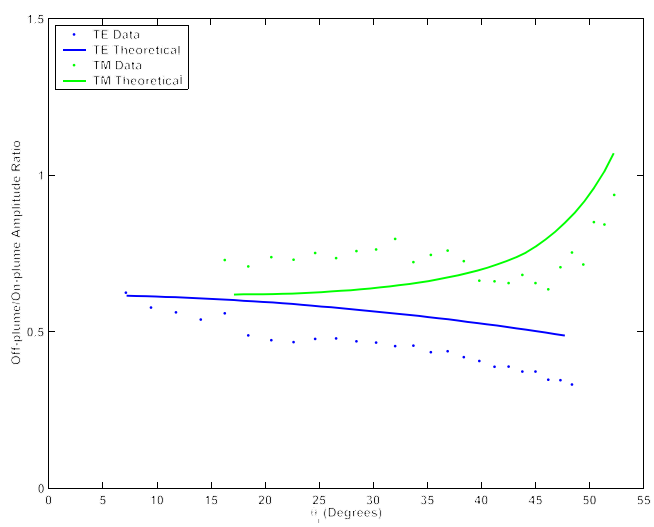

Figure 9. . Comparison of on-plume to off-plume amplitude ratios for the field data and the models shown in Figure 10.

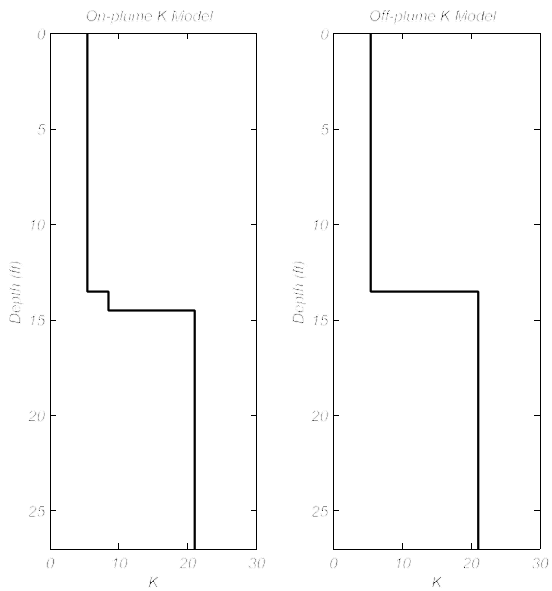

Figure 10. . Relative permittivity models for the on-plume and off-plume areas. Inclusion of an intermediate permittivity layer produces the AVO trend observed in the field data.

compute the root-mean-square (rms) values of vadose zone resistivity measured by Sauck et al. for the on-plume and off-plume areas. The inverse of resistivity gives the conductivity which I convert to the attenuation coefficient using the equation for low loss media given by Davis and Annan (1989). This gives 0.08 dB /ft and 0.02 dB/ft for the on-plume and off-plume areas respectively. This approach gives the minimum attenuation coefficient since I have not accounted for frequency dependence, but the estimates are reasonably close to tabulated values for dry sand (Davis and Annan, 1989). The uncorrected data clearly show the antenna directivity with well developed lobate patterns that have the same character in on-plume and off-plume areas (Figure 8). This suggests that the antenna directivity does not vary significantly along the profile. However, applying the radiation pattern correction using the infinitesimal dipole approximation produces large artifacts. The problem arises because the water table is only about 2.3 wavelengths from the surface and the far field radiation patterns have not yet developed. Applying the semi-empirical TE correction discussed by Bradford (1998), and a smoothed and shifted version of the TM correction produces a better result (Figure 8). The arbitrary nature of this TM correction is unsatisfactory, but I can avoid this problem by basing further analysis on the ratio of the on-plume amplitude to the off-plume amplitude. Assuming the antenna directivity is the same in both areas, Equation 5 shows that taking this ratio will cancel the radiation pattern contribution.

The trend of the corrected amplitude ratios correlates very well with a model having a 1 ft thick intermediate permittivity anomaly just above the water table in the on-plume area, and a simple boundary in the off-plume area (Figures 9,10). I adjusted the thin layer permittivity to provide a reasonable fit to both the TE and TM ratio curves, giving $K_{TL} = 8.5$ (Figure 10). Implicit in the analysis are assumptions of an incident plane wave, isotropic and frequency independent material properties, sharp boundaries at reflecting interfaces, and lateral homogeneity in the permittivity structure . While to first order these assumptions may be reasonable, not including these factors may explain the inability to fit the data curves precisely. Nevertheless, the 3-layer model is consistent with what is known about the site, and provides a reasonable basis for interpreting the AVO response.

There are two scenarios that could result in a zone of intermediate permittivity: 1) The contaminant has low permittivity and a mixed LNAPL/water zone decreases the permittivity in the capillary fringe and upper part of the saturated zone, or 2) the LNAPL zone has anomalously high permittivity giving an increase in the vadose zone permittivity just above the water table. I favor the latter model which is more consistent with the high NAPL zone conductivities observed at the site.

Since the anomaly has both low reflection strength and small gradient, multiplying AxB accentuates the anomalous zone. Plotting time slices at the water table reflection, I observe that the amplitude and AVO anomalies vary significantly throughout the 3D patch (Figure 11). This suggests that the NAPL layer is not distributed uniformly across the plume. The anomaly is broad near the north and south edges then narrows significantly near the center suggesting downgradient channelization.

It is important to note that if only the TE amplitude response were considered, a tempting and plausible explanation for the TE AVO anomaly is a zone of increased attenuation in the vadose zone above

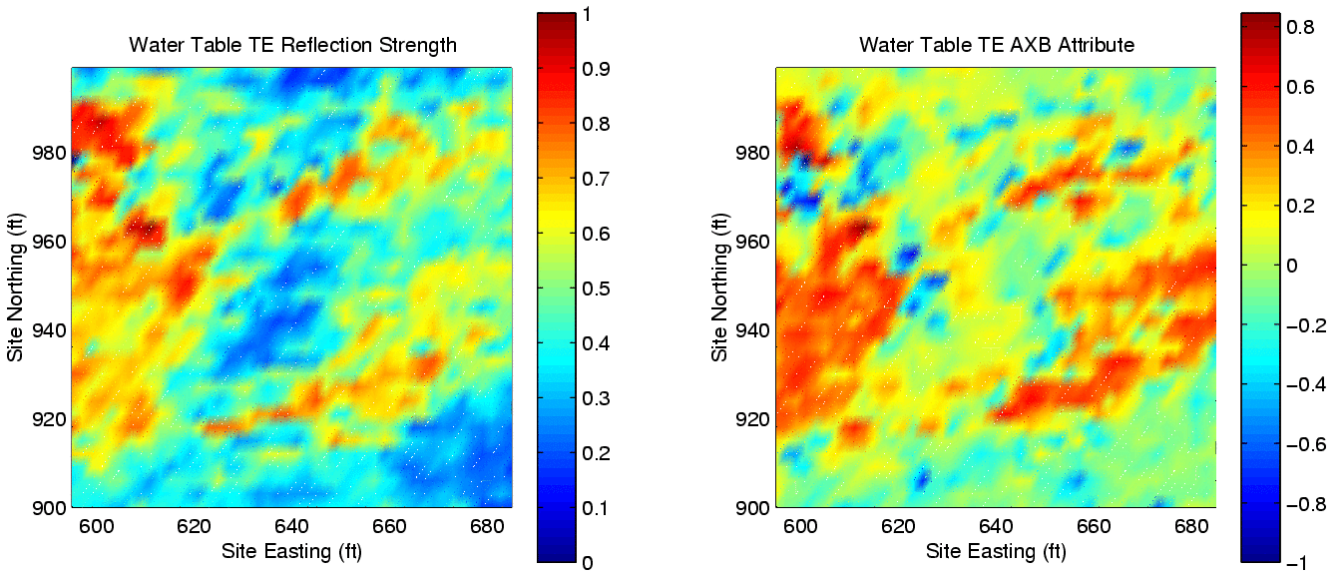

Figure 11. . Time slices (60 ns) at the water table of the TE amplitude and AVO response show significant variability across the 3D patch. Low values in both plots are interpreted as correlating with a thin (~ 1 ft) intermediate permittivity LNAPL layer at the top of the water table. Contaminant migration appears to be channelized in a N/NE direction.

the NAPL plume. This would decrease the near offset amplitude, and dampen the amplitude increase with increasing offset. And in fact, Sauck et al. found elevated conductivities in the vadose zone above the plume so this certainly is a factor in the observed AVO response. It is only by including the TM response in the analysis that I can conclude that a vadose zone attenuation anomaly cannot fully explain the observed amplitude response. In fact, it appears that the vadose zone conductivity anomaly is only a secondary effect. Rather than decreasing in relative amplitude with increasing offset, the on-plume TM data actually increase in relative amplitude at far offsets. This observation requires an explanation beyond the attenuation anomaly. The model of a low permittivity NAPL layer is inconsistent with the data and can be immediately discarded. This leaves the model of a intermediate permittivity NAPL layer, which is consistent with all the data observations.

Discussion and Conclusions

My analysis suggests that I have identified a thin intermediate permittivity NAPL layer present above the water table. Critical to this success was acquisition and analysis of dense, multi-fold data in both TE and TM polarizations. The presence of this layer is somewhat surprising. According to the site manager, free product is no longer present in the monitoring wells, and I did not expect to find a floating hydrocarbon layer. It is likely, however, that a thin layer of residual hydrocarbon remains, and Sauck et al.'s study demonstrates that even very low concentrations of hydrocarbon can have a significant impact on the electric property distribution. I interpret the intermediate permittivity layer as resulting from an increase in the vadose zone permittivity, just above the water table, due to an anomalously high LNAPL zone permittivity. Sauck et al.'s analysis demonstrated that electric conductivity increases by about a factor of 4 in the NAPL zone. An associated 57% increase in permittivity, as suggested by my analysis, is not unreasonable.

It is interesting to note that the extent of AVO and water table amplitude anomalies appear to correlate more closely with the attenuation zone boundaries interpreted by Sauck et al. than those found in the current study. This suggests that, while the zone of hydrocarbon contamination in the saturated zone has decreased in size, the impacted area in the vadose zone has not changed significantly. Additionally,

it appears that there is downgradient channelization of the LNAPL. These two points are significant for future remediation strategies at the site. The results of this study suggest that GPR multi-fold profiling coupled with AVO analysis may hold significant potential for both initial site characterization and continued monitoring of remediation activities.

Acknowledgments

This work was funded under the DOE EMSP Groundwater/Vadose Zone Integration Project, Grant # DE-FG07-99ER15008. I would like to thank the field team of Allen Tanner and Alex McKinley for their efforts.

References

Annan, A.P., Waller, W.M., Strangway, D.W., Rossiter, J.R., Redman, J.D., and Watts, R.D., 1975, The electromagnetic response of a low-loss, 2-layer, dielectric earth for horizontal electric dipole excitation: Geophysics, **40**, 285-298.

Atekwana, E.A., Sauck, W.A., and Werkema Jr., D.D., 2000, Investigations of geoelectrical signatures at a hydrocarbon contaminated site: J. Appl. Geophys., **44**, 167-180.

Baker, G.S., 1998, Applying AVO analysis to GPR data: Geophys. Res. Let., **25**, 397-400.

Bergmann, T., Robertsson, J.O.A., and Holliger, K., 1998, Finite-difference modeling of electromagnetic wave propagation in dispersive and attenuating media: Geophysics, **63**, 856-867.

Bermejo, J.L., Sauck, W.A., and Atekwana, E.A., 1997, Geophysical discovery of a new LNAPL plume at the former Wurtsmith AFB, Oscoda, Michigan: Groundwater Monitoring and Remediation, **17**, 131-137.

Bradford, J.H., 1998, Characterizing shallow aquifers with wave-propagation based geophysical techniques: Imaging and attribute analysis: Ph. D. thesis, Rice University.

Brewster, M.L., and Annan, A.P., 1994, Ground-penetrating radar monitoring of a controlled DNAPL release: 200 MHz radar: Geophysics, **59**, 1211 - 1221.

Campbell, D.L., Lucious, J.E., Ellefson, K.J., and Deszcz-Pan, M., 1995, Monitoring of a controlled LNAPL spill using ground-penetrating radar: SAGEEP '95: Symposium on the Application of Geophysics to Environmental and Engineering Problems, Env. Eng. Geophys. Soc., Proceedings, 511-517.

Castagna, J.P., 1993, AVO Analysis - Tutorial and review, *in* Castagna, J.P., and Backus, M.M., Eds., Offset-dependent reflectivity - Theory and practice of AVO analysis: Soc. Expl. Geophys., Invest. Geophys. **8**, 3-36.

Chew, W.C., and Kong, J.A., 1981, Electromagnetic field of a dipole on a two-layer earth: Geophysics, **46**, 309-315.

Davis, J.L., and Annan, A.P., 1989, Ground-penetrating radar for high-resolution mapping of soil and rock stratigraphy: Geophysical Prospecting, **37**, 531-551.

Deeds, J.C., 2002, Amplitude variation with offset (AVO) of ground penetrating radar data for detection of non-aqueous phase liquids: M.S. thesis, University of Wyoming.

Deeds, J.C., and Bradford, J.H., 2002, Characterization of an aquitard and direct detection of LNAPL at Hill Air Force Base using GPR AVO and migration velocity analysis: GPR 2002, Ninth International Conference on Ground Penetrating Radar, Intl. Soc. for Opt.l Eng., Proceedings, 323-329.

DeRyck, S.M., Redman, J.D., and Annan, A.P., 1993, Geophysical monitoring of a controlled kerosene spill: SAGEEP '93 Symposium on the Application of Geophysics to Environmental and Engineering Problems, Env. Eng. Geophys. Soc., Proceedings, 5-19.

Fisher, E., McMechan, G.A., and Annan, A.P., 1992, Acquisition and processing of wide-aperture ground-

penetrating radar data: Geophysics, **57**, 495-504.
Fisher, S.C., Stewart, R.R., and Jol, H.M., 1996, Ground-penetrating radar (GPR) data enhancement using seismic techniques: J. Env. Eng. Geophys., **1**, 89-96.
Griffiths, D.J., 1989, Introduction to electrodynamics, Prentice-Hall.
King, R.W.P., Owens, M., and etal., 1992, Lateral electromagetic waves: Theory and Applications to communications, geophysical exploration, and remote sensing, Springer-Verlag New York Inc.
Lehmann, F., 1996, Fresnel equations for reflection and transmission at boundaries between conductive media, with applications to georadar problems: GPR '96 6th International Conference on Ground-Penetrating Radar, Intl. Soc. Opt. Eng., Proceedings, 555-560.
Lien, B.K., and Enfield, C.G., 1998, Delineation of subsurface hydrocarbon contaminant distribution using a direct push resistivity method: J. Env. Eng. Geophys., **2**, 173-179.
Loughridge, J., 1998, Application of seismic tools and techniques to ground-penetrating radar (GPR) studies: M.A. thesis, Rice University.
Monier-Williams, M., 1995, Properties of light non-aqueous phase liquids and detection using commonly applied shallow sensing geophysical techniques: SAGEEP '95 Symposium on the Application of Geophysics to Environmental and Engineering Problems, Env. Eng. Geophys. Soc., Proceedings, 1-15.
Newmark, R.L., Daily, W.D., Kyle, K.R., and Ramirez, A.L., 1998, Monitoring DNAPL pumping using integrated geophysical techniques: J. Env. Eng. Geophys., **3**.
Orlando, L., 2002, Detection and analysis of LNAPL using the instantaneous amplitude and frequency of ground-penetrating radar data: Geophys. Prosp., **50**, 27-41.
Papas, C.H., and Engheta, 1982, Radiation patterns of interfacial dipole antennas: Radio Science, **17**, 1557-1566.
Sauck, W.A., 1998, A conceptual model for the geoelectrical response of LNAPL plumes in granular sediments: SAGEEP '98 Symposium on the Application of Geophysics to Environmental and Engineering Problems, Env. Eng. Geophys. Soc., Proceedings, 805-817.
Sauck, W.A., Atekwana, E.A., and Nash, M.S., 1998, High conductivities associated with an LNAPL plume imaged by integrated geophysical techniques: J. Env. Eng. Geophys., **2**, 203-212.
Tsang, L., and Kong, J.A., 1973, Interference patterns of a horizontal electric dipole over layered dielectric media: J. Geophys. Res., **78**, 3287-3300.
Walden, A.T., 1991, Making AVO sections more robust: Geophys. Prosp., **39**, 915-942.
Wensink, W.A., Greeuw, G., Hofman, J., and Van Deen, J.K., 1990, Measured underwater near-field e-patterns of a pulsed, horizontal diplot antenna in air: Comparison with the theory of the continuous wave, infinitesimal dipole: Geophys. Pros., **38**, 805-830.
Zeng, X., McMechan, G.A., and Xu, T., 2000, Synthesis of amplitude versus offset variations in ground-penetrating radar data: Geophysics, **65**, 113-125.

APPENDIX H: APPLICATION OF TWO-PASS MIGRATION TO GROUND-PENETRATING RADAR DATA

Bradford, J.H., and Loughridge, J., 2003, Application of two-pass migration to 3D GPR data: SAGEEP 2003 Symposium on the Application of Geophysics to Environmental and Engineering Problems, Env. Eng. Geophys. Soc., 598-612.

APPLICATION OF TWO-PASS MIGRATION TO 3D GPR DATA

John H. Bradford
Center for Geophysical Investigation of the Shallow Subsurface
Boise State University
Boise, ID

James Loughridge
Loughridge Consulting
Boulder, CO

Abstract

Two-pass migration refers to the method of migrating a three-dimensional data set using only 2D migration routines. The data are migrated twice; once each along two orthogonal axes. The method is easily implemented with any 2D migration code, and in the case of Kirchhoff migration, is far less computationally expensive than one-pass 3D migration. As computing power continues to increase, this savings in computation cost becomes less relevant. However, we maintain that the method, primarily due to availability of 2D migration codes and ease of implementation, holds significant utility in shallow geophysics, and ground-penetrating radar in particular. We review two-pass migration through simple synthetic examples and demonstrate that for a constant velocity medium, it is equivalent to full 3D migration. Then, through a series of test pit studies and a field example, we demonstrate that the method provides results comparable to one-pass 3D migration for a variety of applications and velocity profiles typical of GPR imaging problems.

Introduction

This work arose out of our need for an inexpensive field processing package that could be implemented on a laptop PC. Central to the development of this package was the need for 3D migration for imaging complex anthropogenic and geologic features. Given that 3D migration algorithms are computationally expensive, we chose to investigate two-pass migration as an alternative. In this aproach, 3D migration is performed via separate migration passes along orthogonal axes using only 2D migration algorithms. The use of 2D migration codes minimizes processor and memory requirements, and as an added benefit, the method is easily implemented using codes readily available in any number of free processing packages such as *Seismic Unix* (SU), which is distributed by the Center for Wave Phenomena at Colorado School of Mines. A number of researchers have investigated various implementations of two-pass migration including adaptation of pre-stack algorithms (Canning and Gardner, 1996). For the interested reader, an extended list of references is given at the end of the paper.

With the exception of a field example, we conducted the investigations presented here between 1995 and 1998, which ultimately lead to the development of a graphical user interface for SU (Loughridge, 1998). Since that time, it has become apparent that many GPR practitioners are either not aware of two-pass migration, or question the validity of the technique. Feeling that this methodology still holds significant value for the GPR processing community, we present the method here beginning with a review of two-pass migration. We then demonstrate the method through several test-pit studies and a field example.

Review of Two-Pass Migration

Understanding the Two-Pass Method

To understand the validity of the two pass method, first consider a single point diffractor in a constant velocity medium. The traveltime of scattering from the diffraction forms the surface of a hyperboloid given by (Gibson et al., 1983),

$$t^2 = T_0^2 + \frac{4(x - x_0)^2}{v^2} + \frac{4(y - y_0)^2}{v^2} \tag{1}$$

where v is velocity, t is the two-way travel-time at surface position (x,y), and x_0, y_0, and T_0 are the coordinates of the apex of the hyperboloid (the subsurface location of the point diffractor represented in three dimensions). Useful in understanding the two-pass approach is the recognition that the intersection of any vertical plane through the hyperboloid is a hyperbola characterized by the same velocity v. The intersection of a vertical plane parallel to the y-axis (y-plane) has the form,

$$t^2 = t_0^2 + \frac{4(y - y_0)^2}{v^2} \tag{2}$$

with

$$t_0^2 = T_0^2 + \frac{4(x - x_0)^2}{v^2} \tag{3}$$

Note that x is held constant for any such plane. Both Equations 2 and 3 are equations of hyperbolae.

One-pass 3D Kirchoff migration acts to methodically go through data space summing the energy of all points that fall on the surface of the hyperboloid given by Equation 1 then places this summed energy at T_0 in image space (Schneider, 1978). Let's carry out a two-pass migration by first summing along y-planes. This collapses the hyperboloid to a hyperbola located on the y_0 axis (Figure 1). Now migrating along x-planes the hyperbola is collapsed to a point centered at (x_0,y_0,T_0).

Jakubowicz and Levin (1983) show that for a homogenous medium, this two-pass approach is exactly equivalent to one-pass 3D migration, and that this equivalence can be extended to phase-shift migration and f-k migration. Furthermore, through a detailed heuristic analysis, Gibson et al. (1983) conclude that the two-pass method applied with a moderately varying velocity, v(t), will result in an error smaller than that caused by errors in estimating the velocity.

Migration Efficiency

For any Kirchhoff migration, there is a parameter called the aperture which in effect limits the number of adjacent traces to be summed for each trace in image space. In the case of two-dimensional migration, this number of traces can be considered 2N where N is the number of traces in each direction away from the current trace to include in the summation process (Gibson et al., 1983). In the case of the two-pass method, 4N (2N for each pass) traces will be handled for each migrated trace. For one-pass,

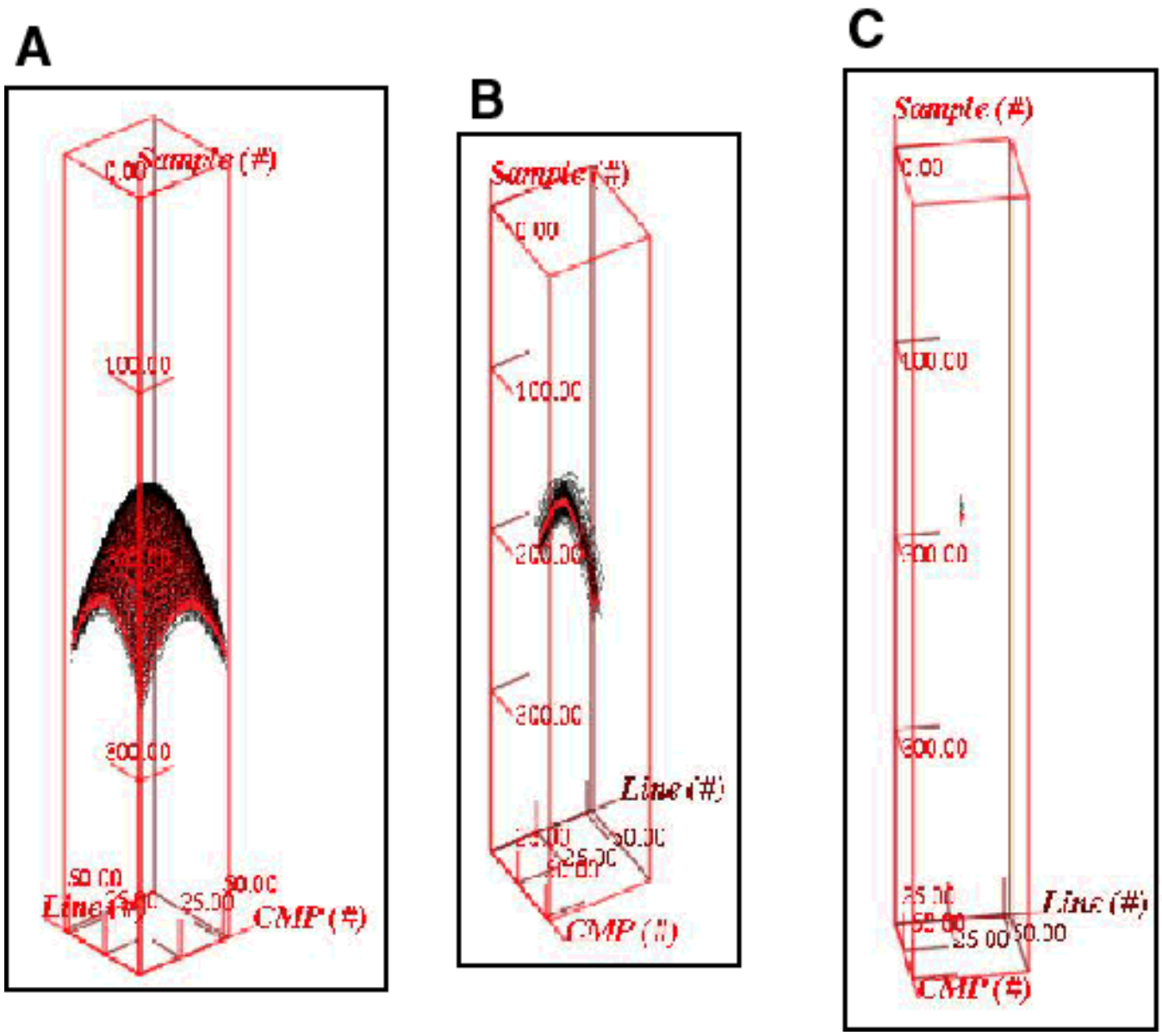

Figure 1. A) Hyperboloid of a point diffractor in three dimensions, B) 2D migration along y-planes collapses the hyperboloid to a hyperbola on the y_0 axis, and C) the second pass of 2D migration along x-planes completes the summation to (x_0, y_0, T_0).

three-dimensional migration, the aperture is defined to circumscribe a circle in the xy-plane. This circular aperture then dictates that roughly πN^2 traces are included in the summation process for each migrated trace. This difference between 4N and πN^2 operations per trace in a dataset is where the performance benefits of the two-pass method originates.

It is interesting to note, however, that while the two-pass Kirchhoff migration method has this inherent efficiency advantage when compared to a one-pass Kirchhoff approach, the same computational advantages do not hold true for the frequency-wavenumber migration methods. These methods require the use of Fourier transformations of the data. Using the two-pass method with an f-k migration algorithm requires a forward and reverse two-dimensional Fourier transform for each two-dimensional section of data. For a given survey this requires 2 (X + Y) Fourier transforms, with X and Y equal to the number of traces per line and the number of lines respectively. However, when performing a one-pass 3D f-k migration, a single forward and reverse three-dimensional Fourier transform is required. Thus, in terms of computing

efficiency, a one-pass 3D f-k migration is more efficient than the equivalent two-pass f-k migration. However, for the three-dimensional Fourier transform, the entire dataset and the Fourier transform of these data must be in memory at the same time. This requires two orders of magnitude more memory for such a migration. Typically GPR datasets are relatively small in comparison to the memory capacity of current PCs, so this is not of great concern.

Test Pit Studies

Test Pit Layout

To carry out experiments simulating a variety of subsurface scenarios, we designed and built a test pit at the Houston Advanced Rearch Center (HARC), in The Woodlands, TX. The pit was excavated into the dense surface clay unit (CL) to a depth of about 4.5 ft over an area of 25 ft x 20 ft, and lined with a heavy plastic sheet. The pit was then backfilled with two sand units. Approximately half the pit was filled with a fine grained sand with10% clay content (CS). The topography of the upper surface of this sand varies significantly throughout the pit giving both thick and thin sections of CS in addition to providing an interesting lithologic boundary (Figure 2). The remainder of the pit was filled with a washed coarse grained sand (QS). Additionally, a set of 9 fully screened wells were installed uniformly throughout the pit and could be used for monitoring, pumping or injecting. On an interesting side note, the CS sand was donated by a local mall after being removed from a holiday sand sculpture exhibit.

Except as noted, we acquired all data presented in the following sections using a Sensors and Software PE1000 system with 450 MHz antennas, and the same data processing flow was used throughout. This included a t_0 correction, bandpass filtering, background removal (average trace method), scaling by t^2, migration velocity analysis, and two-pass migration using an f-k algorithm. All 3D data were acquired in a single direction along sets of parallel lines. Through a variety of experiments, we found that the velocity of the dry sand in the pit varied from about 5500 - 6300 in/µs. Note that all data in this section were processed with SU. Some may wonder about the use of the units in/µs. This is entirely out of convenience. The SU header format is integer, and since we were typically working over very small spatial scales we chose units that ensured our header parameters were accurately represented in integer form.

Imaging Lithology - The Full Pit Experiment

For this dataset, we acquired 96 lines, spanning the full areal extent of the pit, with a cross-line spacing of 3 in, and in-line spacing of 2 in. We designed the survey to image the QS/CS boundary and two 3 in PVC pipes buried at depths of 12 in and 36 in oriented along the cross-line direction. The data were acquired within a few days of backfilling the pit.

An in-line profile near the center of the pit effectively illustrates improved image clarity through two-pass migration (Figure 2). Diffractions from the pipes have collapsed, and the surface of the QS/CS boundary is properly located. Additionally, the 18 in deep well sumps are imaged. A simulated progradation sequence is visible on the left side of the section where the interface between CS and QS begins to deepen. This is likely related to variable levels of water saturation in successive fill loads, as the sand had lain outdoors for several days and the outside of the pile became dryer than the sand found in the center of the pile.

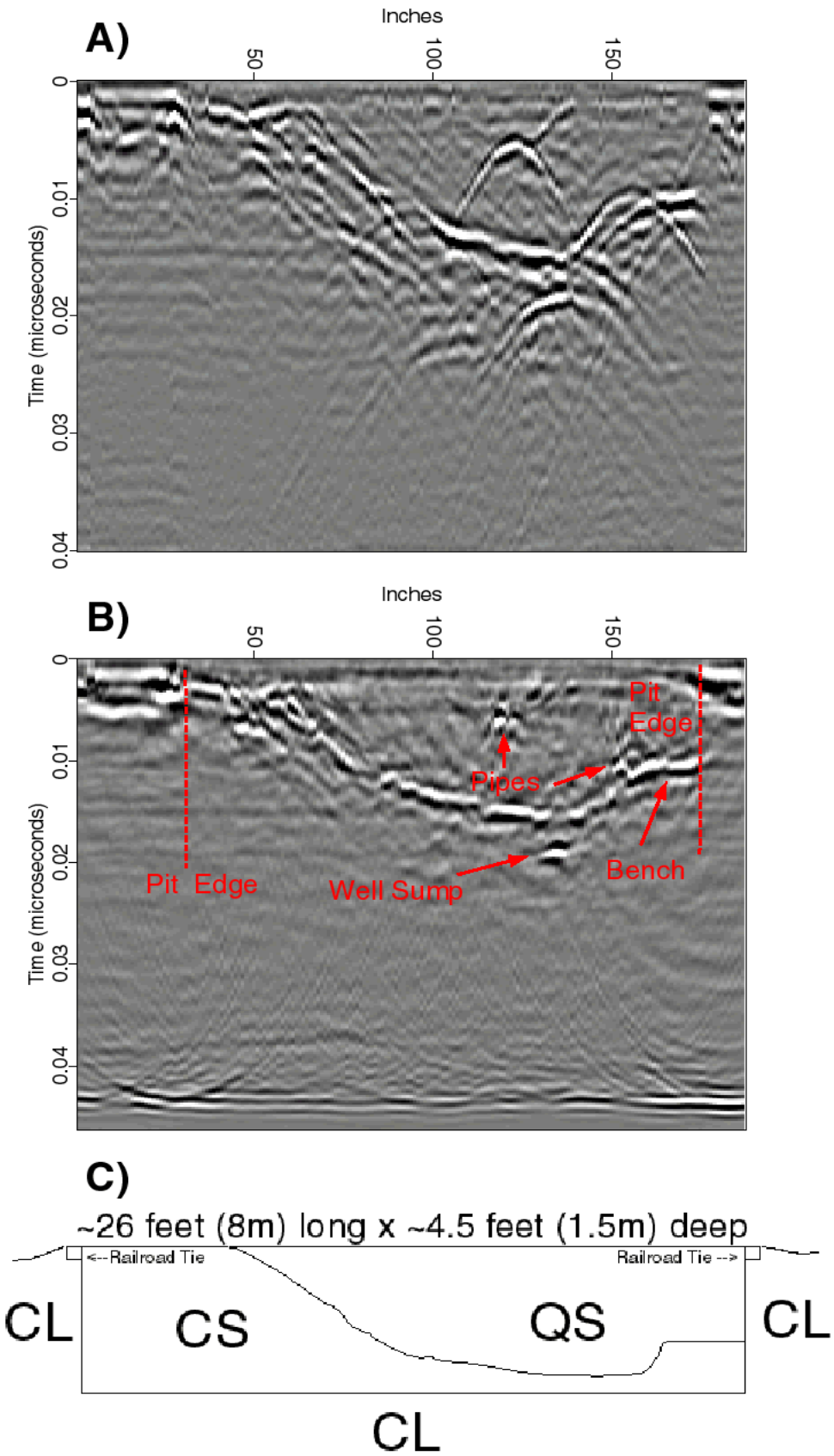

Figure 2. A) Unmigrated data, B) data after two-pass migration, and C) distribution of pit sands. Migration significantly improves the clarity of the image. Several features are clearly imaged including the QS/CS boundary, two 3 in PVC pipes, and an 18 in well sump.

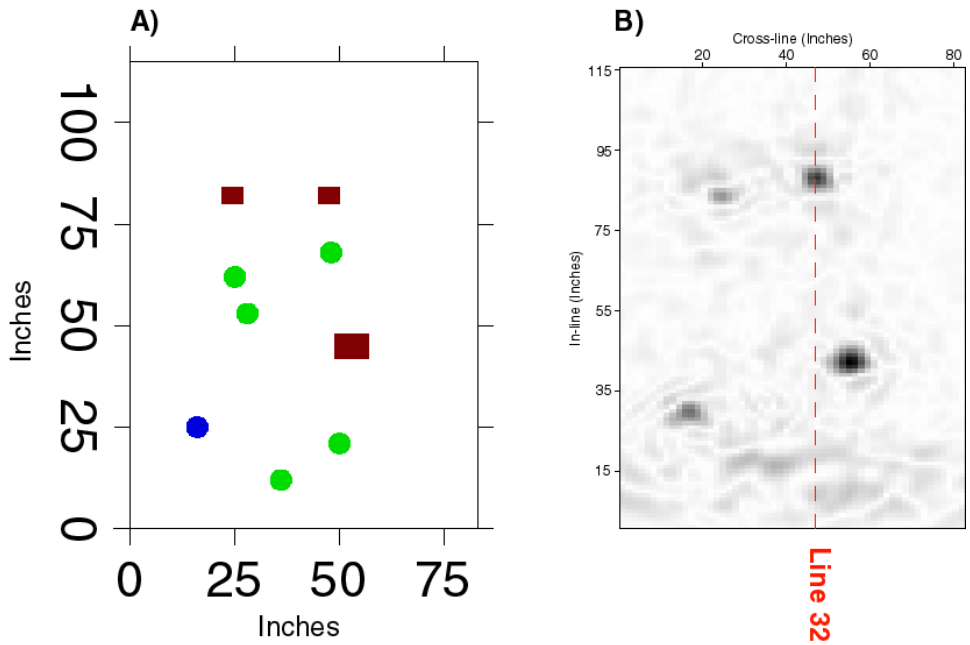

Figure 3. A) Plan view of buried object distribution. Brown objects are horizontally oriented paint cans. Blue item is a vertically oriented paint can. Green items represent location of buried cobbles. B) Time slice (0.0056 µs) through migrated volume. The four paint cans are easily discerned.

Precise Imaging of Buried Objects

A simple experiment was designed to assess the limitations of two-dimensional GPR acquisition and, by comparison, to determine the advantages of three-dimensional GPR studies. Four paint cans were buried 18 in below the surface of the test pit in the QS unit. Two of these cans were gallon sized paint cans and two were pint sized paint cans. Several cobbles of granitic lithologies with relative permittivity (K) values of ~ 4 were also buried at a similar depth (Figure 3). We collected a total of 56, 115 in long lines over this subset of the pit. The cross-line spacing was 1.5 in.

All of the paint cans are easily discernible in the processed data volume. A time slice (0.0056 µs) from the migrated data volume is presented to shows the relative positioning of the resolved objects in plan view (Figure 3).

As the two-pass method is, by definition, performed in two steps, the data can be analyzed after the migration has only been performed in either of the orthogonal directions---the in-line direction or the cross-line direction. Examining the data after the first in-line migration (the first pass) allows us to see the effects of a traditional two-dimensional migration applied to a single two-dimensional line. Out-of-plane events recorded in the time section are inaccurately migrated within the plane of such time section. Interpretation of such a migrated section can lead to false results.

Line 32 is presented in raw form to show the characteristic diffraction hyperbolae from two of the buried paint cans (Figure 4). After the first-pass migration (in-line), two distinct objects are clearly visible in the profile; an apparent scatterer and an actual scatterer. After two-pass 3D migration, the apparent scatterer on the left has been migrated out of this profile to its proper location. If this survey had consisted solely of this single two-dimensional line, the positioning of the two paint cans would obviously be inaccurate. It is not difficult to imagine a “real world” situation in which a need for increased subsurface location accuracy is needed. If these buried paint cans had been

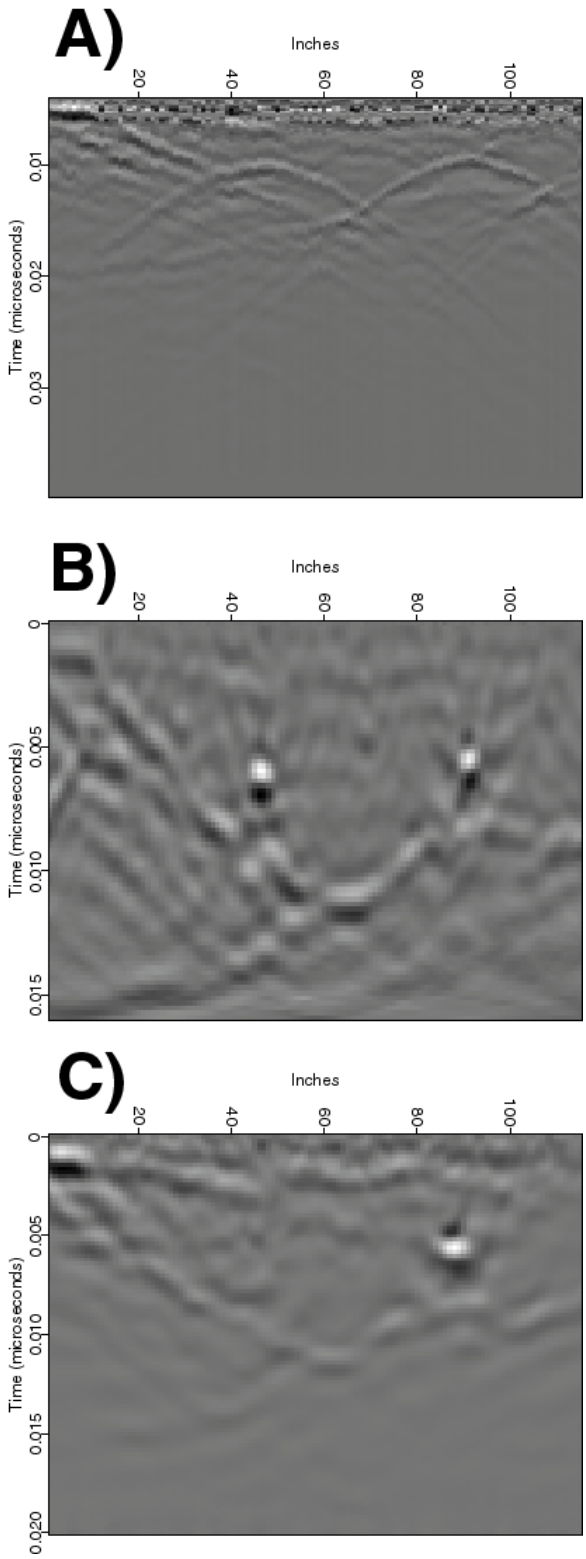

Figure 4. A) Unmigrated data from Line 32 of buried paint can dataset. Two major diffraction hyperbolae are clearly visible. B) After in-line migration two objects are resolved. The object on the left (45 in) is out-of-plane. C) After the second pass (cross-line migration), the diffractor on the left is absent and has been migrated to the correct location.

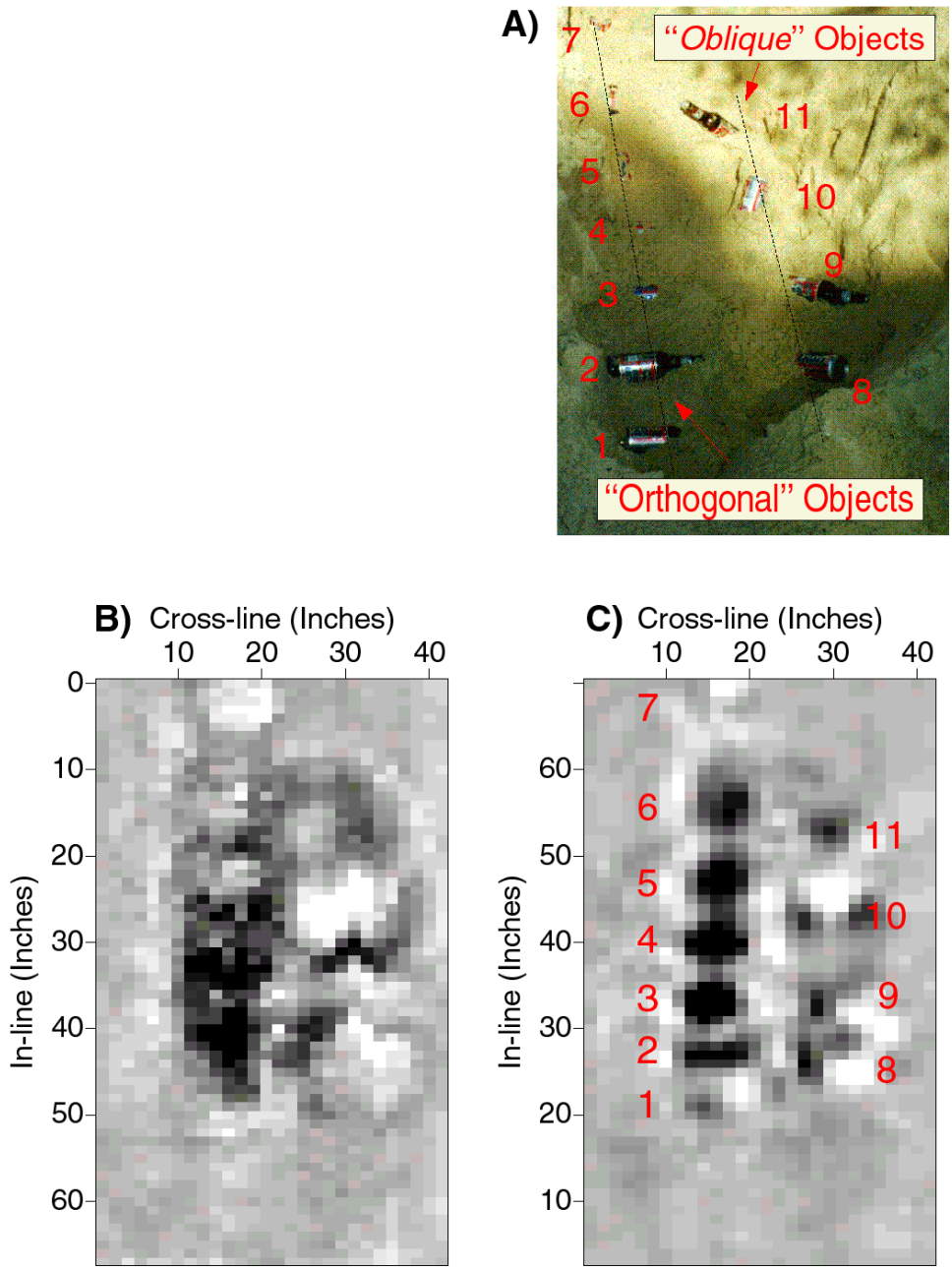

Figure 5. A) Picture of cans and bottles oriented along parallel lines. Line on the left contains orthogonally oriented objects, and the right line contains obliquely oriented objects. B) The time slice at 0.0032 µs through the unmigrated volume reveals the buried objects but they are not well resolved. C) After two-pass migration all objects are well resolved. Lateral resolution of object 2 is approximately 3 in.

buried ordnances or landmines, the need for maximal accuracy is obvious. This dataset clearly demonstrates the importance of appropriate acquisition and processing techniques to accurately locate subsurface features.

Resolution of Densely Packed Objects

We collected this dataset to test GPR resolution limits and how resolution is improved with 3D migration. We designed a test to see if a number of objects of a size and separation on the same order as the signal wavelength, could be resolved as individual objects. Additionally the objects would be placed

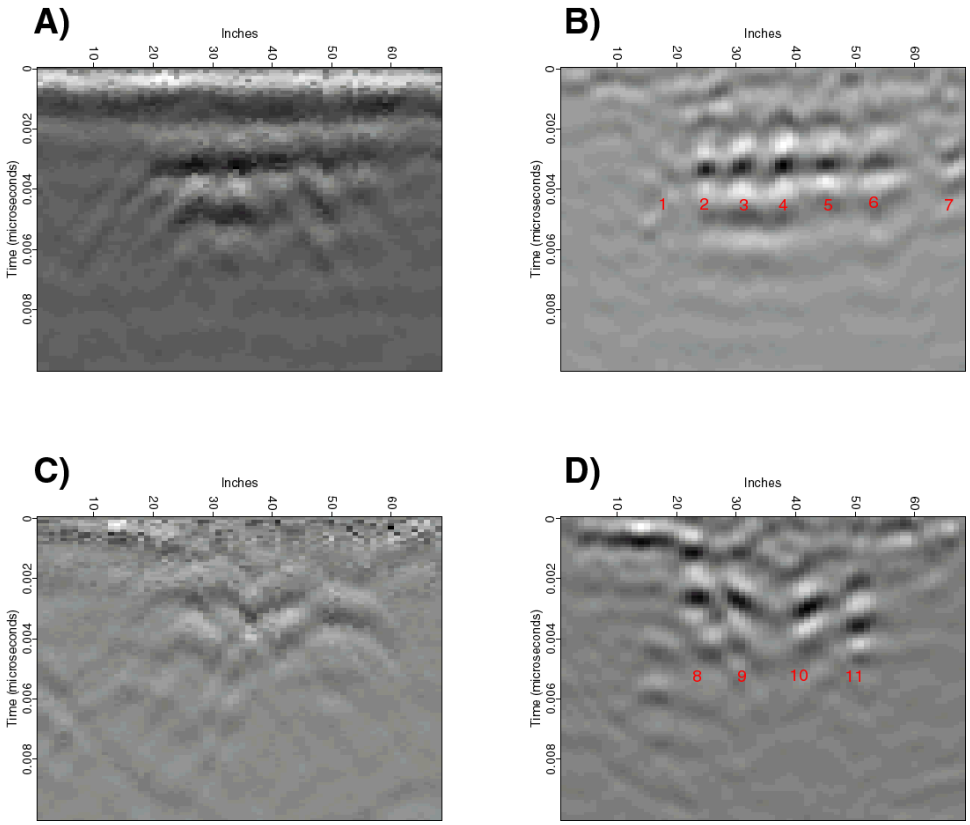

Figure 6. A) Unmigrated line over the orthogonally oriented objects. B) After two-pass migration the objects are easily differentiated. C) Unmigrated line over the obliquely oriented objects. D) After migration the orientation of objects 9 and 10 are evident and consistent with their known positions.

in various orientations ranging from vertical and horizontal alignments to oblique.

Eleven objects were buried in the QS unit along two parallel lines with seven objects in one line and four objects in the other (Figure 5). Five of the objects were 12 ounce glass bottles and six of the objects were 12 ounce aluminum cans. The objects were buried along each of the two parallel lines according to the following considerations: the seven bottles and cans buried along the longer line of objects were placed with their major axes aligned parallel with one of the orthogonal acquisition axes of in-line, cross-line, time; the four objects of the other line were placed such that the major axis of each object was oblique to any of the orthogonal acquisition axes. In-line separation of the objects was about 6 in and each bottle and can has a diameter of about 2.5 in.

The in-line direction was parallel to the lines in which the objects were buried. In contrast to the surveys discussed up to this point, we acquired these data with 900 MHz antennas to maximize the resolution potential. Data were acquired on a dense grid with an in-line spacing of 1 in and a cross-line spacing of 1.5 in. Given that the dominant frequency we actually record with this antenna set is around 700 MHz, the signal wavelength is about 9" at the velocity of QS. Thus, both the object size and separation between objects are less than one wavelength.

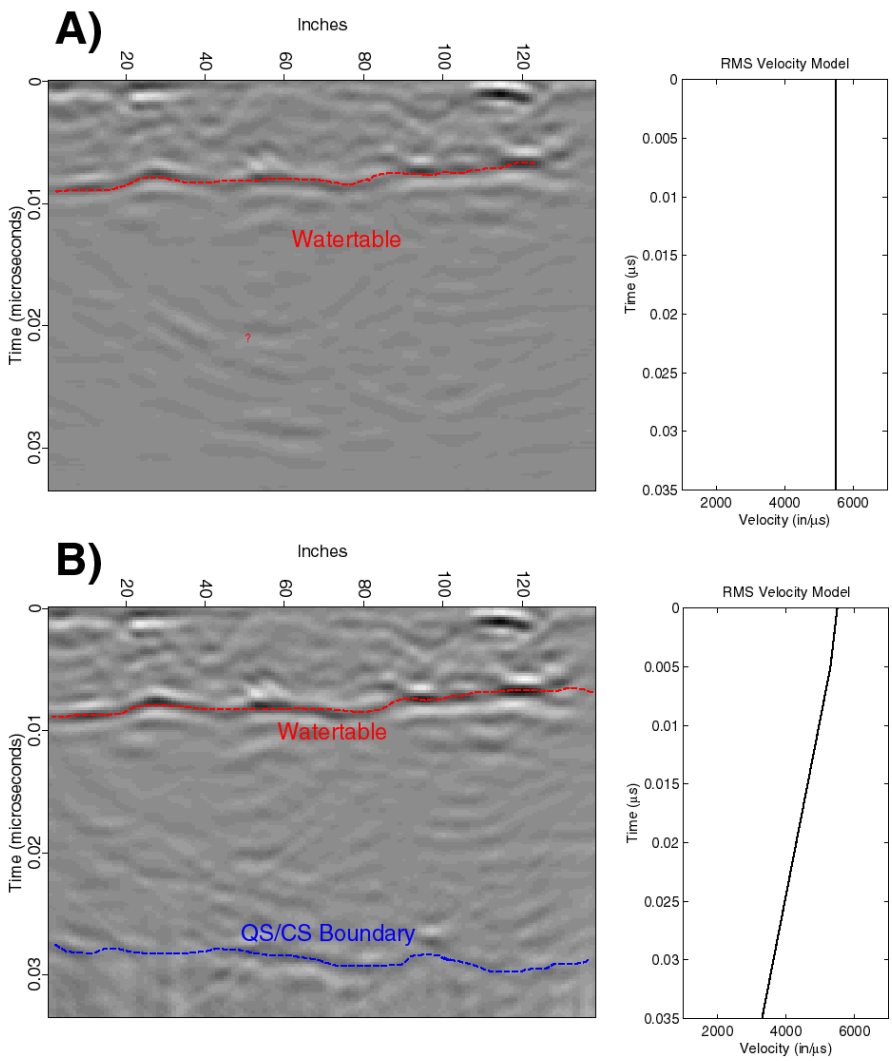

Figure 7. With water in the pit, a large vertical velocity contrast is introduced. A) Two-pass migration at the dry sand velocity gives poor results below the water table. B) Two-pass migration with a vertically varying velocity model produces a clear image both above and below the water table.

We had little trouble detecting the objects which are clearly evident raw data, but not well resolved. After two-pass migration it is possible to discern the individual objects (Figures 5 and 6). Note that Object 1 was an air-filled bottle, and therefore the reflection has opposite polarity relative to reflections from the liquid-filled cans. Data taken from the line directly above the obliquely oriented objects (Figure 6) shows that after migration, the reflections from objects 9 and 10 have collapsed to tilted forms consistent with their known orientation.

Vertically Varying Velocity

For this final test pit example, we introduced a significant vertical velocity gradient by raising the water level in the pit to 20 in below the surface. As the low velocity water (~ 1319 in/µs) displaces high velocity air (11800 in/µs) in the pore space, the bulk formation velocity decreases. In sands, the amount of this decrease is controlled by the porosity. In the case of QS, the velocity decreases by a factor of about 3. This experiment provided a good test for the two-pass technique in the presence of velocity heterogeneity. We acquired 28 profiles over the QS/CS boundary low (Figure 2). The in-line spacing was

1 in and cross-line spacing was 2 in. The in-line direction was oriented along the axis of the trough.

Two-pass migration at the dry sand velocity yielded a very detailed image of the top of the water saturated zone, but a very poor image of the QS/CS boundary (Figure 7). Migrating with a vertically varying velocity model produced an excellent image both above and below the water table (Figure 7). Rarely in the field do we see larger velocity gradients than that induced by the transition from dry or partially saturated sediments to full saturation. Given this observation, this experiment demonstrates that the two-pass migration approach is reasonable for most any GPR imaging studying.

Field Application: An Imaging Experiment at the Dover National Test Site

Site Background

The mission of the Dover National Test Site, administered by SERDP, is to facilitate research in the characterization and remediation of groundwater contaminants. The site provides a number of facilities for the study of various methodologies in a natural aquifer system. For this study, our objective was to image the disturbed soil related to emplacement and excavation of material in a previous reactive transport barrier experiment (MSE Technology Applications Inc., 1998). During the barrier experiment, several vertical barriers were installed via high pressure injection into the pore system (Figure 8). The barriers were keyed in to a shallow clay layer at a depth of about 15 ft b.g.s. Later the formation surrounding the barriers was excavated for evaluation of the emplacement. When our experiment was conducted in August, 2002, it had been more than four years since the excavation and backfill operations, and there was no clear surface expression of the excavation sites or barrier emplacements.

Data Acquisition and Processing

Our primary imaging targets were the barrier excavation sites. The precise location of these features was not known at the time of acquisition. Additionally, rows of trees had been planted along either side of the site since the barrier test, and it was believed that trees could be growing over some of the excavation sites. Consequently, our survey area spanned from tree-line to tree-line and the length was set to cover the full area where the trenches were thought to be (Figure 8). Some variations in surface foliage within the 3D grid were suspected of being over the excavation sites, and this was later verified.

We acquired data along 23 parallel lines at 3 ft line spacing using a Sensors and Software PE100 system with 100 MHz antennas. Each line was 150 ft long with an in-line trace spacing of 1 ft. Source/receiver separation was 3 ft. The cross line spacing is close to the spatial aliasing limit, and although not optimal, experience has shown that good 3D migration results can be obtained at many sites with 100 MHz antennas and 3 ft line spacing. When field time is limited, as in this case where we had less than 3 hrs to complete the survey, these are reasonable acquisition parameters.

Pre-processing included a t_0 correction, bandpass filtering (4 octave pass band centered at 100 MHz), and AGC. Additionally, f-k filtering was applied in the cross-line direction to attenuate scattering from various objects (power line, trees, etc) that were primarily lateral to the in-line direction. The migration velocity was determined by 2D migration velocity analysis along a profile with well developed diffraction hyperbolae from subsurface scatterers. It was found that a constant velocity of 370 ft/μs produced a good result. The data were migrated with both a one-pass 3D phase-shift migration algorithm (Gazdag, 1981), and a two-pass 3D migration with a 2D phase-shift migration algorithm. The results of both migrations are presented here for comparison.

Results and Discussion

Data quality is excellent and several interesting features are imaged (Figure 9). First, two primary

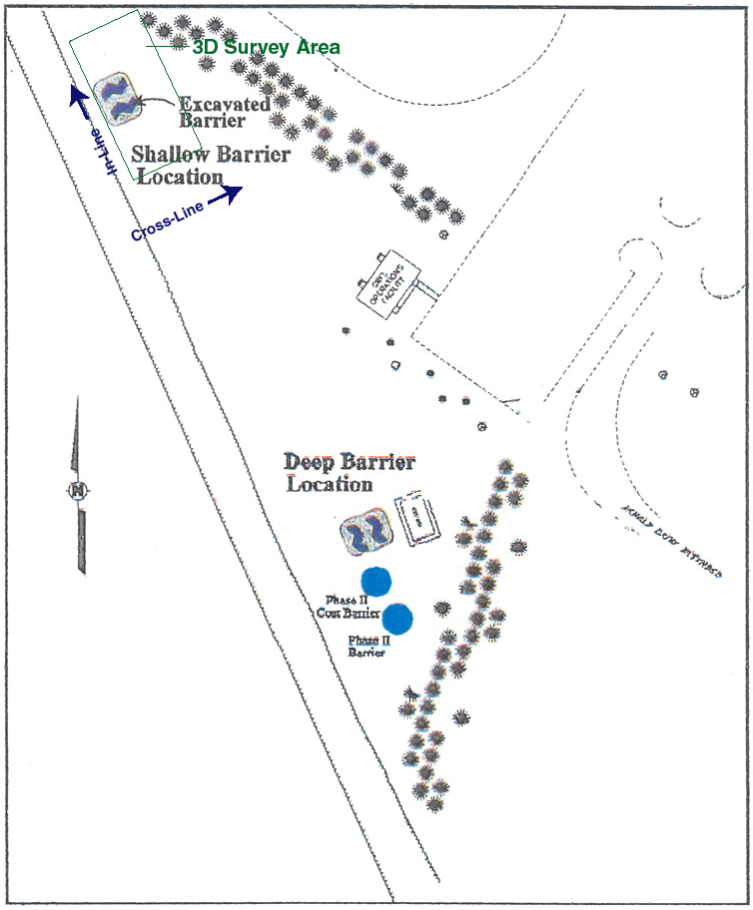

Figure 8. DNTS site map at the time of the barrier wall tests, and location of August, 2002 GPR survey (modified from MSE Technology Applications Inc., 1998).

stratigraphic boundaries are imaged . The first (B1) is between 40 and 60 ns and in cross-lines appears to be an erosional discontinuity. The second boundary, and most prominent reflection is the shallow clay (B2) at times from 70 - 90 ns. This is the lower limit of signal penetration. These two events are subparallel and dip toward the southwest. Three excavation trenches are imaged (Figure 9). Each is approximately 25 x 40 ft with axes oriented in the cross-line direction. Along in-line profiles the trenches are characterized by zones of chaotic reflectivity that cut through both B1 and B2. 3D migration significantly improves the quality of the image. The boundaries of the trenches are well defined and show the Z pattern used for the slurry wall injections.

Perhaps most relevant to this discussion is that the one-pass and two-pass 3D migrated images are virtually indistinguishable. Differencing the images reveals that the most significant variation is the edge effects. There is no systematic correlation between the reflectors in the migrated images and features in the difference sections. This indicates that reflector positioning is the same for both methods. This result is not too surprising given that the migration was performed with a constant velocity, but it does demonstrate that two-pass migration can be used to produce high quality images in field GPR data.

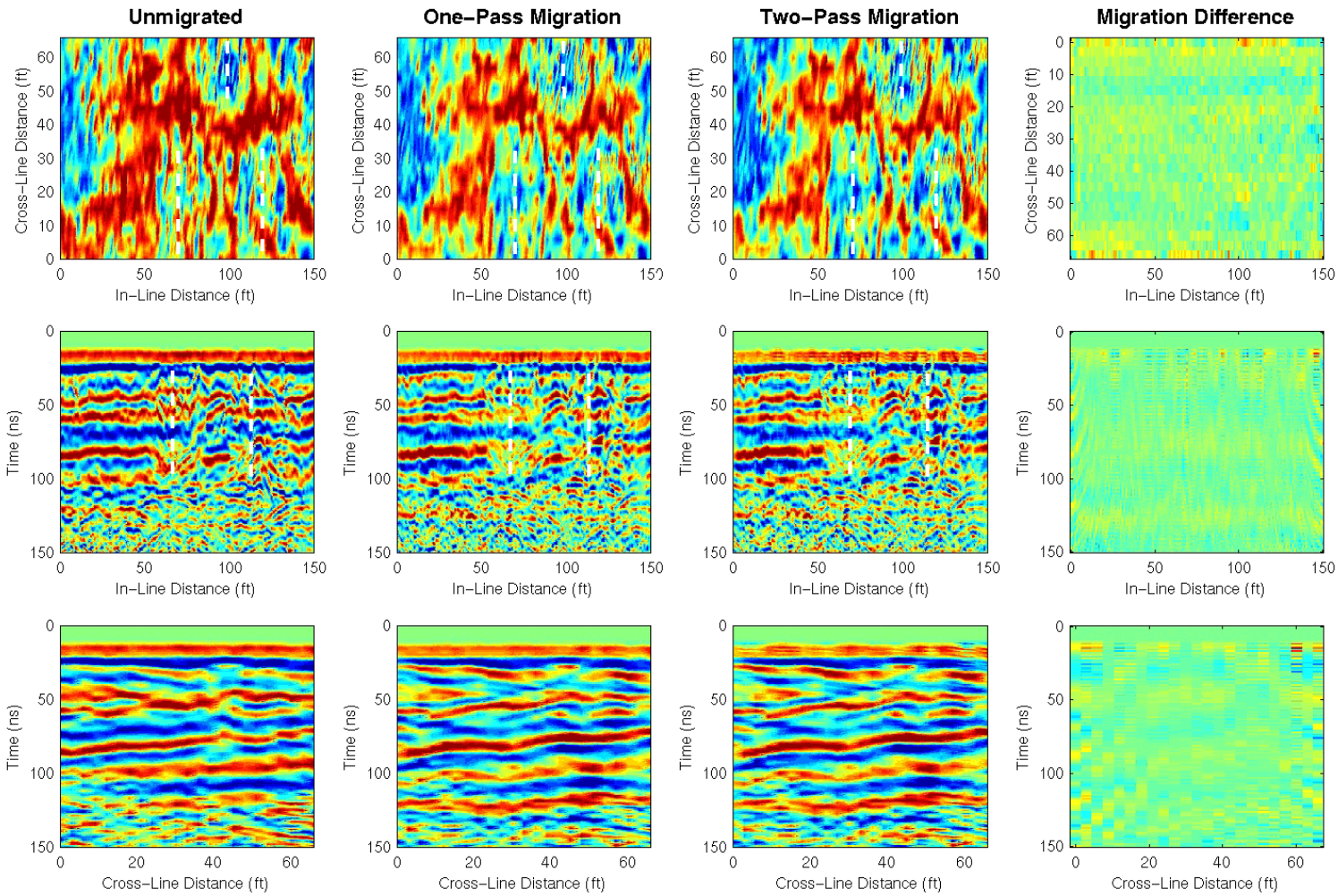

Figure 9. Time slices through the shallower stratigraphic boundary at 46 ns reveal the shape of the excavations. Along the in-line profile at x-line = 15 ft, the excavations are evident where the stratigraphic boundaries are disrupted. Cross-line profiles at in-line = 25 ft show an apparent erosional discontinuity sloping from 55 ns to 45 ns. Migration improves resolution of the excavation boundaries. The results of one-pass 3D migration and two-pass 3D migration do not differ significantly. Trench axes are marked with white dashed lines.

Conclusions

The results of this work clearly demonstrate both the utility of the two-pass approach to 3D migration, and the added benefits of 3D data acquisition. Using this method, we were able to produce high quality images of a variety of complex subsurface targets in both relatively homogeneous subsurface environments, and in the presence of significant heterogeneity. All of the test pit data were processed using a laptop PC with 64 MB of memory and a 75 MHz Pentium processor. Although the spatial extent of these datasets was quite small, they were very dense and consequently the data volume was comparable to larger scale field studies. It is clear from these results that field scale 3D GPR surveys can be processed in near "real time".

Acknowledgments

This work was funded by the Gas Research Institute, Houston Advanced Research Center, and the DOE EMSP Groundwater/Vadose Zone Integration Project, Grant # DE-FG07-99ER15008. I would like to thank Tim McHale and his staff at the DNTS for their assistance in getting access to the site and carrying out the experiments.

References Cited

Canning, A., and Gardner, G.H.F., 1996, A two-pass approximation to 3-D prestack migration: Geophysics, **61**, 409-421.

Gazdag, J., 1981, Modeling of the acoustic wave equation with transform methods: Geophysics, **46**, 854-859.

Gibson, B., Larner, K., and Levin, S., 1983, Efficient 3-D migratin in two steps: Geophys. Prosp., **31**, 1-33.

Jakubowicz, H., and Levin, S., 1983, A simple exact method of 3-D migration - theory: Geophys. Prosp., **31**, 34-56.

Loughridge, J., 1998, Application of seismic tools and techniques to ground-penetrating radar (GPR) studies: M.A. thesis, Rice University.

MSE Technology Applications Inc., 1998, Final Report - Cement Bentonite Thin Diaphragm Wall Jet-Grouting Demonstration Project Dover, Delaware.

Schneider, W.A., 1978, Integral formulation for migration in two and three dimensions: Geophysics, **43**, 49-76.

References for Additional Reading on Two-Pass Migration

Dickinson, J.A., 1988, Evaluation of two-pass three-dimensional migration: Geophysics, 53, 32-49.

Jakubowicz, H., and Miller, D., 1989, Two-pass 3D migration and linearized inversion in the (x,t)-domain: Geophys. Prosp., 37, 143-148.

Kessinger, W., 1999, Two-pass 3-D imaging of the SEG salt model data: 69th Ann. Intl. Mtg., Soc. of Expl. Geophys., 1095-1098.

Mendoza-Amuchastegui, J.A., Diego-Orozco, A., Kessinger, W.P., and Gazdag, J., 1998, Subsalt imaging in Coatzacoalcos, Mexico using two-pass 3-D prestack depth imaging: 68th Ann. Internat. Mtg., Soc. of Expl. Geophys., 1397-1400.

Pan, N., and French, W.S., 1989, Generalized two-pass three-dimensional migration for imaging steep dips in vertically inhomogeneous media: Geophysics, 54, 544-554.

Pan, N., Perkins, W.T., and French, W.S., 1991, Exact two-pass full-dip (>90 degrees) 3-D migration for vertically inhomogeneous media: 61st Ann. Internat. Mtg., Soc. of Expl. Geophys., 1160-1163.

APPENDIX I: CHARACTERIZATION OF AN AQUITARD AND DIRECT DETECTION OF LNAPL AT HILL AIR FORCE BASE USING GPR AVO AND MIGRATION VELOCITY ANALYSES

Deeds, J.C., and Bradford, J.H., 2002, Characterization of an aquitard and direct detection of LNAPL at Hill Air Force Base using GPR AVO and migration velocity analysis: GPR 2002, Ninth International Conference on Ground Penetrating Radar, Intl. Soc. for Optl. Eng., Proceedings, 323-329.

CHARACTERIZATION OF AN AQUITARD AND DIRECT DETECTION OF LNAPL AT HILL AIR FORCE BASE USING GPR AVO AND MIGRATION VELOCITY ANALYSES

Jake Deeds
University of Wyoming
Department of Geology and Geophysics, PO Box 3006, Laramie, Wyoming 82071
jdeeds@uwyo.edu

John Bradford
Boise State University
Boise State University, CGISS, MG-206, 1910 University Drive, Boise, Idaho 83725
johnb@cgiss.boisestate.edu

ABSTRACT

Large quantities of non-aqueous phase liquids (NAPL), contaminate the near surface sediments at Operable Unit 1 (OU1), Hill Air Force Base (HAFB), Utah. In October 2000, a 3D, multi-offset GPR survey was acquired at OU1 with two objectives: 1) to image the aquifer/aquitard boundary at a depth of about 30 ft, and 2) to evaluate quantitative processing and interpretation methodologies for direct detection of NAPL. Using pre-stack depth migration, we map the aquitard boundary to about ± 1 ft throughout the survey area. An unusual reflection is identified within the vadose zone that does not correlate with known geology. The region below this reflection has anomalously high velocity, implying low electric permittivity, and the amplitude of the anomalous reflection deviates significantly from the background AVO trend. Fitting the Fresnel equation to the AVO data, we estimate the velocity contrast at the anomaly boundary and find that it is in good agreement with the migration velocity model. We interpret the anomaly as a previously unidentified NAPL rich zone. Subsequent coring and chemical analyses verify our interpretation. This exciting result implies that these methodologies may be useful for direct detection of NAPL at other HAFB locations and at sites with similar hydrogeology.

Key words: Pre-stack depth migration, AVO, LNAPL, Hill Air Force Base

INTRODUCTION

At Hill Air Force Base (HAFB), Utah, the Provo alluvium forms the surface sediments and consists of 6 to 10 meters of sand and gravel. This is underlain by the Alpine formation; a thick silty clay unit. The Alpine clay acts as an aquitard about which the local water table fluctuates seasonally. HAFB mainly performs mechanical repairs and maintenance for military aircraft. As a result of this duty, large quantities of potential contaminants require disposal, and from 1952 to 1973, they were dumped into unlined chemical disposal pits and combusted. A diverse mixture of light and heavy organics including lubricating oils, fuels, and solvents, entered the sediments in this manner. In 1976, a nearby resident complained of an orange discharge in a well near the base, and investigation began. In 1987, HAFB was placed on the Superfund National Priorities List.

The free phase plume contains an estimated 20,000 gallons of NAPL, covering about 7 acres. The plume is comprised almost entirely of light NAPL (LNAPL) of which weathered jet fuel is the primary component. The maximum thickness of free NAPL is around 1 ft. Both free and residual phase NAPL are present in a roughly 5 ft thick 'smear zone' above the water table that is controlled by the annual fluctuations of the water-saturated zone. As the water table rises buoyant NAPL is smeared upward, and as it falls the contaminant pools under the effect of gravity.

A variety of organic NAPLs exhibit markedly low electric permittivity ($\varepsilon_r \approx 2.5$) and conductivity compared to water ($\varepsilon_r \approx 80$). Introduction of these liquids into the subsurface can significantly alter the bulk electric properties. The primary mechanism of this alteration is the displacement of pore water by NAPL, and the effect may be strongly dependent on the wetting phase (Endres and Redman, 1996). GPR is sensitive to changes in electric permittivity, and has been shown to respond to changes in NAPL concentration (Brewster and Annan, 1994; Daniels et al., 1995; DeRyck et al., 1993; Newmark et al., 1998; Powers and Olhoeft, 1996).

GPR data are typically collected using constant antenna separation. Although this may be adequate for many applications, more information may be extracted by varying the antenna separation. Quantitative analysis of multi-offset

GPR data provides material property estimates (Greaves et al., 1996) including electric permittivity and thus may lead to direct detection of NAPL contaminants. Additionally, significant noise reduction may be achieved in GPR images through multi-offset acquisition and processing techniques such as stacking and velocity filtering (Bradford, 1998; Fisher et al., 1992; Fisher et al., 1996; Loughridge, 1998; Yilmaz, 1987).

In previous work at HAFB, Lien and Enfield (1998) found that NAPL contaminated soils in the vadose zone at OU1 had low electric conductivity. It is likely that the low electric conductivity correlates with low electric permittivity. This coupled with favorable results of previous GPR imaging work at HAFB (Young and Sun, 1996; Young and Sun, 1998) led us to select HAFB as a research site.

We present a detailed, quantitative analysis of multi-offset GPR data collected at OU1 HAFB. The objectives of this study are: 1) to make a detailed image of the aquifer/aquitard interface and 2) to evaluate the potential of directly detecting NAPL contaminants through material property estimation. In particular, we use pre-stack depth migration (PSDM) velocity analysis to estimate radar velocity, and amplitude vs. offset (AVO) analysis to identify large positive permittivity contrasts.

DATA COLLECTION

In October of 2000, we collected a 32,000 square foot, multi-offset, 3D survey. All data were acquired with a Sensors and Software PulseEkko 100^{TM} system using 50 MHz antennae and off-end shooting geometry. Table 1 summarizes the acquisition parameters for the 3D survey. During acquisition, the water table was roughly coincident with the top of the clay.

We collected the data during construction of LNAPL extraction trenches and installation of a bentonite cap. Once the cap was in place, the radar signal would be degraded so we had a firm time limitation. This time limitation, surface noise related to construction activities, and space conflicts with the construction crews forced us to conduct night operations using a generator and halogen lights. Parked construction equipment and the lighting system produced notable surface scatter that reduced data quality. Also, construction activities occasionally destroyed our survey markers, making it necessary to resurvey several times. For the most part, data from the 3D survey are excellent, and a clean signal is reflected from the clay surface for the entire range of offsets (Figure 1).

We designed the 3D survey to bound Chemical Disposal Pit 1 on the east, west, and north, and to extend beyond the known boundary of the free NAPL plume to the north (Figure 2).

Table 1: Summary of Data Collection Parameters for the multi-offset GPR Survey at OU1, HAFB.

Antenna frequency	50 MHz
Near offset	6 ft
Maximum offset	30 ft
# Receivers/common source point	25
Source interval	2 ft
Receiver interval	1 ft
Sampling interval	1.6 ns
Recording time	500 ns
Line spacing	8 ft
Antenna polarity	TE
# Traces stacked	16

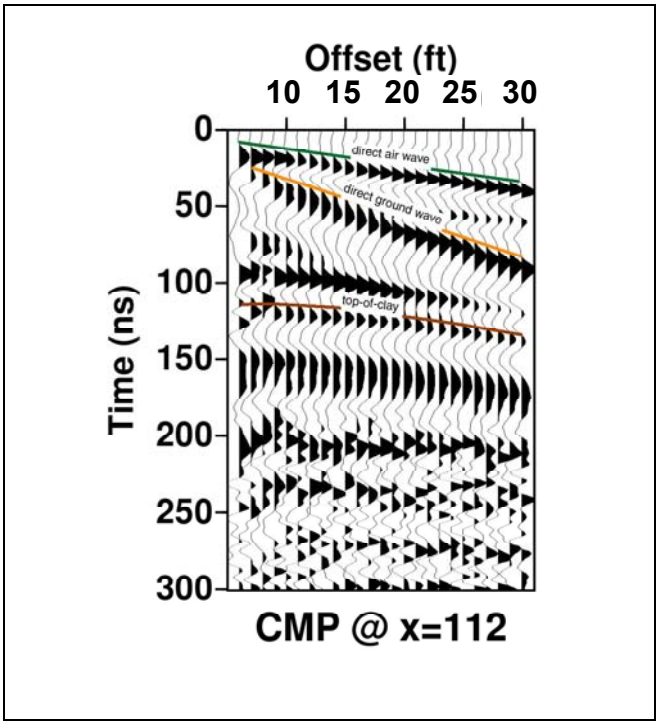

Figure 1: Common mid-point gather from Line 14 of the 3D survey with strong clay reflections present at all offsets. The anomalous reflection is centered at 95 ns.

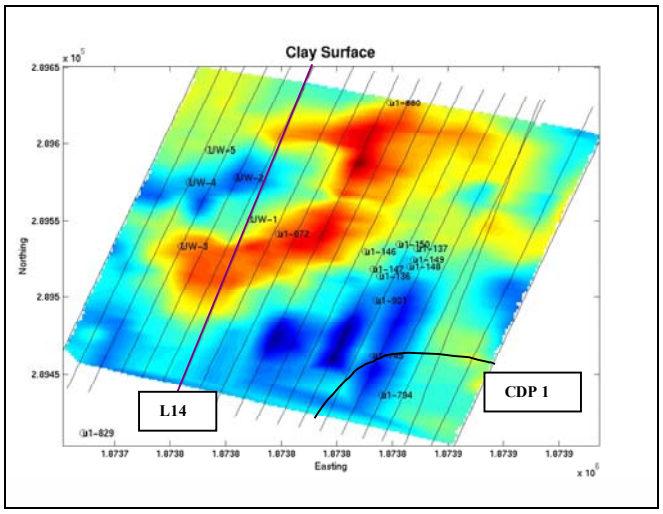

Figure 2: Clay surface with 3D lines and well control.

DATA PROCESSING

Initial data processing consists of a 10-20-100-200 MHz bandpass filter to attenuate high frequency noise and the low frequency transient present at small times and near offsets (DEWOW). This is followed by a time-zero lag correction. For PSDM analysis, we apply AGC. For AVO analysis, we apply a true amplitude correction, which is further discussed below. Additional processing steps are discussed in detail below.

Pre-Stack Depth Migration

Pre-stack depth migration is an iterative technique in which data is migrated with an initial velocity model, then visually inspected to see if reflected energy from a given point migrates to the same depth independent of offset. The model may then be updated from the top down to "focus" all reflected energy (Al-Yahya, 1989; Lafond and Levander, 1993). In this study, all data are migrated in the common-offset domain using a 2D Kirchhoff algorithm that accounts for topography. The migrated data are sorted to common-image point gathers (CIPs) for inspection. CIPs are the PSDM analog of common-midpoint gathers in normal moveout (NMO) processing (Yilmaz, 1987). A "focused" image is obtained when all reflections are flattened in the CIP domain. CIPs are stacked to produce the migrated image. Stacking attenuates random noise and processing artifacts, preparing the data for 3D interpretation.

Velocities estimated from PSDM analysis aren't subject to the assumptions of NMO processing, such as near vertical incidence, horizontal reflections, and a laterally homogeneous velocity field. In general, PSDM analysis produces an accurate and relatively detailed image of the subsurface velocity field.

In this study, the starting velocity model is constructed by first measuring the velocity of the direct ground wave. This is the surface velocity and is held fixed throughout the analysis. NMO velocity analysis is then applied at the clay reflection, and this velocity is initially assumed to be the average propagation velocity above the clay. We then compute a linear velocity gradient based on the NMO and direct wave results, although the actual gradient is probably non-linear. With this starting model, six iterations of PSDM analysis result in the final model (Figure 3). We

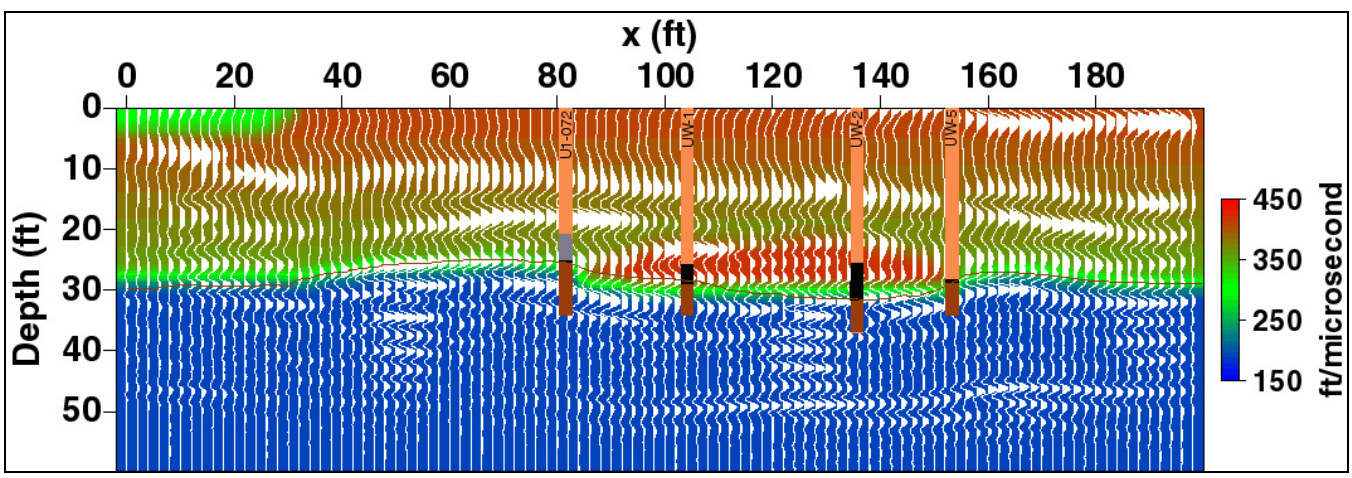

Figure 3: Velocity model for Line 14 from the northwest corner of the 3D survey with verification boreholes projected onto the line and stacked section overlain. . A high velocity anomaly sits in a trough on the clay surface. The anomaly is located between x=85 ft and x=155 ft at depths from 22 ft to 29 ft. The water table is at 29 ft and maximum depth-to-clay below the anomaly is 33 ft. Borehole data show the location of elevated hydrocarbon levels in black. U1-072 was acquired in 1986 as part of the initial site characterization.

velocity field between lines assuming no large lateral velocity gradients exist in the cross-line direction, which appears to be a fair assumption in this case.

Amplitude Variation With Offset Analysis

In AVO analysis, we study the changing amplitude of reflections with increasing antenna separation, or offset (Baker, 1998; Bergmann et al., 1998; Lehmann, 1996; Zeng et al., 2000). This technique has been used successfully ins seismic exploration since the early 1980s to locate oil and gas rich sand bodies (Castagna, 1993). It is especially useful when such reservoirs are laterally discontinuous. However, the fundamental physics governing elastic reflection amplitudes do not apply directly to GPR, and the physics of electromagnetic wave propagation must be considered to make meaningful interpretations.

Our analysis is based on the Fresnel equations, which implies several significant assumptions. These include: 1) a propagating plane wave with a planar but sharp boundary at the reflecting interface, 2) local lateral homogeneity, and 3) isotropic media. Additional assumptions include locally horizontal reflections and frequency independent material properties. While recognizing that in general these assumptions are not valid, we submit that they do provide a fair first order approximation at many sites where the GPR signal propagates efficiently.

The most important and error prone step in the AVO analysis is the amplitude correction. There are a number of factors that influence the amplitude response that are unrelated to the reflection coefficient. This includes spherical spreading (S), the source and receiver radiation patterns (R), and intrinsic attenuation of the propagation medium. Prior to Fresnel analysis, we must attempt to remove these effects. The correction is given by:

$$A_c = \frac{1}{S}\frac{1}{R}e^{at}A_o \qquad (1)$$

where 1/S is the spreading correction, 1/R is the radiation pattern correction, a is the attenuation coefficient, A_o is the observed amplitude, and A_c is the corrected amplitude. We assume spherical spreading. The radiation pattern correction is based on the semi-empirical radiation pattern derived by Bradford (Bradford, 1998). This pattern has the form $1/\cos\theta$, where θ is the take-off angle, at angles less than the critical angle at the earth/air interface, $\theta < \theta_c$. At take-off angles greater than θ_c, the function $1/\cos\theta$ is used until it intersects with the geometric optics approximation (Papas and Engheta, 1982) to an infinitesimal dipole. This radiation pattern approximates experimental data presented by Annan et al. (1975).

For this study, computation of the attenuation coefficient is based on clay reflection amplitudes in locations where the reflection is horizontal and there are no significant shallower reflections. Since we know that the sand/clay interface is a large negative velocity contrast, the attenuation coefficient is calibrated to approximate the Fresnel predicted amplitude behavior for the clay reflection. In this scenario, amplitudes remain nearly constant through our range of incident angles. Computing the attenuation correction in this way includes a "fudge" factor that accounts for errors in spreading and radiation pattern corrections. To identify possible NAPL rich zones, we look for AVO curves that grow significantly with increasing offset, as predicted for a positive velocity contrast.

With these amplitude corrections, and given the stated assumptions, the resulting AVO curve is approximately proportional to the reflection coefficient curve (Castagna, 1993). We apply two two levels of analysis. First, we look for deviations from background amplitude behavior, which in this case is defined by the clay reflection. This can be useful for rapid data assessment and identification of zones deserving more detailed analysis. Second, we estimate the velocity ratio using a least squares curve-fitting algorithm that compares the recorded amplitude behavior with predictions from the TE Fresnel equation (2). Curve fitting is applied in the amplitude versus angle of incidence (AVA) domain where angles of incidence are computed to correspond with each transmitter/receiver separation. For a transversely polarized electric field, the Fresnel amplitude reflection coefficient can be written as a function of incident angle θ_i,

$$\frac{E_R}{E_I} = \left(\frac{1-\alpha\beta}{1+\alpha\beta}\right) \qquad (2)$$

where

$$\alpha = \frac{\sqrt{1-\left[\left(v_2/v_1\right)\sin\theta_i\right]^2}}{\cos\theta_i} \qquad (3)$$

and

$$\beta = \frac{\mu_1 v_1}{\mu_2 v_2} \qquad (4)$$

Subscripts 1 and 2 indicate the upper and lower layers respectively. Magnetic permeability, μ, is assumed constant, and the radar velocity ratio, v_2/v_1, is the parameter varied to fit the corrected amplitude data.

DATA INTERPRETATION AND DISCUSSION

The strongest laterally continuous event is the reflection from the alluvium/clay boundary. The exact location of the interface on the reflected wavelet is uncertain due to processing artifacts and uncertainty in the velocity estimate, so a point on the wavelet is chosen based on clay depth at a control point. We use the monitoring well, OU1-072 to calibrate our picking. With this 'template,' interpretation of the depth-to-clay then proceeds in a fairly straightforward manner. The interpreted clay topography reveals a detailed

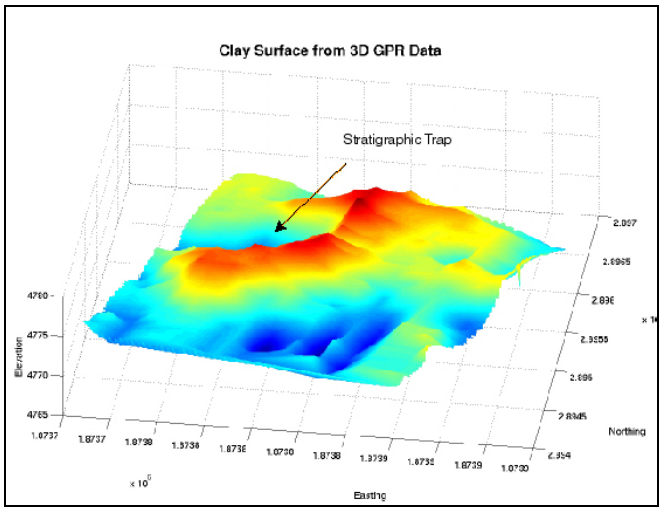

Figure 4: The alluvium/clay interface was mapped in a dense 3D survey. The prominent ridge and trough may be a stratigraphic trap where low permittivity LNAPL accumulates.

and varied surface (Figure 4) that agrees with twelve previously logged wells to within about 1 ft (Figure 2). The notable exception to this good agreement is the southeast corner of the survey where the largest observed error is 3 ft. and the survey footprint is clearly evident (Figures 2 and 4). In this area, scattering from nearby surface objects introduces significant noise. However, both pre-stack migration and post-migration stacking are effective velocity filters, helping to reduce the coherent air velocity noise allowing for a coarse interpretation. Additionally, five verification boreholes (UW-1 – UW-5) were drilled in the northwest corner of the survey subsequent to analysis of our data (Figure 2). The predicted depths to clay in these locations agree with the core data to within ± 0.7 ft with the exception of UW-3 where the error was 1.4 ft.

A significant departure from the background model emerges during PSDM velocity analysis. A high velocity anomaly, which does not correlate with known geology, is identified just above the water table in the northwest section of the 3D survey (Figure 3). It sits in a topographic low on the clay surface, which may act as a stratigraphic trap for accumulation of low permittivity LNAPL.

The high velocity zone is associated with a reflection that arches over the topographic low (Figure3). The AVO response of the anomalous reflection departs significantly from that of the clay reflection (Figure5). Fitting the Fresnel equation to the amplitude data, we estimate a velocity ratio (v_2 / v_1) at the reflecting interface of 1.39 ± 0.16. This is in good agreement with migration velocity model, which predicts a velocity ratio of 1.33. Error is estimated by calculating the standard deviation of velocity ratio estimates over all 20 CMPs used in the AVO analysis.

Suspecting that the high velocity anomaly was associated with a NAPL rich zone, we initiated a verification coring program. In September, 2001, four continuous cores (UW-1 – UW-4) were pulled from within the anomalous zone. The sampling geologist noted the depth to the top of the smear zone (as indicated by hydrocarbon staining and odor) and three soil samples from each core were extracted from within the smear zone for chemical analysis. Additionally, a fifth core was pulled just outside of anomalous zone for background control (UW-5) where only a thin trace of hydrocarbon was detected.

The cores indicate a relatively homogeneous stratigraphy from the surface to the clay layer, and no lithologic boundary is evident that explains the anomalous reflection. Elevated levels of hydrocarbon (varying from 1% - 4% total volume) were discovered above the water table in the sediments approximately 2 ft. below the depth we calculate for the reflection. The hydrocarbon rich zone forms the only significant boundary in the cores and is the most likely explanation for the origin of the reflection. The large velocity increase below the reflection indicates low electric permittivity. This is in contrast with the background effect where increasing water saturation with depth, particularly near the water table, leads to decreased velocity. Given all the available information, we interpret the high velocity zone as correlating with a zone of elevated NAPL saturation. The correlation of low permittivity with NAPL contaminated soil at this site is consistent with the results of a previous resistivity study (Lien and Enfield, 1998) located several hundred feet south of our survey area.

While we are confident that the measured GPR response is caused by the NAPL rich zone, two problems must be addressed. First, the fact that the computed depth to the reflection deviates from the observed depth by about 2ft can be explained by only a 6% error in the velocity model above the reflection. An alternative explanation is that NAPL is present at shallower depths, but did not present the visual cues the sampling geologist used to identify hydrocarbon. It is more difficult to explain how the large observed velocity

increase can originate from the relatively low NAPL concentration recorded in the verification boreholes. Using simple mixing laws or an empirical formulation such as the Topp equation (Greaves et al., 1996), the velocity we measured would require nearly total displacement of the pore water with NAPL or air. This is not the case. We believe that the contaminant has replaced water as the wetting agent in which case relatively low concentrations of NAPL may lead to large increases in velocity. Previous work has indicated that the OU1 plume is a mixed wet system (Meinardus, 2000) so this is a reasonable interpretation. Endres and Redman (1996) present the results of a modeling study of a NAPL/water pore fluid that illustrate the significance of fluid distribution within the pore system. Their results are not directly applicable to this study since we are dealing with a three-phase pore fluid – NAPL/water/air. Further analysis is needed to develop a petrophysical model that describes the measured radar response.

CONCLUSIONS

Clay surface imaging was successful, and the evidence for direct detection of NAPL is compelling. We discovered a high velocity zone that correlates with elevated hydrocarbon levels found in post processing soil samples. Both PSDM velocity analysis and AVO analysis were successful in identifying the high velocity zone. The zone sits in a logical place for contaminant to accumulate.

This result is significant for several reasons. First, we believe this to be the first reported case of GPR AVO and migration velocity analysis being used for direct detection of NAPL in an uncontrolled field setting over an existing plume. And second, the NAPL was found in a location previously thought to lie outside the NAPL plume. The key to this success was quantitative analysis of multi-offset radar data to identify electric property anomalies that may otherwise have gone unnoticed in qualitative interpretation of conventional radar profiles. This again raises the potential for GPR to be used as a NAPL exploration tool at contaminated sites. Clearly there is potential for continued use at HAFB and similar hydrogeologic sites, but we submit that these methods may be more generally applicable. It is well established that high conductivity or permittivity anomalies may be associated LNAPL plumes at some sites in apparent departure with the predicted or theoretical low conductivity/low permittivity NAPL anomaly. We suggest that anywhere that GPR operates effectively, the same quantitative approach may be used to identify contaminate related electrical anomalies, regardless of whether they are high or low conductivity or permittivity deviations. The key is that the contaminant causes a departure from the background electrical properties. It is extremely important to note that there is an inherent non-uniqueness to these methodologies and that positive NAPL identification requires direct sampling of the soils. However, with some

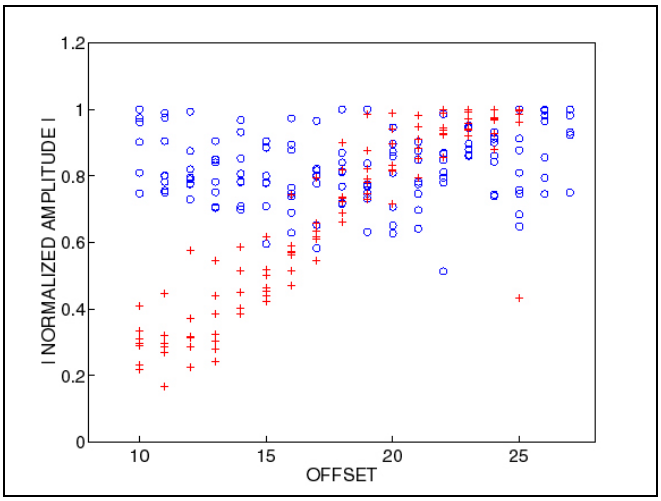

Figure 5: Comparison of AVO behaviors. Blue circles and red crosses indicate clay reflection and anomalous reflection amplitudes respectively. Anomalous reflection amplitudes grow considerably with offset.

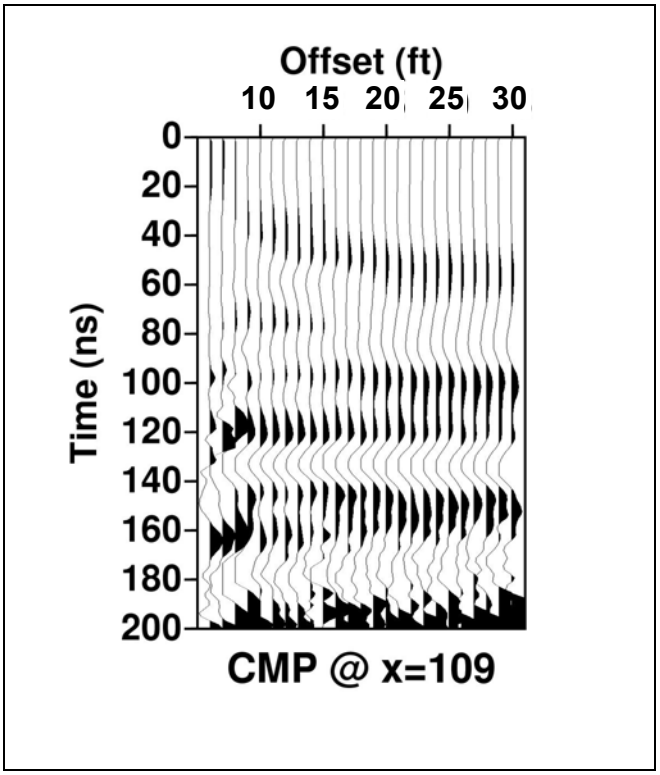

Figure 6: True amplitude CMP gather from Line 14 of the 3D patch with static gain and NMO applied. The anomalous reflection at about 100 ns gets much stronger with increasing offset. The center of the clay reflection is at about 135 ns.

site specific calibration, we believe these analysis tools can help guide and optimize a coring program, both by identifying likely NAPL zones, and by mapping stratigraphic variations that may control contaminant transport.

ACKNOWLEDGEMENTS

Processing and interpretation of the data were funded under the DOE EMSP Groundwater/Vadose Zone Integration Project, Grant #DE-FG07-99ER15008. The field effort was supported by Hill Air Force Base with the contract administered by CH2MHill Inc., who also provided field logistics and survey support. Intera, Inc. collected and analyzed the soil samples.

REFERENCES

Al-Yahya, K.M., 1989. Velocity analysis by iterative profile migration, *Geophysics*, Vol. 54 , pp. 718-729.

Annan, A.P., Waller, W.M., Strangway, D.W., Rossiter, J.R., Redman, J.D., and Watts, R.D., 1975. The electromagnetic response of a low-loss, 2-layer, dielectric earth for horizontal electric dipole excitation, *Geophysics*, Vol. 40, No. 2, pp. 285-298.

Baker, G.S., 1998. Applying AVO analysis to GPR data, *Geophys. Res. Let.*, Vol. 25, No. 3, pp. 397-400.

Bergmann, T., Robertsson, J.O.A., and Holliger, K., 1998. Finite-difference modeling of electromagnetic wave propagation in dispersive and attenuating media, *Geophysics*, Vol. 63, No. 3, pp. 856-867.

Bradford, J.H., 1998. Characterizing shallow aquifers with wave-propagation based geophysical techniques: Imaging and attribute analysis: Ph. D. thesis, Rice University.

Brewster, M.L., and Annan, A.P., 1994. Ground-penetrating radar monitoring of a controlled DNAPL release: 200 MHz radar, *Geophysics*, Vol. 59, No. 8, pp. 1211 - 1221.

Castagna, J.P., 1993. AVO Analysis - Tutorial and review, *in* Castagna, J.P., and Backus, M.M., Eds., Offset-dependent reflectivity - Theory and practice of AVO analysis: Soc. Expl. Geophys., Invest. Geophys., Vol. 8, pp. 3-36.

Daniels, J.J., Robert, R., and Vendl, M., 1995. Ground penetrating radar for the detection of liquid contaminants, *J. Appl. Geophys.*, Vol. 33, No. 1-3, pp. 195-207.

DeRyck, S.M., Redman, J.D., and Annan, A.P., 1993. Geophysical monitoring of a controlled kerosene spill: *SAGEEP '93*;Env. Eng. Geophys. Soc., pp. 5-19.

Endres, A.L., and Redman, J.D., 1996. Modeling the electrical properties of porous rocks and soils containing immiscible contaminants, *J. Env. Eng. Geophys.*, Vol. 0, No. 2, pp. 105-112.

Fisher, E., McMechan, G.A., and Annan, A.P., 1992. Acquisition and processing of wide-aperture ground-penetrating radar data, *Geophysics*, Vol. 57, pp. 495-504.

Fisher, S.C., Stewart, R.R., and Jol, H.M., 1996. Ground-penetrating radar (GPR) data enhancement using seismic techniques, *J. Env. Eng. Geophys.*, Vol. 1, No. 2, pp. 89-96.

Greaves, R.J., Lesmas, D.P., Lee, J.M., and Toksoz, M.N., 1996. Velocity variation and water content estimated from multi-offset, ground-penetrating radar, *Geophysics*, Vol. 61, No. 3, pp. 683-695.

Lafond, C.F., and Levander, A.R., 1993. Migration moveout analysis and depth focusing, *Geophysics*, Vol. 58, No. 1, pp. 91-100.

Lehmann, F., 1996. Fresnel equations for reflection and transmission at boundaries between conductive media, with applications to georadar problems: *6th Internat. Conf. GPR*, pp. 555-560.

Lien, B.K., and Enfield, C.G., 1998. Delineation of subsurface hydrocarbon contaminant distribution using a direct push resistivity method, *J. Env. Eng. Geophys.*, Vol. 2, No. 3, pp. 173-179.

Loughridge, J., 1998. Application of seismic tools and techniques to ground-penetrating radar (GPR) studies: M.A. thesis, Rice University.

Meinardus, H.,2000. Personal Communication

Newmark, R.L., Daily, W.D., Kyle, K.R., and Ramirez, A.L., 1998. Monitoring DNAPL pumping using integrated geophysical techniques, *J. Env. Eng. Geophys.*, Vol. 3, No. 1, pp. .

Papas, C.H., and Engheta, 1982. Radiation patterns of interfacial dipole antennas, *Radio Science*, Vol. 17, No. 6, pp. 1557-1566.

Powers, M.H., and Olhoeft, G.R., 1996. Modeling the response of leaking, buried pipes: *SAGEEP '95 Symposium on the application of geophysics to environmental and engineering problems*, Keystone, CO;Soc. Appl. Geophys. Env. Eng., pp. 525-534.

Yilmaz, O., 1987, Seismic data processing, Soc. Expl. Geophys.

Young, R.A., and Sun, J., 1996. 3D ground penetrating radar imaging of a shallow aquifer at Hill Air Force Base, Utah, *J. Env. Eng. Geophys.*, Vol. 1, No. 2, pp. 97-108.

Young, R.A., and Sun, J., 1998. Extracting a radar reflection from a cluttered environment using 3-D interpretation, *J. Env. Eng. Geophys.*, Vol. 3, No. 3, pp. 121-131.

Zeng, X., McMechan, G.A., and Xu, T., 2000. Synthesis of amplitude versus offset variations in ground-penetrating radar data, *Geophysics*, Vol. 65, No. 1, pp. 113-125.